TECHNISCHE UNIVERSITÄT MÜNCHEN
Physik-Department
Institut für Theoretische Physik
Lehrstuhl Univ.-Prof. Dr. Peter Vogl

Quantum spin transport in semiconductor nanostructures

Christoph Schindler

Vollständiger Abdruck der von der Fakultät für Physik der Technischen Universität München zur Erlangung des akademischen Grades eines

Doktors der Naturwissenschaften (Dr. rer. nat.)

genehmigten Dissertation.

Vorsitzender: Univ.-Prof. Dr. Alexander Holleitner

Prüfer der Dissertation: 1. Univ.-Prof. Dr. Peter Vogl
2. Priv.-Doz. Dr. Dietrich Einzel

Die Dissertation wurde am 08.03.2012 bei der Technischen Universität München eingereicht und durch die Fakultät für Physik am 27.04.2012 angenommen.

Contents

Abstract 7

Introduction 11

I. Predictive electronic structure calculations for semiconductor heterostructures 15

1. Overview over semi-empirical tight-binding theory 17
1.1. Introduction 17
1.2. Basic introduction into semi-empirical tight-binding theory 17
1.2.1. Common approximations in tight-binding theory 19
1.2.2. Parametrization of the tight-binding Hamiltonian 20
1.3. Implementation of spin-orbit coupling 21
1.4. Implementation of strain 22
1.5. Summary 25

2. Novel relativistic tight-binding method for HgTe and CdTe 27
2.1. Introduction 27
2.2. New sp^3d^5 parameters for HgTe and CdTe 27
2.3. Summary 32

3. Results for the k-linear spin-orbit coupling in semiconductor quantum wells 33
3.1. Introduction 33
3.2. Theory of spin-orbit induced k-linear band splitting 33
3.3. New results for symmetric quantum well structures in electric fields . 36
3.4. Prediction of strain-enhanced spin splitting 41
3.5. Influence of higher order in k spin splitting 44
3.6. Summary 46

4. Results for HgTe quantum well structures 49
4.1. Introduction 49
4.2. New results on the subband structure of HgTe quantum wells 50
4.3. Novel envelope function approximation for HgTe quantum wells . . . 53
4.4. Summary 56

II. Spin dependent quantum transport calculations 59

5. Non-equilibrium Green's functions theory for spin-dependent quantum transport 61
5.1. Introduction 61
5.2. Overview over the non-equilibrium Green's function theory 62
5.3. Boundary conditions for open quantum devices 67
5.4. Novel treatment of scattering: The multi-scattering Büttiker probe model 72
5.5. Implementation of external magnetic fields 76
5.6. Spin-resolved observables 80
5.7. Summary 85

6. Results for the spin-dependent electron focusing in external magnetic fields 87
6.1. Introduction 87
6.2. Theory of magnetic focusing and spin-orbit interaction 87
6.3. New results for magnetic focusing in semiconductor heterostructures with external electric and magnetic field 90
6.4. Summary 94

7. Review of the intrinsic spin-Hall effect in nanostructures 95
7.1. Introduction 95
7.2. Origin of the mesoscopic intrinsic spin-Hall effect 96
7.3. Analytic solution for the two level system 102
7.4. Summary 104

8. Prediction of giant intrinsic spin-Hall effect in tensile strained p-GaAs 105
8.1. Introduction 105
8.2. Inverse intrinsic spin-Hall effect in H-shaped structure 105
8.3. Prediction of large current induced spin polarization in three terminal T-shaped structure 109
8.4. Proposal of an all electrical detection scheme for current induced spin polarization 112
8.5. Summary 114

9. Prediction of an all electrical tunable spin polarizer in InSb quantum wells 117
9.1. Introduction 117
9.2. Bias controlled spin polarization in InSb quantum wells 118
9.3. Electrical detection of spin polarization in InSb quantum wells 120
9.4. Summary 122

10. A new sight on topological insulators 123
10.1. Introduction 123

10.2. Microscopic origin of topological insulators and the quantum spin Hall effect 124
10.2.1. Introduction 124
10.3. One-dimensional atomistic tight-binding model 125
10.3.1. Topological quantum number 129
10.4. Two-dimensional tight-binding model 132
10.4.1. Model without spin-orbit interaction 133
10.4.2. Model with spin-orbit coupling 134
10.5. Band inversion in real semiconductors 137
10.6. Prediction of spin transistor in HgTe quantum wells 140
10.7. Summary 144

11. Summary **147**

A. Analytic calculation of the Green's function for the 1D-model of a topological insulator **149**

B. Discrete Hamilton operators **151**

C. The local current operator for the cubic Dresselhaus model **157**

D. The mean free path in the Büttiker probe model **159**

Bibliography **161**

List of publications **173**

Acknowledgments **175**

Abstract

In this work, we study and quantitatively predict the quantum spin Hall effect, the spin-orbit interaction induced intrinsic spin-Hall effect, spin-orbit induced magnetizations, and spin-polarized electric currents in nanostructured two-dimensional electron or hole gases with and without the presence of magnetic fields. We propose concrete device geometries for the generation, detection, and manipulation of spin polarization and spin-polarized currents. To this end a novel multi-band quantum transport theory, that we termed the multi-scattering Büttiker probe model, is developed. The method treats quantum interference and coherence in open quantum devices on the same footing as incoherent scattering and incorporates inhomogeneous magnetic fields in a gauge-invariant and nonperturbative manner. The spin-orbit interaction parameters that control effects such as band energy spin splittings, g-factors, and spin relaxations are calculated microscopically in terms of an atomistic relativistic tight-binding model. We calculate the transverse electron focusing in external magnetic and electric. We have performed detailed studies of the intrinsic spin-Hall effect and its inverse effect in various material systems and geometries. We find a geometry dependent threshold value for the spin-orbit interaction for the inverse intrinsic spin-Hall effect that cannot be met by n-type GaAs structures. We propose geometries that spin polarize electric current in zero magnetic field and analyze the out-of-plane spin polarization by all electrical means. We predict unexpectedly large spin-orbit induced spin-polarization effects in zero magnetic fields that are caused by resonant enhancements of the spin-orbit interaction in specially band engineered and geometrically designed p-type nanostructures. We propose a concrete realization of a spin transistor in HgTe quantum wells, that employs the helical edge channel in the quantum spin Hall effect.

Zusammenfassung

In dieser Arbeit untersuchen wir den Quanten-Spin-Hall-Effekt, den intrinschen Spin-Hall-Effekt, durch die Spin-Bahn-Wechselwirkung induzierten Magnetisierungen und spinpolarisierte elektrische Ströme in nanostrukturierten zweidimensionalen Elektron- und Lochgasen mit und ohne externes Magnetfeld. Wir streben dabei quantitative Vorhersagen zu diesen Effekten an. Wir schlagen konkrete Bauteile vor, die Spinpolarisationen und spinpolarisierte Ströme erzeugen, manipulieren und detektieren können. Wir haben dafür eine neuartige Mehrband – Quantentransport – Theorie entwickelt, die wir multi-scattering Büttiker probe Modell genannt haben. Die Methode behandelt Quanteninterferenz und Kohärenz in offenen Quantensystemen auf derselben Basis wie inkohärente Streuung und erlaubt die nicht störungstheortische und eichinvariante Behandlung von inhomogenen Magnetfeldern. Die Spin-Bahn-Kopplungsparameter, die Effekte wie die spinabhängige Bandenergieaufspaltung, g-Faktoren und Spinrelaxation kontrollieren, werden mit Hilfe der atomistischen und relativistischen Tight-Binding-Theorie berechnet. Wir berechnen die Elektronenfokussierung in externen magnetischen und elektrischen Feldern. Wir haben den intrinschen Spin-Hall-Effekt und seinen inversen Effekt in verschiedenen Materialsystemen und Geometrien ausführlich untersucht. Wir stellen einen geometrieabhängingen Schwellwert für die Spin-Bahn-Wechselwirkung fest, der nicht von elektronenartigen GaAs-Strukturen erreicht wird. Wir schlagen Geometrien vor, die den Ladungsstrom ohne externes Magnetfeld spinpolarisieren und die Spinpolarisation durch eine rein elektrische Messung analysieren können. Wir sagen unerwartet starke spin-bahn-wechselwirkungsinduzierte Spinpolarizationseffekte ohne externes Magnetfeld in speziell band- und geometrieoptimierten lochartigen Nanostrukturen voraus, die durch eine resonante Verstärkung der Spin-Bahn-Wechselwirkung hervorgerufen werden. Wir schlagen eine konkrete Realisierung eines Spintransistors vor, die auf dem Quanten-Spin-Hall-Effekt in HgTe-Nanostrukturen beruht.

Introduction

The seminal proposal of a spin-based transistor by Datta and Das in 1990 [1] has basically created the modern field of semiconductor spintronics. Since then a lot of work has been devoted to the goal to use the spin degree of freedom of the carrier for information processing or quantum computation [2]. An important prerequisite towards spin-based electronic devices is to have control over the spin degree of freedom. Since magnetic fields are hard to localize and to implement in nowadays electronics, spin-orbit coupling in semiconductor nanostrucures comes into focus as it may provide the possibility for spin manipulation on an all semiconductor basis [3] in zero external magnetic field. Among many spin-orbit coupling effects, the spin-Hall effect [4, 5] is one of the most promising ones to provide a possibility to generate and detect spin-polarized electric currents as well as pure spin currents. These spin effects, however, are in generally small and not easily detectable in experiment. Thus, quantitative theoretical predictions that realistically take into account geometrical effects and material properties are needed to guide and interpret experimental efforts and results, respectively.

Another only recently discovered effect with a large device application potential is the so-called quantum spin Hall effect in topological insulators [6–8]. These material have an insulating gap in the bulk but feature gapless helical edge states at boundaries. While first discovered in two-dimensional quantum well structures [9], it is clear now, that also three-dimensional systems can have similar properties [10]. Due to the helical properties, electrical current through these edge channels is almost perfectly spin polarized, which opens new possibilities for spin injection, detection, and manipulation by all electrical means. Since these states are topologically protected, the quantum spin Hall effect is more robust than the intrinsic spin-Hall effect in normal semiconductors.

The main purpose of tis work, is to propose all semiconductor based devices that are capable of polarizing, detecting and manipulating the spin degree of freedom of electrons and holes. We aim at quantitatively predicting the spin-orbit interaction induced intrinsic spin-Hall effect, spin-orbit induced magnetizations, and spin-polarized electron currents as well as the quantum spin Hall effect in nanostructured two-dimensional electron or hole gases with and without the presence of magnetic fields. To this end, we have developed a novel multi-band quantum transport theory, the multi-scattering Büttiker probe (MSB) model that treats quantum interference and coherence on the same footing as incoherent scattering and incorporates inhomogeneous magnetic fields in a gauge-invariant and nonperturbative manner. The spin-orbit interaction parameters that control effects such as band energy spin splittings, g-factors, and spin relaxations are calculated microscopically in terms of an

atomistic relativistic tight-binding model. To quantitatively predict quantum transport properties of topological insulators, we have developed new few-band models that describe all relevant spin-orbit coupling mechanisms in HgTe/CdTe quantum wells. We have performed detailed studies of the intrinsic spin-Hall effect, its inverse effect, and the quantum spin Hall effect in various material systems and geometries. We propose several concrete nanostructured materials and geometries for spintronic devices.

This thesis is organized as follows. In part one we present our results for the electronic structure of semiconductor heterostructures. In particular, we focus on the spin-orbit interaction parameters that control the band energy spin splittings. A precise knowledge of these parameters is curtail for quantitative predictions of spin-transport properties. In Chapter 1, we briefly review the atomistic semi-empirical tight-binding method, that we base our electronic structure calculations on and present our novel parametrization for the II-VI semiconductor materials HgTe and CdTe which we have developed, since HgTe/CdTe quantum wells came into focus recently in the context of topological insulators while a state-of the art tight-binding theory for these materials was not published yet. In Chapter 3, we present our results for the k-dependent spin-orbit induced splittings of nondegenerate bands in various III-V semiconductor heterostructures. We investigate the interplay between the so-called Rashba and Dresselhaus spin-orbit interaction in external electric field and find qualitatively different behavior than predicted by simple envelope function theory. The physical origin of these differences are discussed. Furthermore, we predict huge k-linear spin splitting in tensile strained p-GaAs quantum wells, that is enhanced up to two orders of magnitude and tunable by the applied strain. In Chapter 4, we present our results for the subband structure and dispersion in HgTe quantum wells. We predict strong anticrossing of electron and hole bands as a function of the well thickness and a resonantly enhanced k-dependent spin splitting of the subband dispersion. We further develop two new envelope function models for quantum transport calculations in HgTe quantum wells, that are based on our novel tight-binding results and take into account all relevant spin-orbit coupling mechanisms, in contrast to models presented so far in literature.

In part two of this thesis, we turn to our results on the quantum spin-transport properties of nanostructered two-dimensional electron and hole gases. In Chapter 5, we present our method the non-equilibrium Green's function theory. After a short overview of the non-equilibrium Green's function method for quantum transport calculations, we address the problem of boundary conditions for open quantum systems in the general multi-band situation. We further present our newly developed multi-scattering Büttiker probe model for dissipative quantum transport, that accounts for individual scattering mechanisms and reproduces experimental results quantitatively. It is numerically extremely efficient, in order to allow for predictive transport calculations in realistic, arbitrarily shaped three-dimensional nanostructures. We further show, how external magnetic fields can be incorporated into the theory. Finally, we show how experimentally observable quantities are calculated from the non-equilibrium Green's functions. In Chapter 6, we employ our quantum transport

method in combination with the results of the electronic structure calculations to predict spin-dependent transverse electron focusing in external magnetic and electric fields for various semiconductor nanostructures. In Chapter 7, we review the properties of the intrinsic spin-Hall effect in two-dimensional nanowires and employ a simple analytical model to elucidate the origin of the effect in nanostructures as opposed to the infinite 2DEG. In Chapter 8 and Chapter 9, we show, how the intrinsic spin-Hall effect and its inverse can be employed in realistic nanodevices for spin polarization, manipulation, and detection. We predict several concrete nanostructured materials and device geometries that exhibit large spin-polarization effects. We propose concrete experiments to unambiguously measure the spin polarizations caused by the intrinsic spin-Hall effect. In Chapter 10, we focus on topological insulators. We first develop a simple tight-binding model, that explains the microscopic origin of the quantum spin Hall effect in materials with a so-called inverted band structure. We show, that in contrast to the wide spread assumption, the spin-orbit interaction is not essential for a topological insulator. We further employ our newly developed envelope function model for HgTe quantum wells and propose a concrete realization of a spin transistor, on the basis of the quantum spin Hall effect. Finally, we summarize the thesis in Chapter 11.

Part I.

Predictive electronic structure calculations for semiconductor heterostructures

1. Overview over semi-empirical tight-binding theory

1.1. Introduction

The semi-empirical tight-binding theory as developed by Slater and Koster [11] and later by Harrison [12] gives a physically transparent, semi-quantitative picture of the structural and electronic properties of molecules and solids. The tight-binding theory has been successfully applied to many systems since then such as bulk band structures of ionic solids and semiconductors, superlattices, quantum dots, amorphous solids, surfaces, transition metals, lattice dynamics, and molecular dynamics just to name a few. In this work, we use the atomistic tight-binding theory to calculate the band structure of quantum wells and superlattices with special emphasis on the spin-dependent properties close to the Brillouin zone center, the so-called Γ-point ($\mathbf{k} = 0$). These spin properties also depend crucially on backfolded zone edge states, which are well described in tight-binding theory, in contrast to simple envelope function $\mathbf{k}\cdot\mathbf{p}$ theories, which rely on an expansion of the Hamilton operator for small wave vectors around the Γ-point. We will therefore give a short introduction into the basics of tight-binding theory in Sec. 1.2. More detailed descriptions may be found e.g. in Refs. [11–14]. We will then in Chapter 2 present our novel sp^3d^5 tight-binding model for the II-VI semiconductors HgTe and CdTe. These materials have come into focus recently in the context of topological insulators and the quantum spin Hall effect. However, a quantitative state of the art tight-binding model is still ascent in literature.

1.2. Basic introduction into semi-empirical tight-binding theory

The basic idea behind the tight-binding scheme is that electrons in a crystal are tightly bound to their atoms and that the interaction between the atoms is weak enough, such that an atomistic picture is still meaningful and one can use atomic-orbitals like basis states to expand the crystal wave function. An important result of the seminal work by Harrison [12] is that although it is difficult to determine the crystal Hamiltonian operator H and a basis of orthogonal atomiclike functions $|\,I\,\rangle$ separately, the elements $\langle\, I \,|\, H \,|\, I' \,\rangle$ of the Hamiltonian matrix follow very simple chemical trends. While the diagonal matrix elements are proportional to atomic

ionization energies the off-diagonal elements are approximately universal functions of the interatomic distance. As a consequence most applications of tight-binding theory rely entirely on the formulation of Hamiltonian matrix elements.

In tight-binding theory, the single-particle eigenstates of the crystal are expanded into atomiclike orbitals $|\alpha, I\rangle$, where I is a site index and α is a symmetry related index that specifies the angular momentum and spin quantum numbers. Since we focus on periodic crystals in this work, the vector pointing to the lattice site I can be written as $\mathbf{R}_I = \mathbf{R}_L + \mathbf{R}_\tau$, where L labels the unit cell and τ the various basis atoms within one unit cell. Note that for different lattice sites, the $|\alpha, I\rangle$ are in general not orthogonal. However, Löwdin showed [15], that it is possible to orthogonalize the basis functions while preserving their symmetry properties. These so-called Löwdin orbitals follow the orthogonality relation

$$\langle \alpha', I' \mid \alpha, I\rangle = \delta_{L',L}\delta_{\tau',\tau}\delta_{\alpha',\alpha}. \tag{1.1}$$

In order to avoid too many, confusing indices, we lump together the orbital index α and the intracell site index τ into a single index α. Therefore a sum over α implies a sum over all orbital states within one unit cell. We thus write the lattice vector as $\mathbf{R}_I = \mathbf{R}_{\alpha L}$.

In a periodic crystal, Bloch sums can be formed from the Löwdin functions that are characterized by the crystal momentum $\mathbf{k}$,

$$|\alpha, \mathbf{k}\rangle = \frac{1}{\sqrt{N}} \sum_L e^{i\mathbf{k}\mathbf{R}_{\alpha L}} |\alpha, L\rangle , \tag{1.2}$$

where N is the number of unit cells in the crystal. In the Bloch basis, the crystal Hamiltonian matrix can be represented as,

$$H = \sum_{\mathbf{k}} \sum_{\alpha',\alpha} |\alpha', \mathbf{k}\rangle H_{\alpha',\alpha} \langle \alpha, \mathbf{k}| . \tag{1.3}$$

Note that in this representation the Hamiltonian becomes diagonal in the crystal momentum $\mathbf{k}$. That makes it convenient to work with because the Hamiltonian breaks up into submatrices for each $\mathbf{k}$. That means each wave vector can be treated independently. The dimension of the Hamiltonian thus reduces to the number of atoms in the unit cell times the included orbital states per atom. Note that if scattering is included that mixes different k-states this advantage is at least partly lost. The Hamiltonian matrix elements $H_{\alpha',\alpha}(\mathbf{k})$ read in the basis given in Eq. (1.2),

$$\begin{aligned}
H_{\alpha',\alpha}(\mathbf{k}) &= \langle \alpha', \mathbf{k}| H |\alpha, \mathbf{k}\rangle \\
&= \frac{1}{N} \sum_{L',L} e^{i\mathbf{k}(\mathbf{R}_{\alpha L} - \mathbf{R}_{\alpha' L'})} \langle \alpha', L'| H |\alpha, L\rangle \\
&= \sum_L e^{i\mathbf{k}(\mathbf{R}_{\alpha L} - \mathbf{R}_{\alpha'})} \langle \alpha', 0| H |\alpha, L\rangle \\
&= \varepsilon_\alpha \delta_{\alpha',\alpha} + \sum_{L\neq 0} e^{i\mathbf{k}(\mathbf{R}_{\alpha L} - \mathbf{R}_{\alpha'})} t_{\alpha',\alpha} \left(\mathbf{R}_{\alpha L} - \mathbf{R}_{\alpha'}\right) ,
\end{aligned} \tag{1.4}$$

where $\mathbf{R}_\alpha = \mathbf{R}_{\alpha\, L=0}$ and the summation over L' cancels the normalization factor $1/N$ due to the translational invariance. In Eq. (1.4), we have introduced the on-site matrix elements

$$\varepsilon_\alpha = \langle \alpha, L |\, H \,| \alpha, L \rangle \,, \tag{1.5}$$

and the so-called hopping matrix elements

$$t_{\alpha',\alpha}\left(\mathbf{R}_{\alpha\, L} - \mathbf{R}_{\alpha'\, L'}\right) = \langle \alpha', L' |\, H \,| \alpha, L \rangle \,. \tag{1.6}$$

The on-site matrix elements are connected to the potential energy, while the hopping matrix elements are connected to the kinetic energy of the system, since they allow for an electron to be transfered from one atom to another.

The Bloch eigenfunctions of the Hamiltonian (Eq. (1.4)) are denoted by $|n, \mathbf{k}\rangle$, where n labels the energy bands and includes the Kramers index for the spin degree of freedom. These eigenfunctions are expanded in terms of the Bloch basis (Eq. (1.2)) as,

$$|n, \mathbf{k}\rangle = \sum_\alpha C_{\alpha,n}(\mathbf{k})\, |\alpha, \mathbf{k}\rangle \,, \tag{1.7}$$

where the $C_{\alpha,n}(\mathbf{k})$ are the expansion coefficients which together with the corresponding energy eigenvalues $E_n(\mathbf{k})$ follow from the Schrödinger equation

$$H\, |n, \mathbf{k}\rangle = E_n(\mathbf{k})\, |n, \mathbf{k}\rangle \,. \tag{1.8}$$

In the Bloch basis, we get the following secular equation

$$\sum_\alpha \left[H_{\alpha',\alpha}(\mathbf{k}) - E_n(\mathbf{k}) \langle \alpha', \mathbf{k} \mid \alpha, \mathbf{k}\rangle\right] C_{\alpha,n}(\mathbf{k}) = 0, \tag{1.9}$$

which has to be solved. The complete band structure then follows from the set $\{E_n(\mathbf{k})\}$ for all wave vectors $\mathbf{k}$. Please note, that if one uses the orthogonalized Löwdin orbitals, the overlap matrix $\langle \alpha', \mathbf{k} \mid \alpha, \mathbf{k}\rangle$ in Eq. (1.9) becomes the identity matrix which simplifies the problem significantly. However, the solution of Eq. (1.9) as it stands is still a quite challenging task. Therefore, we will introduce some approximations that are commonly used in tight-binding models.

1.2.1. Common approximations in tight-binding theory

Some very useful simplifications have been proposed by Slater and Koster [11]. By an effective reduction of the basis to a few orbitals, typically 4-20 per atom, the numerical effort can be drastically reduced. The minimal set of orbitals to get physically meaningful results for bulk semiconductors is an sp^3 basis as was pointed out by Chadi and Cohen [16]. Later Vogl et al. [17] have introduced an excited auxiliary s-state, called s^*. Although somehow artificial this additional state models the coupling with higher energy states and improves the results for the conduction band significantly. Because this parametrization still fails to reproduce some important features of the band structure satisfactorily, Jancu et al. [18] have used an $sp^3d^5s^*$

parametrization and could show, that most of the issues of smaller parameter sets can be resolved.

In Eq. (1.6), the distance between coupled atoms is in principle not limited. However, due to the localized basis functions, the matrix elements are getting smaller with distance rapidly. Therefore, it is often enough to consider the nearest neighbor coupling only. Besides reducing the numerical effort another advantage of taking only nearest neighbor coupling into account is the reduction of the parameter space, which in turn reduces the freedom of choice for the parameters and makes the set much clearer. Moreover, it simplifies the way to model interfaces between different materials in heterostructures. We will therefore limit our calculations to nearest neighbor tight-binding models.

Due to the Coulomb potential in the Hamilton operator H, the hopping matrix elements (Eq. (1.6)) include in principle up to four center integrals. The theory can be drastically simplified by only taking up to two-center terms into account which gives the effective potential the character of a two-atomic molecule. The orbitals can be chosen in such a way, that they have a definite projection of the angular momentum on the axis joining the two atoms. We can expand the hopping elements in terms of these molecular couplings,

$$t_{\alpha',\alpha}\left(\mathbf{R}_{\alpha\,L}-\mathbf{R}_{\alpha'\,L'}\right)=\sum_{\mu} d_{\alpha'\alpha\mu}(\mathbf{R}_{\alpha\,L}-\mathbf{R}_{\alpha'\,L'})t_{\alpha'\alpha\mu}, \tag{1.10}$$

where μ is the projection of the angular momentum on the molecular axis, which can be $\{\sigma, \pi, \delta, ...\}$. The sum runs over the possible projections depending on the considered orbitals. The expansion coefficients $d_{\alpha'\alpha\mu}(\mathbf{R}_{\alpha\,L}-\mathbf{R}_{\alpha'\,L'})$ depend on the angels between the molecular axis and the three crystallographic axes via the corresponding direction cosine and on the coupled orbitals α and α'. They have been calculated and tabulated by Slater and Koster [11]. Later Podolskiy and Vogl [19] derived closed expressions to calculate them for arbitrary orbitals and directions of the molecular axis.

1.2.2. Parametrization of the tight-binding Hamiltonian

Instead of making the attempt to calculate the on-site elements (Eq. (1.5)) and the hopping matrix elements (Eq. (1.6)) from first principles, they are treated as parameters for a given bulk material. The parameters are fitted to reproduce certain properties of the band structure such as the energy eigenvalues at high symmetry points which are obtained by ab-initio methods such as the nonlocal, relativistic pseudopotential method, the GW method or experimentally. For all III-V materials, we base our calculations on the relativistic $sp^3d^5s^*$ parametrization of Jancu et al. [18]. This method reproduces the band structures of bulk semiconductors most accurately today. Band gaps, split-off energies, effective masses of conduction and valence band, side valley offsets, as well as strain deformation potentials agree quantitatively with experiments. The parametrization was chosen carefully

to follow the known chemical trends in the electronic structure. Since the parameters are given for bulk binary compounds, some additional adjustments have to be taken into account, when dealing with alloys and heterostructures. For alloys, we employ the simple virtual crystal approximation (VCA), i.e. for an alloy of the kind $Ga_xAl_{1-x}As$ all parameters are averaged with respect to the composition x between the values of binary GaAs and AlAs. For example for the on-site energies, we get $\varepsilon_\alpha(Ga_xAl_{1-x}As) = x\varepsilon_\alpha(GaAs) + (1-x)\varepsilon_\alpha(AlAs)$. It is known that the VCA is actually a very poor approximation due to the influence of alloy disorder. The effect of alloy disorder can be taken into account e.g. by the coherent potential approximation (CPA). However, since we only use alloy materials in the barriers of our superlattices and quantum wells while the well materials are always taken as binary compounds the alloy disorder has only minor influence on the electronic properties of the quantum wells. The VCA therefore is a satisfactorily approximation in our cases. To employ the parametrization of Ref. [18] for heterostructures, we additionally have to include the valence band offsets and their pressure dependence (the so-called absolute deformation potentials). We use the band offsets and absolute deformation potentials calculated by Wei and Zunger in Refs. [20, 21] and rigidly shifted all on-site energies of the binary compounds relative to each other to account for these effects and their volume dependence. Special care has to be taken at the interfaces. Within a heterostructure such as ...–Ga–As–Al–As–..., the on-site energies of the arsenic atoms are taken as symmetric average of those for GaAs and AlAs, yielding effectively a smooth transition of the offset energies across the interface. The next-neighbor interaction is always taken form the corresponding binary compound.

1.3. Implementation of spin-orbit coupling

For our purpose, it is of vital importance to include spin-orbit interaction into our model since we are mainly interested in the spin-dependent dispersion of the lowest conduction and the highest valence band near the Γ-point. We follow the approach of Chadi [22] and include the spin-orbit interaction as intratomic coupling of the p-orbitals.

The spin-orbit part of the relativistic Hamiltonian is given by

$$H_{\mathrm{SO}} = \frac{1}{2m^2c^2} \left(\nabla V \times \mathbf{p}\right) \cdot \mathbf{S}, \tag{1.11}$$

where ∇V is the gradient of the crystal potential, $\mathbf{p}$ is the momentum operator, and $\mathbf{S}$ the spin operator, which may be written in terms of the Pauli matrices as $\mathbf{S} = \hbar/2 \cdot \boldsymbol{\sigma}$, m is the mass of the particle, and c the speed of light. Assuming a spherically symmetric potential $V(r)$ with $r = |\mathbf{r}|$, and using

$$\nabla V = \frac{1}{r}\frac{\mathrm{d}V}{\mathrm{d}r}\mathbf{r}, \tag{1.12}$$

we get a simplified spin-orbit Hamiltonian

$$H_{\mathrm{SO}} = \frac{1}{2m^2c^2}\frac{1}{r}\frac{\mathrm{d}V}{\mathrm{d}r}\mathbf{L}\cdot\mathbf{S}, \tag{1.13}$$

where $\mathbf{L}$ is the angular momentum operator. We still need to find the matrix elements of H_{SO} within the Bloch basis (Eq. (1.2))

$$(H_{\mathrm{SO}})_{\alpha',\alpha,L,L'} = \langle \alpha', L' |\, H_{\mathrm{SO}} \,| \alpha, L \rangle\,. \tag{1.14}$$

As already mentioned, we will assume that only states at the same atom get coupled by the spin-orbit interaction. We have therefore $(H_{\mathrm{SO}})_{\alpha',\alpha,L,L'} \propto \delta_{L',L}\delta_{\tau',\tau}$. Since only states with nonzero angular momentum can produce nonzero matrix elements of H_{SO}, we are left with p and d orbitals. As a further simplification, we will consider only the coupling of the p-states and neglect the much smaller splitting of the d-states. Thus the spin-orbit interaction adds only 6 additional matrix elements per basis atom to the Hamiltonian (Eq. (1.4))

$$\begin{aligned}
\langle p_x, \mathbf{R}_\tau, \uparrow |\, H_{\mathrm{SO}} \,| p_y, \mathbf{R}_\tau, \uparrow \rangle &= -i\Delta_\tau, \\
\langle p_x, \mathbf{R}_\tau, \downarrow |\, H_{\mathrm{SO}} \,| p_y, \mathbf{R}_\tau, \downarrow \rangle &= i\Delta_\tau, \\
\langle p_z, \mathbf{R}_\tau, \uparrow |\, H_{\mathrm{SO}} \,| p_x, \mathbf{R}_\tau, \downarrow \rangle &= -\Delta_\tau, \\
\langle p_z, \mathbf{R}_\tau, \downarrow |\, H_{\mathrm{SO}} \,| p_x, \mathbf{R}_\tau, \uparrow \rangle &= \Delta_\tau, \\
\langle p_y, \mathbf{R}_\tau, \uparrow |\, H_{\mathrm{SO}} \,| p_z, \mathbf{R}_\tau, \downarrow \rangle &= -i\Delta_\tau, \\
\langle p_y, \mathbf{R}_\tau, \downarrow |\, H_{\mathrm{SO}} \,| p_z, \mathbf{R}_\tau, \uparrow \rangle &= -i\Delta_\tau.
\end{aligned} \tag{1.15}$$

Here the Δ_τ are the atomic spin-orbit coupling parameter that may depend on the atom τ in the unit cell.

1.4. Implementation of strain

In this work, we consider primarily superlattices and quantum wells. Since the well material will in general have another lattice constant than the barrier material or the substrate, strain becomes an important issue. Since we will only consider structures grown in the crystallographic [001] direction, we put special emphasis on the uniaxial strain in that direction. Strain can change the symmetry of a solid, which has significant impact on the band structure, especially regarding degeneracies and spin properties. In particular, for strained bulk structures the symmetry is lowered by uniaxial strain, which makes some spin-dependent interactions possible which would be forbidden by symmetry in the unstrained case. As mentioned above, a material can be strained e.g. by growing a layer onto a lattice-mismatched substrate. For layers thinner than a certain critical thickness, the growth can be assumed to be pseudomorphic. Above that thickness, the material relaxes the strain e.g. by cracks and misfits which destroys the translational invariance and thereby significantly lowers the quality of the quantum well for transport experiments. We will always

assume a pseudomorphic growth with an intact translational invariance for our calculations. For the strain, induced by a lattice mismatched substrate, there are two distinct cases. First there is tensile strain. That means, that the lattice constant of the substrate is larger than that of the layer. The lattice constant of the layer material is enlarged perpendicular to the growth direction while in turn the lattice constant in the growth direction gets smaller. The other possibility is compressive strain, where the lattice constant of the substrate is smaller than that of the layer which results in an opposite behavior of the lattice constants as compared to the case of tensile strain.

The new atomic positions $\mathbf{R}'_I$ in the strained case are related to the equilibrium positions $\mathbf{R}_I$ in the untrained case by the strain tensor ϵ in the following way,

$$\mathbf{R}'_L = (1+\epsilon)\mathbf{R}_I. \tag{1.16}$$

The diagonal elements of the strain tensor give the relative displacements of the atoms in the corresponding direction while the off-diagonal elements are related to the change of the angle between the two corresponding axes. In the case of uniaxial strain in the [001] direction as considered in this work, the strain tensor becomes diagonal,

$$\epsilon = \begin{pmatrix} \epsilon_{\|} & 0 & 0 \\ 0 & \epsilon_{\|} & 0 \\ 0 & 0 & \epsilon_{\perp} \end{pmatrix}. \tag{1.17}$$

The biaxial strain component $\epsilon_{\|}$ is determined by the equilibrium lattice constant of the layer material a_0 and the lattice constant of the substrate $a_{\|}$:

$$\epsilon_{\|} = \frac{a_{\|} - a_0}{a_0}. \tag{1.18}$$

The uniaxial strain component $\epsilon_{\perp}$ follows from $\epsilon_{\|}$ as,

$$\epsilon_{\perp} = -\frac{\epsilon_{\|}}{\sigma}, \tag{1.19}$$

where σ is the Poisson ratio, given by the elastic stiffness constants C_{11} and C_{12} of the material

$$\sigma = \frac{C_{11}}{2C_{12}}. \tag{1.20}$$

The lattice constant in the growth direction $a_{\perp}$ can thus be directly calculated from the lattice constant of the substrate and the Poisson ratio of the layer material

$$a_{\perp} = a_0 \left(1 - \sigma \frac{a_{\|} - a_0}{a_0}\right). \tag{1.21}$$

The two possible cases of uniaxial strain can be classified by:

$$\begin{aligned} \text{tensile strain:} \quad & \epsilon_{\|} > 0,\ \epsilon_{\perp} < 0 \Rightarrow a_{\|} > a_{\perp}, \\ \text{compressive strain:} \quad & \epsilon_{\|} < 0,\ \epsilon_{\perp} > 0 \Rightarrow a_{\|} < a_{\perp}. \end{aligned}$$

To incorporate strain into the tight-binding Hamiltonian, we need to know how the matrix elements of the Hamiltonian (Eq. (1.4)) are changed. There are actually two effects of the strain on the band structure. The first is a shift of the band edges due to the change of the crystal volume, which is described by the absolute deformation potential. The absolute deformation potential of the valence band a_V shifts the complete band structure proportional to the relative change in the volume $\Delta V/V$. This means that all on-site elements (Eq. (1.5)) get shifted according to,

$$\varepsilon'_\alpha = \varepsilon_\alpha + a_V \frac{\Delta V}{V}, \tag{1.22}$$

where ε'_α denotes the strained on-site element of the orbital α. The relative change of the volume can be calculated directly from the strain tensor ϵ as,

$$\frac{\Delta V}{V} = \mathrm{Tr}[\epsilon], \tag{1.23}$$

where "Tr" denotes the trace operator.

The second effect is related to the shear. Shear reduces the symmetry and therefore lifts degeneracies of the bands but does not shift their average value. One example would be the four times degenerate Γ_8 representation of the valence band in zincblende bulk semiconductors which is given by the heavy hole and the light hole band, each twice spin degenerate. Uniaxial strain in the [001] direction lifts this degeneracy partly. The spin degeneracy of the bands is unchanged at Γ, but the heavy hole and the light hole band are shifted apart. While compressive strain shifts the heavy hole band up and the light hole band down, tensile strain does the opposite. To incorporate the shear effect into the tight-binding theory, we have to change the hopping elements (Eq. (1.6)) to account for the bond-angle distortion and the changes in the bond lengths. The change in the bond angles effects the phase factors in Eq. (1.4) and the direction cosines in the Slater–Koster couplings (Eq. (1.10)) which can be taken into account using the analytic expressions derived by Podolskiy and Vogl [19]. The change in the bond length is accounted for by a change in the two-center integrals. Harrison [12] has shown that the two-center integrals t_{ijk} can be expressed as a simple function of the nearest-neighbor distance d in the strained material and the equilibrium distance d_0

$$t_{\alpha\alpha'\mu}(d) = t_{\alpha\alpha'\mu}(d_0) \left(\frac{d_0}{d}\right)^{\eta_{\alpha\alpha'\mu}}. \tag{1.24}$$

Originally Harrison proposed that $\eta_{ijk} = 2$ independently of the considered states α, α'. This assumption results in a fairly good description of the changes of the band structure due to strain. Jancu et al. [18] have shown that by taking orbital dependent exponents, the results can be improved significantly. Additionally to the change in the hopping elements, we need to take into account that uniaxial strain in the [001] direction induces a tetragonal crystal field which lifts the degeneracy of

the Γ_4 d-orbitals d_{xy}, d_{xz}, and d_{yz},

$$\begin{aligned} \varepsilon'_{d_{xy}} &= \varepsilon_{d_{xy}} + 2b_{d,\text{eff}}(\epsilon_\perp - \epsilon_\parallel), \\ \varepsilon'_{d_{xz}} &= \varepsilon'_{d_{yz}} = \varepsilon_{d_{yz}} - b_{d,\text{eff}}(\epsilon_\perp - \epsilon_\parallel), \end{aligned} \tag{1.25}$$

where $b_{d,\text{eff}}$ is a material dependent effective shear parameter, which is adjusted to reproduce the observed heavy hole–light hole splitting.

1.5. Summary

In this chapter, we have given a brief introduction into the tight-binding theory for electronic structure calculations. We have discussed the common simplification within the model. We have shown how spin-orbit interaction and strain are incorporated into the theory. The tight-binding method is of importance for this work, since we base our predictions for quantum devices on models, that are obtained from tight-binding calculations, in order to render the band structure effects as exact as possible. In heterostructures, the states close to the Γ-point result from coupling of zone-center bulk states with zone-edge states due to the confinement. This coupling influences the spin-orbit interaction related properties significantly, as we will show in Chapter 3. Since the zone-edge states are not well described in simple $\mathbf{k}\cdot\mathbf{p}$ theories, we rely on the tight-binding theory, that describes states within the entire Brillouin zone more accurately.

2. Novel relativistic tight-binding method for HgTe and CdTe

2.1. Introduction

HgTe quantum well structures with CdTe barriers have attracted considerable interest due to the recent prediction [23] and experimental observation [9] of the quantum spin Hall effect in these structures. Many predictive calculations are based on the 8-band $\mathbf{k}\cdot\mathbf{p}$ method [23–28]. This method reproduces the band structure of the bulk material accurately only for wave vectors close to the Γ-point. In heterostructures, however, the states close to the center of the two-dimensional Brillouin zone consist of a mixtures of bulk zone center states and zone edge states. The latter are not well described by $\mathbf{k}\cdot\mathbf{p}$ theory. Moreover, for the topological classification in the context of the quantum spin Hall effect [29] the two-dimensional band structure has be known in the entire Brillouin zone (for more details see Chapter 10). Therefore, a realistic tight-binding description of these materials is needed. The relativistic tight-binding parameterizations given in the literature so far are based on the sp^3s^* model [30–32] which does not reproduce the electronic bulk band structure with satisfactorily accuracy.

In this chapter, we develop a relativistic $\mathrm{sp}^3\mathrm{d}^5$-model that faithfully reproduces the available experimental electronic structure data such as energy gaps at high symmetric points in the Brillouin zone, effective masses, spin-orbit splittings, of HgTe and CdTe bulk materials and alloys [33–36], as well as band offsets and subband structure in quantum wells [37–41].

2.2. New sp^3d^5 parameters for HgTe and CdTe

We base our new parametrization on the nonrelativistic sp^3d^5 tight-binding theory developed in Refs. [46–48]. The parametrization presented in Ref. [46] differs from the one of Jancu et al. [18] in several important points. First, it does not include the auxiliary s^* orbital. The s^* orbital was originally included by Vogl et al. [17] into the minimal sp^3 model to mimic coupling to more distant bands, which brought significant progress to the accuracy of the conduction band. When the physically real atomic d orbitals are included the s^* is actually not necessary any more since the d orbitals constitute coupling to more distant bands on a direct physical basis. Second, the authors included the cation semicore d orbitals into their model which have been neglected in Ref. [18]. Since in the narrow gap II-VI materials these cation d orbitals

	CdTe		HgTe	
	literature	present work	literature	present work
Γ_8^v	0.00	0.00	0.00	0.00
Γ_6^v	−10.91 [42]	−10.91	−10.80 [33]	−10.81
$\Gamma_7^v\,(\Delta_0)$	−0.89 [43]	−0.88	−0.94 [44]	−0.95
$\Gamma_6^c\,(E_G)$	1.59 [34]	1.6	−0.30 [36]	−0.30
Γ_7^c	5.20 [34]	5.22	4.10 [34]	4.12
Γ_8^c	5.45 [43]	5.44	4.61 [44]	4.78
X_6^v	−1.14 [44]	−0.80	−1.83 [45]	−1.72
X_6^c	4.35 [34]	4.54	3.17 [34]	3.14
X_7^v	−1.35 [35]	−1.37	−2.03 [35]	−2.15
X_7^c	5.82 [26]	6.06	3.57 [34]	3.54
L_6^v	−0.97 [44]	−0.98	−1.42 [34]	−1.49
$L_{4,5}^v$	−0.40 [44]	−0.40	−0.67 [45]	−0.85
L_6^c	3.53 [26]	3.73	1.33 [34]	1.28
L_6^c	6.39 [44]	6.38	5.83 [35]	5.57
$L_{4,5}^c$	6.45 [44]	6.54	6.09 [44]	5.99

Table 2.1.: Band structure energies in eV at high symmetry points for bulk CdTe and HgTe. Values calculated within the present tight-binding scheme and target values taken from the literature obtained experimentally [33–36] and theoretically by *GW* [42] or pseudopotential method [26, 43–45]. All energies given relative to the Γ_8^v top valence band.

have a significant influence on the electronic structure as has been pointed out by Wei and Zunger [49], it is reasonable to include them into a model for HgTe and CdTe. However, in Refs. [46–48] the parameters were obtained by fitting the band structure to results exclusively obtained by the local density approximation (LDA). It is known, that that method cannot reproduce the fundamental band gap satisfactorily. Bulk HgTe is a zero gap semiconductor (semimetal) with a symmetry induced degeneracy of conduction and valence bands at the Brillouin zone center [50]. The lowest conduction band and the highest valence band at the Γ-point are formed by the fourfold degenerate Γ_8 representation. At finite wave vector the light hole band bends up, constituting the lowest conduction band while the highest valence band is actually the negatively bent heavy hole band. The second valence band is known to be the Γ_6 derived band, which constitutes the lowest conduction band in a normal semiconductor. At the Γ-point the Γ_8 and the Γ_6 representation are separated only by approximately 300 mV. This separation is often referred to as negative band gap energy E_G, since in standard semiconductors, the Γ_6–Γ_8 splitting constitutes the fundamental gap $E_G > 0$. In HgTe, at finite k-values close to the Γ-point the Γ_6-derived band has a negative effective mass due to the interaction with the light hole band. Approximately 600 mV lower in energy than the Γ_6 band lies the split-off hole (Γ_7-representation) with a negative effective mass as usual. In LDA calcula-

	CdTe	HgTe		CdTe	HgTe
ε_s^c	1.88	0.33	$\varepsilon_d^c(t_2)$	-6.97	-5.77
ε_s^a	-8.86	-8.36	$\varepsilon_d^c(e)$	-7.42	-6.07
$t_{ss\sigma}$	-0.80	-0.74	$\varepsilon_d^a(t_2)$	15.83	13.97
ε_p^c	10.05	7.96	$\varepsilon_d^a(e)$	14.63	12.80
ε_p^a	0.56	1.76	$t_{sd\sigma}$	-2.11	-1.79
$t_{sp\sigma}$	2.42	1.81	$t_{ds\sigma}$	-0.26	-0.52
$t_{ps\sigma}$	1.39	0.68	$t_{pd\sigma}$	-2.42	-1.73
$t_{pp\sigma}$	1.96	2.90	$t_{dp\sigma}$	-1.52	-1.29
$t_{pp\pi}$	-0.33	-0.55	$t_{pd\pi}$	1.9	1.82
Δ_{SO}^c	0.08	0.27	$t_{dp\pi}$	0.27	0.31
Δ_{SO}^a	0.34	0.38			

Table 2.2.: Resulting sp^3d^5 tight-binding parameters in eV for CdTe and HgTe.

tions this band ordering is predicted incorrectly. The electrons (Γ_6-representation) and the split-off hole (Γ_7-representation) are exchanged. Additionally, the split-off hole acquires a falsely positive effective mass close to the Γ-point due to the interaction with the lower lying Γ_6 band, see e.g. Refs. [51–54]. Moreover, Ref. [46] is a nonrelativistic model that does not take into account the spin-orbit interaction, which is of great importance since the involved ions are very heavy and thus have a large atomic spin-orbit interaction. In turn, these materials have a very large split-off energy of approximately 1 eV for both HgTe as well as CdTe. Both features of the band structure, the correct band gaps as well as the inclusion of spin-orbit interaction is of great relevance for this work, since we are mainly interested in the spin-dependent properties of the subbands in heterostructures. These can only be successfully calculated with an appropriate parametrization for the bulk material. We have therefore adjusted the parametrization in such a way, that the important features of the relativistic bulk band structures of HgTe and CdTe are reproduced.

We have selected target values for the fitting procedure from a large set of band features from ab initio data as well as experimental results. A good overview of calculated and measured results for both HgTe and CdTe can be found in Refs. [26, 30]. The selected target values are given in Table 2.1. The tight-binding parameters have been obtained by a least square fit for these points. Since we only fit the tight-binding band structure at high symmetry points, we have to take great care that we obtain reasonable results for the band structure between these points. In particular, we have to make sure that the known compatibilities relations between representations at the high symmetry points are fulfilled [55]. Furthermore, we have to make sure, that reasonable eigenvectors correspond to the calculated eigenenergies. For example, the electron band (Γ_6 representations close to the fundamental gap) is dominated by the s-orbitals of the metallic cation, while the corresponding hole bands (Γ_8-representation) is dominated by the anion's p-orbital. Additionally, the known chemical trends have to be reproduced. From the universal tight-binding

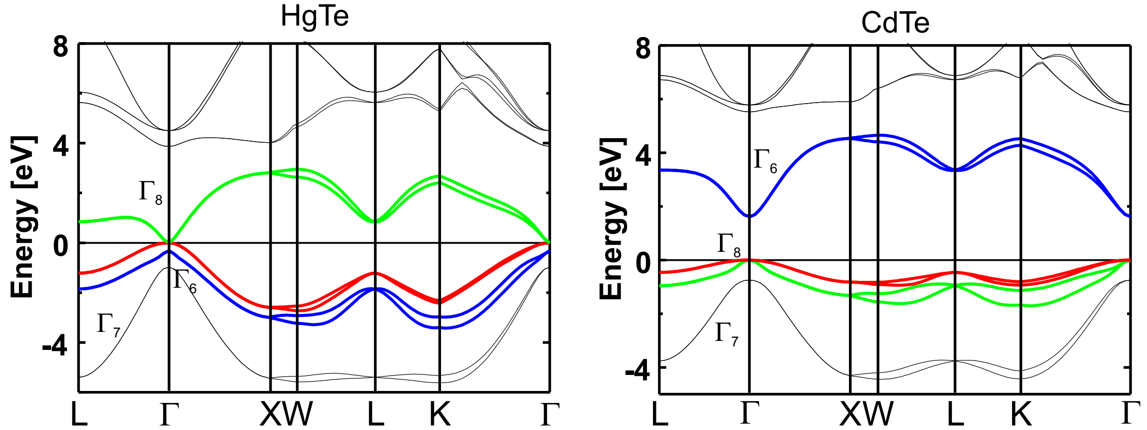

Figure 2.1.: Bulk band structure of HgTe (left) and CdTe (right) calculated with the present tight-binding model. The blue lines show the Γ_6-derived bands and the red and the green lines the Γ_8-derived ones. The red lines depicts the heavy hole, while the green lines shows the light hole. The included k-points are: $\Gamma = (0,0,0)$, $X = (1,0,0)$, $L = (.5,.5,.5)$, $K = (.75,.75,0)$, and $W = (1,.25,0)$.

parameters calculated by Harrison [18], it is known that e.g. the coupling between s-states, $t_{ss\sigma}$, is negative while for the hopping element between p-states $t_{pp\sigma} > 0$ and $t_{pp\pi} < 0$ with $|t_{pp\pi}| < |t_{pp\sigma}|$. In zincblende semiconductors, we generally have different parameters for the hopping between the same states on different atoms. That is the hopping matrix element between the s-orbital on the cation and the p-orbital on the anion, $t_{sp\sigma}$ is different from the one that connects the p-orbital on the cation and the s-orbital on the anion, $t_{ps\sigma}$. Due to the included orbitals, certain relations hold between the coupling parameters. On the cation, we include the semicore d-orbitals which are tightly bound to the core and the valence s and p states which are more extended. That means the ordering of the included orbitals is $d - s - p$. For the anion on the other hand, we include the fully occupied s-orbital, the partially occupied p-orbitals and the empty d-orbitals, i.e. the ordering is $s - p - d$. It is therefore reasonable that $|t_{ds\sigma}| < |t_{sd\sigma}|$, $|t_{ps\sigma}| < |t_{sp\sigma}|$, and $|t_{dp\sigma,\pi}| < |t_{pd\sigma,\pi}|$.

The resulting parameters of our fitting procedure are given in Table 2.2, the energy eigenvalues at the high symmetry points, calculated with the obtained parametrization are also given in Table 2.1, to compare with the target values. The resulting band structure is plotted in Fig. 2.1. The left panel shows results for HgTe and right panel for CdTe. The important bands around the fundamental gap are shown in thick colored lines. The blue line shows the electron band (Γ_6-representation) which constitutes the lowest conduction band in CdTe but the second valence band in HgTe. The calculated effective masses are $m^* = .15$ for CdTe and $m^* = -.04$ for HgTe respectively. The Γ_8-representation is shown as red and green lines. The heavy hole bands with an effective mass of $m^*_{[100]} = -.67$ for CdTe and $m^*_{[100]} = -.55$ for HgTe are given in red while the light hole band with an effective mass of $m^* = -.14$

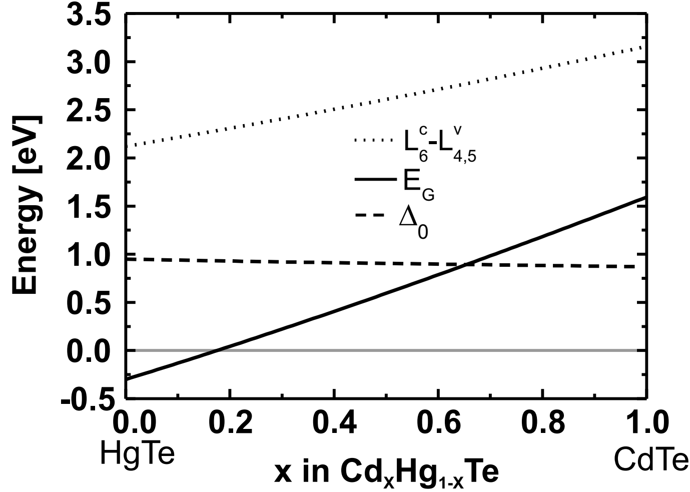

Figure 2.2.: Band structure properties of $Cd_xHg_{1-x}Te$ as a function of the alloy composition x. The dotted line shows the distance between the lowest conduction band and the highest valence band at the L-point ($L^c_6 - L^v_{4,5}$). The solid line shows the value of the fundamental gap $\Gamma^c_6 - \Gamma^v_8$ while the dashed line depicts the value of the spin-orbit splitting $\Gamma^v_8 - \Gamma^v_7$. The gray line depicts the zero of energy.

for CdTe and $m^* = .035$ for HgTe are given in green. The calculated effective masses are well within the reported values in the literature, see Ref. [26] and references therein. Please note that it is known [46] that some features of the band structure cannot be reproduced within a nearest neighbor tight-binding model. Some of these can be corrected if one includes coupling to more distant atoms. However, these features occur in higher conduction bands and lower valence bands away from the Γ-point. Since these bands do not have a significant relevance for the properties we are interested in, we stick with the nearest neighbor model due to the advantages discussed in Sec. 1.2.

To check the consistency of our obtained parameters, we have also calculated the properties of the bulk alloy $Cd_xHg_{1-x}Te$ at the Γ and at the L-point. We use the simple virtual crystal approximation (VCA) without correction for the alloy disorder. The results are shown in Fig. 2.2. The solid line shows the band gap energy E_G which starts at the negative value of $E_G = -.3$ eV at the left for the binary compound HgTe and ends at 1.6 eV at the right side for pure CdTe. A special point is, where the band gap vanishes and the Γ_8 and Γ_6 representation are degenerate. This point is expected between $x = .17$ [26] and $x = .2$ [31], which is well reproduced by our model as we get $x = .18$. At this point the light hole and the electron band are expected to be completely symmetric, i.e. the bands are expected to have the same effective mass with opposite sign, which is exactly reproduced in our calculations. The dependence of the spin-orbit splitting on the alloy composition x is shown by the dashed line in Fig. 2.2. Another special point in the alloy composition is reached

when the band gap E_G equals the spin-orbit splitting $\Delta_{\rm SO}$. We get this point for $x = .66$ which agrees well with literature [26]. We also show the behavior of the gap at the L-point by the dotted line in Fig. 2.2 which also compares well with literature [26, 31]. In Chapter. 4, we will apply the model to heterostructures and quantum wells.

2.3. Summary

In this chapter, we have presented our novel sp^3d^5-parametrization for the semi-empirical tight-binding model for CdTe and HgTe that reproduces very well the bulk band structures and alloy properties taken from ab initio calculations and experiment. Since we include the very important spin-orbit coupling, there is no comparable parametrization published in literature so far to our knowledge. In Chapter 4, we will apply this model to HgTe/CdTe heterostructures that are of great interest in the context of the spin-Hall and the quantum spin Hall effect. We will further develop a novel envelop function theory in Sec. 4.3 for HgTe/CdTe heterostructures on the bases of the tight-binding calculations that we employ to predict quantum transport properties in HgTe nanostructures. In particular, we propose a realization of a spintransistor on the basis of the quantum spin Hall effect in Sec. 10.6.

3. Results for the k-linear spin-orbit coupling in semiconductor quantum wells

3.1. Introduction

By their proposal of a spin transistor, Datta and Das [1] created the modern field of semiconductor spintronics. They proposed the so-called Rashba effect as the mechanism to control the spin current in the device channel. This effect, which was originally predicted by Bychkov and Rashba [56] is caused by a zero-magnetic field spin splitting of nondegenerate band edge states. The splitting is linear in the electron wave vector and my be steered by an applied top gate voltage [57]. The prediction was based on a symmetry analysis of the $\mathbf{k} \cdot \mathbf{p}$ Hamiltonian for semiconductors with a wurzite crystal structure. The effect has been extensively studied theoretically, see e.g. Refs. [3, 58–60]. Most of the work has also employed a $\mathbf{k} \cdot \mathbf{p}$ analysis. As we will show later, the $\mathbf{k} \cdot \mathbf{p}$ theory fails to predict qualitatively the important properties of the dominant spin-orbit related band splitting phenomena. Particularly, we will show that, in contrast to the widespread assumption, the Rashba effect is not dominant in general. We show that another spin-orbit induced k-linear spin splitting of band edge states that is nonzero already at higher symmetry, is controllable by an electric gate field, and can be enhanced by band structure engineering by up to two orders of magnitude. The chapter is organized as follows. In Sec. 3.2, we review the spin-orbit coupling mechanisms for nondegenerate bands, namely the Dresselhaus and the Rashba type spin-orbit coupling. In Sec. 3.3, we present our results for various semiconductor heterostructures in an external electric field, while in Sec. 3.4, we predict unexpectedly strong spin-orbit coupling for specially strain engineered GaAs two-dimensional hole gases. Finally, in Sec. 3.5, we investigate the influence of higher order in k spin-orbit coupling.

3.2. Theory of spin-orbit induced k-linear band splitting

We focus on zincblende heterostructures and superlattices that are grown along the [001] crystallographic axis. This includes uniaxially [001]-strained bulk materials. We chose an orthogonal coordinate system with the z-axis along the growth direction

and the x and y axis along the [100] and [010] direction, respectively. We choose the conventional representation of the Pauli matrices $\boldsymbol{\sigma} = (\sigma_x, \sigma_y, \sigma_z)$ where σ_z is diagonal, i.e. the spin quantization axis is chosen along the growth direction.

The point group symmetry of the considered zincblende structures is at most D_{2d}. The D_{2d} symmetry occurs, for example, in strained bulk materials, in symmetric heterostructures of type $A:B:A$, where A and B denote different semiconductor materials of a given width that either share a common anion or cation (e.g. AlAs:GaAs:AlAs), or in A_nB_m superlattices such as $(\mathrm{GaAs})_n(\mathrm{AlAs})_m$ where $2n+2m$ is a multiple of four. Nonsymmetric heterostructures of type $A:B:C$ or symmetric heterostructures with a finite electric field along the growth direction possess a C_{2v} symmetry, only. All structures possess a translational symmetry in the lateral plane and have spin-degenerate band states at the Brillouin zone center $\mathbf{k}=0$ (Γ-point) in zero magnetic field due to the Kramers theorem. This spin degeneracy is lifted for finite k-states away from the Γ-point. In the case of [001]-strained bulk, the spin degeneracy remains intact along the [001] or Δ-axis in reciprocal space. The relativistic electronic Hamiltonian matrix of a nondegenerate band n up to quadratic order in the inplane wave vector (valid sufficiently close to Γ only) has the general form,

$$H(n\mathbf{k}) = \frac{\hbar^2}{2m^*}\mathbf{k}^2 \cdot \sigma_0 + \alpha_{\mathrm{BIA}}(-k_x\sigma_x + k_y\sigma_y) + \alpha_{\mathrm{SIA}}(k_y\sigma_x - k_x\sigma_y) + \mathcal{O}(k^3), \quad (3.1)$$

where $\mathbf{k} = (k_x, k_y)$ is the inplane wave vector, m^* is the effective mass of the band, and σ_0 denotes the 2×2 unity matrix. The constants α_{BIA} and α_{SIA}, which clearly depend on the band index n arise from the spin-orbit interaction. The constant α_{SIA} is nonzero only in C_{2v} symmetric systems and vanishes for D_{2d} symmetry. It has therefore been termed structural inversion asymmetry (SIA) constant. The term $\propto \alpha_{\mathrm{SIA}}$ is the so-called Rashba spin-orbit interaction term. The constant α_{BIA}, on the other hand, is nonzero also for D_{2d} symmetry and only vanishes in zincblende structures for the full cubic (T_d) point symmetry. The term $\propto \alpha_{\mathrm{BIA}}$ is often referred to as Dresselhaus spin-orbit coupling. The name of this constant stems from $\mathbf{k}\cdot\mathbf{p}$ theory. In the extended 14-band Kane model, a term of that form can be derived which is absent in simple 8-band calculations [3]. In contrast to the 8-band model, the 14-band model takes into account the inversion asymmetry of the bulk zincblende crystal at least perturbatively. The spin-orbit coupling constant has therefore been termed bulk inversion asymmetry (BIA) constant. As will become clear below, this spin-orbit coupling effect does not arise from zone-center electronic states and generally has properties that differ radically from that predicted by simple $\mathbf{k}\cdot\mathbf{p}$ models. Note that the form of the Hamiltonian (Eq. (3.1)) is completely general and does not result from a finite-band $\mathbf{k}\cdot\mathbf{p}$ model. The Hamiltonian (Eq. (3.1)) has the eigenvalues,

$$E_\pm(\mathbf{k}) = \frac{\hbar^2}{2m^*}k_\parallel^2 \pm \sqrt{\alpha_{\mathrm{BIA}}^2 + \alpha_{\mathrm{SIA}}^2 + 2\alpha_{\mathrm{BIA}}\alpha_{\mathrm{SIA}}\sin(2\phi)}\, k_\parallel, \quad (3.2)$$

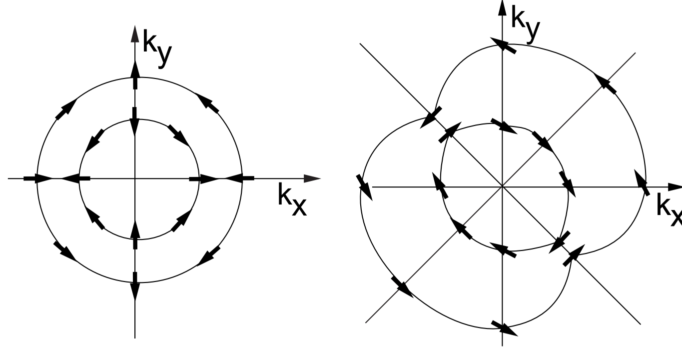

Figure 3.1.: Schematics of the spin orientation in zincblende semiconductor quantum wells. (left) D_{2d} symmetric quantum wells with vanishing Rashba spin-coupling constant. (right) C_{2v} symmetric quantum wells with both Dresselhaus spin-orbit coupling and Rashba spin-orbit coupling.

with the corresponding eigenvectors,

$$\langle \mathbf{r}, \pm \mid \mathbf{k}_{\pm} \rangle = \frac{1}{\sqrt{2}} e^{i\mathbf{k}_{\pm}\mathbf{r}} \begin{pmatrix} ie^{-i\Phi} \\ \pm 1 \end{pmatrix}, \tag{3.3}$$

where we have introduced the absolute value of the lateral wave vector $k_{\|} = |\mathbf{k}|$ and $k_x = k_{\|} \cos\phi$ and $k_y = k_{\|} \sin\phi$. The spin angle Φ is defined as,

$$\Phi = \arg[\alpha_{\mathrm{BIA}} \sin\phi + \alpha_{\mathrm{SIA}} \cos\phi + i(\alpha_{\mathrm{BIA}} \cos\phi + \alpha_{\mathrm{SIA}} \sin\phi)]. \tag{3.4}$$

The k-linear spin-orbit coupling can actually be described by a Zeeman-like effective magnetic field [3], the so-called spin-orbit field. The Hamiltonian (Eq. (3.1)) can be written in the form,

$$H(n\mathbf{k}) = \frac{\hbar^2}{2m^*} \mathbf{k}^2 \cdot \sigma_0 + \mu_B \boldsymbol{\sigma} \cdot \mathbf{B}_{\mathrm{eff}}, \tag{3.5}$$

with the effective magnetic field $\mu_B \mathbf{B}_{\mathrm{eff}}$ given by,

$$\mu_B \mathbf{B}_{\mathrm{eff}}(\mathbf{k}) = \alpha_{\mathrm{BIA}} \begin{pmatrix} k_x \\ -k_y \end{pmatrix} + \alpha_{\mathrm{SIA}} \begin{pmatrix} -k_y \\ k_x \end{pmatrix}. \tag{3.6}$$

This field determines the spin orientation of the eigenstates in C_{2v} symmetric structures (Eq. (3.4)). The spin orientation at the Fermi surface is depicted schematically in Fig. 3.1 for the case of D_{2d} symmetry (left), i.e. $\alpha_{\mathrm{SIA}} = 0$ and the case of C_{2v} symmetry (right), where both spin-orbit coupling mechanisms are present. The spin splitting of the energy bands away but close to Γ is given by,

$$\Delta E_{\mathrm{SO}} = 2k_{\|} \sqrt{\alpha_{\mathrm{BIA}}^2 + \alpha_{\mathrm{SIA}}^2 + 2\alpha_{\mathrm{BIA}}\alpha_{\mathrm{SIA}} \sin(2\phi)}, \tag{3.7}$$

To derive the spin-orbit coupling constants, we can use the unit vectors in polar coordinates $\mathbf{e}_\phi = (-\sin\phi, \cos\phi)$ and $\mathbf{e}'_\phi = (\cos\phi, -\sin\phi)$ to extract the spin-orbit

coupling constants from the effective magnetic field via the following relations,

$$\alpha_{\rm BIA} = \lim_{k_\parallel \to 0} \frac{\mu_B}{2\pi k_\parallel} \int \mathbf{B}_{\rm eff} \cdot \mathbf{e}'_\phi {\rm d}\phi, \qquad (3.8)$$
$$\alpha_{\rm SIA} = \lim_{k_\parallel \to 0} \frac{\mu_B}{2\pi k_\parallel} \int \mathbf{B}_{\rm eff} \cdot \mathbf{e}_\phi {\rm d}\phi.$$

We have employed our semi-empirical tight-binding theory as described in Chapter 1. We wish to compute the spin splitting for heterostructures or pseudomorphic superlattices. For computational convenience, we always use periodic supercells. However, relatively short barriers between the quantum wells are sufficient to obtain converged results corresponding to a quantum well sandwiched between infinitely thick barriers. There are two ways to calculate the k-linear spin-splitting constants for nondegenerate band states from the full-band tight-binding Hamiltonian. One way is to directly diagonalize the entire electronic Hamiltonian $H = H_{\rm NR} + H_{\rm SO}$, where $H_{\rm NR}$ is the nonrelativistic part and $H_{\rm SO}$ is the spin-orbit interaction. According to Eq. (3.7), the moduli of the constants $\alpha_{\rm BIA}$ and $\alpha_{\rm SIA}$ can be determined by calculating the band energy splitting along the [110] and $[1\bar{1}0]$ direction in the limit of $k_\parallel \to 0$. This procedure implicitly maps the full-band tight-binding Hamiltonian onto the 2×2 matrix (Eq. (3.1)) and includes the effects of all other bands nonperturbatively. The second procedure is to use perturbation theory and construct the 2×2 Hamiltonian for a nondegenerate band explicitly. To this end, we determine all nonrelativistic eigenfunctions $|n\mathbf{k}\rangle_{\rm NR}$ of $H_{\rm NR}$ and compute the matrix elements of $H_{\rm SO}$ in the basis of the product states $|n\mathbf{k}\rangle_{\rm NR}|\sigma\rangle$ where $\sigma \in \{\uparrow, \downarrow\}$ are the spin basis states, i.e. we compute the matrix,

$$H_{\sigma,\sigma'}(n\mathbf{k}) = {}_{\rm NR}\langle n\mathbf{k}\sigma | H_{SO} | n\mathbf{k}\sigma' \rangle_{\rm NR}\,, \qquad (3.9)$$

that corresponds to the Hamiltonian matrix (Eq. (3.1)). This procedure gives in polar coordinates,

$$\left.\begin{array}{c}\alpha_{\rm SIA}\\ \alpha_{\rm BIA}\end{array}\right\} = \lim_{k_\parallel \to 0} \frac{1}{2k_\parallel} \left[-iH_{\uparrow\downarrow}(n, \phi = \frac{\pi}{4}) \pm H_{\uparrow\downarrow}(n, \phi = -\frac{\pi}{4}) \right], \qquad (3.10)$$

which is valid for nondegenerate band edges and for sufficiently small values of $\Delta k_\parallel$. Note that the "+" sign has to be used for $\alpha_{\rm SIA}$, while the "−" sign refers to $\alpha_{\rm BIA}$. We will mostly employ the first method, since it gives nonperturbative results for the spin-splitting constants. However, we use the second method as a consistency check for the first one.

3.3. New results for symmetric quantum well structures in electric fields

In this section, we present results for symmetric quantum well structures in constant external electric field. The studied structures are D_{2d} symmetric superlattices of

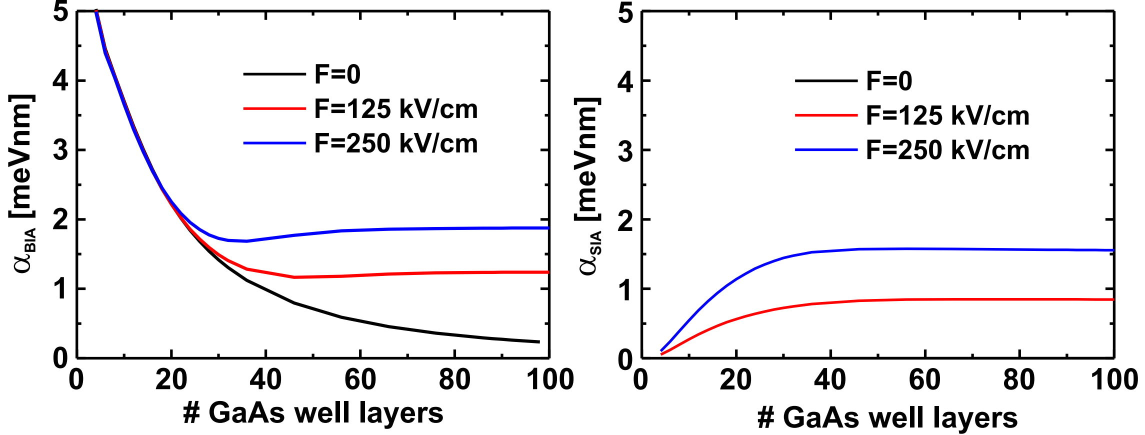

Figure 3.2.: k-linear spin-orbit coupling parameters in $(\mathrm{GaAs})_n(\mathrm{AlAs})_4$ superlattices for various electric fields $\mathbf{F}$ as a function of the well width given by the number of GaAs layers n. The black lines show the case of zero electric field, the red lines $\mathbf{F} = 125\,\mathrm{kV/cm}$, and the blues line $\mathbf{F} = 250\,\mathrm{kV/cm}$. (left) Dresselhaus coupling constant α_{BIA}. (right) Rashba coupling constant α_{SIA}. Note that for $\mathbf{F} = 0$, $\alpha_{\mathrm{SIA}} \equiv 0$.

the kind A_nB_m such as $(\mathrm{GaAs})_n(\mathrm{AlAs})_m$. We always take $2m + 2n$ as a multiple of four in order to have a tetragonal unit cell. In addition, we set the barrier material sufficiently thick so that the wave functions of neighboring quantum wells do not overlap significantly. In the case of AlAs already four layers turn out to be sufficient due to the large conduction band offset to GaAs. For other material combinations thicker barrier layers may be needed. Therefore, we always checked the results for convergence concerning the barrier thickness. While all structures possess D_{2d} symmetry and consequently do not have a nonzero Rashba coupling α_{SIA}, we can lower the symmetry to C_{2v} by applying a constant electric field within the quantum well. Note that an electric field in the barriers does not influence the lowest conduction band states within the quantum wells significantly.

For heterostructures, simple versions of envelope function theory such as 8-band $\mathbf{k}\cdot\mathbf{p}$ models predict the following properties of the spin-splitting coupling constants associated with nondegenerate band edges, in particular the lowest conduction band edge:

1. The Dresselhaus spin-orbit coupling is determined by the relation $\alpha_{\mathrm{BIA}} = \gamma\,\langle k_z^2\rangle$, where γ is the bulk Dresselhaus constant and the average is taken over the wave function at the Γ-point along the growth axis. Consequently, $\alpha_{\mathrm{BIA}} \propto L^{-2}$ decreases rapidly with the quantum well width L.

2. The Rashba spin-orbit coupling vanishes for any symmetric quantum well of type $A : B : A$ and therefore also for A_nB_m superlattices.

3. In an externally applied electric field $\mathbf{F}$ along the growth axis, the Dresselhaus

coupling constant remains unaffected by the field, whereas the Rashba coupling constant increases proportional to it, leading to a dominance of the latter for wide enough quantum wells.

In the following, we present full-band calculations of the spin splitting associated with the lowest conduction band edge in $(GaAs)_n(AlAs)_m$, $(InAs)_n(In_xAl_{1-x}As)_m$, and $(InSb)_n(In_xAl_{1-x}Sb)_m$ superlattices. They show markedly different results due to the strong mixing of the zone center conduction band states with backfolded zone edge conduction band Bloch states and with zone center valence band states that is caused by the field-induced localization. In Fig. 3.2, we show the predicted values for α_{BIA} (left panel) and α_{SIA} (right panel) for the lowest conduction band in the $(GaAs)_n(AlAs)_4$ superlattices, as a function of the number of GaAs-layers n and for various electric fields $\mathbf{F}$ in kV/cm, as calculated with the present tight-binding method. For narrow heterostructures, the Dresselhaus spin-orbit coupling constant α_{BIA} is seen to be independent of the applied field in accord with envelope function theory. For wider wells and high electric fields, however, the potential drop reaches some hundreds of meV. This leads to a localization of the conduction band wave function in real space that is shown in the left panel of Fig. 3.3 for various values of the electric field and the case of $n = 46$ GaAs well layers. This localization enhances the Dresselhaus spin-orbit coupling constant approximately linear with the electric field and saturates for long well width. This saturation can be easily understood. For a given electric field $\mathbf{F}$, the wave function is localized in one part of the quantum well region (depicted schematically by the inset in the right panel of Fig. 3.3) and does not feel a prolongation of the well that does not alter the potential drop. The Rashba spin-orbit coupling constant α_{SIA}, shown in the right panel of Fig. 3.3, shows exactly the same trend as α_{BIA} but saturates at a smaller value. Thus in contrast to the wide spread assumption also the Dresselhaus coupling constant can be excellently steered by an external top-gate voltage, in the case of GaAs quantum wells even better than the Rashba spin-orbit coupling constant. The left panel of Fig. 3.3 shows the absolute square of the total conduction band wave function, which is dominated by s-orbitals of the gallium atoms. Therefore, only a small portion of the wave function is responsible for the k-linear spin splitting. Since the spin-orbit interaction only couples p-states in the tight-binding Hamiltonian with one another (we are ignoring the small d-state spin-orbit coupling here), the relevant part of the wave function that determines the spin splitting is its projection onto the p-basis states. In the right panel of Fig. 3.3, we show the absolute square of the p_z-component of the conduction band wave function at the Γ-point. The localization of the wave function is seen to markedly enhance the p_z contributions to the conduction band wave function near the interface. In the bulk these states predominantly form the light hole bands.

Finally, we want to point out, that the spin splitting depends dominantly on the spin-orbit interaction within the quantum well. In order to show that, we have repeated the calculation for $(GaAs)_{96}(AlAs)_4$ superlattice with a constant field of $\mathbf{F} = 125\,\text{kV/cm}$. An artificial increase of the spin-orbit interaction in the AlAs barrier material by 20% changes α_{BIA} by only 3% and α_{SIA} by 8%, respectively.

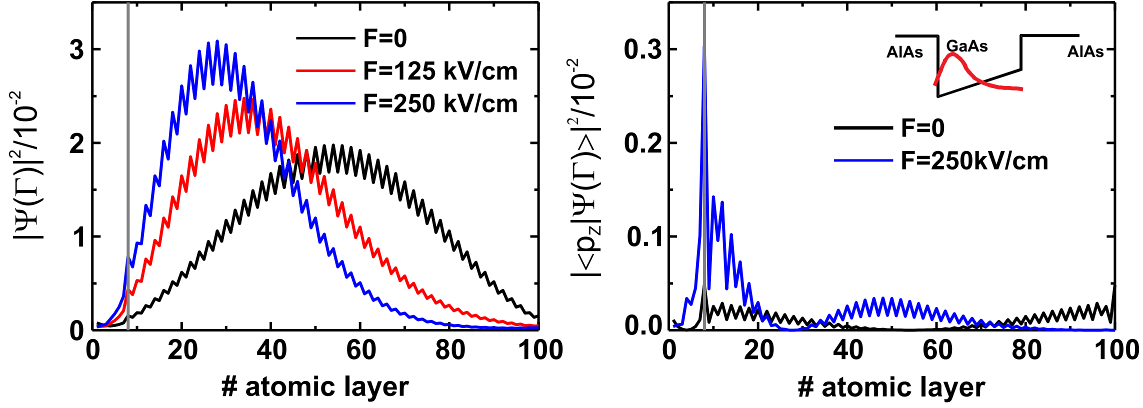

Figure 3.3.: Absolute square of the lowest GaAs-like conduction band wave function at $\mathbf{k} = 0$ for a $(\mathrm{GaAs})_{46}(\mathrm{AlAs})_4$ superlattice as a function of the number of the atomic layer for various electric fields $\mathbf{F}$. Note that the total number of atomic layers is 100 in this case. The black lines shows the case of zero electric field, the red line $\mathbf{F} = 120\,\mathrm{kV/cm}$, and the blue lines $\mathbf{F} = 250\,\mathrm{kV/cm}$. The vertical gray line depicts the material interface. (left) Absolute square of the total wave function, including contributions from all orbitals. (right) Absolute square of the p_z contribution only.

We now turn to InAs heterostructures. In particular, we present results for $(\mathrm{InAs})_n(\mathrm{In}_{.75}\mathrm{Al}_{.25}\mathrm{As})_m$ superlattices which can be grown pseudomorphically [61]. Since the lattice constants of InAs and AlAs are quite different, a significantly higher Aluminum concentration in the barrier would induce high strain to the structure, such that it would not be pseudomorphic any more. In Fig. 3.4, we show again the predicted values for α_{BIA} (left panel) and α_{SIA} (right panel) for the lowest conduction band in the InAs quantum well, as a function of the number of InAs-layers n and for various electric fields $\mathbf{F}$. The trends are the same as in the GaAs case. We find an α_{BIA} of about the same magnitude as before. From simple envelope function approximation (EFA), however, we would expect a Dresselhaus coupling, that is approximately twice as large due the enlarged material parameter γ. Since InAs has a much smaller band gap, the p-content should be enhanced and therefore also the spin-orbit coupling constants. The reason for the unexpected small α_{BIA} is the penetration of the conduction band wave function into the barrier. The barrier for the InAs case is much lower than for the GaAs case due to the smaller conduction band offset of InAs to the alloy $\mathrm{In}_{.75}\mathrm{Al}_{.25}\mathrm{As}$ in the barrier. Therefore, the wave function is less localized, which leads to a decrease in the Dresselhaus spin-orbit coupling. This relative effective prolongation of the well is largest for short wells, where the lowest conduction band state is closer to the band edge in the barrier such that the wave function penetrates deeply into the barrier layers. Note that we need approximately $m = 98$ barrier layers to get converged results for smaller well width. The Rashba spin-orbit coupling constant, on the other hand, reaches much higher values with the electric field applied, as compared to the GaAs quan-

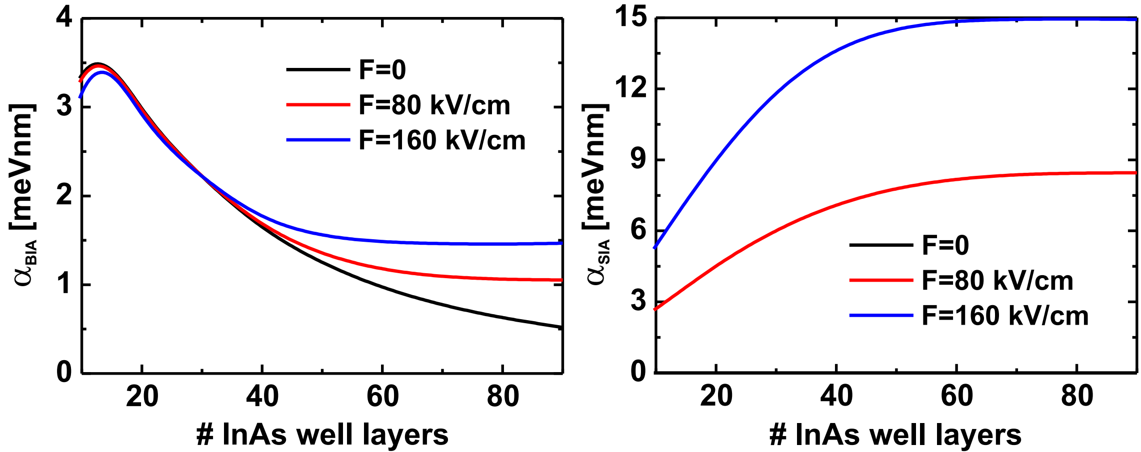

Figure 3.4.: k-linear spin-orbit coupling parameters in $(\mathrm{InAs})_n(\mathrm{In}_{.75}\mathrm{Al}_{.25}\mathrm{As})_{98}$ superlattices for various electric fields $\mathbf{F}$ as a function of the well width given by the number of InAs well layers n. The black lines show the case of zero electric field, the red lines $\mathbf{F} = 80\,\mathrm{kV/cm}$, and the blue lines $\mathbf{F} = 160\,\mathrm{kV/cm}$. (left) Dresselhaus coupling constant α_{BIA}. (right) Rashba coupling constant α_{SIA}. Note that for $\mathbf{F} = 0$, $\alpha_{\mathrm{SIA}} \equiv 0$.

tum wells. As a last material system, we study $(\mathrm{InSb})_n(\mathrm{In}_{.8}\mathrm{Al}_{.2}\mathrm{Sb})_m$ superlattices. InSb quantum wells with $\mathrm{In}_{.8}\mathrm{Al}_{.2}\mathrm{Sb}$ barriers can be grown pseudomorphically [62–64]. InSb has an even smaller band gap than InAs. In fact, already intermediate external electric field break the gap of a wide InSb quantum well. We restrict the applied electric fields such that the band gap stays intact and the lowest conduction band is formed predominantly by the indium s-orbitals. In Fig. 3.5, we show the results of our calculations. Just as before, we plot the calculated α_{BIA} in the left panel and α_{SIA} in the right panel as a function of the well width for various electric fields. As expected both spin-orbit coupling constants are drastically enhanced as compared to GaAs and also compared to the InAs superlattices. Again, as in the InAs case, the Dresselhaus spin-orbit interaction is limited for shorter wells due to the small barrier heights. Again, we need approximately $m = 98$ barrier layers, due to the wave function penetration into the barrier layers. The calculated trends in the spin-orbit coupling constants make InSb quantum wells a very interesting material system for spintronic applications. For zero or small external electric field, the spin-orbit coupling mechanism is dominated by the Dresselhaus type coupling with a very large value of α_{BIA} compared to the other studied material systems. On the other hand the steering of the Rashba coupling constant with the electric field is excellent. Therefore, already for moderate fields, one reaches the interesting case of $\alpha_{\mathrm{BIA}} = \alpha_{\mathrm{SIA}}$. For larger electric fields the Rashba coupling becomes dominant.

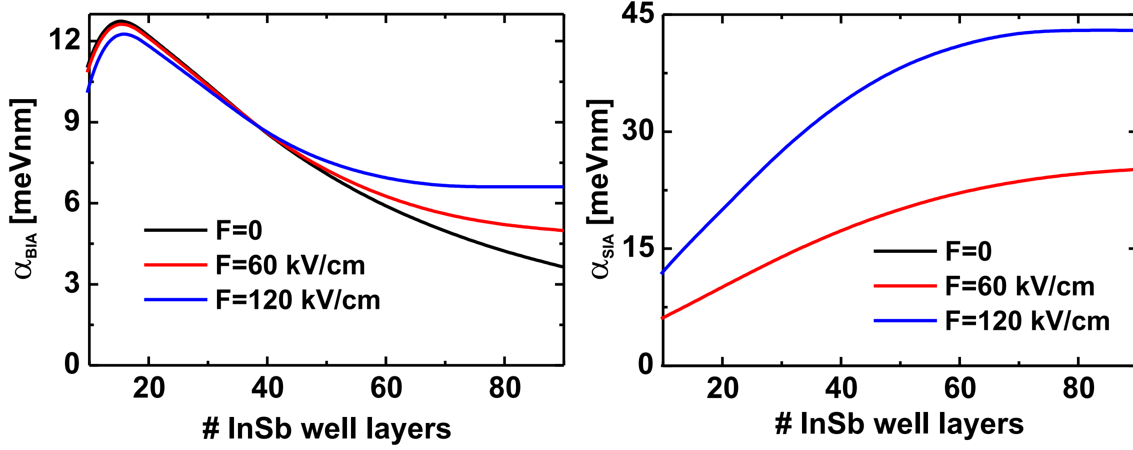

Figure 3.5.: k-linear spin-orbit coupling parameters in $(\mathrm{InSb})_n(\mathrm{In}_{.8}\mathrm{Al}_{.2}\mathrm{Sb})_{98}$ superlattices for various electric fields $\mathbf{F}$ as a function of the well width given by the number of InSb well layers n. The black lines show the case of zero electric field, the red lines $\mathbf{F} = 60\,\mathrm{kV/cm}$, and the blue lines $\mathbf{F} = 120\,\mathrm{kV/cm}$. (left) Dresselhaus coupling constant α_{BIA}. (right) Rashba coupling constant α_{SIA}. Note that for $\mathbf{F} = 0$, $\alpha_{\mathrm{SIA}} \equiv 0$.

3.4. Prediction of strain-enhanced spin splitting

In this section, we show that the k-linear spin-orbit band splitting can be enhanced by up to two orders of magnitude, both in bulk material as well as in heterostructures by strain engineering. We focus on valence bands in this section where we find this effect to be particularly pronounced. Consider (001)-strained bulk GaAs, grown pseudomorphically onto a substrate such as $\mathrm{In}_x\mathrm{Al}_{1-x}\mathrm{As}$. Since InAs possesses a larger lattice constant than GaAs, depending on the indium content x the GaAs will be tensile strained. We note that tensile strained GaAs structures can also be achieved by incorporation of phosphorus during the growth [65, 66]. The tensile strain leads to a splitting of the light hole and the heavy hole bands in such a way that the light hole forms the nondegenerate top valence band edge at the Γ-point. The degeneracy of the Γ_8-representation is lifted because the strain actually reduces the symmetry of the bulk to D_{2d}, which in turn leads to a finite k-linear spin splitting in the lateral plane off the Γ-point and hence to a finite value for α_{BIA}. In $\mathrm{GaAs/In}_x\mathrm{Al}_{1-x}\mathrm{As}$ heterostructures, where $\mathrm{In}_x\mathrm{Al}_{1-x}\mathrm{As}$ acts as the barrier and sets the lateral lattice constant [67], the confinement already lifts the degeneracy of the heavy and the light hole bands leading to a nonzero α_{BIA} already in the unstrained case. However, the confinement effect lifts the degeneracy in such a way, that the heavy hole band becomes the highest valence band. It thus counteracts to the tensile strain. Indeed, a change of the highest valence band from heavy hole like to light hole like as a function of the strain has already been observed experimentally for GaAs superlattices [68]. We have calculated α_{BIA} of the topmost light hole like valence band both for strained bulk GaAs as well as for strained GaAs heterostructures for

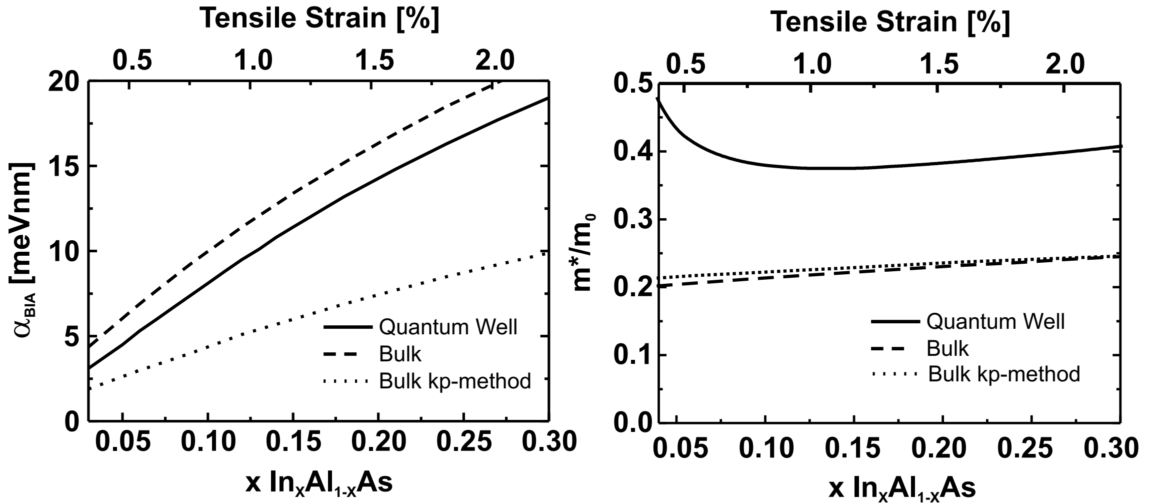

Figure 3.6.: (left) Dresselhaus spin-orbit coupling parameter α_{BIA} and (right) effective mass m^* for the top valence band in tensile strained GaAs on $\text{In}_x\text{Al}_{1-x}\text{As}$ as a function of the indium content x and tensile strain, respectively. The solid lines show the result for $(\text{GaAs})_{50}(\text{In}_x\text{Al}_{1-x}\text{As})_{16}$ superlattices, the dashed lines for bulk, both calculated with the present tight-binding method. The dotted line shows results for bulk calculated with 14-band $\mathbf{k}\cdot\mathbf{p}$ theory.

lateral tensile strain characterized by the parameter $\varepsilon = (a_\parallel - a_{\text{GaAs}})/a_{\text{GaAs}}$ ranging from approximately 0.5% to approximately 2%, which corresponds to an indium composition x in the barrier material or substrate that ranges from $x = .05$ to $x = .3$, respectively. In Fig. 3.6, we show the resulting spin-splitting constant α_{BIA} as predicted by the present tight-binding method for the topmost valence band state in strained bulk GaAs and in $(\text{GaAs})_{50}(\text{In}_x\text{Al}_{1-x}\text{As})_{16}$ superlattices corresponding to approximately 14 nm wide GaAs quantum wells, respectively. Additionally, we show results from a 14-band $\mathbf{k}\cdot\mathbf{p}$ calculation [69]. The calculations show that α_{BIA} increases drastically as a function of the tensile strain. This result is quite unexpected as the spin-orbit interaction itself is a mostly intra-atomic interaction and therefore insensitive to strain. Also the strain induced splitting of the d-orbitals does not directly influence the spin-orbit interaction, since we neglect the generally small spin splitting of the d-states. Indeed, there is no such drastic increase of α_{BIA} for the lowest conduction band. For the same GaAs heterostructure, for example, we find $\alpha_{\text{BIA}} = .9$ meVnm for zero strain and $\alpha_{\text{BIA}} = 1.0$ meVnm for 2% tensile strain. In the right panel of Fig. 3.6, we show the calculated effective mass m^* of the topmost valence band for the same superlattice and the strained bulk as a function of tensile strain or indium composition x, respectively. Also shown are again the results for the strained bulk from the $\mathbf{k}\cdot\mathbf{p}$ theory. The calculated effective masses do not depend on the strain much. The strong variation of m^* in the superlattice case for smaller values of the strain can be explained by the band crossing of the heavy

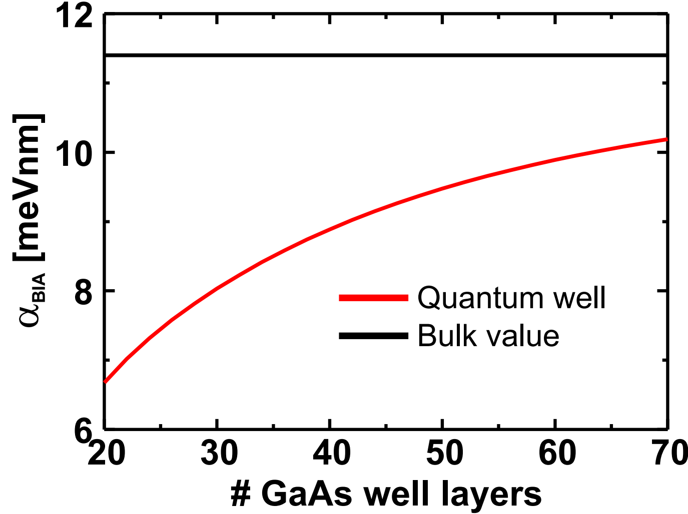

Figure 3.7.: Dresselhaus spin-orbit coupling parameter α_{BIA} for the top valence band in tensile strained $(\mathrm{GaAs})_n(\mathrm{In}_{.12}\mathrm{Al}_{.88}\mathrm{As})_{16}$ superlattices as a function of the well width given by the number of GaAs well layers n (red line). The black line shows the corresponding bulk value.

and the light hole [68]. For the effective mass of the strained bulk, we find excellent agreement between the present tight-binding method and the $\mathbf{k}\cdot\mathbf{p}$ calculations, whereas $\mathbf{k}\cdot\mathbf{p}$ theory predicts an about a factor of two smaller effect for the spin-orbit splitting. However, the increase of α_{BIA} as a function of the strain is still significant. From the tight-binding calculations, we find that the strain induced enhancement of the Dresselhaus spin-orbit coupling constant is actually largest for the topmost valence band in tensile strained bulk. In Fig. 3.7, we show the calculated Dresselhaus spin-orbit coupling constant for $(\mathrm{GaAs})_n(\mathrm{In}_{.12}\mathrm{Al}_{.88}\mathrm{As})_{16}$ superlattices corresponding to approximately 1% strain as a function of GaAs well layers n. Also shown is the corresponding value for an equally strained bulk system. As the well width increases, α_{BIA} increases as well and approaches the bulk value for large well widths. This behavior can be understood as follows. With the tensile stain the heavy and the light hole separate. However, as already mentioned, the quantization effect in the quantum well, which decreases with well width, countercats the effect of the tensile strain. That means that for a given strain the separation between the heavy and the light hole bands is largest in the case of tensile strained bulk and decreases with decreasing width of the quantum well. To prove the relevance of the heavy and light hole splitting for the predicted strain enhancement of the spin splitting, we show in Fig. 3.8 (right) the calculated α_{BIA} for the $(\mathrm{GaAs})_{50}(\mathrm{In}_x\mathrm{Al}_{1-x}\mathrm{As})_{16}$ superlattices and for the bulk system as function of the heavy and light hole splitting, induced by the tensile strain. In this case, both systems show a good agreement which proves that it is actually the splitting of the hole bands that induces the drastic increase of the spin-orbit coupling constant with strain. The physical origine can be understood by the relative composition of the wave functions. In Fig. 3.8 (left), we show the relative

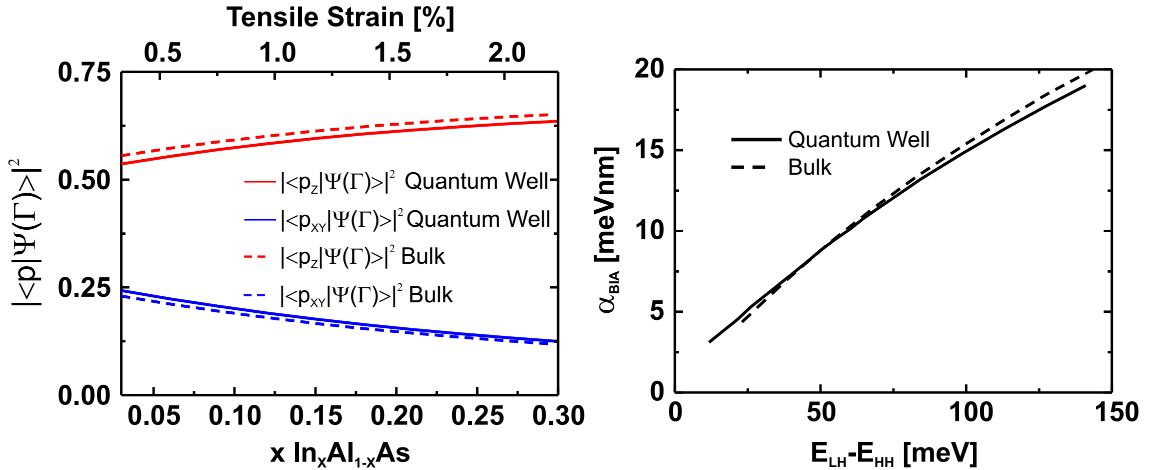

Figure 3.8.: (left) Absolute square of the p-content of the wave function for the top valence band in tensile strained GaAs on $\mathrm{In}_x\mathrm{Al}_{1-x}\mathrm{As}$ as a function of the indium content x and tensile strain, respectively. The solid lines show results for $(\mathrm{GaAs})_{50}(\mathrm{In}_x\mathrm{Al}_{1-x}\mathrm{As})_{16}$ superlattices and the dashed lines for bulk. Red shows the p_z content while blue shows the sum of p_x and p_y contributions. (right) Dresselhaus spin-orbit coupling parameter α_{BIA} for the top valence band in tensile strained GaAs on $\mathrm{In}_x\mathrm{Al}_{1-x}\mathrm{As}$ as a function of the energy splitting between the heavy hole and the light hole state at $\mathbf{k} = 0$. The solid line shows results for $(\mathrm{GaAs})_{50}(\mathrm{In}_x\mathrm{Al}_{1-x}\mathrm{As})_{16}$ superlattices and the dashed line for bulk.

p_z contribution as well as the relative contribution of the sum of p_x and p_y states to the absolute square of the total wave function at the Γ-point of the topmost valence band as a function of strain for the same heterostructure and for strained bulk. In the unstrained bulk case the p_x and p_y-orbitals form the heavy hole states while the p_z-oribitals predominantly form the light hole states. We find an increase of the p_z content with strain whereas the $p_{x,y}$ contribution decreases. For the tensile strained bulk, the p_z contribution is always larger and the $p_{x,y}$ content lower as compared to the heterostructure. Thus, we find that it is the p_z contribution that is responsible for the k-linear spin splitting of a nondegenerate band close to the Γ-point, which agrees with the findings in the previous Sec. 3.2.

3.5. Influence of higher order in k spin splitting

In this section, we want to investigate the influence of higher order in k terms on the spin splitting of nondegenerate band edges. In Eq. (3.1), the expansion in the lateral wave vector only includes terms up to quadratic order in the wave vector. We will show, that this is sufficient only for very small values of the wave vector $k_{\|}$, smaller than approximately 1% of the reciprocal lattice vector $\mathbf{G}$. We first focus on D_{2d} symmetric structures. In Fig. 3.9, we plot the calculated spin-splitting energy

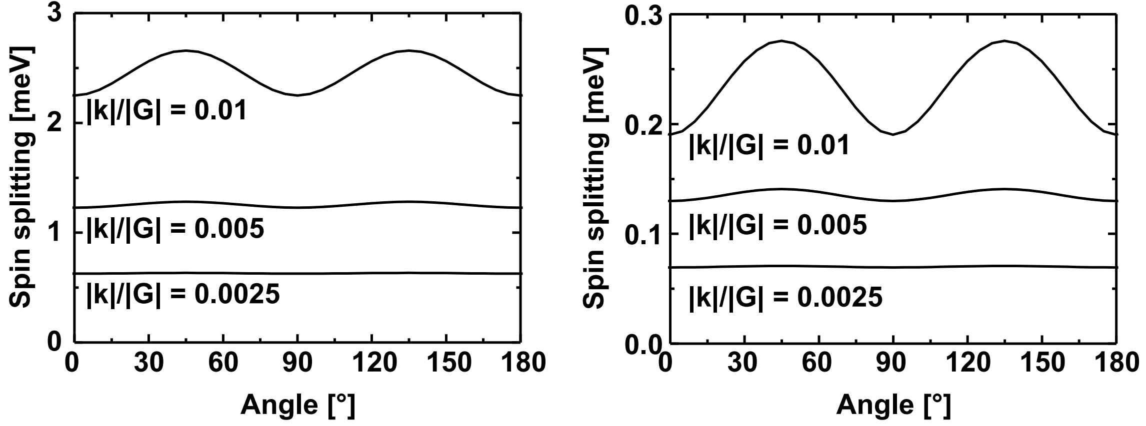

Figure 3.9.: Spin-splitting energy in a tensile strained $(GaAs)_{50}(In_{.1}Al_{.9}As)_{16}$ superlattice for various values of the absolute value of the wave vector $|\mathbf{k}| = k_{\|}$ in units of the reciprocal lattice vector $|\mathbf{G}|$ as a function of the polar angle relative to [100]. (left) Top valence band. (right) Lowest conduction band.

of the top valenece band (left) and the lowest conduction band (right) for a tensile strained $(GaAs)_{50}(In_{.1}Al_{.9}As)_{16}$ superlattice, corresponding to a strain of .75%, as a function of the polar angle ϕ for various values of $k_{\|}$ given in units of $\mathbf{G}$. We find pronounced oscillations of the spin-splitting energy as a function of ϕ already for $k_{\|}/|\mathbf{G}| \approx 0.01$. These oscillations stem from higher order contribution in k and can be understood as follows. The general Hamiltonian for a nondegenerate band in a D_{2d} symmetric structure up to $k_{\|}^3$ can be written as [70],

$$H(n\mathbf{k}) = \frac{\hbar^2}{2m^*}k_{\|}^2 \cdot \sigma_0 + \Omega_x(\mathbf{k})\sigma_x - \Omega_y(\mathbf{k})\sigma_y, \tag{3.11}$$

where Ω_x and Ω_y are given by,

$$\begin{aligned} \Omega_x(\mathbf{k}) &= \alpha_{\mathrm{BIA}}k_x + c_1 k_x k_y^2 + c_2 k_x^3, \\ \Omega_y(\mathbf{k}) &= \alpha_{\mathrm{BIA}}k_y + c_1 k_x^2 k_y + c_2 k_y^3, \end{aligned} \tag{3.12}$$

where c_1 and c_2 are parameters associated with the k-cubic spin-orbit coupling. Note that this is the most general form for D_{2d} symmetry. In 14-band $\mathbf{k}\cdot\mathbf{p}$ theory, one gets $c_2 \equiv 0$ [3]. The Hamiltonian (Eq. (3.12)) has the eigenvalues,

$$E_{\pm}(k_{\|}, \phi) = \frac{\hbar^2}{2m^*}k_{\|}^2 \pm \left(\alpha_{\mathrm{BIA}}k_{\|} + 2(c_1 + c_2)\frac{k_x^2 k_y^2}{k_{\|}} + c_2 k_{\|}^3\right). \tag{3.13}$$

For the spin-splitting energy, we thus get,

$$\Delta E_{SO} = 2\alpha_{\mathrm{BIA}}k_{\|} + c_2 k_{\|}^3 + (c_1 + c_2)\sin^2(2\phi)k_{\|}^3. \tag{3.14}$$

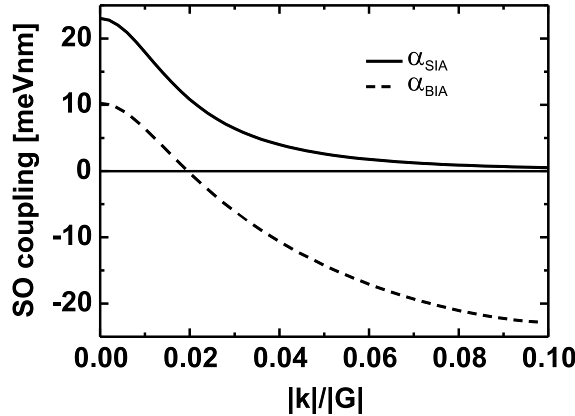

Figure 3.10.: Dresselhaus (α_{BIA}) and Rashba (α_{SIA}) spin-orbit coupling parameter for a $(\mathrm{InSb})_{30}(\mathrm{In}_{.8}\mathrm{Al}_{.2}\mathrm{Sb})_{98}$ superlattice in an external electric field of $\mathbf{F} = 100\,\mathrm{kV/cm}$ as a function of the absolute value of the wave vector $|\mathbf{k}|$ in units of the reciprocal lattice vector $|\mathbf{G}|$, calculated as $\Delta E_{SO}/k_{\|}$. The gray line depicts the zero of the vertical axis.

We can fit the calculated angle dependence in Fig. 3.9 to the angle dependence for a k-cubic spin-orbit coupling (Eq. (3.14)). For the top valence band, we get $c_1 = -91.2\,\mathrm{meVnm}^3$ and $c_2 = 15.9\,\mathrm{meVnm}^3$. For the lowest conduction band we calculate $c_1 = -23.5\,\mathrm{meVnm}^3$ and $c_2 = -1.1\,\mathrm{meVnm}^3$. We note that these k-cubic coupling constants are almost independent of the strain.

When the absolute value of the wave vector increases further, also the k-cubic approximation becomes invalid and even higher order terms dominate the behavior of the spin splitting. To illustrate this effect, we have calculated the spin-orbit coupling constants for a C_{2v}-symmetric structure, to also include the Rashba effect, as a function of $k_{\|}$ assuming the validity of the k-linear model also for larger $k_{\|}$. This assumption in turn leads to a dependence of the coupling constants on the lateral wave vector. In particular, we have studied the spin-orbit coupling constants for an $(\mathrm{InSb})_{30}(\mathrm{In}_{.8}\mathrm{Al}_{.2}\mathrm{Sb})_{98}$ superlattice in constant external electric field of $\mathbf{F} = 100\,\mathrm{kV/cm}$. The results for the k-dependent α_{BIA} and α_{SIA} are shown in Fig. 3.10 as a function of $k_{\|}$ up to 10% of $|\mathbf{G}|$. We find, that the Rashba effect is completly quenched for larger wave vectors, while the Dresselhaus spin-orbit coupling constant changes sign, and aquires a large magnitude again. Thus, one has to be careful about the interpretation of experimental results in terms of the k-linear or k-cubic model if the densities are high and the Fermi wave vector becomes considerably larger than approximately 1% of the reciprocal wave vector.

3.6. Summary

In this chapter, we have studied the k-dependent spin splitting of nondegenerate subbands in semiconductor heterostructures using our atomistic tight-binding the-

ory. We find remarkably different results than that predicted by simple envelope function theory, that does not take into account the symmetry of the problem adequately. In particular, we have studied the interplay between the Dresselhaus and the Rashba-type spin-orbit interaction in perpendicular electric fields. In contrast to the widespread assumption, we find, that the Dresselhaus spin-orbit coupling is not negligible for wider quantum wells, due to the field induced localization of the wave function. We predict particularly large Dresselhaus and Rashba effects for InSb quantum with a large steering effect by the electric field of the latter while in GaAs quantum wells both effects are small and of similar magnitude also for large electric field. We have studied the spin-orbit coupling for hole subbands in tensile strained GaAs heterostructures. We find an enhancement of the Dresselhaus spin-orbit coupling constant by almost two orders of magnitude for the top (light hole) valence band as a function of the applied strain. We will later predict concrete quantum spin-device geometries based on both, tensile strained p-GaAs in Chapter 8 as well as InSb in Chapter 9, that are based on the results presented here. Further, we have shown, that the model of k-linear spin-orbit coupling becomes invalid already for quite small values of the lateral wave vector $k_{\|}$. Thus, in experiments one has to keep the density accordingly small, in order to interpret the results in terms of these theories.

4. Results for HgTe quantum well structures

4.1. Introduction

HgTe quantum wells are interesting systems for the investigation of spin-dependent transport phenomena due the very large spin-orbit coupling. Very recently, the inverse intrinsic spin-Hall effect could be detected in nanostructures based on HgTe/-$Hg_xCd_{1-x}Te$ quantum wells [24]. Moreover, the quantum spin Hall effect was observed in these structures [9] just as previously predicted [23]. These properties make HgTe very interesting for spintronic device applications as well as for fundamental research. HgTe quantum wells have a so called type-III alignment of the band structure [37, 71]. While in the bulk material the heavy and light hole bands are degenerate due to the tetrahedral symmetry, in the quantum well, they separate. As usual the light hole state is pushed down while the heavy hole state is pushed up due to the quantization along the growth direction. This quantization also causes the electron band to shift upwards. Since the gap between the electron band and the heavy hole band is negative in the bulk, the resulting band structure in the quantum well depends crucially on the well width. For wide wells the band order of the bulk stays intact. That means the lowest electron level lies below the highest heavy hole level. This is the regime of the so called inverted band structure where the quantum spin Hall effect was observed. For the higher or lower subbands the ordering is as usual in semiconductor heterostructures. When the width of the well gets smaller, the electron band is pushed up further, while the heavy hole is effectively unchanged due to the large effective mass along the growth direction. At some critical quantum well thickness, the band structure becomes normal, i.e. the lowest conduction band is derived from the first electron subband, while the highest valence band is derived from the first heavy hole subband. For the normal band structure the quantum spin Hall effect vanishes.

Furthermore, since the band gap in HgTe quantum wells is very small, typically of the order of 20 meV, it is possible to tune the Fermi energy by an applied top gate voltage all the way from the valence bands, crossing the gap, into the conduction bands. It is thus possible to study the whole quantum transport regime from metallic behavior (hole and electron like transport) to the quantum spin Hall effect, which occurs when the Fermi energy lies within the band gap, within a single structure [9, 24, 72, 73]. This possibility is of great interest for the spintronic device application that we will show in Sec. 10.6 by the proposal of a spin transistor based on a HgTe

quantum well structure.

This chapter is organized as follows. In Sec. 4.2, we present new results for the subband structure in HgTe quantum wells, based on the novel tight-binding model, presented in Sec. 2. In Sec. 4.3, we develop two models in the envelope function approximation (EFA) that describe the relevant subbands and spin-orbit coupling mechanisms and are thus suitable for quantum transport calculations that we present later in Sec. 10.6 of this thesis.

4.2. New results on the subband structure of HgTe quantum wells

In this section, we study HgTe heterostructures using our newly developed tight-binding model. In particular, we study $(\mathrm{HgTe})_m(\mathrm{Hg}_x\mathrm{Cd}_{1-x}\mathrm{Te})_n$ superlattices. We assume a valence band offset between the HgTe and CdTe of 400 mV as calculated in Ref. [74]. Experimentally, the measured band offsets lie between 350 meV and 500 meV [38]. We take $n = 26$, large enough, in order to decouple adjacent quantum wells from each other. Former studies of HgTe quantum wells have relied to a great extent on the 8-band $\mathbf{k}\cdot\mathbf{p}$ method [23–28]. In 8-band $\mathbf{k}\cdot\mathbf{p}$ theory a crossing of the lowest conduction band and the highest valence band at the Γ-point for a critical well thickness of about $d_{\mathrm{crit}} = 6.4\,\mathrm{nm}$ is predicted [23] since in this model an interaction between the Γ_6 derived band (electron) and the Γ_8 derived band (heavy hole) is forbidden at $\mathbf{k} = 0$. However, due to the missing bulk inversion symmetry such an interaction is actually allowed by symmetry [75]. In the atomistic tight-binding theory, on the other hand, all interactions that are allowed in a D_{2d}-symmetric quantum well are included, since the underlying symmetry of the crystal is included on an atomistic level. We have calculated the subband structure of $(\mathrm{HgTe})_n(\mathrm{Hg}_{.3}\mathrm{Cd}_{.7}\mathrm{Te})_{26}$ superlattices at $\mathbf{k} = 0$ as a function of the well thickness. In Fig. 4.1 (left), the results are shown for the first electron subband E1 (blue line), the first heavy hole subband HH1 (red line) and the second heavy hole subband HH2 (black line). We find a clear anticrossing of the electron and the heavy hole band. The bands come closest at about $d_{\mathrm{crit}} = 7.0\,\mathrm{nm}$ which is slightly larger than the critical width predicted by $\mathbf{k}\cdot\mathbf{p}$ theory, however, still within the reported experimental findings [76]. At a well width of $d = 8.3\,\mathrm{nm}$, we find a crossing between the first electron subband and the second heavy hole subband. In this case, we find a crossing rather than an anticrossing. Although the interaction between electron and heavy hole is allowed in principle, the overlap of both wave functions is suppressed due the different parity of the envelope functions in the growth direction. We will therefore focus on structures with a well width $7.0 - 8.3\,\mathrm{nm}$ for an inverted band alignment. Our calculated energy levels differ slightly form the predictions by $\mathbf{k}\cdot\mathbf{p}$ theory [77]. It is known, that the details of the subband structure depend strongly on the value of the valence band offset [71]. Therefore, the quantitative differences to our results are mainly due to the assumed valence band offset of 570 meV [40]

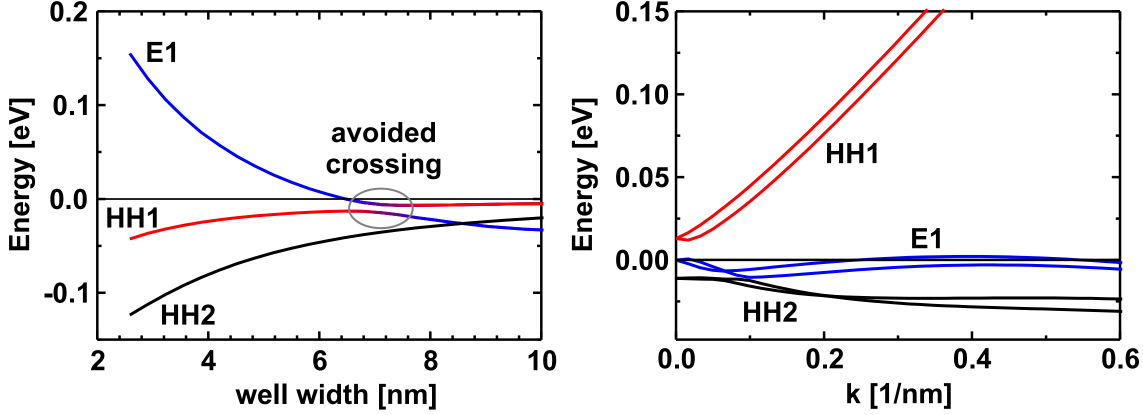

Figure 4.1.: (left) Subband energies at $\mathbf{k} = 0$ in $(HgTe)_n(Hg_{.3}Cd_{.7}Te)_{26}$ superlattices as a function of the well width. The blue line shows the first electron level (E1), the red line the first heavy hole level (HH1) and the black line the second heavy hole level (HH2). (right) Subband dispersion in a $(HgTe)_{24}(Hg_{.3}Cd_{.7}Te)_{26}$ superlattice, corresponding to a 7.8 nm wide $HgTe/Cd_{.7}Hg_{.3}Te$ quantum well as a function of the wave vector in [110] direction. The colors are in correspondence with the left figure.

which somewhat larger than the one we assume. However, our results agree well with the available experimental results on the subband structure and band offset [37, 39, 41].

In the right panel of Fig. 4.1, we plot the subband dispersion for a $(HgTe)_{24}$-$(Hg_{.3}Cd_{.7}Te)_{26}$ superlattice, corresponding to a 7.8 nm wide $HgTe/Cd_{.7}Hg_{.3}Te$ quantum well. The colors are in correspondence with the figure on the left. We find a very large k-dependent spin splitting for all bands. Spin splitting energies of this order have been found experimentally [76, 78]. The reason for this large spin splitting is a resonant enhancement of the spin-orbit interaction [79]. The physical origin of this resonance can be understood as follows. We have seen that the spin-orbit interaction lifts the spin degeneracy of any nondegenerate energy band away from the Γ-point but has no effect directly at $\mathbf{k} = 0$. The situation changes, however, when there is a band degeneracy of the nonrelativistic bands. If two nonrelativistic bands cross at the Γ-point, the spin-orbit coupling induces an interesting nonperturbative effect. It lifts the degeneracy and produces a finite energy gap at the Γ-point and leads to a resonantly enhanced spin splitting, that cannot be interpreted in terms of a simple one-band model. Thus the effect is largest for the critical well thickness, but still appreciable for a small gap between the nonrelativistic bands. Also note the camel-back like structure in the dispersion of the highest valence band. This effect stems from the interaction with lower lying hole bands. Du to this camel-back, the valence band maximum is shifted away from the Γ-point to larger wave vectors.

In Fig. 4.2, we plot the probability density of the lowest conduction subband (right panel) and the highest valence subband (left panel). The black lines show the overall

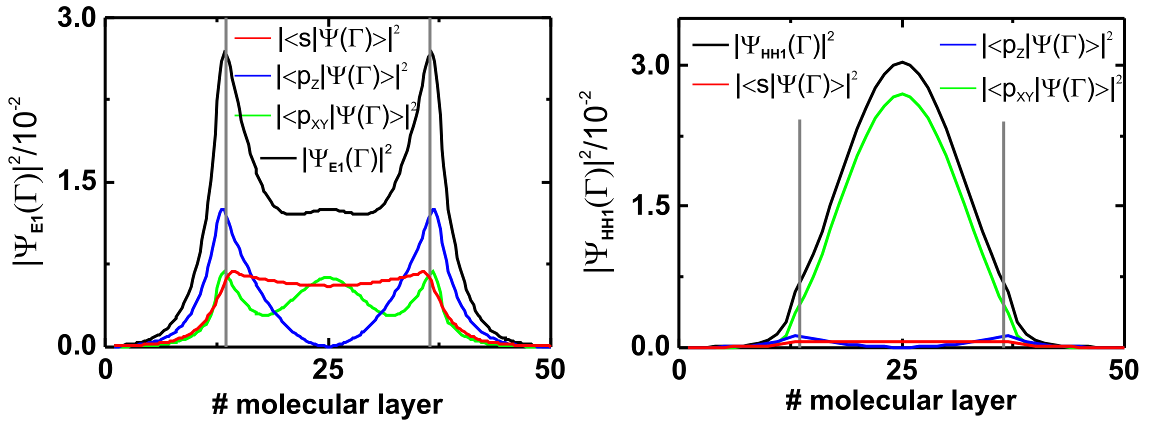

Figure 4.2.: Absolute square of the wave function of the first electron level E1 (left) and the first heavy hole level HH1 (right) in a $(HgTe)_{24}(Hg_{.3}Cd_{.7}Te)_{26}$ superlattice as a function of the number of the molecular layer. Note that there are in total 50 molecular layers. The wave functions have been averaged over each molecular layer for clarity. The black line shows the total wave function, including the contributions from all orbitals. The red lines show the contribution of the s-orbitals only, the blue lines the contribution of the p_z-orbitals, and the green lines the sum of the p_x and the p_y-orbitals. The vertical gray lines denote the material interfaces.

probability density. Note that the form of the total wave function agrees well with the $\mathbf{k} \cdot \mathbf{p}$ results [77] for both sublevels. The highest valence band state has two maximums right at the interfaces between the well and the barrier. It has therefore also been termed interfacial state $I1$ rather than $E1$ before [80]. The content of the s-orbitals, shown as red line, is almost constant over the well width while the admixture of the p_z-orbitals shown in blue has maximums at the interfaces and is suppressed within the well. Note that we have seen the same behavior of the p_z-states for the lowest conduction band state of III-V semiconductors in Chapter 3 where we found that the admixture of p_z-states in the s-dominated conduction band accounts for the spin-orbit splitting. In the HgTe quantum well the relative content of the p_z-states is enhanced drastically as compared to e.g. GaAs due to the smaller energy separation between the sates which accounts for a large spin-orbit splitting. Moreover, we find that a substantial part of the wave function is heavy hole like, shown by the sum over the p_x and p_y contributions as yellow line in the figure. It is the admixture of the heavy hole state, that accounts for the anticrossing as well as for the resonantly enhanced spin splitting. The corresponding heavy hole state in the right panel of the figure shows admixtures of the s-states and p_z-states, however, the admixtures are relatively small compared to the contribution of p_x and p_y-states that clearly dominate the wave function, as expected for a heavy hole state.

Our results clearly show that the bulk inversion asymmetry in HgTe quantum wells leads to a relevant spin splitting as well as to an anticrossing of the relevant

Parameter	4-band	6-band	Parameter	6-band
B [meVnm^2]	1140	720	D_2 [meVnm^2]	-14
D [meVnm^2]	-200	-14	M_2 [meV]	11
M [meV]	-13	-13	A_2 [meVnm]	-33
A [meVnm]	-244	-146	S_2 [meVnm^2]	540
γ [meVnm]	111	90	S_3 [meVnm^2]	150
S [meVnm^2]	190	144	T_2 [meVnm]	11
T [meVnm]	115	87	T_3 [meVnm]	7

Table 4.1.: Parameters of the 4- and 6-band EFA model for a 7.8 nm wide HgTe/$Hg_{.3}Cd_{.7}Te$ quantum well.

subbands. Hence, it is not justified to neglect this effect, as is done in simple 8-band $\mathbf{k} \cdot \mathbf{p}$ theory.

4.3. Novel envelope function approximation for HgTe quantum wells

In this section, we will develop an effective model for the band structure in HgTe quantum wells that only includes the relevant bands in order to be able to calculate quantum transport properties of nanostructures that are based on HgTe quantum wells. In particular, we will base that model on the envelope function approximation (EFA) as in Sec. 3.2 for the k-linear spin-orbit coupling models. However, due to strong mixing of the electron and hole states such a simple model with a Rashba and Dresselhaus like spin-orbit interaction cannot satisfactorily describe the properties of neither the electron nor the hole band. Moreover, in order to capture the quantum spin Hall effect (QSHE) in the calculations, minimally a model with two electronic bands plus spin, i.e. a 4-band model is required. The original model proposed by Bernevig, Hughes, and Zhang [23], the so called BHZ-model, includes the QSHE but neglects mixing of the spin states due to spin-orbit coupling. Since HgTe quantum wells are interesting also for spintronic applications that employ also the ordinary spin-Hall effect [24], it is highly desirable to include the spin-orbit interactions into the model. A model based on 8-band $\mathbf{k} \cdot \mathbf{p}$ calculations [25] that takes into account spin-orbit interaction due to the structural inversion asymmetry in structures with C_{2v} symmetry but neglects the spin-orbit coupling in the D_{2d} symmetric case has been proposed recently in Ref. [28]. This model still neglects the effects of the bulk inversion asymmetry, which are quite important in these structures as we have shown in the previous (Sec. 4.2). We have developed an effective 4-band model based on our tight-binding calculations that takes into account all symmetry related aspects of the spin-orbit coupling. As it turns out this minimal model does not reproduce the band structure of the highest valence bands satisfactorily since coupling to lower valence bands is not included explicitly. We have therefore extended the effective model to

six bands (three electronic bands times spin) in order to improve the dispersion of the highest valence band as compared to the full-band tight-binding results. However, since the 4-band model can describe the conduction band dispersion close to the Γ-point quite well, it is useful when the transport is dominanted by the conduction band, since it is numerically much easier to handle in quantum transport calculations than the more complex 6-band model. To derive the EFA models, we follow Graf and Vogl [81]. We expand the tight-binding Hamiltonian (Eq. (1.4)) up to second order in the wave vector $\mathbf{k}$ around a given $\mathbf{k}^*$. In matrix notation, we get,

$$H(\mathbf{k}) = H(\mathbf{k}^*) + \nabla_{\mathbf{k}} H(\mathbf{k})|_{\mathbf{k}^*}(\mathbf{k}-\mathbf{k}^*) + \frac{1}{2}(\mathbf{k}-\mathbf{k}^*)\cdot\nabla_{\mathbf{k}}\nabla_{\mathbf{k}} H(\mathbf{k})|_{\mathbf{k}^*}\cdot(\mathbf{k}-\mathbf{k}^*) + \mathcal{O}[(\mathbf{k}-\mathbf{k}^*)^3]. \quad (4.1)$$

In the Bloch eingenbasis (Eq. (1.2)), we can define an effective momentum operator $\mathbf{p}_{n,n'}$ and an operator $T_{n,n'}$ related to the kinetic energy,

$$\begin{aligned}\mathbf{p}_{n,n'}(\mathbf{k}^*) =& \frac{m_0}{\hbar}\mathbf{C}^\dagger(n\mathbf{k}^*)\nabla_{\mathbf{k}} H(\mathbf{k})|_{\mathbf{k}^*}\mathbf{C}(n'\mathbf{k}^*) \qquad (4.2)\\ =& \frac{m_0}{\hbar}\sum_{\alpha,\alpha'} C^*_{\alpha'}(n\mathbf{k}^*)\sum_L i(\mathbf{R}_{\alpha' L}-\mathbf{R}_\alpha)e^{i\mathbf{k}^*(\mathbf{R}_{\alpha' L}-\mathbf{R}_\alpha)}t_{\alpha',\alpha}(\mathbf{R}_{\alpha' L}-\mathbf{R}_\alpha)C_\alpha(n'\mathbf{k}^*),\\ T_{n,n'}(\mathbf{k}^*) =& \frac{m_0}{\hbar}\mathbf{C}^\dagger(n\mathbf{k}^*)\nabla_k\nabla_{\mathbf{k}} H(\mathbf{k})|_{\mathbf{k}^*}\mathbf{C}(n'\mathbf{k}^*).\end{aligned}$$

Here m_0 is the bare electron mass, $\mathbf{C}(n\mathbf{k}^*)$ is the vector of the Bloch coefficients $C_\alpha(n\mathbf{k}^*)$ (Eq. (1.2)) for band index n and wave vector $\mathbf{k}^*$. With these definitions, we can write the matrix elements of the Hamiltonian in the Bloch basis $|n\mathbf{k}^*\rangle$ as,

$$\begin{aligned}H_{n,n'}(\mathbf{k}) =& E_n(\mathbf{k}^*)\delta_{n,n'} + \frac{\hbar}{m_0}\mathbf{p}_{n,n'}(\mathbf{k}^*)(\mathbf{k}-\mathbf{k}^*) + \frac{\hbar^2}{2m_0}(\mathbf{k}-\mathbf{k}^*)T_{n,n'}(\mathbf{k}^*)(\mathbf{k}-\mathbf{k}^*)\\ &+ (\mathbf{k}-\mathbf{k}^*)\cdot\frac{\hbar^2}{2m_0^2}\sum_{m\neq n,n'}\mathbf{p}_{n,m}(\mathbf{k}^*)\mathbf{p}_{m,n'}(\mathbf{k}^*)\left(\frac{1}{E_n(\mathbf{k}^*)-E_m(\mathbf{k}^*)}\right.\\ &\left.+\frac{1}{E_{n'}(\mathbf{k}^*)-E_m(\mathbf{k}^*)}\right)\cdot(\mathbf{k}-\mathbf{k}^*). \quad (4.3)\end{aligned}$$

From that expression, we calculate the effective models by taking $\mathbf{k}^* = 0$. To this end, we calculate the eigenvalues and eigenfunctions for a given quantum well structure at $\mathbf{k} = 0$ numerically within our tight-binding model. For the effective model with four bands, we include the first electron bands $|\mathrm{E1},\uparrow\rangle$ and $|\mathrm{E1},\downarrow\rangle$ and the first hole bands $|\mathrm{HH1},\uparrow\rangle$ and $|\mathrm{HH1},\downarrow\rangle$ explicitly. That means, $n, n' \in \{|\mathrm{E1},\uparrow\rangle, |\mathrm{E1},\downarrow\rangle, |\mathrm{HH1},\uparrow\rangle, |\mathrm{HH1},\downarrow\rangle\}$ while the index m runs over all other bands. In what follows, we focus on the $(HgTe)_{24}(Hg_{.3}Cd_{.7}Te)_{26}$ superlattice that corresponds to a 7.8 nm wide $HgTe/Hg_{.3}Cd_{.7}Te$ quantum well. Hence, we focus on a structure in the inverted regime. The heavy hole like eigenfunctions $|\mathrm{HH1},\uparrow\downarrow\rangle$ belong to the lowest conduction band while the electron like eigenfunctions $|\mathrm{E1},\uparrow\downarrow\rangle$

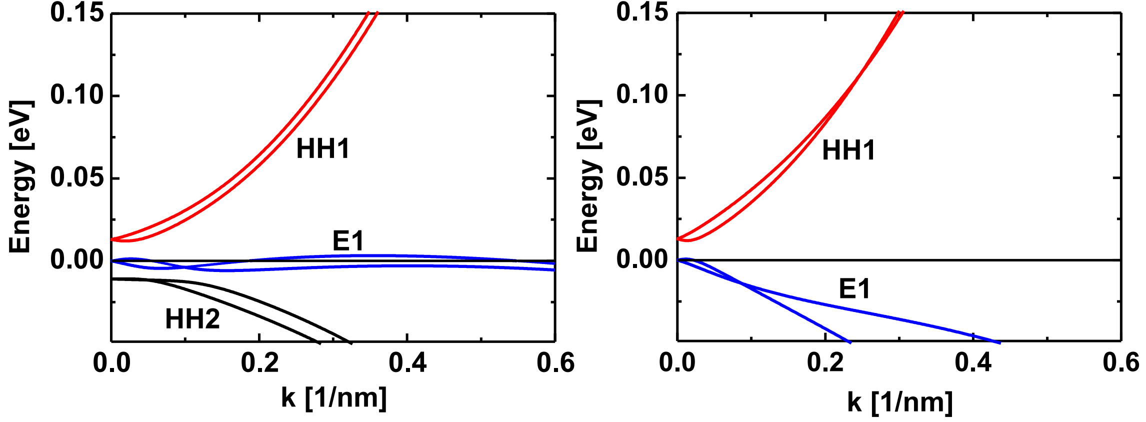

Figure 4.3.: Subband dispersion in a 7.8 nm wide $HgTe/Hg_{.3}Cd_{.7}Te$ quantum well as a function of the wave vector in [110] direction, calculated with the relativistic 6-band model (left) and the relativistic 4-band model (right). The red lines depict the first heavy hole state HH1, the blue lines the first electron state E1, and the black lines the second heavy hole state HH2. Note that the HH2 is only included in the 6-band model.

belong to the highest valence band. The calculated matrix elements (Eq. (4.3)) lead to the following 4-band model in the basis $|E1,\uparrow\rangle$, $|HH1,\uparrow\rangle$, $|E1,\downarrow\rangle$, and $|HH1,\downarrow\rangle$,

$$H_{4b}(k_x, k_y) = \begin{pmatrix} Bk_\parallel^2 & Ak_+ & \gamma k_+ & -Sk_\parallel^2 \\ Ak_- & Dk_\parallel^2 - M & Sk_\parallel^2 & Tk_- \\ \gamma k_- & Sk_\parallel^2 & Bk_\parallel^2 & -Ak_- \\ -Sk_\parallel^2 & Tk_+ & -Ak_+ & Dk_\parallel^2 - M \end{pmatrix}, \tag{4.4}$$

where we have introduced the abbreviations $k_\parallel = \sqrt{k_x^2 + k_y^2}$ and $k_\pm = k_x \pm ik_y$. The band structure parameters B and D describe the quadratic intraband coupling of electron and hole, respectively. A is the k-linear electron-hole coupling, γ is the Dresselhaus like spin-orbit coupling of the electron, T is the k-linear spin-orbit coupling of the hole, and S denotes the k-quadratic coupling between electron and hole with opposite spin. M is the energy separation of the electron and the hole state at $\mathbf{k} = 0$. Please note that a k-independent coupling between the electron and the hole with opposite spin as proposed in Ref. [75] for the BHZ-model is already included in the basis states of our model and hence incorporated into the level splitting M. The phase relations between the basis states have been chosen in order to reproduce the BHZ-Hamiltonian without spin-orbit coupling and to have a Dresselhaus-like coupling between the spin states of the electron. The numerically calculated values for the parameters using Eq. (4.3) leads to a model, that reproduces the subband dispersion (Fig. 4.1 (right)) only for very small values of the wave vector. Since for the nanostructures that we study later in Sec. 10.6 higher wave vectors are mixed in due to the additional confinement in the lateral directions, we have improved the parameters by a least square fit to the exact dispersion. The resulting

parameters are given in Table 4.1. The calculated subband dispersion using the 4-band model is shown in Fig. 4.3 (right). We find a good agreement of the conduction band dispersion up to $|\mathbf{k}| \approx 0.15\,\mathrm{nm}^{-1}$, which is sufficient for our purposes. The valence band, however, is reproduced very poorly. The camel-back like structure visible in Fig. 4.1 (right) cannot be reproduced by any such 4-band model since the camel back stems from an interaction with lower hole subband, which have to be included explicitly into the model. The camel back leads to a band maximum of the valence band away from the Γ-point, such that the band structure becomes indirect in k-space which will clearly effect the transport properties of p-like quantum wells. To capture this effect, we have developed an effective 6-band EFA model. We additionally include the second heavy hole subband explicitly. The Hamiltonian calculated from Eq. (4.3) in the basis $|\mathrm{E1},\uparrow\rangle$, $|\mathrm{HH1},\uparrow\rangle$, $|\mathrm{HH2},\uparrow\rangle$, $|\mathrm{E1},\downarrow\rangle$, $|\mathrm{HH1},\downarrow\rangle$, and $|\mathrm{HH2},\downarrow\rangle$ reads,

$$H_{6b}(k_x,k_y) = \begin{pmatrix} Bk_\parallel^2 & Ak_+ & A_2k_+ & \gamma k_+ & -Sk_\parallel^2 & -S_2k_+^2 \\ Ak_- & Dk_\parallel^2 - M & S_3k_-^2 & Sk_\parallel^2 & Tk_- & T_3k_- \\ A_2k_- & S_3k_+^2 & D_2k_\parallel^2 - M_2 & S_2k_+^2 & T_3k_- & T_2k_- \\ \gamma k_- & Sk_\parallel^2 & S_2k_-^2 & Bk_\parallel^2 & -Ak_- & -A_2k_- \\ -Sk_\parallel^2 & Tk_+ & T_3k_+ & -Ak_+ & Dk_\parallel^2 - M & S_3k_+^2 \\ -S_2k_-^2 & T_3k_+ & T_2k_+ & -A_2k_+ & S_3k_-^2 & D_2k_\parallel^2 - M_2 \end{pmatrix}. \quad (4.5)$$

Additionally to the parameters of Eq. (4.4), we have D_2 for the quadratic intraband coupling of the extra hole band, M_2 for its level spacing to the electron state. A_2 is the k-linear coupling to the electron states, T_2, T_3 are the additional k-linear spin-orbit coupling parameters between the hole states, and S_2 and S_3 are the additional k-quadratic couplings. The calculated parameters are also shown in Table 4.1. They are again obtained by taking the parameters derived form Eq. (4.3) as input for a least square fit to the exact dispersion. The resulting subband dispersion for the 6-band model is shown in Fig. 4.3 (left). The overall agreement with the exact dispersion is good up to relatively large wave vectors. Especially the camel-back structure of the valence band is nicely reproduced. Note that the agreement for the conduction band is actually better in the 4-band model. Therefore, we will use the 4-band model for the transport calculations if the transport is dominated by the conduction band.

4.4. Summary

In this chapter, we have presented results for the electronic structure of HgTe/CdTe heterostructures using the novel semi-empirical tight-binding parametrization, presented in Sec. 2. We have calculated the subband structure in HgTe quantum wells as a function of the well width. We find an inverted band structure for wells wider than the critical thickness $d_{\mathrm{crit}} \approx 7\,\mathrm{nm}$, in accordance with experiment and previous

theoretical investigations. However, in contrast to simple 8-band $\mathbf{k} \cdot \mathbf{p}$ theory, we find a substantial interaction between the first electron subband and the first hole subband at the Γ-point, that leads to an anti-crossing of both bands as a function of well width rather than a simple crossing between both states. This previously neglected interaction is also the reason for the large k-dependent spin splitting of the subbands that we predict.

We have further developed two envelope function models for HgTe quantum wells, based on our tight-binding results. We find that minimally four bands are necessary to describe the lowest conduction band in these structures satisfactorily, while six bands are needed to also describe the highest valence band. We have given concrete parameters for the model for a 7.8 nm wide HgTe/$Hg_{.3}Cd_{.7}Te$. We will later in Sec. 10.6 employ these models, to predict quantum transport properties of complex device geometries based on this material.

Part II.

Spin dependent quantum transport calculations

5. Non-equilibrium Green's functions theory for spin-dependent quantum transport

5.1. Introduction

A detailed understanding of carrier dynamics is crucial for the design and improvement of modern semiconductor nanodevices. However, neither a classical or semiclassical nor a strictly coherent, ballistic quantum mechanical theory can capture the tight interplay between incoherent relaxation processes and quantum interference effects [82].

A general and rigorous framework to capture all of these effects was developed in the 1960s by Keldysh [83] and, independently by Kadanoff and Baym [84] and Schwinger [85]. Today, it is well established that this so-called non-equilibrium Green's function (NEGF) theory is among the most general schemes for the prediction of quantum transport properties [86–89].

The basic NEGF equations, including scattering, are complex, mathematically tough, and a quantitative implementation is still a highly challenging task, even with the recent advances of modern computer hardware [90, 91]. Furthermore, it is very difficult to develop approximations within the NEGF formalism which maintain charge and current conservation and obey Pauli's principle [92]. In the limit of ballistic transport the contact block reduction (CBR) method can be used to efficiently calculate quantum transport in three dimensional nanostructures [93, 94].

This chapter is organized as follows. We shortly review the basic NEGF formalism in Sec. 5.2, define the basic Green's functions and discuss their equation of motion with special emphasis on stationary systems. A more extensive introduction into the theory of non-equilibrium processes can be found e.g. in Ref. [95]. We discuss the boundary conditions in general multi-band theories for transport in open quantum devices in Sec. 5.3. We will present our novel method to calculate stationary transport properties that we termed multi-scattering Büttiker probe (MSB) model in Sec. 5.4. This theory generalizes the so-called Büttiker porbe (BP) model [96] and accounts for individual scattering mechanisms. Current conservation is ensured and the MSB method is orders of magnitude faster than a full NEGF approach, which makes it possible to address problems which are not accessible with the full NEGF

approach due to the numerical expenses as e.g. transport through multi channel two and three dimensional nano-structures. Finally, in Sec. 5.6, we derive the observable quantities from the non-equilibrium Green's functions.

5.2. Overview over the non-equilibrium Green's function theory

We start with the definition of the one-particle Green's function $G(\mathbf{r},t,\sigma;\mathbf{r}',t',\sigma')$ in the Heisenberg picture $\mathcal{H}$,

$$\begin{aligned} G(\mathbf{r},t,\sigma;\mathbf{r}',t',\sigma') =& \frac{-i}{\hbar}\left\langle T_C\left\{\psi_{\mathcal{H}}(\mathbf{r},t,\sigma)\psi^{\dagger}_{\mathcal{H}}(\mathbf{r}',t',\sigma')\right\}\right\rangle, \\ =& \frac{-i}{\hbar}\left\{\theta(t,t')\left\langle\psi_{\mathcal{H}}(\mathbf{r},t,\sigma)\psi^{\dagger}_{\mathcal{H}}(\mathbf{r}',t',\sigma')\right\rangle\right. \\ & \left. -\theta(t',t)\left\langle\psi^{\dagger}_{\mathcal{H}}(\mathbf{r}',t',\sigma')\psi_{\mathcal{H}}(\mathbf{r},t,\sigma)\right\rangle\right\}. \end{aligned} \tag{5.1}$$

The quantum field operators $\psi^{\dagger}_{\mathcal{H}}(\mathbf{r},t,\sigma)$ and $\psi_{\mathcal{H}}(\mathbf{r},t,\sigma)$ create and annihilate a particle at position $\mathbf{r}$ at time t and with spin σ. T_C is the time ordering operator defined on a general, complex time contour C. The function $\theta(t,t')$ generalizes the Heaviside step function to the contour C, i.e. $\theta(t,t')=1$ if t is later on the contour C than t' and $\theta(t,t')=0$ otherwise. For fermions the quantum field operator obey the usual anti-commutation relations,

$$\begin{aligned} \left[\psi_{\mathcal{H}}(\mathbf{r},t,\sigma),\psi^{\dagger}_{\mathcal{H}}(\mathbf{r}',t,\sigma')\right]_+ &= \delta(\mathbf{r}-\mathbf{r}')\delta_{\sigma,\sigma'}, \\ \left[\psi^{\dagger}_{\mathcal{H}}(\mathbf{r},t,\sigma),\psi^{\dagger}_{\mathcal{H}}(\mathbf{r}',t,\sigma')\right]_+ &= 0, \\ \left[\psi_{\mathcal{H}}(\mathbf{r},t,\sigma),\psi_{\mathcal{H}}(\mathbf{r}',t,\sigma')\right]_+ &= 0. \end{aligned} \tag{5.2}$$

The so defined non-equilibrium Green's function expresses the correlation between two positions $\mathbf{r}$ and $\mathbf{r}'$ and spin states σ and σ' at times t and t'. If t is later on the time contour than t', $G(\mathbf{r},t,\sigma;\mathbf{r}',t'\sigma')$ describes the response of the system to a perturbation that is created at position $\mathbf{r}'$ at time t' and propagates to the position $\mathbf{r}$ at time t, where it is annihilated. A similar interpretation holds for the exchanged time order. The non-equilibrium Green's function is therefore often termed propagator.

The time evolution of the Green's function is determined by its equation of motion for a system with the Hamilton operator H. To derive the equation of motion, it is convenient to split the Hamiltonian into two parts $H=H_0+V$, where H_0 denotes the one particle part, i.e. the kinetic energy and the potential, while V denotes the many particle interactions, in particular the two particle scattering processes. Interaction with other kinds of particles, like phonons, can be treated along the same lines but is left out here for brevity. The representation of the Hamiltonian in the

quantum field operators reads,

$$H = \sum_{\sigma\sigma'} \int \mathrm{d}\mathbf{r} \psi^\dagger(\mathbf{r},\sigma) H_0(\mathbf{r},\sigma,\sigma')\psi(\mathbf{r},\sigma') + \frac{1}{2}\sum_{\sigma\sigma'} \int \mathrm{d}\mathbf{r} \int \mathrm{d}\mathbf{r}' \psi^\dagger(\mathbf{r}',\sigma')\psi^\dagger(\mathbf{r},\sigma) V(\mathbf{r}-\mathbf{r}')\psi(\mathbf{r},\sigma)\psi(\mathbf{r}',\sigma'), \quad (5.3)$$

where we allow spin-orbit interaction in the one particle part H_0 of the Hamiltonian. The equations of motion for $G(\mathbf{r},t,\sigma;\mathbf{r}',t'\sigma')$ are given by the time derivatives with respect to t and t'. To simplify the notation, we use the following abbreviations,

$$\begin{aligned} (\mathbf{r},t,\sigma) &= 1, \\ V(\mathbf{r}-\mathbf{r}')\delta(t-t') &= V(1-1'), \\ \delta(\mathbf{r}-\mathbf{r}')\delta(t,t')\delta_{\sigma\sigma'} &= \delta(1,1'), \\ \int_C \mathrm{d}1 \,\hat{=} \int_C \mathrm{d}t \int \mathrm{d}\mathbf{r}, \end{aligned} \quad (5.4)$$

where the time integral is a contour integral along the complex time contour C. For the derivative with respect to t, we get,

$$\begin{aligned} \frac{\mathrm{d}}{\mathrm{d}t} T_C\left\{\psi_{\mathcal{H}}(1)\psi^\dagger_{\mathcal{H}}(1')\right\} =& T_C\left\{\frac{\mathrm{d}}{\mathrm{d}t}\psi_{\mathcal{H}}(1)\psi^\dagger_{\mathcal{H}}(1')\right\} \\ &+ \delta(t,t')\left[\psi_{\mathcal{H}}(1),\psi^\dagger_{\mathcal{H}}(1')\right]_+, \\ =& T_C\left\{\frac{\mathrm{d}}{\mathrm{d}t}\psi_{\mathcal{H}}(1)\psi^\dagger_{\mathcal{H}}(1')\right\} + \delta(1,1'). \end{aligned} \quad (5.5)$$

The second term $\propto \delta(t,t')$ stems from the time derivative of the Heaviside step functions, included through the time ordering operator T_C. In the second step, we made use of the anti-commutator relations Eq. (5.2). In a next step, we derive the time evolution of the quantum field operator $\psi^\dagger_{\mathcal{H}}(1')$. In the Heisenberg picture, we obtain,

$$\begin{aligned} i\hbar\frac{\mathrm{d}}{\mathrm{d}t}\psi_{\mathcal{H}}(1) =& [\psi_{\mathcal{H}}(1), H(\mathbf{r})]_- \\ =& H_0(\mathbf{r})\psi_{\mathcal{H}}(1) + \int \mathrm{d}1' V(1-1')\psi^\dagger_{\mathcal{H}}(1')\psi_{\mathcal{H}}(1')\psi_{\mathcal{H}}(1). \end{aligned} \quad (5.6)$$

To obtain the equation of motion for the Green's function $G(1,1')$, we have to multiply Eq. (5.6) from the right by $\psi^\dagger_{\mathcal{H}}(1')$, take the quantum statistical expectation value, and add the delta-function term Eq. (5.5). We obtain for the equation of motion with respect to t,

$$\left(i\hbar\frac{\mathrm{d}}{\mathrm{d}t} - H_0(\mathbf{r})\right) G(1,1') = \delta(1,1') - i\hbar\int_C \mathrm{d}2 V(1-2) G^{\mathrm{II}}(12;1'2^+). \quad (5.7)$$

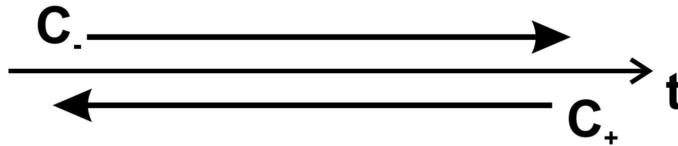

Figure 5.1.: Schematics of the Keldysh contour, $C_- \rightarrow (-\infty, \infty)$ and $C_+ \rightarrow (\infty, -\infty)$. The contour lies entirely on the real time axis. The shift of C_- and C_+ is meant for clarity only.

where we have introduced the two-particle Green's function $G^{\mathrm{II}}(12; 1'2^+)$. The argument $2^+ = \mathbf{r}_2 t_2^+$ has been introduced to ensure the correct time ordering. A time t^+ is meant to be infinitesimally later on the contour C than a time t. Generally, the two-particle Green's function $G^{\mathrm{II}}(12; 1'2')$ is defined as,

$$G^{\mathrm{II}}(12; 1'2') = -\frac{1}{\hbar^2} \left\langle T_C \left\{ \psi_{\mathcal{H}}(1) \psi_{\mathcal{H}}(2) \psi^{\dagger}_{\mathcal{H}}(2') \psi^{\dagger}_{\mathcal{H}}(1') \right\} \right\rangle . \tag{5.8}$$

Similar considerations lead to the equation of motion with respect to t',

$$\left(-i\hbar \frac{\mathrm{d}}{\mathrm{d}t'} - H_0(\mathbf{r}) \right) G(1, 1') = \delta(1, 1') - i\hbar \int_C \mathrm{d}2 V(1' - 2) G^{\mathrm{II}}(12; 1'2^+), \tag{5.9}$$

The derived equations of motion Eq. (5.7) and Eq. (5.9) constitute an infinite hierarchy of equations, since the time evolution of the one-particle Green's function depends on the two-particle one. In turn, the calculation of the two-particle Green's function requires the knowledge of the three-particle one and so on. As a starting point of any approximation, both equations are recast in a form, that eliminates the two-particle function,

$$\begin{aligned} \left(i\hbar \frac{\mathrm{d}}{\mathrm{d}t} - H_0(\mathbf{r}) \right) G(1, 1') &= \delta(1, 1') + \int_C \mathrm{d}2 \Sigma(1, 2) G(2, 1'), \\ \left(i\hbar \frac{\mathrm{d}}{\mathrm{d}t} - H_0(\mathbf{r}) \right) G(1, 1') &= \delta(1, 1') + \int_C \mathrm{d}2 G(1, 2) \Sigma(2, 1'). \end{aligned} \tag{5.10}$$

Here, we have introduced the self-energy $\Sigma(1, 1')$. This self-energy can be derived in any desired approximation by Feynman diagram technique, using Wick's theorem or functional derivatives. Common approximations are e.g. the Hartree-Fock or the second order Born approximation. Any kind of one electron scattering, e.g. with phonons or charged impurities can be treated in a similar framework. We will come back to that later, when we discuss the approximate treatment of scattering in more detail in Sec. 5.4.

We have not specified the time contour C up to now. Since we are interested in non-equilibrium but stationary processes the so-called Keldysh contour is best suited. The Keldysh contour is schematically shown in Fig. 5.1. The contour lies on the real axis and extents from $-\infty$ to ∞ and back. Instead of working with the contour ordered Green's function, it has become standard in the literature to work with

piecewise defined Green's functions, which are more convenient to handle. These new Green's functions agree with the contour ordered one for specific constellations of the time arguments. The four piecewise Green's functions are defined as,

$$G(1,1') = \begin{cases} G^c(1,1') & \text{if } t,t' \text{ on } C_- \\ G^a(1,1') & \text{if } t,t' \text{ on } C_+ \\ G^<(1,1') & \text{if } t \text{ on } C_- \text{ and } t' \text{ on } C_+ \\ G^>(1,1') & \text{if } t \text{ on } C_+ \text{ and } t' \text{ on } C_- \end{cases} \tag{5.11}$$

According to this definition, we get for the chronological Green's function $G^c(1,1')$,

$$G^c(1,1') = -\frac{i}{\hbar}\left\langle T_-\left\{\psi_{\mathcal{H}}(1)\psi^\dagger_{\mathcal{H}}(1')\right\}\right\rangle, \tag{5.12}$$

where the time ordering operator T_- is defined on the part C_- of the contour, see Fig. 5.1, i.e. if $t > t'$ it follows that t is later on the contour than t'. For the anti-chronological Green's function, we get,

$$G^a(1,1') = -\frac{i}{\hbar}\left\langle T_+\left\{\psi_{\mathcal{H}}(1)\psi^\dagger_{\mathcal{H}}(1')\right\}\right\rangle, \tag{5.13}$$

where now the time ordering operator T_+ is defined on the part C_+ of the contour, see Fig. 5.1, i.e. if $t > t'$ it follows that t' is later on the contour than t. The lesser Green's function reads,

$$G^<(1,1') = \frac{i}{\hbar}\left\langle \psi^\dagger_{\mathcal{H}}(1')\psi_{\mathcal{H}}(1)\right\rangle. \tag{5.14}$$

Note that time ordering is already taken care of, since the time arguments lie on different parts of the contour, such that it is clear which one is later on C. In the case of the lesser function, we have that t' always follows later on the time contour than t, which is reversed for the greater Green's function which is given by,

$$G^>(1,1') = -\frac{i}{\hbar}\left\langle \psi_{\mathcal{H}}(1)\psi^\dagger_{\mathcal{H}}(1')\right\rangle. \tag{5.15}$$

These four function are actually not linearly independent, but obey the relation,

$$G^c(1,1') + G^a(1,1') = G^<(1,1') + G^>(1,1'). \tag{5.16}$$

Thus the knowledge of three of the Green's functions is sufficient to completely characterize a non-equilibrium system. In quantum transport problems, $G^<(1,1')$ and $G^>(1,1')$ are directly related to observables. These functions are also referred to as correlation functions. Instead of $G^c(1,1')$ and $G^a(1,1')$, two other Green's functions, called the retarded Green's function $G^R(1,1')$ and advanced Green's function $G^A(1,1')$, are widely used in the literature since their physical interpretation is clearer. They are defined as,

$$\begin{aligned} G^R(1,1') &= G^c(1,1') - G^<(1,1'), \\ G^A(1,1') &= G^c(1,1') - G^>(1,1'). \end{aligned} \tag{5.17}$$

In what follows, we will exclusively use the Green's functions G^R, G^A, $G^<$, and $G^>$. The linear dependence between those functions is expressed as,

$$G^R - G^A = G^> - G^<, \tag{5.18}$$

which is related to the spectral function and thus to the density of states, as will be discussed later in Sec. 5.6. The equations of motion for the piecewise defined Green's functions follow from Eq. (5.10) with the help of Langreth's theorem [95]. With respect to t, they read,

$$\begin{aligned}\left(i\hbar\frac{\mathrm{d}}{\mathrm{d}t} - H_0(\mathbf{r})\right) G^{R,A}(1,1') =& \delta(1,1') + \int_{C_-} \mathrm{d}2\Sigma^{R,A}(1,2)G^{R,A}(2,1'), \\ \left(i\hbar\frac{\mathrm{d}}{\mathrm{d}t} - H_0(\mathbf{r})\right) G^{\lessgtr}(1,1') =& \int_{C_-} \mathrm{d}2\Sigma^{R}(1,2)G^{\lessgtr}(2,1') + \Sigma^{\lessgtr}(1,2)G^{A}(2,1'),\end{aligned} \tag{5.19}$$

and with respect to t',

$$\begin{aligned}\left(-i\hbar\frac{\mathrm{d}}{\mathrm{d}t} - H_0(\mathbf{r})\right) G^{R,A}(1,1') =& \delta(1,1') + \int_{C_-} \mathrm{d}2\Sigma^{R,A}(1,2)G^{R,A}(2,1'), \\ \left(-i\hbar\frac{\mathrm{d}}{\mathrm{d}t} - H_0(\mathbf{r})\right) G^{\lessgtr}(1,1') =& \int_{C_-} \mathrm{d}2\Sigma^{R}(1,2)G^{\lessgtr}(2,1') + \Sigma^{\lessgtr}(1,2)G^{A}(2,1'),\end{aligned} \tag{5.20}$$

In stationary transport problems, all Green's function depend on the difference of the time arguments only. Since the stationary self-energies depend solely on the time deference as well, it is convenient to Fourier transform with respect to $t - t'$ to the energy domain E. The Green's functions $G^i(\mathbf{r}, \mathbf{r}'; E)$, where $i \in \{R, A, <, >\}$, in energy space are defined as,

$$G^i(\mathbf{r}, \mathbf{r}'; E) = \int \mathrm{d}(t - t') e^{iE(t-t')/\hbar} G^i(\mathbf{r}, \mathbf{r}'; t - t'), \tag{5.21}$$

and the inverse transformation reads,

$$G^i(\mathbf{r}, \mathbf{r}'; t - t') = \int \frac{\mathrm{d}E}{2\pi\hbar} e^{-iE(t-t')/\hbar} G^i(\mathbf{r}, \mathbf{r}'E). \tag{5.22}$$

As it turns out, only two Green's functions are independent in this case, since we get $G^R = (G^A)^\dagger$. Thus, in stationary systems, the knowledge of two Green's function is sufficient to characterize the system completely. As we will discuss further in Sec. 5.6, the retarded Green's function can be associated with the eigenstates of the system and their broadening, while the lesser Green's function includes the information on how these states are occupied and thus determines the charge and current density. The two relevant equations, that have to be solved are the Dyson equation for G^R,

$$(E - H_0(\mathbf{r}))\, G^R(\mathbf{r}, \mathbf{r}'; E) = \delta(\mathbf{r} - \mathbf{r}') + \int \mathrm{d}\mathbf{r}_1 \Sigma^R(\mathbf{r}, \mathbf{r}_1; E) G^R(\mathbf{r}_1, \mathbf{r}'; E), \tag{5.23}$$

and the Keldysh equation for $G^<$,

$$G^<(\mathbf{r}, \mathbf{r}'; E) = \int \mathrm{d}\mathbf{r}_1 \int \mathrm{d}\mathbf{r}_2 G^R(\mathbf{r}, \mathbf{r}_1; E) \Sigma^<(\mathbf{r}_1, \mathbf{r}_2; E) G^A(\mathbf{r}_2, \mathbf{r}'; E). \tag{5.24}$$

Note that the two equation are coupled and have to be solved simultaneously. The self-energies $\Sigma^{R,<}$ depend on the scattering mechanisms at hand. For inelastic scattering processes, e.g. with polar optical phonons, $\Sigma^<$ and Σ^R get coupled, which markedly complicates the situation. We will therefore discuss in Sec. 5.4 how the treatment of scattering can be simplified, without sacrificing to much accuracy.

5.3. Boundary conditions for open quantum devices

In this work, we are mainly interested in the transport properties of arbitrarily shaped two dimensional conductors. To this end, we need to solve Eq. (5.23) and Eq. (5.24) for arbitrary $H(\mathbf{r})$. To do so, we will follow the common approach and solve the continuous real space equations on a discrete lattice. In particular, we will apply a finite differences scheme to Hamiltonian operators of the form as discussed in Sec. 3.2 and Sec. 4.3. For the concrete finite differences Hamiltonian matrices, we refer to Appendix B. In this section, we will only assume that the Hamiltonian is given in a discrete real space basis ($H(\mathbf{r}) \rightarrow H(\mathbf{m})$, where $\mathbf{m}$ denotes a lattice site vector). That means that e.g. the retarded Green's function $G^R(\mathbf{r}, \mathbf{r}'; E)$ becomes a matrix with spatial indices $G^R_{i,j}(E)$. We will adopt the full matrix notation, that can be applied for any discrete basis, e.g. also the atomistic tight-binding bases. In this notation, the Dyson equation Eq. (5.23) reads,

$$G^R(E) = (E - H - \Sigma^R(E))^{-1}, \tag{5.25}$$

and the Keldysh equation Eq. (5.24) beomes a simple matrix product,

$$G^<(E) = G^R(E) \Sigma^<(E) G^{R\dagger}(E). \tag{5.26}$$

In quantum transport calculations, we model so-called open devices. That means, we assume the device to be connected to several semi-infinite leads that provide large reservoirs in thermal equilibrium, that inject and/or extract carriers form the device. That means that the matrices that describe the whole system (device + leads) which appear in Eq. (5.25) and Eq. (5.26), have infinite dimension. A simple truncation of the matrix with Dirichlet or Neumann boundary conditions would correspond to a closed device with reflecting boundaries. We will use a truncation scheme instead, that ensures absorbing boundary conditions and thus model an open quantum device. We will focus on the two-dimensional situation, however, the generalization to three dimensions is straight forward, whereas the one-dimensional case is trivial [87]. We will assume, that the scattering self-energies are local, i.e. they

only depend on one spatial coordinate and are hence diagonal matrices in the discrete real space basis. This assumption is fulfilled for the treatment of scattering that we adopt in this work, see Sec. 5.4.

We can decompose the retarded Green's functions into a device part G_D^R, a lead part G_C^R, and two parts that connect the leads and the device G_{DC}^R and G_{CD}^R, respectively. For a moment, we will omit the superscript R for convenience, since we deal solely with retarded quantities here. Concretely, we have,

$$\begin{bmatrix} G_C & G_{CD} \\ G_{DC} & G_D \end{bmatrix} = \begin{bmatrix} E - H_C - \Sigma_C & \tau_C \\ \tau_C^\dagger & E - H_D - \Sigma_D \end{bmatrix}^{-1}, \tag{5.27}$$

where H_D and H_C represent the Hamiltonin matrix of the isolated device and leads respectively, that are both assumed to have Dirichlet boundary conditions at the lead–device interfaces. τ_C represents the coupling between the leads and the device. The coupling matrix τ_C in turn is nonzero only at the device–lead interfaces. Σ_C and Σ_D denote the scattering self-energies of the leads and device, respectively. Note that a nonlocal scattering self-energy would imply that $\Sigma_{CD} \neq 0$, which complicates the situation markedly. Eq. (5.27) yields the expressions for the blocks of the Green's function,

$$\begin{aligned} [E - \Sigma_C - H_C]\, G_{CD} + \tau_C G_D &= 0, \\ [E - \Sigma_D - H_D]\, G_D + \tau_C^\dagger G_{CD} &= I. \end{aligned} \tag{5.28}$$

From the first equation, we obtain,

$$G_{CD} = -g_C \tau_C G_D \tag{5.29}$$

where we have defined the retarded Green's function of the isolated semi-infinite lead,

$$g_C = [E - \Sigma_C - H_C]^{-1}. \tag{5.30}$$

Finally, we obtain for the retarded Green's function of the device,

$$G_D = \left[E - H_C - \tau_C^\dagger g_C \tau_C\right]^{-1}. \tag{5.31}$$

Note that the matrices in Eq. (5.31) have a finite dimension, that equals the number of points in the device region times the number of bands considered in the Hamiltonian. The coupling of the device to the leads is taken into account exactly by the term $\tau_C^\dagger g_C \tau_C$. Although, g_C is still an infinite dimensional matrix, we only need its part for each lead at the corresponding device–lead interface. As it turns out, with some additional assumptions, we can calculate this part of the lead Green's function analytically [97–99] or with very efficient numerical methods [100, 101]. As usually done, we will refer to the coupling term between the leads and the device in the Dyson equation for the device as coupling self-energy to the leads or contact self-energy Σ_C^R. We define,

$$\Sigma_C^R = \sum_{l \in C} \Sigma_l^R, \quad \text{with} \quad \Sigma_l^R = \tau_l^\dagger g_l \tau_l, \tag{5.32}$$

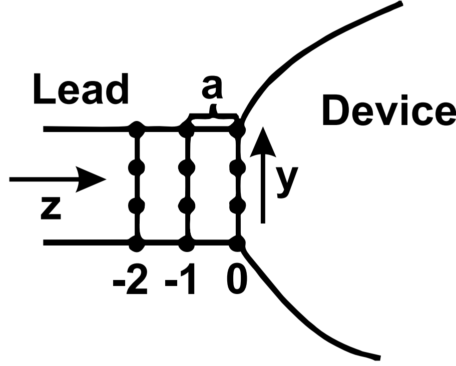

Figure 5.2.: Schematic drawing of the lead model. The dots indicate the two or three dimensional slabs in the semi-infinite lead, with the lattice spacing a.

where C denotes the set of all leads or contacts and we have assumed all leads to be independent, such that their effect is directly additive. In this work, we adopt the common approach to treat each of the lead as semi-infinite quantum wire with finite circumference, such that we can regard the lead as coupled slaps or slices with finite dimension as depicted schematically in Fig. 5.2. We assume the leads to be completely homogeneous in one direction, that means no quantity depends on the longitudinal coordinate along the wire. The present method to calculate the coupling self-energy takes into account general multi-band Hamiltonians in one, two, and three dimensions [97]. To calculate the contact self-energy, we need to solve the Dyson equation for the semi-infinite wire. To obtain the required part of the wire Green's functions at the lead–device interface, we have to solve the following two equations that follow from the Dyson equation for the isolated wire [102] simultaneously,

$$\begin{aligned} D_{00}g_{00} + T_{0-1}g_{-10} &= I, \\ D_{-1-1}g_{-10} + T_{-1-2}g_{-20} + T_{-10}g_{00} &= 0. \end{aligned} \tag{5.33}$$

where we have omitted the energy argument as well as the superscript R to straiten the notation and we have introduced the abbreviation $E - h_{ii} - \Sigma_{ii} = D_{ii}$ and $h_{ij} = -T_{ij}$, where h and g are the Hamiltonian and retarded Green's function of the isolated, semi-infinite wire, respectively. The subscripts denote the slab under consideration, i.e. h_{ii} is the Hamiltonian within the ith slab and h_{ij}, with $i \neq j$, is the coupling between the ith and j^{th} slab. We assume the slabs to be defined in such a way, that only nearest neighbor slabs couple. Further, $i = 0$ denotes the last slab of the wire, i.e. $i < 0$ is a slab in the lead, whereas $i > 0$ is in the device, which is not considered in the case of the isolated wire, since the isolated wire does not couple to the device. Since the leads are assumed to be homogeneous, we have e.g. $T_{-1-2} = T_{0-1}$ and $D_{00} = D_{-1-1}$.

Since Eq. (5.33) can actually be solved by considering the Schrödinger equation for the infinite wire, we consider an infinite quantum wire for a moment. The

corresponding Schrödinger equation reads,

$$D_{ii}\xi_l + T_{ii+1}\xi_{i+1} + T_{ii-1}\xi_{i-1} = 0, \tag{5.34}$$

where ξ_i denotes the solution of the Schrödinger equation within the slab i and $i = 0, \pm 1, \pm 2, ...$ Since the wire is homogeneous, the Bloch condition $\xi_i = e^{ik_\mu a}\xi_{i+1}$ holds, where a is the distance between adjacent slabs. With the help of the Bloch condition, we can rewrite Eq. (5.34) as a non-Hermitian linear eigenvalue problem for the complex wire band structure $k_\mu(E)$ and the transverse eigenfunctions of the wire ξ_i^μ,

$$\begin{pmatrix} D_{ii} & T_{ii+1} \\ 1 & 0 \end{pmatrix} \cdot \begin{pmatrix} \xi_i \\ \xi_{i+1} \end{pmatrix}_\mu = e^{ik_\mu a} \begin{pmatrix} -T_{ii-1} & 0 \\ 0 & 1 \end{pmatrix} \cdot \begin{pmatrix} \xi_i \\ \xi_{i+1} \end{pmatrix}_\mu \tag{5.35}$$

The solution of Eq. (5.35) yields the wire modes $k_\mu(E)$. Half of them decay for $i \to \infty$ and the other half decays for $i \to -\infty$. Note that in the ballistic case, we also get modes that propagate in the direction of increasing or decreasing i, respectively. We are going to express the retarded Green's function of the semi-infinite wire by those states that decay or propagate into the wire, i.e. in the direction of $i \to -\infty$. The decaying modes are easy to determine, however, to decide for the correct propagating modes, we have to calculate the group velocity $v_G^\mu(E)$, which is given by,

$$v_G^\mu(E) = -\frac{2a}{\hbar\,|\xi_i^\mu|^2}\mathrm{Im}\left[(\xi_i^\mu)^\dagger T_{ii-1}\xi_i^\mu e^{-ik_\mu a}\right], \tag{5.36}$$

and is independent of the slab index i. We select the states μ with $v_G^\mu < 0$. To straighten the notation, we define the matrix Ξ which has the selected eigenfunctions ξ_i^μ as column vectors and the diagonal matrix Λ with the corresponding eigenvalues $e^{ik_\mu a}$ on the diagonal.

We now return to the retarded Green's function of the semi-infinite wire. Both equations in Eq. (5.33) have to be fulfilled. We first make an ansatz that solves the second equation of Eq. (5.33),

$$g_{ij} = \Xi\,\Lambda^i\,\tilde{g}\,\Lambda^j\,\Xi^{-1}. \tag{5.37}$$

We insert this ansatz into the first equation in Eq. (5.33) to calculate $\tilde{g}$. We find,

$$\tilde{g} = \left(\Xi^{-1}\,D_{00}\,\Xi + \Xi^{-1}\,T_{0-1}\,\Xi\,\Lambda^{-1}\right)^{-1}. \tag{5.38}$$

Finally, we arrive at the self-energy that couples the lead with the device [97],

$$\Sigma_C = \tau_C g_{00}\tau_C^\dagger = \tau_C\,\Xi\,\tilde{g}\,\Xi^{-1}\,\tau_C^\dagger, \tag{5.39}$$

where τ_C denotes the coupling between the lead and the device. Using the Schrödinger equation of the infinite wire Eq. (5.34) once again and assuming that the coupling between the lead and the device is the same as the coupling within the lead $\tau_C = -T_{-10}$, we arrive at the compact expression for the contact self-energy [94],

$$\Sigma_C = \tau_C\,\Xi\,\Lambda\,\Xi^{-1}. \tag{5.40}$$

In the single-band case the equation for the contact self-energy Eq. (5.40) reduces to [103],

$$\Sigma_C(i,j) = -t \sum_{\mu} \langle i \mid \psi^{\mu} \rangle \, e^{ik_{\mu}a} \, \langle \psi^{\mu} \mid j \rangle \,, \tag{5.41}$$

where i, j are spatial indices in the lead–device interlace, t is the coupling between adjacent sites that is assumed to be constant here, a is the distance between sites, and ψ^{μ} is the solution of the single band Schrödinger equation in a slab of the wire,

$$h_{ii} \, | \psi^{\mu} \rangle = \varepsilon^{\mu} \, | \psi^{\mu} \rangle \,, \tag{5.42}$$

and the wire dispersion follows from the relation [87],

$$E = \varepsilon^{\mu} + 2t[1 - \cos(k^{\mu}a)]. \tag{5.43}$$

Thus, in the single-band case, the wire dispersion has to be calculated only once, while in the general multi-band case or with spin-orbit coupling the wire dispersion has to be calculated numerically for each energy E separately.

We note, that in some multi-band calculations the method described above turns out to be numerically instable. Since the original eigenvalue problem Eq. (5.35) is non-Hermitian, a standard eigenvalue solver does not yield orthogonal eigenstates ξ^{μ}. Therefore, the matrix Ξ is not unitary and we need to invert it numerically or apply an orthogonalization scheme which, however, turns out to fail numerically in certain situations that are not predictable a priori. A possibility to calculate the retarded Green's function in such a case, is to use an iterative scheme to solve the Dyson equation,

$$g_{00}^{i} = \left(E - h_{00} - \tau_C {g_{00}^{i-1}}^{-1} \tau_C^{\dagger} \right) , \tag{5.44}$$

where the superscript i denotes the iteration index. Using an initial guess, e.g. ${g_{00}^{i=0}}^{-1} = i\eta$, with $\eta > 0$, the solution of Eq. (5.44) describes the surface Green's function g_{00} of a wire with $i + 1$ slabs. Thus, after enough iterative steps one arrives at a good approximation for the semi-infinite wire eventually. Such an iterative scheme has successfully been applied to quasi one-dimensional transport [104], in two-dimensional or three-dimensional nanostructures on the other hand, a direct iteration of Eq. (5.44) might lead to some tens of thousands steps until convergence is reached. Especially in the vicinity of resonances and for nearly ballistic problems the situation is worst. In Refs. [100, 101] an iterative scheme has been proposed, that takes 2^i slices after i iterative steps into account. This scheme works relatively robust also for nanostructures and requires the worst some fifty iterations until convergence is reached.If the direct calculation of the lead self energy fails due to the above mentioned purely numerical reasons, we rely on the iterative scheme proposed in Ref. [100, 101] to calculate the contact self-energy.

Once the retarded coupling self-energy is known, we still have to obtain the lesser coupling Green's function, needed to calculate the lesser Green's function of the device via the Keldysh equation (Eq. (5.24)). Since we assume the lead to be in

equilibrium with a reservoir described by a Fermi distribution $f(E-\mu_C)$ with the chemical potential μ_C of contact C, we can use the fluctuation dissipation theorem,

$$\Sigma_C^< = if(E-\mu_C)\left(\Sigma_C^R - \Sigma_C^{R\dagger}\right), \tag{5.45}$$

which holds in equilibrium only.

Note that using Eq. (5.40) or the iterative scheme described above includes the same interband and spin-orbit interactions in the leads as in the device. This is important to inhibit artificial reflections at the device–lead interface. The spin-orbit coupling in the leads has usually been neglected in the literature on the intrinsic spin-Hall effect, e.g. [105–108]. An abrupt change of the band structure or spin-orbit coupling parameters, however, causes uncontrollable oscillation within the device and overestimates the spin-polarization effects. We will therefore use the same band-structure and spin-orbit coupling parameters in the leads as in the device, to model a smooth, refection-free lead–device interface.

5.4. Novel treatment of scattering: The multi-scattering Büttiker probe model

A full implementation of the non-equilibrium Green's functions method requires, additionally to the solution of Eq. (5.23) and Eq. (5.24), the calculation of the self-energies Σ^R and $\Sigma^<$. Thus, for stationary transport problems in open quantum systems the self-consistent solution of four coupled integro-differential equations is required. In operator form, they read [87],

$$\begin{aligned}
G^R =& (E - H_D - \Sigma^R)^{-1}, \\
G^< =& G^R \Sigma^< G^{R\dagger}, \\
\Sigma^R =& \Sigma_c^R + G^R D^R + G^R D^< + G^< D^R, \\
\Sigma^< =& \Sigma_c^< + G^< D^<,
\end{aligned} \tag{5.46}$$

where H_D is the device Hamilton operator and $\Sigma^{R,<}$ are the retarded and the lesser total scattering self-energy, respectively. These self-energies are built up from the sum of all environmental Green's functions $D^{R,<}$ that account for the specific scattering mechanism. The self-energies $\Sigma_c^{R,<}$ represent the coupling self-energy between the leads and the device. As shown in Sec. 5.2 all Green's functions and self-energies are direct functions of two spatial coordinates $\mathbf{r}$ and $\mathbf{r}'$ and the energy E. Especially, we want to stress the coupling between the retarded self-energy Σ^R and the lesser Green's function $G^<$. This coupling induces an indirect dependence of the retarded Green's function on the lesser Green's function $G^R = G^R[G^<]$. That means, that the broadening of the states depends on their occupation. Note, that for inelastic scattering, e.g. with polar optical phonons, it is this coupling that accounts for Pauli's principle and cannot be neglected [92]. On the other hand, it makes the solution of Eq. (5.46) markedly difficult and unstable.

An obvious and wide spread simplification is to neglect scattering at all and treat the transport strictly ballistic. In this case the scattering self-energies are assumed to vanish and only the coupling self-energies appear in Eq. (5.46). Therefore, no self-consistent calculation is necessary. Actually, the knowledge of G^R is sufficient to completely characterize the system. In fact, not even the whole retarded Green's function $G^R(\mathbf{r}, \mathbf{r}'; E)$ is needed, but only of a small part, where $\mathbf{r}$ and/or $\mathbf{r}'$ are in the contact–device interface [93, 94]. From this part, all observables can be calculated. For example the energy resolved charge current that passes through contact s is given by the Landauer formula [109],

$$j_s(E) = \frac{e}{h} \sum_{s' \in C} T^{s',s}(E)(f(E - \mu_s) - f(E - \mu_{s'})), \tag{5.47}$$

where C is the set of all contacts, $T^{s',s}(E)$ is the ballistic transmission and $f(E-\mu_s)$ is the Fermi distribution function in contact s with the fixed chemical potential μ_s. The transmission function can be derived from the contact block of the retarded Green's function [94] and is related to the S matrix via the Fisher-Lee relation [87], that describes the carrier transport through the device by a unitary scattering problem. However, purely ballistic transport is plagued with artifacts that are caused by the strict energy conservation and the infinitely long-range correlations, that hamper realistic predictions especially in complicated device geometries on the nanometer scale [104].

A simple and very efficient model to include inelastic and phase breaking scattering is the so-called Büttiker probe method [96, 110]. It uses phenomenological parameters to model the scattering self-energies via a fixed scattering potential and thus bypasses any self-consistent solution of the Green's functions and their corresponding self-energies. In fact, within this model, scattering processes can be viewed as additional floating contacts [111] (so-called probes) within the device that remove, thermalize, and/or re-inject carriers. The equations for the retarded scattering self-energy Σ^R within the Büttiker probe model read,

$$\begin{aligned} \Sigma^R(\mathbf{r}, \mathbf{r}'; E) &= \Sigma_c^R(\mathbf{r}, \mathbf{r}'; E) + B^R(\mathbf{r}; E)\delta(\mathbf{r} - \mathbf{r}'), \\ \Sigma_c^R(\mathbf{r}, \mathbf{r}'; E) &= \sum_{l \in C} \Sigma_l^R(\mathbf{r}, \mathbf{r}'; E), \\ B^R(\mathbf{r}; E) &= \sum_{p \in P} B_p^R(E)\delta(\mathbf{r} - \mathbf{r}_p), \end{aligned} \tag{5.48}$$

where C is the set of all contacts, P is the set of all probes, B_p^R is the phenomenological scattering potential, and $\mathbf{r}_p$ is the position of probe p. In general the probes are distributed homogeneously within the device region. The simplest model for the scattering potential is $B_p^R = i\eta$ with the constant $\eta > 0$, independent of energy and position. A more realistic model for the scattering potential that can be related to the mean free path of the carriers depends on the momentum of the carriers [112, 113], as described in Appendix D. The contact self-energies are the same as

in the full NEGF formalism and nonzero only at the contact–device interface. The lesser self-energy of the device $\Sigma^<$ is calculated within a quasi-equilibrium approximation,

$$\Sigma^<(\mathbf{r},\mathbf{r}';E) = \sum_{l\in C} f(E-\mu_l)\Gamma_l(\mathbf{r},\mathbf{r}';E) + \sum_{p\in P} f(E-\mu_p)\Gamma_p(\mathbf{r},\mathbf{r}';E), \tag{5.49}$$

where $\Gamma_l = \Sigma_l^R - \Sigma_l^{R\dagger}$ and $\Gamma_p = B_p^R - B_p^{R\dagger}$ are the so-called broadening functions. $f(E-\mu_{l,p})$ denotes the Fermi distribution with the local chemical potentials $\mu_{l,p}$ which are associated with each contact or probe, respectively. The chemical potentials for the contacts μ_l are fixed by the applied bias, the chemical potentials in the probes μ_p on the other hand are calculated in such a manner to obey current conservation. Given the lesser self-energy $\Sigma^<$, the energy resolved current at each probe or contact s within the non-equilibrium Green's function formalism reads [114, 115],

$$j_s(E) = \frac{q}{2\pi\hbar} \sum_{s'\in\{C,P\}} (T^{s,s'} f(E-\mu_s) - T^{s',s} f(E-\mu_{s'}), \tag{5.50}$$

where $T^{s,s'} = \mathrm{Tr}[\Gamma_s G^R \Gamma_{s'} G^{R\dagger}]$ is the transmission function between probe or contact s and probe or contact s', Tr is the trace operator, q is the carrier's charge. Since the probes are floating they do not carrier any net current and the condition,

$$\int \mathrm{d}E j_p(E) = 0 \quad \forall p \in P, \tag{5.51}$$

must hold. Eq. (5.51) constitutes a system of nonlinear equations for the chemical potentials μ_p in each probe, which has to be solved, e.g. iteratively by a Newton-Raphson method.

Our novel MSB method combines the treatment of individual scattering mechanisms from the NEGF scheme with the basic idea of the BP model to handle scattering via floating contacts. Within the MSB model, the scattering potential B becomes a functional of the local density of states $\rho(\mathbf{r},E)$. The general form of B now reads,

$$B_p^R(E) = -i \int_{-\infty}^{+\infty} \mathrm{d}E'\; M_p(E,E')\; \rho(\mathbf{r}_p,E'), \tag{5.52}$$

where M is the sum over all scattering kernels for the individual scattering mechanisms. In general, the derivation of the scattering kernels for the MSB model follows the derivation of the scattering self-energies within the full NEGF scheme [88]. Thus, we get for the scattering kernel for acoustic phonons (AP) within the MSB model,

$$M_p^{\mathrm{AP}}(E,E') = \frac{V_D(\mathbf{r}_p)^2 k_B T\; \theta(E_{\mathrm{AP}}(\mathbf{r}_p) - |E-E'|)}{\rho_M(\mathbf{r}_p) v_s^2(\mathbf{r}_p)\; 2E_{\mathrm{AP}}}, \tag{5.53}$$

where θ is Heaviside's unit step function, V_D is the scalar deformation potential, ρ_M is the density of the material, v_s is the velocity of sound in the material, and E_{AP} is

the maximum energy of acoustic phonons. The scattering kernel for dispersionless polar optical (PO) phonons reads

$$M_p^{\mathrm{PO}}(E,E') = \frac{q^2 k_B T \xi^2(\mathbf{r}_p)}{2\epsilon_0}\left(\frac{1}{\epsilon_\infty(\mathbf{r}_p)} - \frac{1}{\epsilon_s(\mathbf{r}_p)}\right) \times \delta(E_{\mathrm{PO}}(\mathbf{r}_p) - |E - E'|),$$

where q is the charge of the carriers, ξ is the screening length, ϵ_0 is the electric vacuum permittivity, ϵ_∞ is the electric permittivity at the high frequency limit, ϵ_s is the static low frequency permittivity, and E_{PO} is the energy of the polar optical phonons.

Within the MSB model, the scattering potential depends on the local density of states $\rho(\mathbf{r}, E)$ via Eq. (5.52). The local density of states can be calculated within the NEGF framework from the retarded Green's function G^R as follows [87],

$$\rho(\mathbf{r}, E) = -\frac{i}{2\pi}(G^R(\mathbf{r}, \mathbf{r}, E) - G^{R\dagger}(\mathbf{r}, \mathbf{r}, E)). \tag{5.54}$$

Therefore, Eq. (5.52) constitutes a self-consistent relation between Σ^R and G^R that, in principle, has to be solved in an iterative scheme. However, the density of states $\rho(\mathbf{r}, E)$ and thus the self-energy Σ^R depend on the diagonal part of G^R only. Therefore, only the diagonal part of G^R is required during the iteration, which can be calculated very efficiently, e.g. with the fast-inverse-using-nested-dissection (FIND) algorithm [116, 117].

A further simplification that side-steps the complex and error prone solution of the nonlinear system of equations for the μ_p can be achieved within the MSB model for devices with only two current-carrying contacts (source and drain). Such devices are e.g. quantum cascade lasers or MOSFETs, if the small gate-leakage currents are neglected. In such two-contact devices, we assume that the distribution functions of each probe p is a linear combination of the source and drain Fermi distributions, $f(E - \mu_S)$ and $f(E - \mu_D)$, respectively,

$$f(E - \mu_p) = c_p f(E - \mu_S) + (1 - c_p) f(E - \mu_D) \qquad \forall\, p \in P, \tag{5.55}$$

Now, Eq. (5.50) leads to a linear system of equations for the constants c_p.

One of the difficulties of the NEGF formalism is that current conservation and Pauli's principle are not automatically guaranteed. Particularly, the calculation of the self-energies in any non-self-consistent approximation violates current conservation [87]. To remedy such a result, the iteration over the four coupled Green's functions and self-energies has to be carried out to infinite order [92]. In contrast, the main advantage of the BP model is that it sidesteps any self-consistent calculations for the Green's functions and self-energies. Moreover, it inherently guarantees current conservation and Pauli's principle is always obeyed since a quasi-equilibrium expression for $\Sigma^<$ is assumed and thus, the fluctuation dissipation theorem [87, 118] holds. However, the BP model introduces a phenomenological scattering potential that does not distinguish between individual scattering mechanisms, and the

strength of the scattering potential is to be tuned manually, e.g. by fitting to experimental data.

Within the MSB model, we reduced the mathematical complexity to only two coupled equations, Σ^R and G^R, but the treatment for individual scattering mechanisms is retained. The iterative solution of only two coupled equations is far more robust and faster than iteration over four coupled equations within the full NEGF formalism. Moreover, current conservation and Pauli's principle are inherently guaranteed during every step of the iterative solution of the MSB model, since we explicitly calculate the chemical potentials μ_p of the probes. Therefore even in a non-self-consistent Born approximation, current conservation is not violated. Note, that the initial value of the local density of states $\rho(\mathbf{r}, E)$ and thus the initial value of Σ^R can be calculated within another formalism, e.g. by a Schrödinger solver.

We have applied the MSB model to state-of-the-art quantum cascade laser (QCL) structures. A QCL device is a laterally homogeneous, layered heterostructure. In these structures the interplay between quantum coherence and dissipation on the one hand and between the various scattering mechanisms on the other hand is particularly important [82]. In the studied cases, we found excellent agreement with results from a full scale NEGF implementation as well as with experimental results. Further details will be discussed in Ref. [119].

5.5. Implementation of external magnetic fields

It is well known, that external magnetic fields couple to the spin degree of freedom via the Zeeman term and independently to the momentum of a charged particle. In a spin-orbit coupled system, the magnetic field additionally couples to the spin degree of freedom indirectly due to the coupling of spin and momentum. Indeed, we have seen in Sec. 3.2 that the spin-orbit coupling for nondegenerate bands can be expressed as a k-dependent effective Zeeman-like term. Interesting effects occur in the case, when this internal spin-orbit field and the external magnetic field are of the same magnitude. The interaction of the two fields leads to spin-dependent cyclotron radii [120], effects the Shubnikov-de Hass oscillation [56], and causes the anomalous Hall effect [121] to name a few of these effects. Magnetic fields are thus widely used in experiment to probe the spin dynamics of the carriers.

From the theoretical point of view, the implementation of magnetic fields for arbitrarily shaped nanostructures, in a manifestly gauge invariant and nonperturbative manner is surprisingly nontrivial. The normally applied minimal coupling, that leads to the covariant momentum $\mathbf{p} \to \mathbf{p} + e\mathbf{A}$ takes the magnetic field $\mathbf{B}$ into account via the vector potential $\mathbf{A}$, where $\mathbf{B} = \nabla \times \mathbf{A}$. In quantum mechanics the covariant momentum leads to the gauge covariant derivative, when the correspondence principle $p_i \to \hbar/i\, \partial_i$ is applied,

$$D_i = \partial_i + i\frac{e}{\hbar}A_i(\mathbf{r}), \tag{5.56}$$

where the subscript $i \in \{x, y, z\}$. In the envelop function approximation for arbitrary

shaped nanostructures, the wave vector $\mathbf{k}$ is usually interpreted as the momentum operator and thus as spatial derivative. Commonly, the derivative operators are discretized on a finite lattice. A straight forward discretization of the gauge covariant derivatives, however, leads to results for the spectrum that depend on the particular choice of gauge for the vector potential. In a recent publication, Andlauer et al. [122] have presented a manifestly gauge invariant discretization scheme for the Schrödinger equation in general multi-band envelop function theories that is non-perturbative in the magnetic field. This scheme is based on the concept of gauge covariant derivatives that has been developed in the context of latice gauge theories originally. The magnetic field is included via Peierls-like phase factors that multiply the zero field Hamilton matrix.

In a finite differences scheme all functions $F(\mathbf{r})$ are defined on a discrete lattice only, $F(\mathbf{r}) \to F(\mathbf{m})$, where $\mathbf{m}$ denotes a point on the lattice. Thus, derivative operators are approximated as difference operators, according to,

$$\partial_i F(\mathbf{r}) \to \delta_i = \frac{1}{\epsilon}\left[F(\mathbf{m}+\boldsymbol{\epsilon}_i) - F(\mathbf{m})\right], \tag{5.57}$$

For the second derivative operator the finite differences scheme yields,

$$\partial_i \partial_i F(\mathbf{r}) \to \delta_{ii} = \frac{1}{\epsilon^2}\left[F(\mathbf{m}+\boldsymbol{\epsilon}_i) - 2F(\mathbf{m}) + F(\mathbf{m}-\boldsymbol{\epsilon}_i)\right], \tag{5.58}$$

where ϵ is the grid spacing and $\boldsymbol{\epsilon}_i$ the vector, connecting adjacent grid points in direction $i \in \{x, y, z\}$. We now follow the notation of Andlauer et al. [122] to explain the gauge covariant discretization scheme that we apply also in this work to study the interplay between the externally applied magnetic field and the spin-orbit coupling induced magnetic field. The derivative operators are written in the compact form,

$$\begin{aligned} \delta_i F(\mathbf{m}) &= \frac{1}{\epsilon}\sum_{s_i} C_i(s_i) F(\mathbf{m} + si\boldsymbol{\epsilon}_{\mathbf{i}}) \\ \delta_{ii} F(\mathbf{m}) &= \frac{1}{\epsilon^2}\sum_{s_i} C_{ii}(s_i) F(\mathbf{m} + si\boldsymbol{\epsilon}_{\mathbf{i}}) \end{aligned} \tag{5.59}$$

where $s_i \in \{0, \pm 1\}$, such that the sums run over the lattice point $\mathbf{m}$ and its nearest neighbors. The coefficients C_i and C_{ii} are defined according to the discretization scheme, where for finite difference, we have,

$$C_i(1) = 1, \quad C_i(0) = -1, \quad C_i(-1) = 0, \tag{5.60}$$

$$C_{ii}(0) = -2, \quad C_{ii}(\pm 1) = 1. \tag{5.61}$$

We can now define the covariant derivatives Δ_i as discretized version of $D_i = \partial_i + ie/\hbar A_i(\mathbf{m})$,

$$\begin{aligned} \Delta_i F(\mathbf{m}) &= \frac{1}{\epsilon}\sum_{s_i} C_i(s_i) U(\mathbf{m}, \mathbf{m} + s_i\boldsymbol{\epsilon}_i) F(\mathbf{m} + s_i\boldsymbol{\epsilon}_i), \\ \Delta_{ii} F(\mathbf{m}) &= \frac{1}{\epsilon^2}\sum_{s_i} C_{ii}(s_i) U(\mathbf{m}, \mathbf{m} + s_i\boldsymbol{\epsilon}_i) F(\mathbf{m} + s_i\boldsymbol{\epsilon}_i), \end{aligned} \tag{5.62}$$

where the discrete connection U is defined by,

$$U(\mathbf{m},\mathbf{n}) = \exp\left(i\frac{e}{\hbar}\int_{S(\mathbf{m},\mathbf{n})}\mathbf{A}(\mathbf{r})\mathrm{d}\mathbf{r}\right). \tag{5.63}$$

The trajectory $S(\mathbf{m},\mathbf{n})$ connects the grid points $\mathbf{m}$ and $\mathbf{n}$. We note that some care concerning the ordering of the operators has to be taken, if there are mixed derivatives e.g. $\partial_i\partial_j$. In Ref. [122], it was shown how to handle these mixed second derivatives.

In this work, we consider only two-dimensional electron and hole gases. We always assume that the confinement induced quantization in the z- (growth) direction is stronger than the Landau quantization induced by the magnetic field components perpendicular to the growth direction. Since these inplane components of the magnetic field are described by the z-component of the vector potential, we neglect the coupling of the vector potential to the momentum in the growth direction and take into account only the coupling to the spin degree of freedom via the Zeeman term [123]. For magnetic fields applied along the growth direction on the other hand the vector potential has components in the plane of the quantum well and we have to take into account the coupling to the in-plane momentum making use of the discretization scheme, described above. Originally, this scheme has been proposed for and applied to multi-band Schrödinger equations in the envelope function approximation.

To transfer the scheme to the Green's function method in open quantum devices, we have the additional problem of how to handle the semi-infinite leads with applied magnetic field. One possible and simple approach is to assume the leads to be field free e.g. by decreasing the magnetic field in the device towards the contacts adiabatically [124–126]. In the experimental relevant situation, magnetic fields are mainly created by large coils. Since we consider structures on the nanometer scale, it seems quite unrealistic, that the magnetic field is present only in the device and zero in the leads. It would be much more sensible to assume a homogeneous magnetic field to be present also in the leads.

To include a finite magnetic field in the semi-infinite leads poses the problem of how to define the scattering states in the isolated semi-infinite leads [127–130]. In Sec. 5.3, we have assumed, that the eigenstates are plane-waves in the longitudinal direction of the lead. In finite magnetic fields, this only holds if the gauge is also purely longitudinal, i.e. that the vector potential does not depend on the longitudinal coordinate of the lead under consideration.

We are dealing with devices that have contacts in x- as well as y-direction, i.e. there is no simple standard gauge like the Landau or Coulomb gauge that is longitudinal for both kinds of leads. While for example the Landau gauge $A_x(x,y) = -By$ yields a longitudinal gauge for leads in x-direction. For leads in y-direction, on the other hand, this gauge field is purely transverse. The commonly used symmetric or Coulomb gauge on the other hand yields a mixed form for leads in both directions. A possible solution would be to use different gauges for the various leads [131].

However, the resulting total vector potential for the device and the leads in this case is noncontinuous, which causes spurious magnetic fields, that influence the properties of the system considerably. We now develop a gauge that is longitudinal for any lead but is continuous everywhere. To do so, we start with Landau gauge,

$$\mathbf{A}(\mathbf{r}) = \begin{pmatrix} -B \cdot y \\ 0 \\ 0 \end{pmatrix}. \tag{5.64}$$

We can apply a gauge to the vector field $\mathbf{A} \rightarrow \mathbf{A} + \nabla f(x, y)$ with the function of the kind $f(x, y) = B \cdot \eta(x) \cdot x \cdot y$. Adjusting the auxiliary function $\eta(x)$, we wish to achieve a longitudinal gauge for the contacts in y-direction while the gauge for leads in the x-direction remains unchanged. We define the function $\eta(x)$ piecewise in six sections as,

$$\eta(x) = \begin{cases} 0 & \text{for } x < x_0 \\ \frac{1}{2}\left(1 - \cos\left(\frac{\pi}{x_1 - x_0}(x - x_0)\right)\right) & \text{for } x_0 \leq x \leq x_1 \\ 1 & \text{for } x_1 \leq x \leq x_2 \\ \frac{1}{2}\left(1 + \cos\left(\frac{\pi}{x_3 - x_2}(x - x_2)\right)\right) & \text{for } x_2 \leq x \leq x_3 \\ 0 & \text{for } x > x_3 \end{cases} \tag{5.65}$$

with $x_0 < x_1 < x_2 < x_3$ where x_0 is chosen to be to the right of the left most contact in x-direction, x_1 to the left of the leftmost contact in y-direction, x_2 to the right of the rightmost contact in y-direction, and x_3 to the left of the rightmost contact in x-direction. For the gradient of $f(x, y)$ that adds to the vector potential, we get,

$$\nabla_x f(x, y) = B\eta(x)x \tag{5.66}$$

$$\nabla_y f(x, y) = Bxy\partial_x \eta(x) + B\eta(x)y \tag{5.67}$$

with the piecewise defined partial derivative of the auxiliary function $\eta(x)$,

$$\partial_x \eta(x) = \begin{cases} 0 & \text{for } x < x_0 \\ \frac{\pi}{2(x_1 - x_0)} \sin\left(\frac{\pi}{x_1 - x_0}(x - x_0)\right) & \text{for } x_0 \leq x \leq x_1 \\ 0 & \text{for } x_1 \leq x \leq x_2 \\ -\frac{\pi}{2(x_3 - x_2)} \sin\left(\frac{\pi}{x_3 - x_2}(x - x_2)\right) & \text{for } x_2 \leq x \leq x_3 \\ 0 & \text{for } x > x_3 \end{cases} \tag{5.68}$$

Thus, we get for the x-component of the vector potential,

$$A_x(x, y) = -By + Bxy\partial\eta(x) + B\eta(x)y, \tag{5.69}$$

and for the y-component,

$$A_y(x, y) = Bx\eta(x). \tag{5.70}$$

For the phase factors, that appear in the gauge invariant discretization of the Hamiltonian matrix, we need to evaluate the path integral of the vector potential along the connection of two adjacent grid points. We get for connection in x-direction,

$$\begin{aligned}\int_{x_i}^{x_i+\epsilon} A_x \mathrm{d}x &= -By\epsilon + By\int_{x_i}^{x_i+\epsilon} \mathrm{d}x\,\{\eta(x) + x\partial_x\eta(x)\} \\ &= -By\epsilon + Byx\eta(x)|_{x_i}^{x_i+\epsilon} + By\int_{x_i}^{x_i+\epsilon} \mathrm{d}x(\eta(x) - \eta(x)) \\ &= -By\epsilon + By\left((x_i+\epsilon)\eta(x_i+\epsilon) - x_i\eta(x_i)\right), \end{aligned} \tag{5.71}$$

and for the connection in y-direction,

$$\int_{y_i}^{y_i+\epsilon} A_y \mathrm{d}y = Bx\eta(x)\epsilon. \tag{5.72}$$

These phases have to be applied, to achieve a longitudinal gauge in all attached leads and thus the same homogeneous magnetic field as in the device. Note that usually, the path integral is approximated by a rectangular formula with the vector potential being evaluated at half the way between the grid points. This, however is only valid, if the vector potential depends linearly on the coordinates. If the vector potential is nonlinear as in our case, we need to evaluate the integrals exactly, see Eq. (5.71) and Eq. (5.72), in order to achieve a gauge invariant formulation of the problem.

5.6. Spin-resolved observables

In this section, we want to show how the physical observables can be derived within the non-equilibrium Green's function formalism. While most observables like charge and electrical current density which depend on the occupation of electronic states are derived from the lesser Green's function, the local density of states $\rho(\mathbf{r}, E)$ follows from the spin-summed diagonal elements of the retarded Green's function $G^R(\mathbf{r}, \mathbf{r}'; E)$

$$\rho(\mathbf{r}, E) = -\frac{1}{\pi}\sum_\sigma \mathrm{Im}[G^R(\mathbf{r}, \sigma, \mathbf{r}, \sigma; E)], \tag{5.73}$$

where $\sigma \in \{\uparrow, \downarrow\}$ denotes the spin index. With the spectral function, which is defined by,

$$\begin{aligned}A(\mathbf{r}, \mathbf{r}', E) =& i\sum_\sigma (G^R(\mathbf{r}, \sigma, \mathbf{r}', \sigma; E) - G^A(\mathbf{r}, \sigma, \mathbf{r}', \sigma; E)) \\ =& i\sum_\sigma (G^R(\mathbf{r}, \sigma, \mathbf{r}', \sigma; E) - G^{R\dagger}(\mathbf{r}, \sigma, \mathbf{r}', \sigma; E)),\end{aligned} \tag{5.74}$$

the local density of states can be calculated from,

$$\rho(\mathbf{r}, E) = \frac{1}{2\pi} A(\mathbf{r}, \mathbf{r}, E). \tag{5.75}$$

It is useful to note, that the spectral function can also be calculated from,

$$A = G^R \Gamma G^A, \tag{5.76}$$

which is given in full matrix notation. Γ denotes the broadening function, due to scattering and the coupling to the leads. Although the relation Eq. (5.76) appears more complicated than Eq. (5.74), it has some useful advantages. Since the broadening function is defined by,

$$\Gamma = \sum_C (\Sigma_C^R - \Sigma_C^{R\dagger}) + (\Sigma_S^R - \Sigma_S^{R\dagger}), \tag{5.77}$$

where the superscripts C and S denote the contacts and the scattering respectively, in the evaluation of Eq. (5.76) one only needs to know those columns of G^R that correspond to grid points with a nonzero broadening function Γ. If e.g. ballistic transport is considered, $\Sigma_S^R = 0$, the broadening function is only nonzero at the lead–device interfaces, and thus only at very few points compared to total number of device points.

From Eq. (5.76), we define the lead connected spectral function A_C and thus the lead connected density of states by,

$$A_C = G^R \Gamma_C G^A, \tag{5.78}$$

where Γ_C denotes the brocading function due to the single contact C. The lead connected density of states is then given by the diagonal elements of A_C,

$$\rho_C(\mathbf{r}, E) = \frac{1}{2\pi} A_C(\mathbf{r}, \mathbf{r}, E). \tag{5.79}$$

This quantity denotes the probability for a carrier to propagate coherently from contact C to the point $\mathbf{r}$ within the device. Coherently in this context means without a scattering event. The lead connected density of states is proportional to the transmission between the considered contact and e.g. a tip of a scanning tunnel microscope placed at point $\mathbf{r}$. It is thus a measurable quantity [132].

We will now turn to the occupation dependent quantities in non-equilibrium situations. We start with the charge density. Note that, in thermal equilibrium, the charge density can be calculated from the local density of states and the Fermi distribution function. In non-equilibrium, the energy resolved local charge density is given by [87],

$$n(\mathbf{r}, E) = \frac{-i}{2\pi} \sum_\sigma G^<(\mathbf{r}, \sigma, \mathbf{r}\sigma; E). \tag{5.80}$$

For the total local density, we integrate over the energy

$$n(\mathbf{r}) = \int \mathrm{d}E n(\mathbf{r}, E). \tag{5.81}$$

The averaged total density within the device can be calculated by averaging over the device volume $n = 1/V \int \mathrm{d}\mathbf{r} n(\mathbf{r})$. In the case of quantum spin transport, we

are also interested in spin-resolved densities, so-called polarizations. We define the spin-resolved local density $n(\mathbf{r}, \sigma, \sigma')$ by,

$$n(\mathbf{r}, \sigma, \sigma') = \frac{-i}{2\pi} \int_E \mathrm{d}E G^<(\mathbf{r}, \sigma, \mathbf{r}, \sigma'; E). \tag{5.82}$$

Note that the charge density follows from the trace of spin-resolved density over the spin variables,

$$n(\mathbf{r}) = \sum_\sigma n(\mathbf{r}, \sigma, \sigma) \tag{5.83}$$

As the local spin polarization, we define the difference of the spin-up ($\sigma =\uparrow$) and the spin-down ($\sigma =\downarrow$) density,

$$S_z(\mathbf{r}) = n(\mathbf{r}, \uparrow, \uparrow) - n(\mathbf{r}, \downarrow, \downarrow). \tag{5.84}$$

Since we use the representation of the Pauli matrices with a diagonal σ_z throughout this work, S_z in Eq. (5.84) indeed denotes the spin polarization in z-direction. Since the spin-orbit field lies in the plane of the quantum well, perpendicular to the z-direction, the analogous quantities $S_x(\mathbf{r})$ and $S_y(\mathbf{r})$ are also of interest. They can be obtained by an appropriate rotation in spin space. A rotation around the axis $\mathbf{e}$ by the angle α in spin space is given by the $SU(2)$ matrix,

$$R_{\mathbf{e}}^{SU(2)}(\alpha) = e^{-i\alpha\mathbf{e}\cdot\boldsymbol{\sigma}/\hbar} = \cos\frac{\alpha}{2}\sigma_0 - i\mathbf{e}\cdot\boldsymbol{\sigma}\sin\frac{\alpha}{2}, \tag{5.85}$$

where $\boldsymbol{\sigma} = (\sigma_z, \sigma_y, \sigma_z)$ is the vector of the Pauli matrices and σ_0 is the 2×2 unity matrix. For the polarization in x-direction S_x, we apply a rotation by $\alpha = -\pi/2$ around $\mathbf{e}_y$ and find,

$$S_x(\mathbf{r}) = n(\mathbf{r}, \uparrow, \downarrow) + n(\mathbf{r}, \downarrow, \uparrow). \tag{5.86}$$

For the polarization in y-direction S_y, we apply a rotation by $\alpha = \pi/2$ around $\mathbf{e}_x$,

$$S_y(\mathbf{r}) = i(n(\mathbf{r}, \uparrow, \downarrow) - n(\mathbf{r}, \downarrow, \uparrow)). \tag{5.87}$$

Note that we can also define the spin-resolved lead connected density of states $\rho_C(\mathbf{r}, E, \sigma)$ in an analogous way. This quantity equals the probability, that a carrier that propagates coherently from contact C to the point $\mathbf{r}$ has the spin σ at $\mathbf{r}$ no matter what the spin state is at the contact C.

While the charge and spin densities can be calculated from the spatially diagonal elements of $G^<(\mathbf{r}, \sigma, \mathbf{r}', \sigma'; E)$, off-diagonal correlations are needed for the current. Since in spin-orbit coupled system, the conventional definition of the charge current is not applicable in general [133], we follow a general approach from the continuity equation to derive the current operator. We focus directly on the discrete case of a finite differences Hamiltonian. We follow the book of Mahan [134] and define the charge polarization vector,

$$\mathbf{P} = \sum_{\sigma,\mathbf{m}} = \mathbf{m} c^\dagger_{\mathbf{m},\sigma} c_{\mathbf{m},\sigma}, \tag{5.88}$$

where $\mathbf{m}$ denotes a point on the discrete lattice, $c^\dagger_{\mathbf{m},\sigma}$ denotes the creation operator, that creates a particle at point $\mathbf{m}$ with spin σ, and $c_{\mathbf{m},\sigma}$ annihilates the same particle. The current operator can be calculated from the commutator,

$$\sum_{\mathbf{m}} \mathbf{j}(\mathbf{m}) = \frac{i}{\hbar} \sum_{\mathbf{m},i} [H(\mathbf{m}, \boldsymbol{\epsilon}_i), \mathbf{P}]_- \,, \tag{5.89}$$

where the Hamiltonian matrix in the finite difference representation has the general form,

$$\begin{aligned} H &= \sum_{\mathbf{m},i} H(\mathbf{m}, \boldsymbol{\epsilon}_i), \\ &= \sum_{\substack{\mathbf{m},i \\ \sigma,\sigma',}} \left(t^{\sigma,\sigma'}_{\mathbf{m},\mathbf{m}+\boldsymbol{\epsilon}_i} c^\dagger_{\mathbf{m},\sigma} c_{\mathbf{m}+\boldsymbol{\epsilon}_i,\sigma'} + t^{\sigma',\sigma}_{\mathbf{m}+\boldsymbol{\epsilon}_i,\mathbf{m}} c^\dagger_{\mathbf{m}+\boldsymbol{\epsilon}_i,\sigma'} c_{\mathbf{m},\sigma} \right), \end{aligned} \tag{5.90}$$

and includes couplings between sites $\mathbf{m}$ and $\mathbf{m} + \boldsymbol{\epsilon}_i$, which can be on-site elements ($\epsilon_i = 0$), nearest, or more distant neighbors coupling and $t_{\mathbf{m}+\boldsymbol{\epsilon}_i,\mathbf{m}} = (t_{\mathbf{m},\mathbf{m}+\boldsymbol{\epsilon}_i})^\dagger$. Since Eq. (5.89) is a direct result of the continuity equation, it has to hold for arbitrary volumes. Therefore, we can drop the sum over the site $\mathbf{m}$ and get a definition for the local current operator,

$$\mathbf{j}(\mathbf{m}) = \frac{i}{\hbar} \sum_{i} [H(\mathbf{m}, \boldsymbol{\epsilon}_i), \mathbf{P}]_- \,, \tag{5.91}$$

To calculate the current, we have to evaluate the commutators,

$$\left[c^\dagger_{\mathbf{m},\sigma_1} c_{\mathbf{m}+\boldsymbol{\epsilon}_i,\sigma_2}, c^\dagger_{\mathbf{n},\sigma} c_{\mathbf{n},\sigma}\right]_- = c^\dagger_{\mathbf{m},\sigma_1} c_{\mathbf{n},\sigma} \delta_{\sigma_2,\sigma} \delta_{\mathbf{n},\mathbf{m}+\boldsymbol{\epsilon}_i} - c^\dagger_{\mathbf{n},\sigma} c_{\mathbf{m}+\boldsymbol{\epsilon}_i,\sigma_2} \delta_{\sigma_1,\sigma} \delta_{\mathbf{n},\mathbf{m}}, \tag{5.92}$$

$$\left[c^\dagger_{\mathbf{m}+\boldsymbol{\epsilon}_i,\sigma_1} c_{\mathbf{m},\sigma_2}, c^\dagger_{\mathbf{n},\sigma} c_{\mathbf{n},\sigma}\right]_- = c^\dagger_{\mathbf{m}+\boldsymbol{\epsilon}_i,\sigma_1} c_{\mathbf{n},\sigma} \delta_{\sigma_2,\sigma} \delta_{\mathbf{n},\mathbf{m}} - c^\dagger_{\mathbf{n},\sigma} c_{\mathbf{m},\sigma_2} \delta_{\sigma_1,\sigma} \delta_{\mathbf{n},\mathbf{m}+\boldsymbol{\epsilon}_i}. \tag{5.93}$$

Putting everything together, we arrive at the general expression for the charge current operator,

$$\mathbf{j}(\mathbf{m}) = \frac{i}{\hbar} \sum_{i,\sigma_1,\sigma_2} \epsilon_i \left(t^{\sigma_1,\sigma_2}_{\mathbf{m},\mathbf{m}+\boldsymbol{\epsilon}_i} c^\dagger_{\mathbf{m},\sigma_1} c_{\mathbf{m}+\boldsymbol{\epsilon}_i,\sigma_2} - t^{\sigma_1,\sigma_2}_{\mathbf{m}+\boldsymbol{\epsilon}_i,\mathbf{m}} c^\dagger_{\mathbf{m}+\boldsymbol{\epsilon}_i,\sigma_1} c_{\mathbf{m},\sigma_2} \right). \tag{5.94}$$

Finally, we take the quantum statistical average, and note that [87],

$$\left\langle c^\dagger_{\mathbf{m},\sigma} c_{\mathbf{n},\sigma'} \right\rangle = \frac{\hbar}{i} \int_E G^<(\mathbf{n}, \sigma', \mathbf{m}, \sigma; E), \tag{5.95}$$

which results in the final expression for the local charge current at site $\mathbf{m}$,

$$\begin{aligned} \mathbf{j}(\mathbf{m}) = \sum_{i,\sigma_1,\sigma_2} \epsilon_i \int_E \mathrm{d}E \, \big(& t^{\sigma_1,\sigma_2}_{\mathbf{m},\mathbf{m}+\boldsymbol{\epsilon}_i} G^<(\mathbf{m} + \boldsymbol{\epsilon}_i, \sigma_2, \mathbf{m}, \sigma_1; E) - \\ & t^{\sigma_1,\sigma_2}_{\mathbf{m}+\boldsymbol{\epsilon}_i,\mathbf{m}} G^<(\mathbf{m}, \sigma_2, \mathbf{m} + \boldsymbol{\epsilon}_i, \sigma_1; E) \big), \end{aligned} \tag{5.96}$$

which agrees with the operator proposed in Ref. [105]. The finite differences Hamiltonian matrices for the k-linear and the k-cubic operator are presented in Appendix B.

For the local current in the k-linear model Eq. (3.1), we get (note that in order to shorten the notation we write $G^<_{\mathbf{m},\mathbf{n}}(\sigma\sigma')$ for $\int_E \mathrm{d}E G^<(\mathbf{m},\sigma,\mathbf{n},\sigma';E)$),

$$\begin{aligned} j_x(\mathbf{m}) = \epsilon_x \left\{ t_x \left(G^<_{\mathbf{m},\mathbf{m}+\boldsymbol{\epsilon}_x}(\uparrow\uparrow) + G^<_{\mathbf{m},\mathbf{m}+\boldsymbol{\epsilon}_x}(\downarrow\downarrow) - G^<_{\mathbf{m}+\boldsymbol{\epsilon}_x,\mathbf{m}}(\uparrow\uparrow) - G^<_{\mathbf{m}+\boldsymbol{\epsilon}_x,\mathbf{m}}(\downarrow\downarrow) \right) \right\} + \\ \frac{1}{2\epsilon_x}(i\alpha_{\mathrm{BIA}} - \alpha_{\mathrm{SIA}}) \left(G^<_{\mathbf{m},\mathbf{m}+\boldsymbol{\epsilon}_x}(\uparrow\downarrow) + G^<_{\mathbf{m}+\boldsymbol{\epsilon}_x,\mathbf{m}}(\uparrow\downarrow) \right) + \\ \frac{1}{2\epsilon_x}(i\alpha_{\mathrm{BIA}} + \alpha_{\mathrm{SIA}}) \left(G^<_{\mathbf{m},\mathbf{m}+\boldsymbol{\epsilon}_x}(\downarrow\uparrow) + G^<_{\mathbf{m}+\boldsymbol{\epsilon}_x,\mathbf{m}}(\downarrow\uparrow) \right), \end{aligned} \tag{5.97}$$

$$\begin{aligned} j_y(\mathbf{m}) = \epsilon_y \left\{ t_y \left(G^<_{\mathbf{m},\mathbf{m}+\boldsymbol{\epsilon}_y}(\uparrow\uparrow) + G^<_{\mathbf{m},\mathbf{m}+\boldsymbol{\epsilon}_y}(\downarrow\downarrow) - G^<_{\mathbf{m}+\boldsymbol{\epsilon}_y,\mathbf{m}}(\uparrow\uparrow) - G^<_{\mathbf{m}+\boldsymbol{\epsilon}_y,\mathbf{m}}(\downarrow\downarrow) \right) \right\} + \\ \frac{1}{2\epsilon_y}(\alpha_{\mathrm{BIA}} - i\alpha_{\mathrm{SIA}}) \left(G^<_{\mathbf{m},\mathbf{m}+\boldsymbol{\epsilon}_y}(\uparrow\downarrow) + G^<_{\mathbf{m}+\boldsymbol{\epsilon}_y,\mathbf{m}}(\uparrow\downarrow) \right) - \\ \frac{1}{2\epsilon_y}(\alpha_{\mathrm{BIA}} + i\alpha_{\mathrm{SIA}}) \left(G^<_{\mathbf{m},\mathbf{m}+\boldsymbol{\epsilon}_y}(\downarrow\uparrow) + G^<_{\mathbf{m}+\boldsymbol{\epsilon}_y,\mathbf{m}}(\downarrow\uparrow) \right), \end{aligned} \tag{5.98}$$

where ϵ_x and ϵ_y are the lattice spacing in x- and y-direction and $\boldsymbol{\epsilon}_x$ and $\boldsymbol{\epsilon}_y$ are the vectors connecting nearest neighbors in x- and y-direction, respectively, and $t_{x,y} = \hbar^2/(2m^*\epsilon^2_{x,y})$

For the k-cubic Dresselhaus model, the expression for the local current gets rather complicated due to the various couplings to 2nd and 3rd nearest neighbors. We therefore refer to the appendix C for the expression.

Note that the so-called terminal current, i.e. the current that flows through the attached leads, can be calculated independently of the model Hamiltonian by Eq. (5.50). However, the spatial resolution is lost, which includes additional information like the current profile within the device [135].

We want to note, that a lot of work has been devoted to the calculation of spin currents in systems with spin-orbit coupling. Especially pure spin currents, which means spin transport without an accompanying charge current have been investigated due to the possible applications in next generations transistors. Unfortunately a fundamental problem arises already from the definition of the spin current. In spin-orbit coupled systems the conventional definition of the spin current does not lead to a conserved current, due the so-called spin-transfer torque that is caused by the k-dependent spin-orbit magnetic field. In Ref. [136], it was shown, that the non-conservation of the translational motion of the spin can rephrased as an angular spin current, that describes rotational motion (precession). Later, in Ref. [137] the definition of a conserved spin current was proposed. The definition was used to calculate the spin-Hall conductivity in infinite two-dimensional electron and hole gases [138]. However, in nanostructures, the definition of the conserved spin current leads to an unphysical dependence on the origin of the coordinate system [139]. Moreover,

the spin current is not directly measurable in experiment. Thus, in order to avoid any ambiguity in the definition of the spin current, we refrain from any attempt to calculate spin currents directly. Instead, we either calculate its effect on the carriers via the spin-current induced electric field [136, 140] or we rely on the spin polarizations, which are well defined and directly measurable in experiment in principle. We find that the spin polarization in static transport gives direct information on how the spin evolves in the system and is thus sufficient to interpret the results.

5.7. Summary

In this chapter, we have given a short introduction to non-equilibrium Green's functions theory, as it is the method we use, to calculate spin-dependent quantum transport in open semiconductor nanostructures. In particular, we have presented a method to calculate the coupling self-energy between the device and the leads in open quantum geometries, that takes into account all band-interactions in multi-band theories and includes scattering within the leads, which is both very important to inhibit artificial reflections at the lead–device interface that might cloak the properties of the actual device. For realistic predictions, it is also very important to take inelastic and phase-breaking scattering into account. That lead us to develop the novel multi scattering Büttiker probe model, which renders it possible to include realistic scattering mechanisms in three-dimensional nanostructures with reasonable computational effort. We have also presented, how external magnetic fields can be incorporated into the non-equilibrium Green's function method for open devices in a manifestly gauge invariant way via Peierl's-like phase factors. We thereby allow for the same finite magnetic field within the leads as within the device. Finally, we have shown how the physical observables in spin-dependent transport calculation can be obtained from the Green's functions. In particular, we have given expressions for the spin-polarization and the local electrical current density for the studied models of spin-orbit coupling.

6. Results for the spin-dependent electron focusing in external magnetic fields

6.1. Introduction

As a first application of the quantum transport method, we present results for the spin-dependent electron focusing in external magnetic fields in near ballistic two-dimensional electron gases (2DEGs). Transverse electron focusing between two quantum point contacts (QPCs) in 2DEGs was reported for the first time in 1989 [141] and repeatedly in various semiconductor heterostructures and geometries since then. The experiments require nearly ballistic charge transport, i.e. the distance between the QPCs has to be smaller than the mean free path of the carriers. Since the typical distance between the QPCs is of the order of $1\,\mu$m, high quality 2DEGs are required. Electron focusing has also been used successfully to elucidate fundamental properties e.g. the shape of the Fermi surface [142]. Since in systems with spin-orbit interaction the shape of the Fermi surface of the conduction band is determined by the relative strength of the Rashba and Dresselhaus spin-orbit coupling constants, see Sec. 3.2, transverse electron focusing opens a way to measure the strength of both coupling constants independently [143]. The combination of external magnetic field and strong spin-orbit interaction might also be used to generate and analyze spin-polarized carriers in high mobility 2DEGs [120, 132, 144–147]. This chapter is organized as follows. In Sec. 6.2, we review the general properties of spin-orbit coupled systems in magnetic fields, with special emphasis on the transverse focusing. In Sec. 6.3, we predict spin-dependent transverse focusing of electrons in various semiconductor quantum well structures in external magnetic and electric fields.

6.2. Theory of magnetic focusing and spin-orbit interaction

We show the schematics of transverse electron focusing in Fig. 6.1 without (top) and with (bottom) spin-orbit coupling in an external magnetic field perpendicular to the quantum well. In the case without spin-orbit coupling, the carriers which are injected through the left QPC (injector) follow a single cyclotron orbit. Whenever the distance between two QPCs is a multiple integer of the cyclotron diameter, the

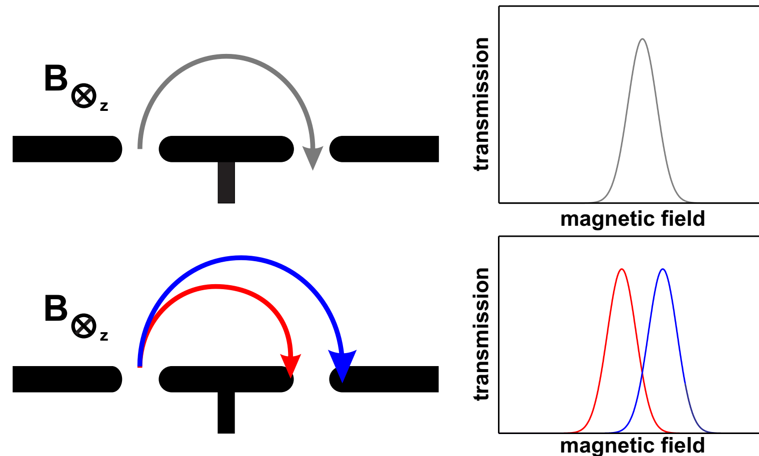

Figure 6.1.: Schematics of the electron focusing in semiconductor quantum wells with an external transverse magnetic field. (top) Without spin-orbit interaction, the injected carriers follow one cyclotron orbit which shows up as a single peak in the transmission between the QPCs if their distance equals an integer multiple of the cyclotron diameter. (bottom) With spin-orbit interaction, the injected carriers follow one of two possible cyclotron orbits depending on their spin orientation which shows up as a double peak in the transmission between the QPCs.

carriers are focused onto the right QPC (collector) and hence, we get a peak in the transmission between the two contacts. In the case with a finite k-linear spin splitting of the conduction band the injected carriers follow two different cyclotron orbits, depending on their spin orientation [148]. The case without spin-orbit coupling is trivial and can be found in many textbooks on quantum mechanics. For the case with spin-orbit coupling however, an analytical quantum mechanical solution is only known for a single type of spin-orbit coupling, where mainly the effect of the Rashba type spin-orbit interaction has been studied [149–151]. For an interplay of Rashba and Dresselhaus spin-orbit couping, no analytical solution is known in finite magnetic field. We want to present the solution for the Dresselhaus spin-orbit coupling since the Dresselhaus spin-orbit interaction is more fundamental and nonzero ($\alpha_{\mathrm{BIA}} \neq 0$) already for D_{2d} symmetric structures whereas the Rashba spin-orbit coupling vanishes for D_{2d} ($\alpha_{\mathrm{SIA}} = 0$). In this case the solution of the two-dimensional Schrödinger equation in magnetic field yields the secular equation for the eigenenergy E in the basis of the Landau wave function without spin-orbit interaction [152],

$$\det \begin{bmatrix} (n-1/2)\hbar\omega_c + E_+ & \alpha_{\mathrm{BIA}}/l_c\sqrt{2n} \\ \alpha_{\mathrm{BIA}}/l_c\sqrt{2n} & (n-1/2)\hbar\omega_c + E_- \end{bmatrix} = 0, \tag{6.1}$$

where $\omega_c = eB/m^*$ is the cyclotron frequency, $l_c = \sqrt{\hbar/m^*\omega_c}$ is the magnetic length, and $E_\pm = -E \pm g\mu_B B$, where $g\mu_B B$ is the usual Zeeman term. Note that due to the spin-orbit interaction the Landau levels n and $n+1$ get coupled with one another.

The solutions of Eq. (6.1) correspond to spin-dependent Landau levels. We get one spin-degenerate level for $n = 0$ with,

$$E^{\pm}_{n=0} = E_0 = \frac{1}{2}\hbar\omega_c - g\mu_B B, \tag{6.2}$$

and spin-split branches, corresponding to $n > 0$,

$$E^{\pm}_n = n\hbar\omega_c \pm \sqrt{E_0^2 + \frac{2n\alpha_{\mathrm{BIA}}^2}{l_c^2}}. \tag{6.3}$$

The ground state (Eq. (6.2)) is spin aligned with the magnetic field which we assume in z-direction perpendicular to the quantum well. For the excited states the spin is tilted into the plane due to the spin-orbit interaction. In the weak field limit that corresponds to $E_0^2 \ll 2(\alpha/l_c)^2$, we get $\langle\sigma_z\rangle \approx 0$ and the spin lies completely in the plane [150]. This limit corresponds to a dominance of the spin-orbit field over the external magnetic field. This is the limit for the spin-dependent focusing experiments that we will focus on.

Due to Eq. (6.3), the two spin branches correspond to different Landau levels n for a given Fermi energy and consequently possess different Cyclotron radii, which in the considered large n limit reads,

$$r_c^2 = 2l_c^2 n, \tag{6.4}$$

which leads to a difference in the cyclotron radius that is approximately given by,

$$\Delta r_c = 2\frac{\alpha_{\mathrm{BIA}}}{\hbar\omega_c}. \tag{6.5}$$

In the described experimental setup for electron focusing, however, this difference cannot be measured directly. Instead, one measures the difference in the magnetic field, that is required to focus the two branches onto the collector. This difference for the first focusing peak is given by

$$\Delta B_z = \frac{4m^*}{\hbar e L}\alpha_{\mathrm{BIA}}, \tag{6.6}$$

where L is the distance between the injector and the collector QPC. In the case when the structure possesses only C_{2v} symmetry and the Rashba spin-orbit coupling constant α_{SIA} is also nonzero, the splitting of the focusing peak depends on the crystallographic orientation due to the anisotropic Fermi surface. In this case, semiclassical arguments lead to [143],

$$\Delta B_z(\phi) = \frac{4m^*}{\hbar e L}\alpha_{\mathrm{BIA}}\sqrt{1 + \left(\frac{\alpha_{\mathrm{SIA}}}{\alpha_{\mathrm{BIA}}}\right)^2 - 2\frac{\alpha_{\mathrm{SIA}}}{\alpha_{\mathrm{BIA}}}\sin(2\phi)}, \tag{6.7}$$

where ϕ is the angle of the crystallographic orientation of the structure relative to the [100]-direction.

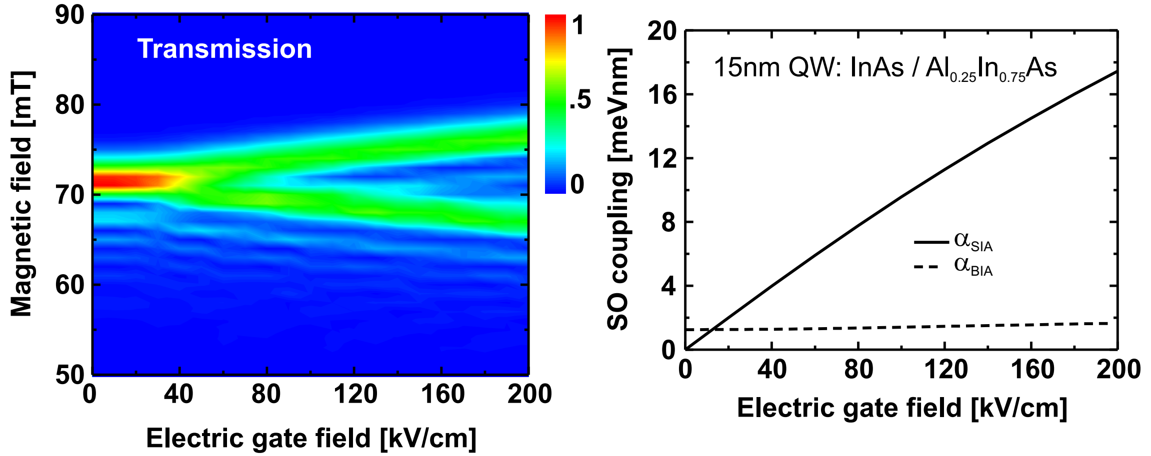

Figure 6.2.: (left) Contour plot of the peak normalized transmission probability between injector and collector quantum point contact for a 15 nm wide $InAs/In_{.75}Al_{.25}As$ quantum well as a function of the external electric and magnetic field. (right) k-linear spin-orbit coupling parameters in the same quantum well as a function of electric field. The solid line shows the Dresselhaus parameter α_{BIA} and the dashed one shows the Rashba parameter α_{SIA}.

6.3. New results for magnetic focusing in semiconductor heterostructures with external electric and magnetic field

In this section, we present results for the calculated spin-dependent electron focusing in InAs and InSb quantum wells subject to both an external magnetic and electric field. In Sec. 3.3, we have seen that the spin-orbit coupling constants in these materials are particularly large and can be steered excellently by a top gate voltage. We have calculated the transmission for a 2DEG in a 15 nm wide $InAs/In_{.75}Al_{.25}As$ with a sheet density of $n_{2D} = 1.7 \cdot 10^{11}\,\mathrm{cm}^{-2}$ from a 70 nm wide injector QPC to a detector QPC of equal width, that were placed 1.8 μm separated from each other as a function of the magnetic and electric field. In Fig. 6.2 (left), we plot the results for the peak normalized transmission as a density plot. On the vertical axis, the magnetic field is depicted, while the electric field is depicted on the horizontal axis. In the right panel of that figure, we plot the calculated spin-orbit coupling constants α_{BIA} and α_{SIA} as a function of the electric field, see Sec. 3.3. We find a well resolved splitting only for fairly large electric fields ($\mathbf{F} \geq 70\,\mathrm{kV/cm}$), which is due to the finite width of the focusing peaks that hampers a resolution for smaller electric fields and thus smaller spin-orbit coupling strength. Note, that we have used rounded barriers for the QPCs with a radius of 15 nm to improve the resolution, since it is known that such QPC have a collimation effect on the injected electron beam [153–155].

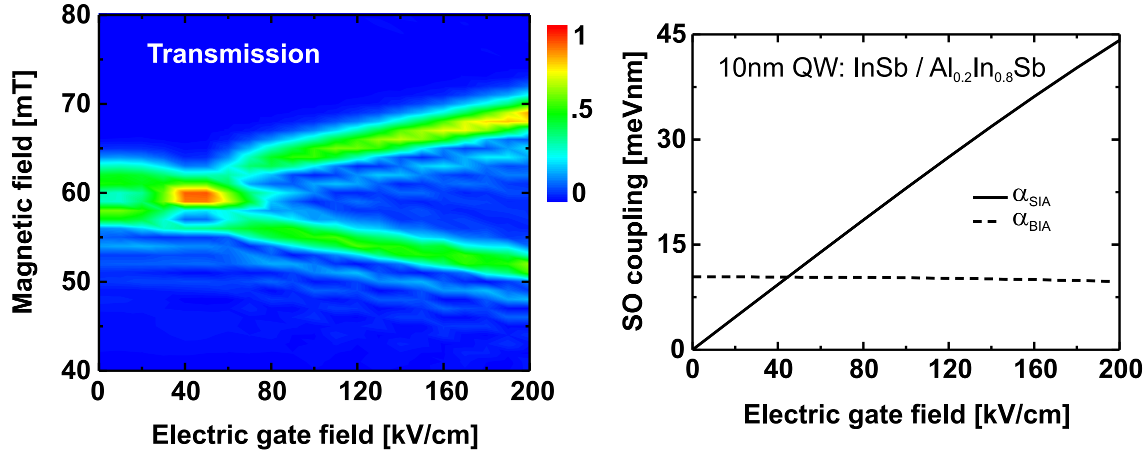

Figure 6.3.: (left) Contour plot of the peak normalized transmission probability between injector and collector quantum point contact for a 10 nm wide InSb/In$_{.8}$Al$_{.2}$Sb quantum well as a function of the external electric and magnetic field. (right) k-linear spin-orbit coupling parameters in the same quantum well as function of electric field. The solid line shows the Dresselhaus parameter α_{BIA} and the dashed one the Rashba parameter α_{SIA}.

Nonetheless, we find a minimal spin-orbit coupling strength of $\alpha_{\mathrm{SIA}} \approx 7\,\mathrm{meVnm}$. Therefore, it is not possible to observe a spin-splitting effect in n-GaAs quantum wells, due to the small spin-orbit coupling, see Sec. 3.3.

For InSb quantum wells on the other hand, we find both spin-orbit coupling constants to be above this limit. We therefore turn to InSb quantum wells. We have repeated the previous calculation for a 2DEG in a 10 nm wide InSb/In$_{.8}$Al$_{.2}$Sb quantum well with a sheet density of $n_{2D} = 1.1 \cdot 10^{11}\,\mathrm{cm}^{-2}$ and the same QPC geometry as before. The results are shown in Fig. 6.3. On the left, we plot again the peak normalized transmission between the two QPCs as a function of magnetic field on the vertical axis and electric field on the horizontal axis, respectively. In the right panel, the corresponding α_{BIA} and α_{SIA} are depicted as a function of the electric field. For zero electric field the splitting of the first focusing peak is solely due to the Dresselhaus spin-orbit interaction. The numerically calculated splitting agrees well with the expectation from the analytic solution Eq. (6.6). In Fig. 6.4 (left), we plot the peak normalized density of states at the Fermi energy for electrons injected from the left QPC at a fixed magnetic field of $B_z = 60\,\mathrm{mT}$ and zero electric field. This quantity is proportional to the transmission probability from the injector to a probe attached to a point in the device, see Sec. 5.6. Such a probe could be realized by the tip of a scanning tunnel microscope. Recently, such a measurement was carried out successfully for a transverse electron focusing experiment [132]. We can clearly see that two separated cyclotron orbits form. That the corresponding electron beams are actually spin polarized can be seen in the right panel of the figure.

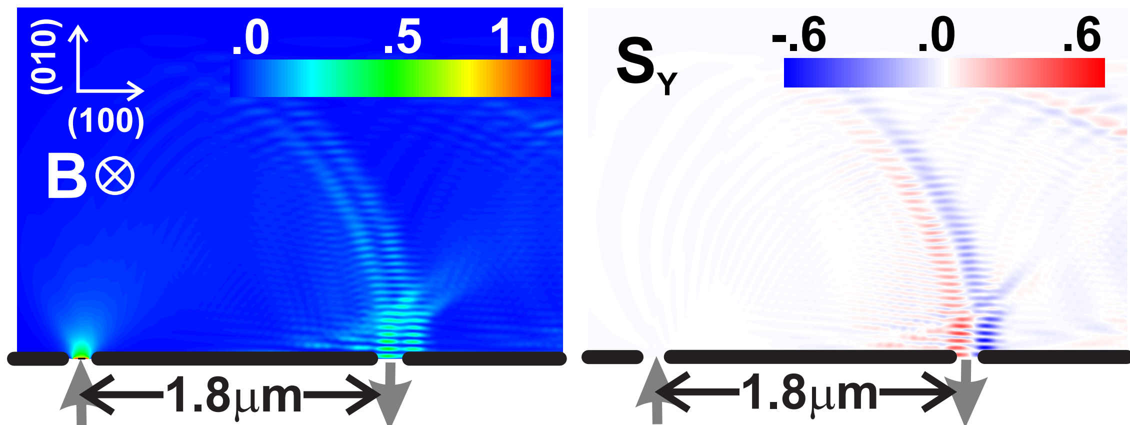

Figure 6.4.: (left) Contour plot of the peak normalized lead connected local density of states of the injector quantum point contact at the Fermi energy for the InSb quantum well at zero electric field and an external magnetic field $\mathbf{B} = 60\,\mathrm{mT}$. (right) Peak normalized spin polarization in y-direction relative to the lead connected local density of states.

Here, we plot the peak-normalized spin polarization in y-direction (crystallographic [010]-direction) relative to the density of states for carriers emerging coherently from the injector. We find that the carriers are highly spin polarized in this direction as they approach the collector, since in the [010]-direction the spin-orbit field of the Dresselhaus Hamiltonian points in the y-direction. The other spin directions (not shown) have no significant values, which shows that we are indeed in the low external magnetic field field limit and the spin-orbit coupling dominates.

For nonzero electric field, also the Rashba spin-orbit coupling constant becomes nonzero. For large electric field the Rashba effect is expected to dominate over the Dresselhaus effect. The calculated splitting of the cyclotron orbits in this limit agrees well with the expectation from the semiclassical prediction of Eq. (6.7). In Fig. 6.5 (left), we plot the peak normalized density of states at the Fermi energy for electrons injected through the left QPC for a fixed magnetic field of $B_z = 60\,\mathrm{mT}$ and a fixed electric field of $\mathbf{F} = 200\,\mathrm{kV/cm}$. The two cyclotron orbits are clearly visible and well separated. In the right panel, we plot again the peak-normalized spin polarization relative to the density of states, but this time for the x-direction (crystallographic [100]-direction), since for systems with dominating Rashba spin-orbit interaction the eigenspinor is approximately perpendicular to the direction of motion. The other spin directions are again insignificant. We note that the two cyclotron orbits are almost perfectly spin polarized in this case. We attribute this fact to the larger spin-orbit field and the larger separation of the orbits, whereas in the case of zero electric field the two orbits where still partly overlapping, which reduces the effective polarization of each peak.

A special situation is the case of competing Dresselhaus and Rashba spin-orbit coupling, when the associated spin-orbit coupling constants α_{BIA} and α_{SIA} have

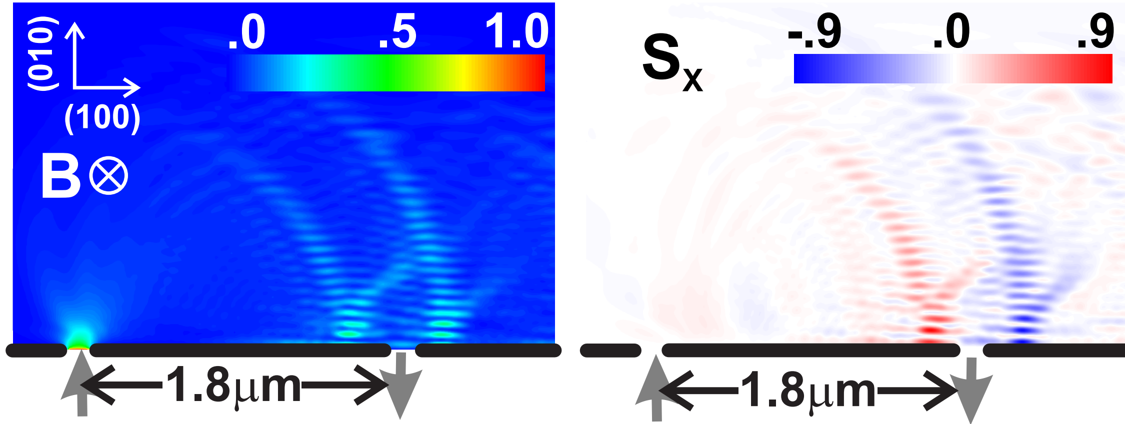

Figure 6.5.: (left) Contour plot of the peak normalized lead connected local density of states of the injector quantum point contact at the Fermi energy for the InSb quantum well at an electric field of $\mathbf{F} = 200\,\mathrm{kV/cm}$ and a magnetic field of $\mathbf{B} = 60\,\mathrm{mT}$. (right) Peak normalized spin polarization in x-direction relative to the lead connected local density of states.

about the same magnitude. In Fig. 6.3 this point is reached for electric fields around $\mathbf{F} \approx 40\,\mathrm{kV/cm}$. For this case the semiclassical prediction is obviously qualitatively wrong since no spin split cyclotron orbits are found from the numerically exact calculation. For the case of exactly equal coupling constants $\alpha_{\mathrm{BIA}} = \alpha_{\mathrm{SIA}}$, the absence of spin-split cyclotron orbits can be explained with the effective decoupling of spin and Landau-level. For $\alpha_{\mathrm{BIA}} = \alpha_{\mathrm{SIA}}$ the eigenspinor is independent of the wave vector and the Fermi surface turns into two independent spheres, shifted from the origin in reciprocal space. For slightly larger electric fields, when the Rashba spin-orbit coupling constant is only a little larger than the Dresselhaus one, we get three independent peaks in the transmission as a function of the magnetic field. As it turns out, the middle peak is not spin polarized and appears exactly at the magnetic field expected for a system without spin-orbit coupling. This phenomena is related to the so-called magnetic break down and can be attributed to tunneling between the two cyclotron states at points in reciprocal space, where the Fermi surfaces of both spin states come closest [143].

Finally, we want to point out that we find no splitting of the second focusing peak (not shown) which can be attributed to spin-dependent reflexion of the barrier for the skipping orbits [156]. Due to the mixing of the spin states at the barrier [150] the up state with the smaller cyclotron radius scatters into the down state with the larger cyclotron radius and vice versa. Therefore, both spin states are focused onto the same region in space, leading to a single non-split peak in the transmission of the second focusing peak.

6.4. Summary

In this chapter, we have presented results for the spin-dependent transverse electron focusing in magnetic field. In particular, we have studied semiconductor nano-structures in external electric and magnetic field and predict a large spin splitting of the first focusing peak in InSb and InAs quantum wells. The effect can be employed to realize highly effective spin polarizer as well has highly sensitive spin filter that work for various spin-polarization directions which is selectable by the applied gate voltage. In particular, we predict for InSb quantum wells, that for low external electric fields, the spin-split electron beams are highly polarized in the x-direction, perpendicular to the direction, that connects the injector and collector QPC. In higher external electric field, on the other hand, the polarization of the electron beams point in the y-direction, along the connection of the QPCs.

7. Review of the intrinsic spin-Hall effect in nanostructures

7.1. Introduction

The modern field of spintronics has caused a tremendous interest in spin-orbit coupling effects in semiconductors. The name spintronics summarizes the research both theoretically and experimentally to use the carrier's spin degree of freedom instead of or in combination with its charge for information processing or quantum computing [2]. A key challenge in the development of applications, e.g. the spin transistor proposed by Datta and Das [1], is to gain control over the spin degree of freedom in semiconductor nanostructures. To achieve this goal, the so-called spin-Hall effect is expected to play a major role [4, 5].

The spin-Hall effect was first predicted by Dyakonov and Perel [157] in the 1970s and in a more recent paper by Hirsch [158]. If an electrical current passes through a two-dimensional electron gas (2DEG) with spin-orbit coupling it induces a spin polarization with opposite orientation at opposite edges. The effect requires neither external magnetic fields nor ferromagnetic elements. Instead, it is caused by spin-dependent impurity scattering, as side jump and skew scattering effects [159, 160]. Therefore this effect is termed extrinsic spin-Hall effect today, as opposed to the intrinsic spin-Hall effect [161, 162], that is caused entirely by the spin splitting of the band-structure and nonzero without any impurity scattering. For the intrinsic spin-Hall effect a universal spin conductivity was predicted [163] and thus pure spin currents perpendicular to the electrical charge current. However, it turned out that the intrinsic spin-Hall conductivity in an infinite 2DEG vanishes for arbitrary small spin-independent impurity scattering [164, 165].

In contrast to the infinite 2DEG, in finite structures on the nanometer scale the intrinsic spin-Hall effect is robust against spin-independent coherent [166, 167] as well as incoherent scattering [168] and shows up as finite spin accumulation at the opposite edges of a quantum wire with finite width [107, 169–172]. It has therefore also been termed mesoscopic spin-Hall effect to delimit it from the infinite case. Thus, in nanostructures both the intrinsic and the extrinsic spin-Hall effect are always present. While in clean samples where the mean free path exceeds the device dimensions, the intrinsic effect is dominant, the extrinsic effect becomes important in the diffusive regime [173]. In this work, we focus on near ballistic nanostructures where the intrinsic spin-Hall effect is most important. In this chapter, we present a detailed study of the intrinsic mesoscopic spin-Hall effect in two-dimensional quan-

tum wires with a finite width together with a simple, analytically solvable model, to elucidates the origin of the spin polarization.

7.2. Origin of the mesoscopic intrinsic spin-Hall effect

To elucidated the origin of the mesoscopic spin-Hall effect, we consider an infinite two-dimensional quantum wire. We take the wire to be infinitely extended along x-axis and confined by impenetrable barriers along the y-direction. For the k-linear model, see Eq. (3.1), we can obtain an analytic solution. The solution for a quantum wire with pure Rashba coupling has been presented in Ref. [174]. However, since the Dresselhaus effect is nonzero already in D_{2d} symmetric structures and the Rashba effect is nonzero only for C_{2v} symmetry, we allow for both spin-orbit coupling mechanisms in the derivation. We make a plane-wave ansatz for the x-direction. Thus, the Hamiltonian operator Eq. (3.1) reads,

$$H = \frac{\hbar^2 k_x^2}{2m^*} - \frac{\hbar^2}{2m^*}\partial_y^2 + (\alpha_{\mathrm{SIA}}\sigma_x - \alpha_{\mathrm{BIA}}\sigma_y)k_x + i(\alpha_{\mathrm{SIA}}\sigma_y - \alpha_{\mathrm{BIA}}\sigma_x)\partial_y. \tag{7.1}$$

We now expand the wave functions in the basis of the solution $f_j(y)$ for the infinite wire without spin-orbit coupling,

$$f_j(y) = \sqrt{\frac{2}{d}}\sin\left(\frac{\pi j y}{d}\right), \tag{7.2}$$

where j is the quantum number of the state and d denotes the width of the quantum wire. The ansatz for the wave function thus reads,

$$\phi^{\sigma}_{nk_x} = \sum_j C^{\sigma}_{nk_xj} f_j(y), \tag{7.3}$$

where the sum runs over all states j. To find an equation for the coefficients $C^{\sigma}_{nk_xj}$, we consider the Schrödinger equation for the wave function $\phi^{\sigma}_{nk_x}$. The Hamiltonian acts on this wave function according to,

$$\begin{aligned}\left(H - \frac{\hbar^2 k_x^2}{2m^*}\right)\phi^{\uparrow,\downarrow}_{nk_x} = \sqrt{\frac{2}{d}}\sum_j &\left\{\frac{\hbar^2\pi^2 j^2}{2m^* d^2} C^{\uparrow,\downarrow}_{nk_xj}\sin\left(\frac{\pi j y}{d}\right)\right.\\ &\pm\alpha_{\mathrm{BIA}} k_x C^{\downarrow,\uparrow}_{nk_xj}\sin\left(\frac{\pi j y}{d}\right) \pm \alpha_{\mathrm{BIA}}\frac{j\pi}{d}C^{\downarrow,\uparrow}_{nk_xj}\cos\left(\frac{\pi j y}{d}\right)\\ &\left.\pm i\alpha_{\mathrm{SIA}} k_x C^{\downarrow,\uparrow}_{nk_xj}\sin\left(\frac{\pi j y}{d}\right) - i\alpha_{\mathrm{SIA}}\frac{j\pi}{d}C^{\downarrow,\uparrow}_{nk_xj}\cos\left(\frac{\pi j y}{d}\right)\right\}.\end{aligned} \tag{7.4}$$

We now multiply the Schrödinger equation from the right with $f_i(y)$ and integrate over y to extract an relation for the expansion coefficients. We thereby use the

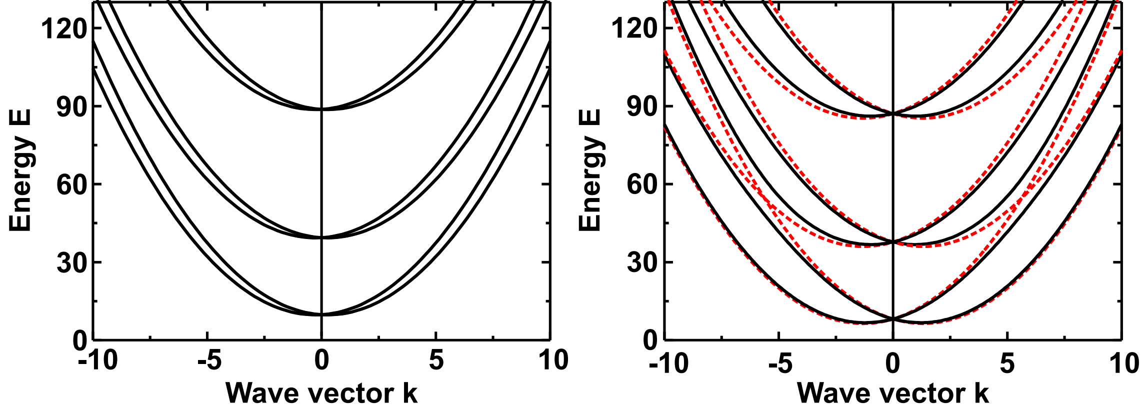

Figure 7.1.: Dispersion relation in a quantum wire with Dresselhaus spin-orbit coupling. The energy is given in units of $\hbar^2/2m^*d^2$ and the wave vector in units of $1/d$. (left) Weak spin-orbit coupling regime with $l_{\mathrm{SO}} = 6d$ (right) Close to the strong coupling regime with $l_{\mathrm{SO}} = 1.2d$. The black solid lines show the calculated numerically exact dispersion. The red dashed lines show a parabolic model dispersion.

orthonormality of the basis functions,

$$\int_0^d \mathrm{d}y f_i(y) f_j(y) = \delta_{ij}. \tag{7.5}$$

For the mixed cosine and sine terms, we get,

$$I_{ij} = \int_0^d \mathrm{d}y \sin\left(\frac{i\pi y}{d}\right) \cos\left(\frac{i\pi y}{d}\right) = -\frac{2i(-1+(-1)^{i+j})}{\pi(i^2-j^2)}. \tag{7.6}$$

To shorten the notation, we introduce the following units,

$$\frac{\hbar^2}{2m^*d^2} = 1 \quad \text{and} \quad d = 1 \tag{7.7}$$

Finally, we get the secular equation for the expansion coefficients $C^{\sigma}_{nk_xj}$ and the energy eigenvalues ε_{k_xn},

$$0 = (\varepsilon_{jk_x} - \varepsilon_{k_xn})\, C^{\uparrow,\downarrow}_{nk_xj} + (\alpha_{\mathrm{BIA}} \pm \alpha_{\mathrm{SIA}})\, k_x C^{\downarrow,\uparrow}_{nk_xj} + \sum_l I_{jl} l\pi(\pm\alpha_{\mathrm{BIA}} - i\alpha_{\mathrm{SIA}}) C^{\downarrow,\uparrow}_{nk_xl}, \tag{7.8}$$

where ε_{k_xn} are the energy eigenvalues of the spin-orbit coupled quantum wire and the ε_{jk_x} are the energy eigenvalues of the quantum wire without spin-orbit interaction at k_x,

$$\varepsilon_{jk_x} = \frac{\hbar^2\pi^2 j^2}{2m^*d^2} + \frac{\hbar^2 k_x^2}{2m^*} = \pi^2 j^2 + k_x^2, \tag{7.9}$$

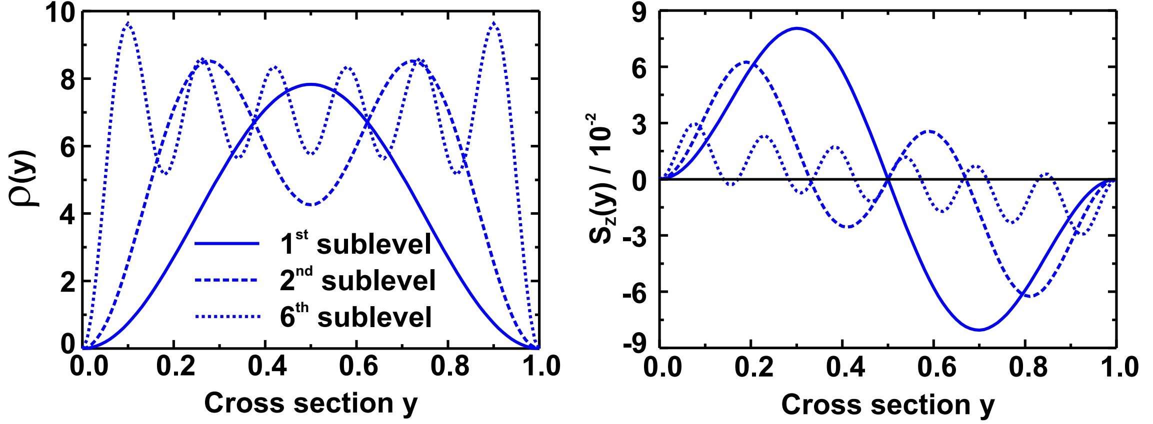

Figure 7.2.: Local density of states $\rho(y)$ (left) and out-of-plane spin polarization $S_z(y)$ (right) at the Fermi energy E_F in a quantum wire as a function of the cross sectional coordinate y within the weak spin-orbit coupling regime with $l_{\mathrm{SO}} = 6d$ for various values of E_F. For the solid line, E_F lies within the first conducting state at $E_F = 26$, for the dashed line within the second conducting state at $E_F = 65.5$, and for the dotted line within the sixth conducting state at $E_F = 420$. Note, that only positive Fermi wave vectors k_F are taken into account.

where the second equality holds for the introduced units of energy and length in Eq. (7.7). From the Schrödinger equation Eq. (7.8), we see, that the spin-orbit interaction induces a coupling between the energy eigenstates of the quantum wire without spin-orbit interaction, very similar to the case of the coupling between Landau levels in external magnetic field, see Sec. 6.2. As we will show now, this coupling causes the finite spin accumulation in the quantum wire and is thus the origin of the mesoscopic spin-Hall effect. The interaction between the unperturbed levels decreases with their energy separation, as becomes clear from Eq. (7.6). Thus, we can truncate the summation over l in Eq. (7.8) after some tens of states to achieve convergence.

In Fig. 7.1, we show the results for the wire dispersion for two different values of the Dresselhaus spin-orbit coupling. The energy E is given in units of $\hbar^2/2m^*d^2$ and the wave vector k_x in units of $1/d$. We assume, that the quantum well structure has D_{2d} symmetry and thus the Rashba spin-orbit coupling constant vanishes. We compare the numerically calculated dispersion (solid lines) Eq. (7.8) with the parabolic dispersion of the infinite 2DEG for each sublevel shifted according to the sublevel energy at $k_x = 0$, ε_j (dashed line). Note that this assumptions is correct in the absence of spin-orbit coupling. We discriminate the regime of weak and strong spin-orbit coupling, depending on the spin-precession length in relation to the wire cross-section [175]. In the left panel, we plot the dispersion in the weak spin-orbit coupling regime, when the spin-precession length l_{SO} is much larger than the wire width d, $l_{\mathrm{SO}} \gg d$. Concretely, we assume $l_{\mathrm{SO}} = 6d$. We find that the calculated

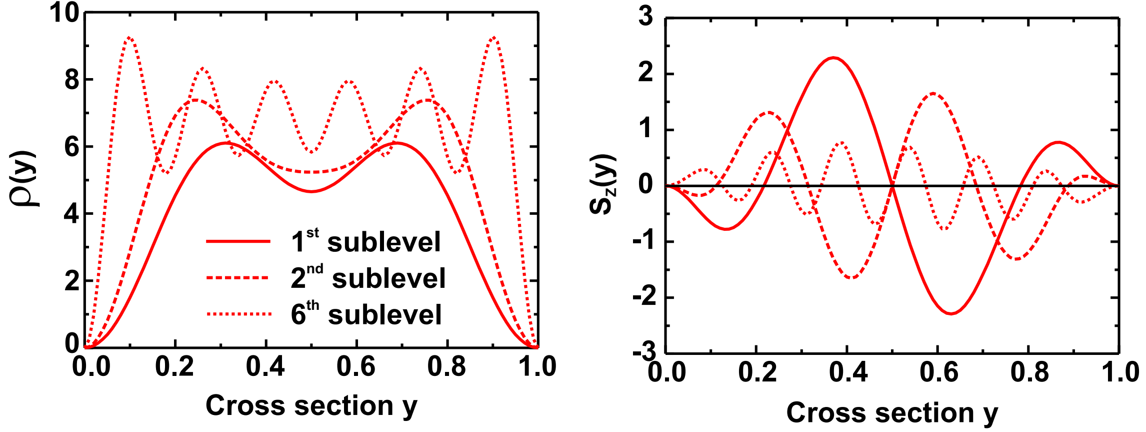

Figure 7.3.: Local density of states $\rho(y)$ (left) and out-of-plane spin polarization $S_z(y)$ (right) at the Fermi energy E_F in a quantum wire as a function of the cross sectional coordinate y within the strong spin-orbit coupling regime with $l_{\rm SO} = .6d$ for various values of E_F. For the solid line, E_F lies within the first conducting state at $E_F = 26$, for the dashed line within the second conducting state at $E_F = 65.5$, and for the dotted line within the sixth conducting state $E_F = 420$. Note, that only positive Fermi wave vectors k_F are taken into account.

wire dispersion and the simple model dispersion agree well. Actually there is no difference visible on the given scale. In the right panel of Fig. 7.1, we show results for the case of spin-orbit coupling close to the strong-coupling regime, that is when the spin-precession length is on the order or shorter than the well width $l_{\rm SO} \lesssim d$. Concretely, we plot the dispersion for $l_{\rm SO} = 1.2d$. For the simple model dispersion (dashed lines), we find several level crossings, due to the spin-orbit coupling induced Mexican hat like dispersion. For example, we find a crossing between the spin-up parabola of the first subband and the spin-down parabola of the second state. From Eq. (7.8), we can see, that these states are actually interacting. Therefore, the crossings are absent in the numerically calculated dispersion (solid lines). Instead, we find strong anti-crossings between these levels. Due to the interaction induced avoided crossings the spin splitting of the wave vector $\Delta k_{\rm SO}$ and thus the effective magnetic spin-orbit field becomes energy and sublevel dependent. Thus, also the observed spin-precession length becomes energy and sublevel dependent, which, in turn, means, that the various sublevels do not contribute coherently additive to the spin precession necessarily.

We now study the density of states and the spin polarization for the infinite quantum wire. From Eq. (7.8), we can also calculate the expansion coefficients $C^{\sigma}_{nk_xj}$ and thus reconstruct the wave functions of the sublevels using Eq. (7.3). The density

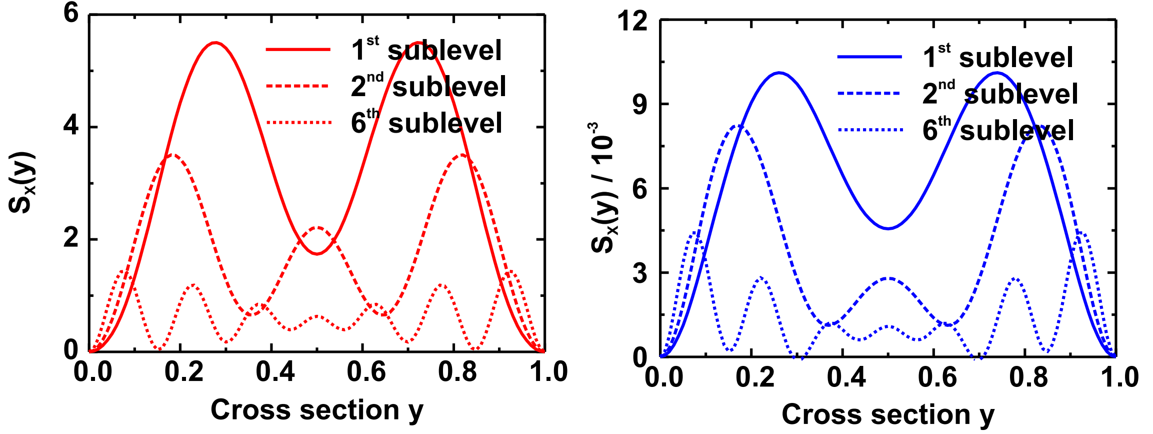

Figure 7.4.: Spin polarization along the wire $S_x(y)$ at the Fermi energy E_F in a quantum wire as function of the cross sectional coordinate x within the strong spin-orbit coupling regime $l_{\text{SO}} = .6d$ (left) and weak spin-orbit coupling regime $l_{\text{SO}} = 6d$ (right) for various values of E_F. For the solid line, E_F lies within the first conducting state at $E_F = 26$, for the dashed line within the second conducting state at $E_F = 65.5$, and for the dotted line within the sixth conducting state at $E_F = 420$. Note, that only positive Fermi wave vectors k_F are taken into account.

of states follows from the cross sectional wave functions $\phi^{\sigma}_{nk_x}$ according to,

$$\rho(E) = \frac{1}{2\pi}\sum_{\sigma}\int \mathrm{d}k_x \delta\left(E - \varepsilon_{k_x n} - \frac{\hbar^2 k_x^2}{2m^*}\right)\left|\phi^{\sigma}_{nk_x}\right|^2, \tag{7.10}$$

which can be formulated more conveniently for the numerical implementation, using the group velocity $v_G(nk_x) = \hbar^2 k_x/m^* + \mathrm{d}\varepsilon_{k_x n}/\mathrm{d}k_x$,

$$\rho(E) = \frac{1}{2\pi}\sum_{\sigma}\int \mathrm{d}k_x \frac{1}{v_G(k_n)}\delta(k_x - k_n)\left|\phi^{\sigma}_{nk_x}\right|^2. \tag{7.11}$$

Accordingly, we can derive the local spin polarization $S_i(E)$, where $i \in \{x, y, z\}$:

$$S_i(E) = \frac{1}{2\pi}\sum_{\sigma,\sigma'}\int \mathrm{d}k_x \frac{1}{v_G(k_n)}\delta(k_x - k_n)\phi^{\sigma}_{nk_x}\,\hat{\sigma}^i_{\sigma,\sigma'}\,\phi^{\sigma'}_{nk_x}, \tag{7.12}$$

where $\hat{\sigma}^i$ are the standard Pauli matrices. Note, that in the equilibrium situation, where all positive and negative k_x-states are occupied equally, due to the Kramers theorem, the spin polarization of the states with $-k_x$ cancels the spin polarization of the states with $+k_x$, which results in a vanishing spin polarization in all directions, as expected.

We are, however, interested in the non-equilibrium situation, with finite spin polarization due to a mismatch in the occupation of plus and minus k_x-states which

is caused e.g. by an applied bias along the wire. In what follows, we will therefore consider only the states with $k_x > 0$.

In Fig. 7.2, we plot the calculated density of states $\rho(E_F)$ (left panel) and the out-of-plane spin polarization $S_z(E_F)$ (right panel) for three values of the Fermi energy as a function of the spatial coordinate across the wire y, given in units of the wire width d. The spin-orbit coupling is assumed within the weak coupling regime, with $l_{\mathrm{SO}} = 6d$. The solid lines show the situation for the Fermi energy between the first and the second wire state, with $E_F = 26$, such that only the lowest subband is occupied. The density of states shows the expected behavior $\propto \sin^2(\pi y)$, known from the quantum well with infinite barriers without spin-orbit coupling. For the spin polarization S_z, we find the behavior that is expected from the phenomenology of the spin-Hall effect. Spin-up density accumulates at the left side of the wire, while spin-down density accumulates at the right side of the wire, in such a way, that the overall polarization, i.e. the integral over the cross-section, vanishes. The polarization in the lowest subband resembles a function $\propto \sin(2\pi y)$ very closely. For the dashed and the dotted line the Fermi level lies within the second and sixth conducting state with $E_F = 65.6$ and $E_F = 420$, respectively. The density becomes more oscillatory the higher the states are and follow the behavior known for the unperturbed states without spin-orbit coupling, which is $\propto \sin^2(\pi j y)$, where j is the quantum number of the sublevel. Thus, the spin-summed density of states is not considerably influenced by the spin-orbit coupling. The spin polarization gets more oscillatory as well. The largest magnitude of the spin polarization is still found at the edges of the wire, however the magnitude of the polarization gets markedly smaller. We note, that similar oscillations in the out of plane spin polarization were also predicted for a hard wall boundary in the semi-infinite 2DEG [176].

We now turn to the case of the strong coupling regime and set the spin-precession length to $l_{\mathrm{SO}} = .6d$. We have seen in Fig. 7.1 that the dispersion in the strong spin-orbit coupling regime deviates markedly from the parabolic one. In Fig. 7.2, we plot the resulting density of states (left panel) and the spin polarization (right panel) for the same Fermi energies as in the case of weak spin-orbit coupling. The density of states of the first sublevel (solid line) deviates strongly from the one in the weak coupling case. Obviously, the coupling between the first and second subband, is strong enough to alter the density of states qualitatively. Instead of one maximum in the middle of the wire, we get two maximums shifted to the edges of the wire, which is a clear sign for the strong influence of the second conducting state, since the density of states of the second unperturbed sublevel is $\propto \sin^2(2\pi y)$. Also the spin polarization of the first sublevel (solid line) differs qualitatively from the weak coupling case. Apart from the expected magnification of the polarization due to the stronger spin-orbit coupling, we find that at the left edge of the wire the spin accumulation becomes negative, while the positive spin-polarization peak shifts more into the bulk of the wire. On the right edge the behavior is opposite in sign, in such a way, that the integrated overall polarization in z-direction is zero. For the higher sublevels the changes compared to the weak coupling regime are similar but not as pronounced as for the lowest sublevel. That means, that in the

strong coupling regime the intrinsic spin-Hall effect is actually suppressed, since the maximal magnitude of the polarization shifts into the bulk of the wire away from the edges, while at the edges the polarization is small, in contrast to the expected behavior of the spin-Hall effect.

For completeness, we have also calculated the other spin polarizations in the x- and y-direction. In the y-direction, perpendicular to the homogeneous wire direction, the spin polarization (not shown) vanishes identically. For the x-direction, along the wire, on the other hand, we get a finite polarization that is shown in Fig. 7.4. In the left panel, we show results for the strong coupling regime (red lines) while the right panel shows the weak coupling regime (blue lines). Again, we show results for the three values of the Fermi energy as before. We find, that the strong and the weak coupling regime do not differ qualitatively but only quantitatively in magnitude. As one would expect, the strong spin-orbit coupling leads to a larger effect than for a weak coupling. Integrating S_x over the wire cross-section results in a finite overall magnetization, in contrast to out-of-plane polarization S_z. For Dresselhaus spin-orbit interaction, the effective spin-orbit field is expected to point predominantly along the wire-direction, as can be seen from Eq. (3.6). The finite magnetization is in agreement with the magnetoelectric effect predicted for the infinite 2DEG [162, 177, 178]. We note, that the magnitude of the effect is also largest for the lowest wire sublevel.

7.3. Analytic solution for the two level system

We can gain some more inside into the formation of the spin polarizations already from a simple two level system, i.e. we truncate the summation in Eq. (7.8) after $l = 2$. We thus have four states all together, including spin. In this case, we can solve Eq. (7.8) analytically. We focus on the two spin-resolved ground states of the system. Although, we can not expect a converged result, we can still clarify the origin of the spin polarization for the mesoscopic spin-Hall effect. According to Eq. (7.3) the wave functions of the two ground states with $n = 1$ and $n = 2$ in that case read,

$$\begin{aligned} \phi_1 &= \sum_\sigma \phi_1^\sigma(y) = \sum_\sigma \left(C_{11}^\sigma \sin \pi y + C_{12}^\sigma \sin 2\pi y \right), \\ \phi_1 &= \sum_\sigma \phi_2^\sigma(y) = \sum_\sigma \left(C_{21}^\sigma \sin \pi y + C_{22}^\sigma \sin 2\pi y \right), \end{aligned} \tag{7.13}$$

where we have omitted the k_x dependence for simplicity. Note, however, that the two wave functions ϕ_1 and ϕ_2 correspond to states with different k_x at a given Fermi energy. We consider a quantum wire with pure Dresselhaus spin-orbit coupling. In that case, we analytically find the following relations between the C_{1j}^σ,

$$\begin{aligned} C_{11}^\uparrow &= a & C_{11}^\downarrow &= -a, \\ C_{12}^\uparrow &= b & C_{12}^\downarrow &= b, \end{aligned} \tag{7.14}$$

and between the C^{σ}_{2j}:

$$\begin{aligned} C^{\uparrow}_{21} &= \alpha & C^{\downarrow}_{21} &= \alpha, \\ C^{\uparrow}_{22} &= \beta & C^{\downarrow}_{22} &= -\beta, \end{aligned} \tag{7.15}$$

where the parameters a, b, α, and β are real and positive. The parameters depend on the spin-orbit coupling and we find $\alpha \neq a$, $\beta \neq b$. We calculate the spin polarization S_i of the first level, according to:

$$S_i = \sum_{n=1}^{2} \langle \phi_n \,|\, \hat{\sigma}_i \,|\, \phi_n \rangle \,. \tag{7.16}$$

To simplify the notation, we assume the group velocity v_G (Eq. (7.12)) to be included in the expansion parameters. For the out-of-plane spin polarization S_z, we get,

$$\begin{aligned} \langle \phi_1 \,|\, \hat{\sigma}_z \,|\, \phi_1 \rangle &= 4ab \sin \pi y \sin 2\pi y, \\ \langle \phi_2 \,|\, \hat{\sigma}_z \,|\, \phi_2 \rangle &= -4\alpha\beta \sin \pi y \sin 2\pi y, \end{aligned} \tag{7.17}$$

and thus for S_z,

$$S_z = 4(ab - \alpha\beta) \sin \pi y \sin 2\pi y, \tag{7.18}$$

which is finite due to the difference in the expansion coefficients of ϕ_1 and ϕ_2 and the difference in the corresponding group velocity. Note that indeed we have $S_z \propto \sin 2\pi y$. In the same way, we obtain for the y-polarization S_y=0, where each summand in Eq. (7.16) vanishes individually. For the remaining x-polarization, we obtain,

$$\begin{aligned} \langle \phi_1 \,|\, \hat{\sigma}_x \,|\, \phi_1 \rangle &= -2a^2 \sin^2 \pi y + 2b^2 \sin^2 2\pi y, \\ \langle \phi_2 \,|\, \hat{\sigma}_x \,|\, \phi_2 \rangle &= 2\alpha^2 \sin^2 \pi y - 2\beta^2 \sin^2 2\pi y, \end{aligned} \tag{7.19}$$

which leads to,

$$S_x = 2(\alpha^2 - a^2) \sin^2 \pi y + 2(b^2 - \beta^2) \sin^2 2\pi y, \tag{7.20}$$

which is again finite due to the difference in the two spin eigenstates and shows the correct dependence on the transverse coordinate. In particular it leads to a finite overall polarization, when integrated over the width of the wire.

Thus, we find, that the finite spin polarization in the quantum wire, i.e. the mesoscopic spin-Hall effect for the out-of plane component S_z and the magnetoelectrical effect for S_x are solely due to the coupling between the spin states in different sublevels of the wire and due to the thereby caused nonparabolic dispersion of the individual sublevels. Thereby, we find that the coupling between adjacent levels dominates the effect. For the weak coupling regime, the nonparabolic effects are small, and thus the spin polarization. When the spin-precession length is of the order of the wire width, on the other hand, the nonparabolic effects become large

and hence, cause large polarization effects. For even stronger spin-orbit coupling, in the strong coupling regime, coupling to more distant levels influences the effect drastically and leads to a suppression of the spin accumulation at the sample edges.

Note that very similar results can be obtained for the artificial case of pure Rashba spin-orbit coupling. In this case, we find a vanishing x-polarization and a finite y-polarization. Indeed, we obtain $S_z(\alpha_{\mathrm{BIA}}) = -S_z(\alpha_{\mathrm{SIA}})$ and $S_x(\alpha_{\mathrm{BIA}}) = -S_y(\alpha_{\mathrm{SIA}})$. For the special case $\alpha_{\mathrm{BIA}} = \alpha_{\mathrm{SIA}}$ all polarizations vanish identically. In this case, the spin eigenstate of the infinite 2DEG ceases to depend on the momentum. Thus, spin and momentum are effectively decoupled. In the quantum wire, the coupling between the sublevels in the wire vanishes and the dispersion is indeed parabolic, as depicted by the dashed lines in Fig. 7.1. Due to the absence of nonparabolicities also the spin-polarization effects in the quantum wire vanish.

7.4. Summary

In this chapter, we have studied the mesoscopic spin-Hall effect in an infinite two-dimensional quantum wire. We have calculated the dispersion relation, the local density of states, and the spin polarizations. Further, we have shown within an analytically solvable two-level approximation, that the spin polarizations arise from the nonparabolicity of the dispersion, that is caused by the spin-orbit induced interaction between subbands. We have identified two qualitatively different regimes. The weak coupling regime, where the spin-precession length is much larger than the wire width and the strong coupling regime, where the spin-precession length is shorter than the wire width. In particular, we find that only within the weak-coupling regime, the out-of-plane spin-polarization effects are largest at the sample edges, whereas for the strong coupling regime the polarization is more pronounced in the bulk of the wire. Additionally, we have found that the spin-polarization effects are largest for the lowest sublevel. Thus, for an application of the mesoscopic spin-Hall effect in spintronic devices, the best conditions are met, if only the lowest conducting state is occupied and the wire width is of the order of the spin-precession length, right in between the weak and the strong coupling regime.

8. Prediction of giant intrinsic spin-Hall effect in tensile strained p-GaAs

8.1. Introduction

The intrinsic spin-Hall effect (SHE) in semiconductors predicted by Murakami et al. [161] and Sinova et al. [179] is a very promising tool to manipulate the spin degree of freedom without ferromagnetic elements or external magnetic fields and to generate spin-polarized currents, solely caused by the spin-orbit interaction (SOI). The intrinsic SHE has been detected experimentally in semiconductors for two-dimensional hole gases (2DHGs) by optical means [180, 181]. For two-dimensional electron gases (2DEGs) optical results have only been reported on the extrinsic spin-Hall effect [182–184] that is caused by spin-dependent scattering off impurities. Most theoretical work on the intrinsic spin-Hall effect has concentrated on the spin-Hall conductivity in infinite 2DEGs or 2DHGs [159, 185–189] or the spin-Hall conductance in simple nanostructures [105, 106, 108, 190–192]. The studied pure spin currents, however, are not measurable directly. An indirect method to measure pure spin currents is provided by the inverse intrinsic spin-Hall effect that converts spin currents into charge currents [193–197]. Such transport based measurements of spin currents have successfully been performed for the extrinsic inverse spin-Hall effect in metals [158] with strong SOI like Platinum [198–201]. Very recently electrical measurements of intrinsic spin currents in semiconductor have been successfully performed in HgTe quantum wells [24]. In this chapter, we predict concrete nanostructured materials and device geometries that exhibit a large intrinsic inverse spin-Hall effect. We provide detailed studies of an H-shaped 2DHG originally proposed by Hankiewicz et al. [202] and for several more complex three terminal devices.

8.2. Inverse intrinsic spin-Hall effect in H-shaped structure

The present atomistic electronic structure calculations show an exceptionally large k-linear SOI for the top valence band in tensile strained GaAs quantum wells. As discussed in Sec. 3.4 this large k-linear spin splitting is caused by the strain, which may be generated by growing GaAs on $In_xAl_{1-x}As$ buffer material that sets the

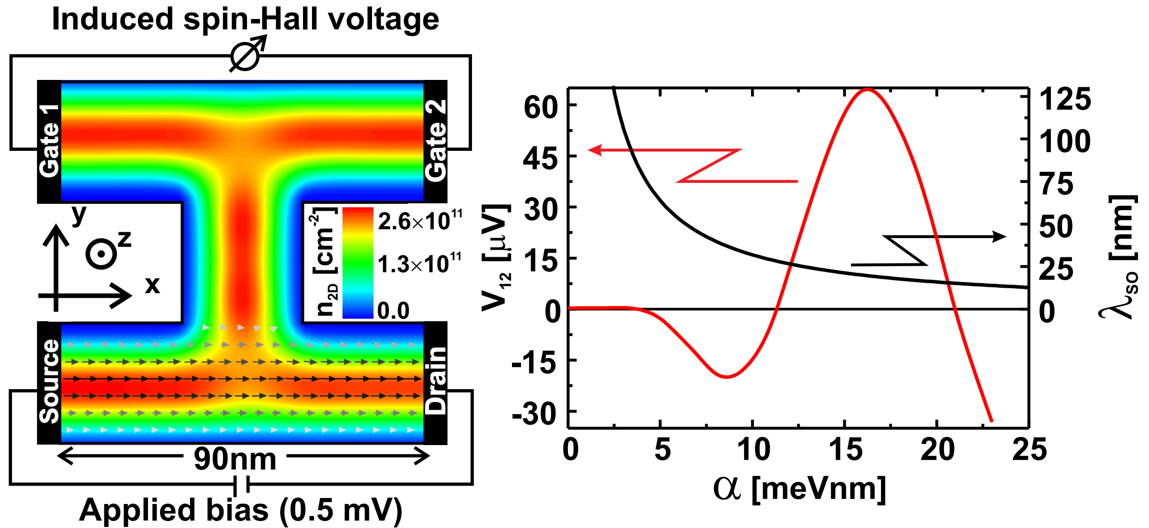

Figure 8.1.: (left) Contour plot of the two-dimensional local charge density in the H-bar structure. The cross section of the wires is taken to be 30 nm. The average sheet density amounts to $n_{2D} = 1.75 \times 10^{11}\,\mathrm{cm}^{-2}$. The gray scale arrows depict the local charge current that flows through the structure. The darker the arrow the larger the local current at this point. For the applied source-drain bias of $V_{\mathrm{SD}} = .5\,\mathrm{mV}$, the total charge current between source and drain amounts to $I_{\mathrm{SD}} = 22.5\,\mathrm{nA}$. (right) Induced spin-Hall voltage V_{12} shown as the red line on the left vertical axis and spin-precession length shown as black line on the right vertical axis, both as a function of the Dresselhaus spin-orbit coupling parameter.

lateral lattice constant and acts as barrier material. We note that the SOI in the conduction band remains unaffected by the strain. The tensile strain causes the light hole band to lie above and to be well separated from the heavy hole band. We therefore focus on light hole gases in tensile strained GaAs quantum wells in this chapter.

The investigated two-dimensional geometry is shown in Fig. 8.1 (left). The figure shows a top view of the gate defined nanostructure in a 2DHG. We model the geometry by impenetrable barriers. The local sheet density is shown as a surface plot. The results have been obtained by the present spin-resolved non-equilibrium Grenn's function method, including inelastic and phase-breaking scattering via spin-independent Büttiker probes. The mean free path has been set to 200 nm. The proposed experiment works as follows. An applied source–drain bias drives a charge current in the lower leg, which is depicted by the gray-scale arrows. Due to the spin-Hall effect, a pure spin current flows through the vertical connection into the upper leg that, in turn, induces a voltage drop between the two gates due to the inverse spin-Hall effect [202]. The calculated local charge current shows indeed, that there is effectively no carrier transport through the connection into the upper leg.

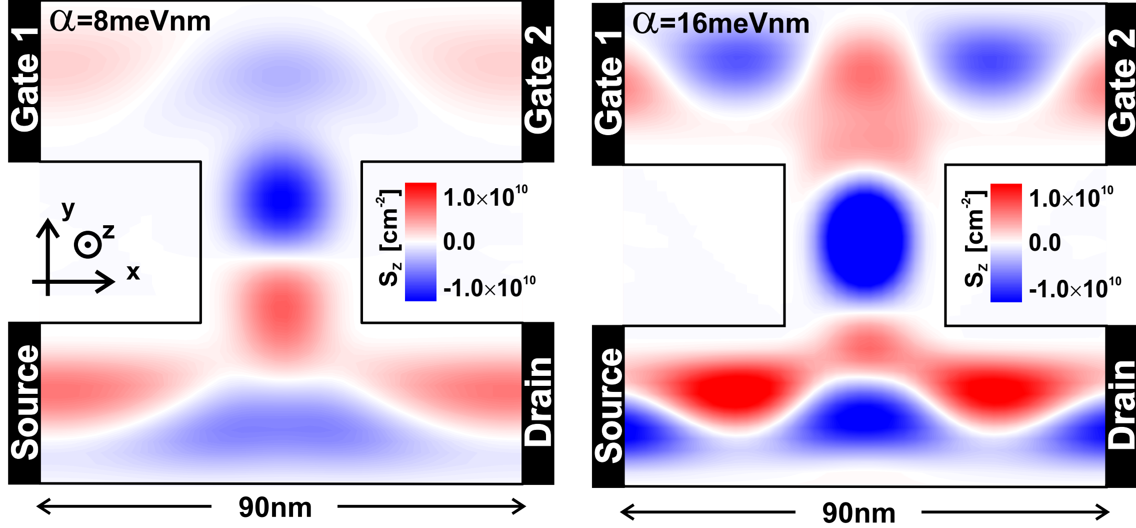

Figure 8.2.: Contour plot of the local out-of-plane spin polarization S_z for the H-bar structure with a wire cross section of 30 nm for an applied bias .5 mV and a charge density of $n_{2D} = 1.75 \times 10^{11}\,\text{cm}^{-2}$. (left) For a Dresselhaus spin-orbit coupling parameter of $\alpha_{\text{BIA}} = 8\,\text{meVnm}$. (right) For $\alpha_{\text{BIA}} = 16\,\text{meVnm}$.

In the right panel, the calculated induced spin-Hall voltage V_{12} between the contacts Gate 1 and Gate 2 is shown as a function of the k-linear coupling parameter that can be set by the tensile strain, see Sec. 3.4. Since the other parameters of the k-cubic Dresselhaus model Eq. (3.12) show only a weak dependence on the strain, we assumed constant values for simplicity. In particular, we use $m^* = .375$, $c_1 = -91.2\,\text{meVnm}^3$, and $c_2 = 15.9\,\text{meVnm}^3$. We assume the widths of all channels to be equal to 30 nm. The length of the vertical bar is also taken to be 30 nm. The applied source–drain bias $V_{\text{SD}} = .5\,\text{mV}$ causes a charge current to flow between the source and the drain. We get $I_{\text{SD}} = 22.5\,\text{nA}$. The hole density amounts to $n_{2D} = 1.75 \times 10^{11}\,\text{cm}^{-2}$ at a temperature of $T = 1\,\text{K}$ such that only the highest hole subband is occupied. The calculations show an oscillatory behavior of the spin-Hall voltage V_{12} as a function of the spin-orbit coupling constant which can be explained as follows. The magnitude and sign of the spin-Hall voltage V_{12} is roughly proportional to the average out-of-plane spin polarization S_z in the hole gas at the junction in the upper leg that has been induced by the charge current in the lower leg. With increasing SOI, the spin-precession length λ_{SO} changes as is also depicted in Fig. 8.1 (right). The spin-precession length is the distance in real space over which a spin precesses by an angle of π, i.e a spin-up changes into spin-down and vice versa. The spin-precession length is determined by the spin splitting of the wave vector in reciprocal space. For k-linear spin splitting in a D_{2d} symmetric

structure, it is given by,

$$\lambda_{\rm SO} = \frac{\pi\hbar^2}{2m^*\alpha_{\rm BIA}}. \tag{8.1}$$

Whenever the device width is an even (odd) integer of this length, S_z becomes a maximum or minimum (zero) which explains the finding for V_{12}. For $\alpha < 5\,$meVnm, the calculated spin-Hall voltage is negligible. Therefore, the intrinsic inverse SHE is negligible in n-type GaAs, which holds independently of the mobility. For the strained p-GaAs quantum wells, by contrast, the two extrema in Fig. 8.1 (right) correspond to a fairly low Indium composition of $x = .11$ and $x = .21$. In Fig. 8.2, we plot the out-of-plane spin polarization S_z as contour plot for the two values of the spin-orbit coupling strength that correspond to the extrema of the induced spin-Hall voltage. In the left panel, the Dresselhaus spin-orbit coupling parameter is $\alpha_{\rm BIA} = 8\,$meVnm which corresponds to a spin-precession length $\lambda_{\rm SO} \approx 42\,$nm, that is approximately half the device width. The averaged induced spin polarization at the junction in the upper leg amounts to $\langle S_z \rangle = -1.4 \times 10^9\,{\rm cm}^{-2}$, which in turn induces a spin-Hall voltage of $V_{12} = -20\,\mu$V. In contrast, in the right panel of the figure, where we set $\alpha_{\rm BIA} = 16\,$meVnm, which corresponds to $\lambda_{\rm SO} \approx 22\,$nm and thus approximately a quarter of the device width, the induced spin polarization at the junction in the upper leg now is $\langle S_z \rangle = 2.6 \times 10^9\,{\rm cm}^{-2}$, which leads to a spin-Hall voltage of $V_{12} = 60.5\,\mu$V. We thus find approximately a quadratic relation between the spin polarization and the induced spin-Hall voltage $V_{12} \propto {\rm sign}\left(\langle S_z \rangle\right) \langle S_z \rangle^2$. The resistance signal, i.e. the spin-Hall voltage V_{12} divided by the source-drain current $I_{\rm SD}$, is approximately $1\,{\rm k}\Omega$ for $x = .11$ and $3\,{\rm k}\Omega$ for $x = .21$, which is markedly larger than those predicted for HgTe quantum wells [24]. Fig. 8.3 shows the spin-Hall voltage V_{12} and the source-drain current $I_{\rm SD}$ as a function of applied source-drain bias $V_{\rm SD}$ for both structures with $x = .11$ and $x = .21$, respectively. Since the current $I_{\rm SD}$ is almost equal in both cases, in contrast to the spin-Hall voltage V_{12}, we can be sure that the latter is caused by the SOI rather than by a change in the longitudinal conductance. We note that the situation changes drastically, when more than one subband is occupied. In this case, the geometry of the nanostructure induces a coupling between the occupied sublevels, due to the non-conservation of the wave-vector. This effect occurs independently of the spin-orbit interaction. Apart from altering the spin properties [203], more importantly, it also induces a finite voltage drop V_{12} in the H-bar structure, that is not caused by the inverse intrinsic spin-Hall effect and is also nonzero in systems without spin-orbit interaction. Unfortunately, we find that the spin-orbit induced and the geometry induced signal are on the same order of magnitude and cannot be determined separately in experiment. Thus, the occupation of a single sublevel is vital for the detection of the intrinsic spin currents. Note, that similar conclusions, concerning the influence of higher sublevels have been drawn in Ref. [204].

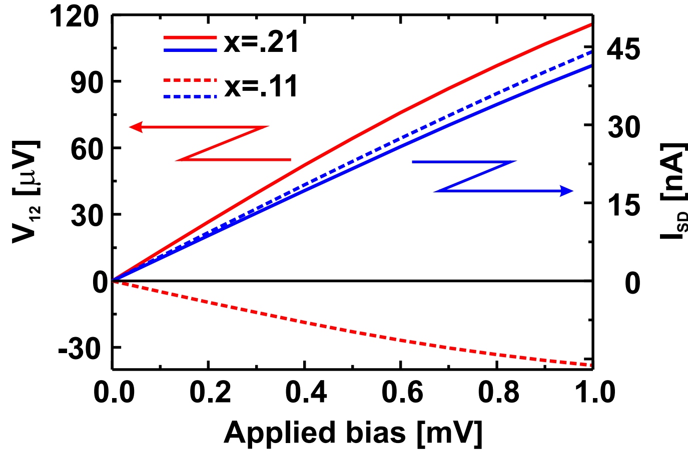

Figure 8.3.: Induced spin-Hall voltage V_{12} (red lines) and source-drain current I_{SD} (blue lines) for the H-bar structure as a function of applied bias. The dashed lines show results for an indium content of $x = .11$ while for the solid lines $x = .21$ holds.

8.3. Prediction of large current induced spin polarization in three terminal T-shaped structure

Three terminal devices with a single source and two drain contacts have been proposed as spin filter in the literature [205–208]. We have studied a T-shaped geometry using the present spin-resolved non-equilibrium Green's function method, assuming a mean free path of 200 nm for the inelastic, phase-breaking scattering modeled by spin-independent Büttiker probes. The used geometry is depicted in Fig. 8.4. The figure shows top views of the gate defined nanostructure in a tensile strained 14 nm wide p-GaAs/$In_{.9}Al_{.91}As$ quantum well. The channel width is 30 nm. The length of the horizontal part between the two drain contacts is taken to be 70 nm. We model the geometry by impenetrable barriers. The local sheet hole density is shown as contour plot in part (a) of the figure it amounts to $n_{2D} = 2.5 \times 10^{11}\,\mathrm{cm}^{-2}$ at a temperature of $T = 1\,\mathrm{K}$, such that only the highest hole subband is occupied. An applied bias of $V_{\mathrm{SD}} = 1.5\,\mathrm{mV}$ between the top source contact and the two bottom drain contacts to the right and to the left of the horizontal arm drives a charge current through the structure. The calculated local charge current density is shown by gray scale arrows in part (a) of the figure. The darker the arrows, the larger the current that flows locally at this point. The overall current between the source and one of the drains amounts to $I_{\mathrm{SD}} = 36.4\,\mathrm{nA}$. We have shown previously [209] that large spin polarizations are generated close to the two drain contacts assuming strictly ballistic transport. In part (b) - (d) of Fig. 8.4, we plot the local spin polarizations S_i, with $i \in \{x, y, z\}$. We find a large out-of-plane spin polarizations at the drain contacts, which amounts to 15% of the total hole density and has oposite signs

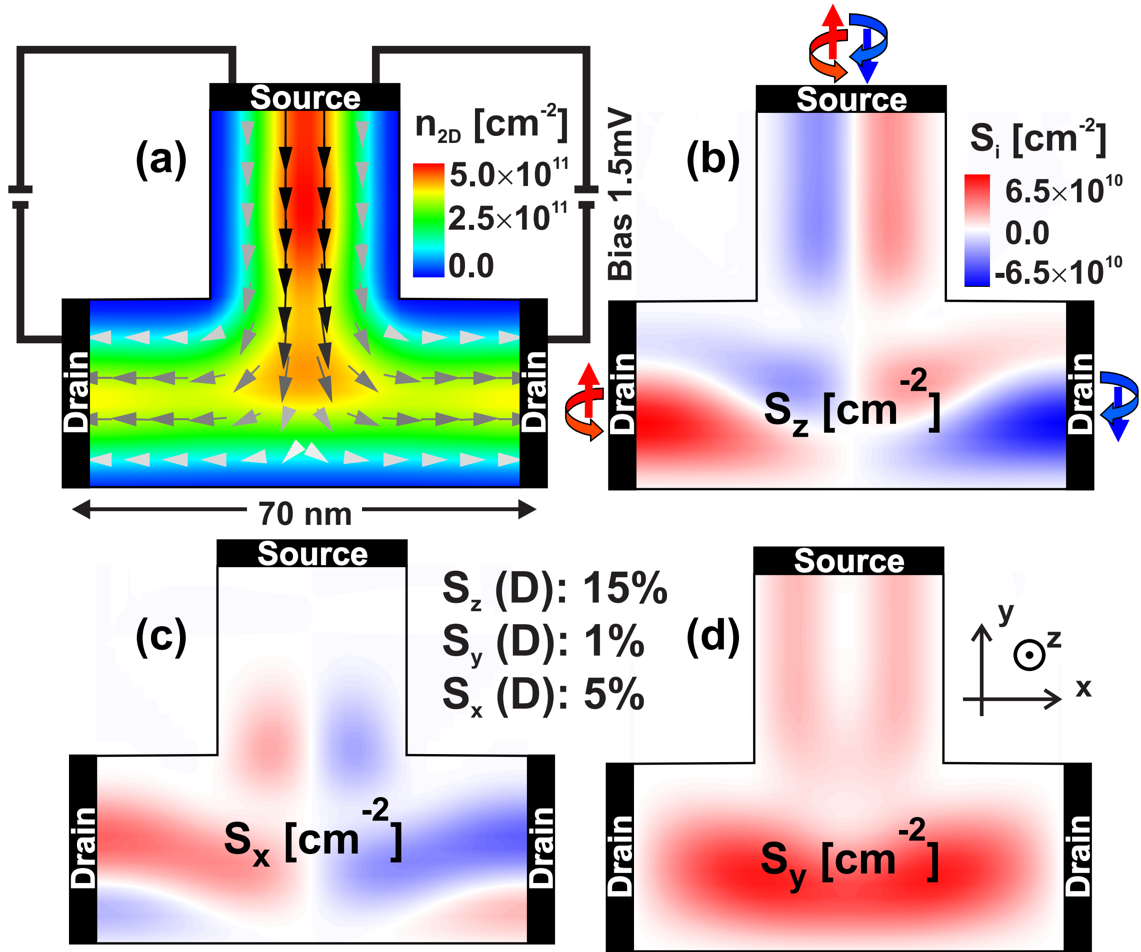

Figure 8.4.: Contour plots of the local two-dimensional hole (a) and spin densities S_x (b), S_y (c), and S_z (d) in the T-shaped structure defined in a tensile strained 14 nm wide p-GaAs/In$_{.9}$Al$_{.91}$As quantum well for an applied source drain bias of 1.5 mV. The wire cross section is 30 nm. $S_i(D)$ denotes the relative spin polarization in direction i at the drain contacts. The gray scale arrows in (a) depict the calculated local charge current. The darker the arrows the larger the current that flows at this point. The total source–drain current amount to $I_{\mathrm{SD}} = 36.4\,\mathrm{nA}$.

at the two drain contacts. Additionally, we find a spin polarization in x-direction (direction of the horzontal arm) of 5%, with equal sign at both drains. The spin polarization in y-direction is small and amounts to only about 1%. The calculated spin polarization shows, that the charge current that flows in the horizontal bar of the structure is highly spin polarized. Thus, such a device geometry generates highly spin-polarized charge currents. We gain further inside into the mechanism that causes the spin polarization, when we consider the dependence of all spin polarizations on the length of the horizontal channel. In Fig. 8.5, we show results for

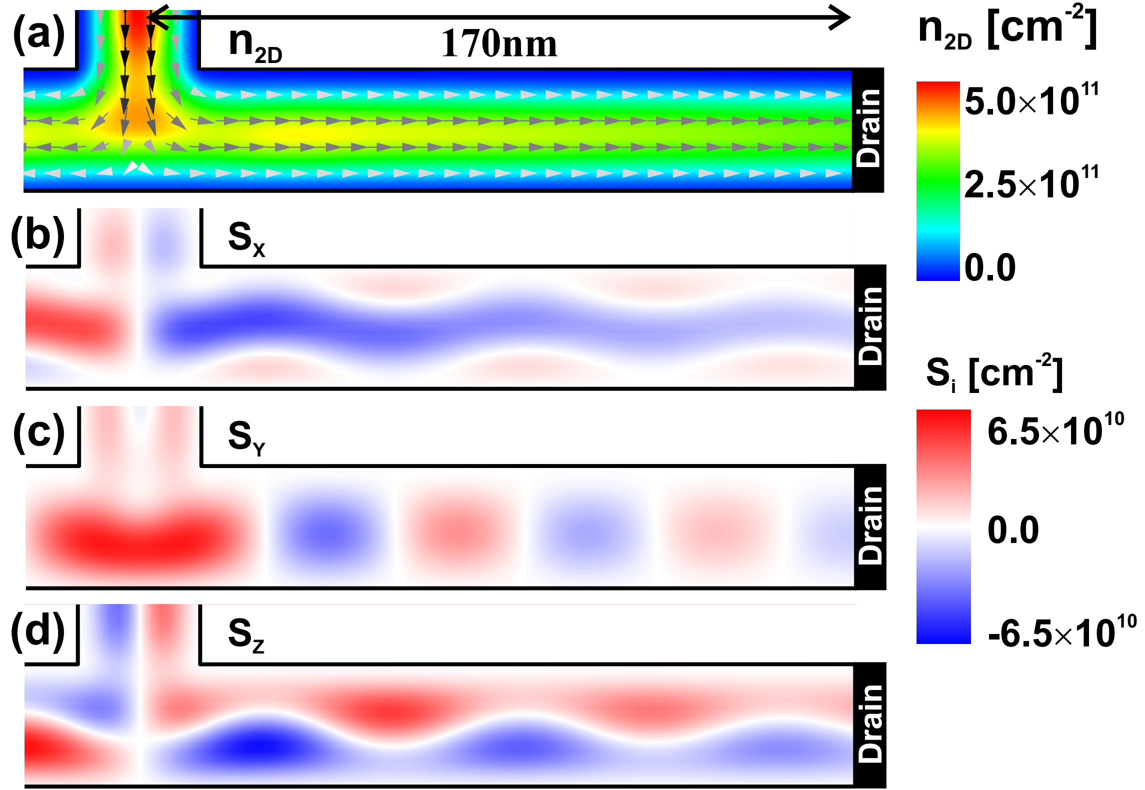

Figure 8.5.: Contour plots of the local two-dimensional hole (a) and spin densities S_x (b), S_y (c), and S_z (d) in a T-shaped structure defined in a tensile strained 14 nm wide p-GaAs/$In_{.9}Al_{.91}$As for an applied source drain bias of 1.5 mV. The gray scale arrows in (a) depict the calculated local charge current. The darker the arrows the larger the current that flows at this point. The total source–drain current amount to $I_{SD} = 33.1$ nA.

the same T-shaped structure but with an elongated distance between the two drain contacts of 340 nm. For simplicity, we only show the right part of the structure. While the local carrier density and the local charge current, shown in part (a), do not depend on the longitudinal x-coordinate in the side arm, the y- and z-component of the spin polarization ((c) and (d)), are predicted to oscillate in correspondence with the spin-precession length, which amounts to $\lambda_{SO} = 30$ nm in this structure. The extrema of the z-polarization occur at points where the y-polarization vanishes while the z-polarization is zero, when the y-polarization is extremal. These findings are elucidated in Fig. 8.6 which shows the three components of the spin polarization at the rightmost drain contact averaged over the width of the horizontal arm as a function of the length of the side arm. We can clearly see, that S_y and S_z oscillate with a period of 30 nm and a phase shift of $\pi/2$, i.e. $|S_z|$ is maximal when $|S_y| = 0$ and vice versa. S_x is constant and does not oscillate. All polarization amplitudes decrease in magnitude due to the phase breaking scattering. The calculated pattern of the spin polarizations is in accordance with a precession around a magnetic field

in x-direction. The spin-orbit field Eq. (3.6) lies predominantly in x-direction in this part of the structure. Thus, the x-component of the spin lies parallel to the spin-orbit field and does not show any precession. However, as can be seen in Fig. 8.5, S_x as well as S_z show an serpentine pattern transverse to the wire. This pattern can be understood with the help of the semiclassical spin force $\boldsymbol{\mathcal{F}}^\sigma$, introduced in Refs. [172, 194] for the infinite 2DEG. For the k-linear spin-orbit coupling model Eq. (3.1), it reads:

$$\boldsymbol{\mathcal{F}}^\sigma = 2\left(\alpha_{\mathrm{SIA}}^2 - \alpha_{\mathrm{BIA}}^2\right)\sigma_z \begin{pmatrix} k_y \\ -k_x \end{pmatrix}. \tag{8.2}$$

The spin force is proportional to $\langle\sigma_z\rangle \propto S_z$ and stems solely from the spin-orbit interaction. Since this force only acts on the z-component of the spin it vanishes when $S_z = 0$ and therefore does not effect the precession pattern of S_y in Fig. 8.5 (c). The force always acts perpendicular to the wave vector. Thus, for carriers, that propagate through the horizontal bar of the T-shaped structure, the spin force points predominantly into the y-direction perpendicular to the wire direction, which explains the calculated serpentine pattern.

8.4. Proposal of an all electrical detection scheme for current induced spin polarization

In the previous section, we have seen, that the T-shaped geometry acts as a very efficient spin polarizer. In Fig. 8.7 (left) the schematics of the polarizer is shown again. An unpolarized current is injected through the source contact. Due to the intrinsic (mesoscopic) spin-Hall effect spin-up and spin-down carriers accumulate at the right and left edge of the vertical wire, respectively. However the average of the out-of-plain component of the spin polarization S_z over the wire cross section remains zero. At the junction with the horizontal bar, the net zero polarization leads to finite net polarization in the horizontal bar in such a way, that a spin-up polarized current is injected into the right horizontal arm, while the current injected into the left arm is spin-down polarized. Due to the spin-orbit field the polarization precesses while the carriers propagate towards the drain contacts. To convert this polarization into an electrical bias voltage, we add two analyzing vertical bars into the right horizontal arm of the T-shaped structure as shown in Fig. 8.7 (right). These vertical probes exhibit a finite voltage drop in proportion to the spin-polarized current flowing towards the drain contact. The principle is closely related to the anomalous Hall effect and has been used experimentally in metallic systems, where the polarized current has been injected from a ferromagnet [198–201]. In our case, the spin-polarized current is generated directly by the T-shaped geometry due to the intrinsic SHE. The calculated spin-Hall voltage V_{AB} turns out to be a direct measure for the z-component of the spin polarization S_z. When the probe is attached at a position where positively (negatively) polarized carriers dominate, we obtain a positive (negative) voltage signal V_{AB}. The calculated spin-

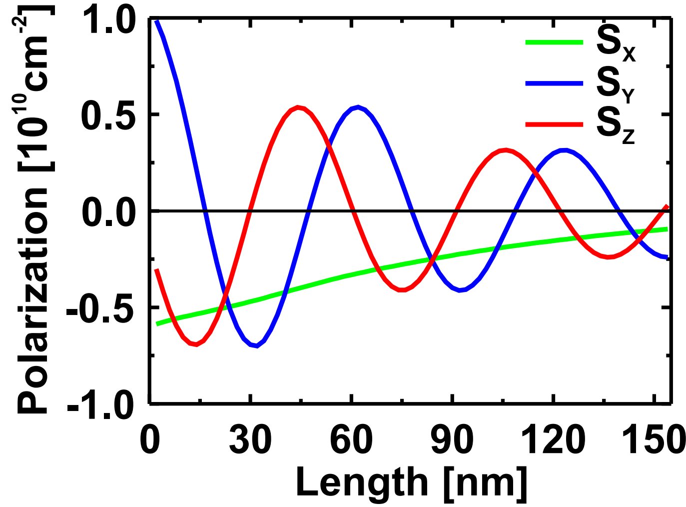

Figure 8.6.: Spin densities as in Fig. 8.5 averaged over the vertical cross section of the right horizontal bar of the structure as a function of the length of that part.

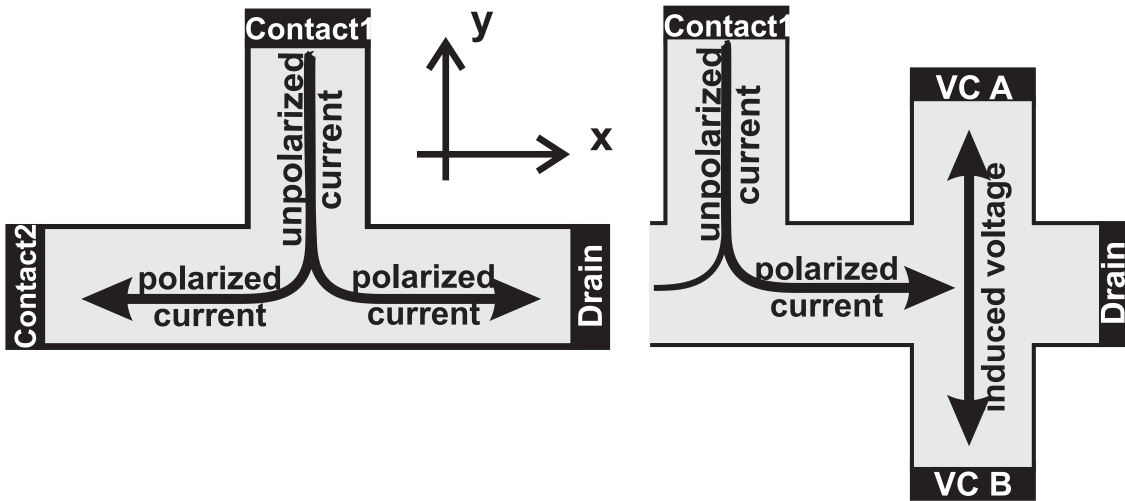

Figure 8.7.: Schematics of the structure proposed to electrically measure the current induced spin polarization. (left) Original T-shaped structure that generate spin-polarized current. (right) T-shaped structure with additional vertical bars in the right horizontal arm that act as voltage probe.

Hall voltage is shown in Fig. 8.8. The top panel shows again the out-of-plane spin polarization in the right horizontal part of the three-terminal T-shaped structure averaged over the cross section of the wire as a function of the distance from the junction with the vertical bar that acts as the source contact for an applied source drain bias of $V_{\mathrm{SD}} = 1.0\,\mathrm{mV}$. In the bottom panel, we plot the induced spin-Hall

voltage as a function of the position of the attached voltage probes relative to the source contact. The schematic drawings on the right side of the figure, illustrate the various positions of the spin-analyzing probes. We find a maximum induced voltage of $V_{AB} \approx 20\,\mu\mathrm{V}$ when the probe is attached at a 45 nm distance from the junction. That corresponds to a spin-Hall resistance, i.e. the absolute value of induced voltage divided by the source drain current $R^{sH} = |V_{AB}|/I_{\mathrm{SD}}$ of $R^{sH} = .96\,\mathrm{k}\Omega$. At a distance of 75 nm, we get an induced voltage of $V_{AB} \approx -15.6\,\mu\mathrm{V}$, that corresponds to a spin-Hall resistance of $R^{sH} = .74\,\mathrm{k}\Omega$. The magnitude of the induced voltage decreases compared to the maximum voltage as does the out-of-plane spin polarization due to the phase breaking inelastic scattering. Note that the distance between the extrema agrees exactly with the spin-precession length.

We note that the detection scheme does not work if more than one sublevel contribute to the transport due to the same reasons as explained in Sec. 8.2 for the H-shaped structure. This fact effectively limits the possible charge carrier density to very low values. A similar scheme based on a conductance measurement rather than the measurement of dc-voltage, has been proposed for a cascade of two Y-shaped structures gate defined in an InAs quantum well [210]. Recently, this proposal has been successfully realized experimentally [204].

8.5. Summary

In this chapter, we have studied and proposed nanostructered devices based on tensile strained p-GaAs. We predict a giant intrinsic spin-Hall effect due to the strain enhanced Dresselhaus spin-orbit coupling in this material. In particular, we have studied an H-bar structure, that electrically measures pure spin currents employing the intrinsic inverse spin-Hall effect. We predict a large spin-Hall resistance of up to $3\,\mathrm{k}\Omega$. We have propose a very efficient spin polarizer based on a three-terminal T-shaped structure. We have demonstrated, that the spin polarization can be measured by a dc-voltage drop induced between additional probe contacts, that we have added to the T-shaped structure. We predict a spin-Hall resistance in this structures of up to $1\,\mathrm{k}\Omega$. Both detection schemes, for the pure spin current in the H-bar structure as well as for the spin-polarized currents in the T-shaped structure measure the spin signal unambiguously only if only the lowest conducting sublevel in the structure is occupied. This requirement limits the carrier density at which the experiments can be performed to very low values.

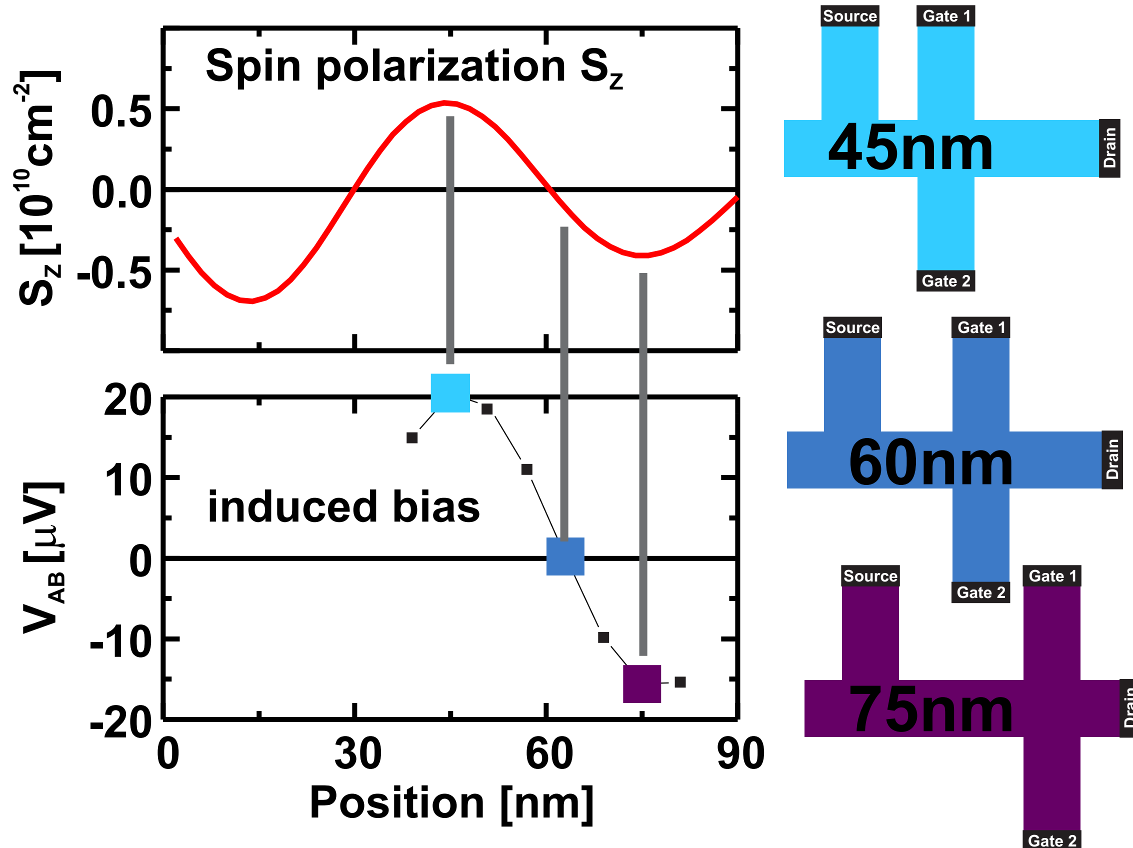

Figure 8.8.: (top) Out-of-plane component of the spin polarization S_z as in Fig. 8.6. (bottom) Induced spin-Hall voltage V_{AB} between the two additional probe contacts as a function of their position along the right bar of the T-structure.

9. Prediction of an all electrical tunable spin polarizer in InSb quantum wells

9.1. Introduction

The success of modern semiconductor spintronics depends on the realization of working devices. In particular the well controlled injection, manipulation, and detection of spin currents are important prerequisites for applications in information processing or quantum computing. For the injection of spin polarization one can use ferromagnetic metals. However, the conduction mismatch between the metal and the semiconductor hampers an efficient injection [211]. Spin manipulation by external magnetic fields is spatially not well controlled and hard to integrate into modern semiconductor electronics due to the large spatial extent of the fields. For the detection of spin polarization optical means, as the Kerr or Farrady rotation have been used successfully [182]. However, optical techniques only offer a spatial resolution on the μm scale and are thus not suitable for the intrinsic spin-Hall effect, where a resolution on the nm scale is needed. Thus, functional spintronic devices, on an all semiconductor basis, that inject, manipulate, and detect spin currents and spin polarization and work without external magnetic fields are highly desirable.

Since InSb quantum wells exhibit a large Dresselhaus spin-orbit coupling constant and an excellent tunability of the Rashba parameter by an external gate voltage as we have shown in Sec. 3.3, it is a very promising material system for spintronic applications [212–214]. In this chapter, we propose a concrete all semiconductor based nanostructure, that spin-polarizes the charge current, allows for an easy manipulation of the magnitude and sign of the spin polarization, and detects the spin current by a simple dc-voltage measurement. In particular, we present a systematic study of gate defined nanostructures in n-InSb quantum wells. We show results for a T-shaped three terminal device, similar to the one proposed in Sec. 8.3. We predict that the out-of-plane spin polarization S_z in these structures can be completely controlled all electrically simply by the applied bias. The detection of the spin polarization is based on the inverse intrinsic spin-Hall effect as in Sec. 8.4.

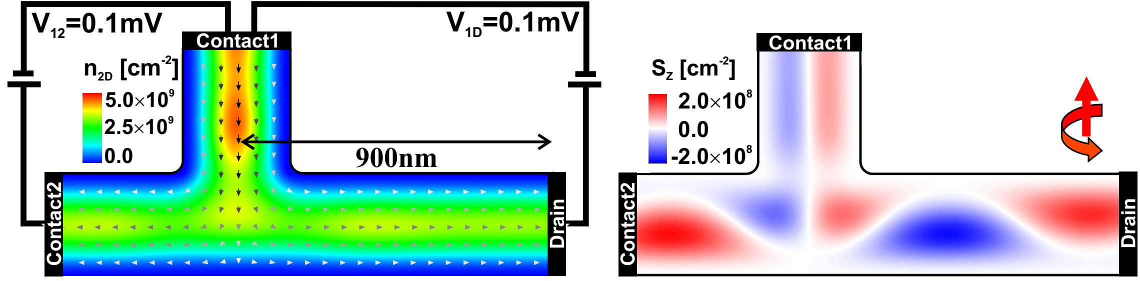

Figure 9.1.: Contour plots of the two-dimensional local electron density n_{2D} (left) and out-of-plane spin polarization S_z (right) for the gate (not shown) defined T-shaped structure in a 10 nm wide InSb/In$_{.8}$Al$_{.2}$As quantum well. A bias .1 mV is applied in such a way, that carriers propagate from Contact 1 to the Drain and Contact 2, as is shown by the gray scale arrows (arbitrary units), depicting the calculated charge current. The total charge current at the drain amounts to $I_D = 2.7$ nm. The polarization at the Drain is positive or up, as illustrated by the spin symbol.

9.2. Bias controlled spin polarization in InSb quantum wells

We present results for a 10 nm wide InSb/In$_{.8}$Al$_{.2}$As quantum well. The electron sheet density is $n_{2D} = 2 \times 10^9\,\text{cm}^{-2}$ at a temperature of $T = .1\,\text{K}$ such that only the lowest conduction subband in the gate-defined quantum wires is occupied. We model scattering by spin-independent Büttiker probes which are phase breaking and energy relaxing. We assume a mean free path of 1 μm.

In Fig. 9.1 (left), we show a top view of the nanostructure. The cross section of the gate defined wires is taken to be 300 nm which is on the order of the calculated spin-precession length which amounts to 400 nm in this quantum well. The local electron density is given as a contour plot. A bias is applied between the top contact called “Contact 1” and the two bottom contacts of the horizontal arm at the left called “Contact 2” and at the right called “Drain” in such a way, that current flows from Contact 1 to Contact 2 and to the Drain. In particular, we apply a bias of $V_{12} = .1\,\text{mV}$ between Contact 1 and Contact 2 as well as between Contact 1 and the Drain $V_{1\text{D}} = .1\,\text{mV}$ that drives a current of $I_{1\text{D}} = 2.7\,\text{nA}$. The gray scale arrows depict the local charge current density for that bias configuration. The darker the arrow, the larger the local current at this point. We want to focus on the out-of-plane spin polarization S_z at the Drain. Fig. 9.1 (right) shows a contour plot of the locally resolved spin polarization S_z. As already described in Sec. 8.4, the spin-Hall effect separates the spins of the injected electrons in the vertical bar, in such a way, that spin-up electrons accumulate at the right side of the wire while spin-down electrons accumulate at the left. At the junction with the horizontal arm, this separation leads to an injection of spin-polarized current into the horizontal

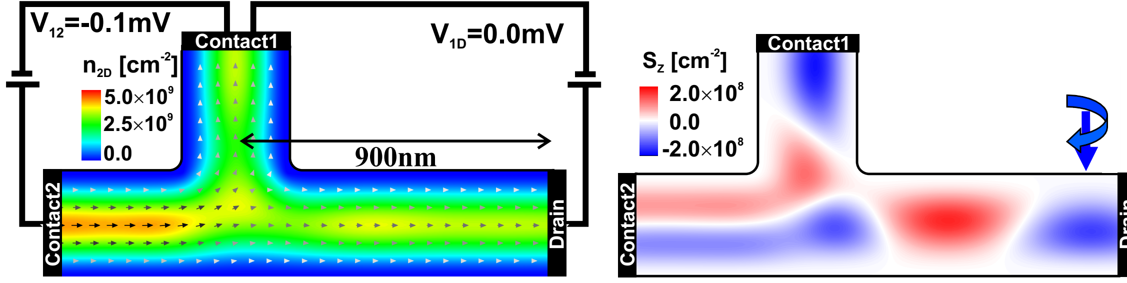

Figure 9.2.: Contour plots of the two-dimensional local electron density n_{2D} (left) and out-of-plane spin polarization S_z (right) for the gate (not shown) defined T-shaped structure in a 10 nm wide InSb/In$_{.8}$Al$_{.2}$As quantum well. A bias .1 mV is applied in such a way, that carriers propagate from Contact 2 to the Drain and Contact 1, as is shown by the gray scale arrows (arbitrary units), depicting the calculated charge current. The total charge current at the drain amounts to $I_D = 2.7$ nm. The polarization at the Drain is negative or down, as illustrated by the spin symbol.

part of the structure. In particular, a spin-up polarized current is injected into the right arm. The spin of this current precesses along the wire due the spin-orbit field, as is shown by the oscillating spin polarization S_z. The period of the oscillation agrees with the spin-precession length. We have chosen the length of the right arm commensurate with the spin-precession length in such away, that the polarization has a positive maximum at the Drain. We find, that approximately 5% of the total density is spin polarized.

In Fig. 9.2 (left) the bias configuration for the structure is changed, in such a way, that the carriers are injected through Contact 2 and propagate to Contact 1 and the Drain, as depicted by the calculated current density shown again as gray scale arrows. In particular, we apply a bias of $V_{12} = -.1$ mV between the Contact 1 and Contact 2 and keep the Drain on the same potential as Contact 1 $V_{1\mathrm{D}} = 0$ mV. All other properties of the structure are kept as in Fig. 9.1. The resulting out-of-plane spin polarization S_z is shown in the right panel of Fig. 9.2. We find a negative value with same magnitude as for the bias configuration considered before. The reason is, that carriers injected form the left Contact 2 are again subject to the spin-Hall effect, that now leads to an accumulation of spin-up at the top barrier and spin-down at the lower barrier of the left arm. At the junction with the vertical bar, a spin-up polarized current is injected into the vertical bar, while the current injected into the right part is spin-down polarized. At the Drain, the spin has precessed by 2π, such that a negatively polarized current arrives at the Drain. The spin polarization at the Drain has thus been changed from a large positive value to a large negative value simply by changing the bias configuration between the three contacts of the structure. Note that, any desired value between the two extrema can also be reached by appropriately biasing the structure as will be shown in detail in the next section.

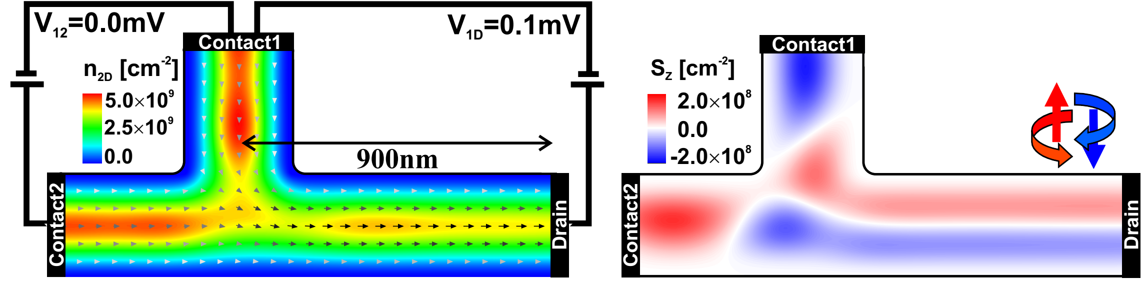

Figure 9.3.: Contour plots of the two-dimensional local electron density n_{2D} (left) and out-of-plane spin polarization S_z (right) for the gate (not shown) defined T-shaped structure in a 10 nm wide InSb/In$_{.8}$Al$_{.2}$As quantum well. A bias .1 mV is applied in such a way, that carriers propagate from Contact 1 and Contact 2 to the Drain, as is shown by the gray scale arrows (arbitrary units), depicting the calculated charge current. The total charge current at the drain amounts to $I_D = 5.4$ nm. There is no net polarization at the Drain, as illustrated by the spin symbols.

Here, we just want to show the case of zero net spin polarization at the Drain, as depicted in Fig. 9.3. The bias is applied such that carriers propagate from Contact 1 and Contact 2 to the Drain. In particular, we apply a bias of $V_{1\mathrm{D}} = .1$ mV between Contact 1 and the Drain while Contact 1 and Contact 2 are kept on the same potential $V_{12} = 0$ mV. We find that the two effects described above exactly cancel each other. The carriers in the right arm now show the accumulation of the spin, expected for the spin-Hall effect. However, integrated over the wire cross section, the total out-of-plane spin polarization amounts to zero. Note that the current injected into the structure through Contact 1 and Conact 2 is not spin-polarized. The finite spin polarization, in the vertical arm, that can be seen in Fig. 9.3 (right) is caused by carriers originating from the left Contact 2. While the polarization in the left arm is caused by carriers originating from the top Contact 1. Although both contacts possess the same chemical potential and thus no net charge current flows between them, there is a finite, precessing spin current that flows between Contact 1 to Contact 2. In this sense this spin current is pure, i.e. not accompanied by a net charge current.

9.3. Electrical detection of spin polarization in InSb quantum wells

In this section, we show, that the generated spin polarization in the T-shaped nanostructure presented in the last section can be probed by a simple voltage measurement. To this end, we study a device geometry as in Sec. 8.4 depicted schematically in the right panel of Fig. 8.7, i.e. we add two analyzing vertical probes into the right horizontal arm of the T-shaped structure at a distance of $2\lambda_{\mathrm{SO}} \approx 800$ nm from the

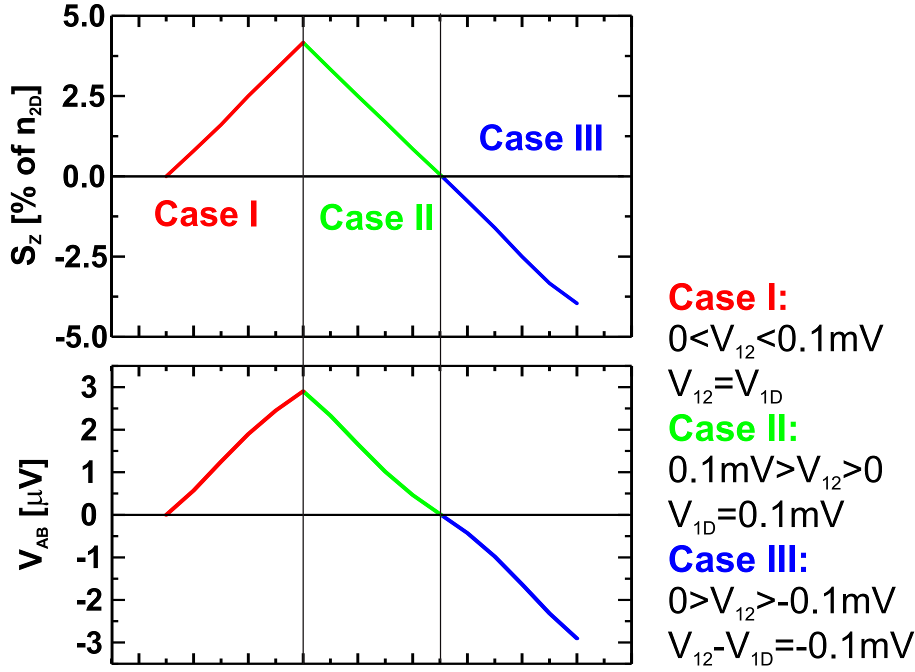

Figure 9.4.: (top) Relative out-of-plane spin polarization S_z at the Drain of the T-shaped structure (see Figs. (9.1, 9.2, 9.3)) as a function of applied bias for the three cases of bias configuration as given to the right of the figure. (bottom) Resulting induced spin-Hall voltage V_{AB} between the two additional probe contacts.

junction of the T-shaped structure, that convert the polarization at this point into an electrical voltage. The induced voltage is directly proportional to the out-of-plane spin polarization. As shown in the previous section this spin polarization can be tuned by appropriately biasing the structure.

In Fig. 9.4 (top), we plot the spin polarization in the T-shaped structure at the position of the attached probes, averaged over the cross section of the wire. The different colors mark the various bias configurations. For the red line, called "Case I" in the figure, we start from zero bias and increase the bias between Contact 1 and Contact 2 to $V_{12} = .1\,\text{mV}$. The bias between Contact 1 and the Drain is also increased such that $V_{12} = V_{1\text{D}}$. We find that the spin polarization increases proportional to the bias. For the green line, called "Case II" in the figure, we thus start with $V_{12} = V_{1\text{D}} = .1\,\text{mV}$. We then keep $V_{1\text{D}}$ fixed and reduce V_{12} to zero. The spin polarization is found to linearly decrease with V_{12}. For the blue line, called "Case III", we have the following initial situation: $V_{1\text{D}} = .1\,\text{mV}$ and $V_{12} = 0\,\text{mV}$. We then decrease both biases simultaneously, such that in the end we reach $V_{1\text{D}} = 0\,\text{mV}$ and $V_{12} = -.1\,\text{mV}$. The magnitude of the spin polarization rises again reaching the same value as in Case I, but with a negative sign. Thus, we find that the spin polarization can be continuously tuned to any desired value by the appropriate bias configuration.

Finally, in Fig. 9.4 (bottom), we plot the calculated induced voltage between the probe contacts. We find that the voltage signal is proportional to the out-of-plane spin polarization and thus depends accordingly on the bias configuration. The maximum spin-Hall resistance, i.e. the induced voltage divided by the Drain charge current amounts to $R^{sH} = 1.1\,\mathrm{k}\Omega$.

Please note, that the detection scheme fails, if more than one wire sublevel is occupied. In this case ballistic effects as described in Sec. 8.2 generate a voltage signal independent of the spin polarization that is superimposed on the voltage generated by the inverse intrinsic spin-Hall effect. The signal in this case does not follow the predicted bias dependence for the spin effect. However, it is unfortunately not possible to distinguish between both effects. Thus, the experiment has to be performed with very low charge and current densities. In Sec. 10.6, we propose a structure, based on the quantum spin Hall effect, that is more robust and allows for higher densities.

9.4. Summary

In this chapter, we have proposed an all semiconductor three terminal device, based on InSb quantum wells, that generates spin-polarized currents without external magnetic field or ferromagnetic elements by utilizing the intrinsic spin-Hall effect. The spin polarization can be tuned to any desired value by the appropriate bias configuration between the three contacts. We have further shown, that the generated spin polarization can be probed by measuring a dc-voltage between two additional voltage probes, that are added to the structure. The signal is generated by the inverse intrinsic spin-Hall effect. We predict a spin-Hall resistance of $1.1\,\mathrm{k}\Omega$. Since the detection scheme requires, that only the lowest sublevel contributes to the transport, the experiment is limited to low densities and temperatures.

10. A new sight on topological insulators

10.1. Introduction

The prediction of the quantum spin Hall effect (QSHE) by Kane and Mele [215, 216] and independently by Bernevig and Zhang [29] has created the new and fast growing field of topological insulators, see e.g. the review papers Refs. [6–8] and references therein. This new field has triggered a lot of work both theoretically and experimentally [9, 24, 72, 217] due to the possible applications in spintronic devices and quantum computing [218, 219]. Topological insulators are insulating in the bulk but metallic on the surface. By cutting out a strip from a two-dimensional (2D) topological insulator, one obtains one-dimensional (1D) edge states that form along the two boundaries [220]. These edge states are helical [75], i.e. only one spin direction is allowed to propagate within a given edge channel. Therefore, elastic back-scattering in these channels is suppressed and the conductance through these channels becomes quantized [72]. Just two years after the original prediction of this effect for graphene, the quantum spin Hall effect was predicted [23] and subsequently realized experimentally [9] in HgTe quantum wells with a so-called inverted band structure. In this context, the term inverted band structure has been introduced to indicate that the conduction band is derived form p-states and the valence band from s-states unlike to the normal situation in semiconductors. Although originally predicted for 2D systems, it has been realized later that the effect can also occur in some three-dimensional bulk insulators that support metallic states at the 2D surface [10, 221]. Since the quantum spin Hall effect was first observed in HgTe quantum wells with an inverted band structure [9], this system has become the reference system for topological insulators. The search for other topological insulators has therefore focused on materials with similar band structure properties.[52, 222–224]

The chapter is organized as follows. In Sec. 10.2, we present a simple model, which can be solved analytical, that elucidates the microscopic origin of the edge channels in topological insulators. In Sec. 10.6, we show a concrete device application of topological insulators. In particular, we propose a realization of a spin transistor in HgTe quantum wells, that utilizes the quantum spin Hall effect.

10.2. Microscopic origin of topological insulators and the quantum spin Hall effect

10.2.1. Introduction

Today, the understanding of topological insulators is predominantly based on symmetry arguments. Similar to the Chern number in the quantum Hall effect, topological insulators are characterized by a $\mathbb{Z}_2$ topological invariant [216]. While the topological distinction between topological and ordinary insulators is well understood [225–228] and it was shown [229] in terms of a continuum envelope function model for HgTe quantum wells [23] that the band inversion leads to a nontrivial $\mathbb{Z}_2$ topological index, an atomistic understanding of the underlying physics and the microscopic criteria that leads to topological insulators and the formation of edge channel formation is still incomplete.

In this section, we present criteria for a semiconductor to form a topological insulator in terms of its microscopic electronic structure and explain the atomistic origin of the edge channels in topological insulators and the quantum spin Hall effect semi-quantitatively and qualitatively. Importantly, we show that no spin-orbit coupling is needed for topological insulators to be characterized by the $\mathbb{Z}_2$ topological invariant, in contrast to what has been widely accepted and assumed [229–232].

In Sec. 2, we have developed a realistic atomistic model based on the relativistic sp^3d^5 semi-empirical tight-binding method that has been carefully adapted to reproduce the available experimental electronic structure data such as energy gaps, effective masses, spin-orbit splittings, of II-VI bulk alloys [33–36] as well as band offsets and subband structure in quantum well materials [37–41]. To elucidate the essential physics and atomistic mechanism of the quantum spin Hall effect, we have additionally developed two very simple atomistic models that capture the crucial properties of topological insulators but can be solved analytically. These models illustrate the formation of edge channels and illuminate the microscopic origin of the topological distinction from trivial insulators by the $\mathbb{Z}_2$ topological invariant. We study the influence of spin-orbit coupling on an atomistic level and find that no spin-orbit coupling is needed for topological insulators that feature gapless edge channels and are characterized by the $\mathbb{Z}_2$ topological invariant. However, in order for these edge channels to be helical, spin-orbit coupling is indeed necessary. This leads us to distinguish between topological insulators and the quantum spin Hall effect with its helical channels.

Relatively few realistic electronic structure calculations have been published for 2D topological insulators so far [75, 233]. In Ref. [75], a semi-empirical sp^3s^* tight-binding model [30] was employed to show that helical edge channels form in HgTe quantum wells with an inverted band structure despite the missing inversion symmetry. Most first-principles types of studies have focused on three-dimensional topological insulators [222–224, 229, 234, 235] and predicted topological insulators such

as Bi_2Se_3, Bi_2Te_3, Bi_xSb_{1-x} and more complicated compounds. Recently, another interesting class of three-dimensional topological insulators has been proposed and termed crystalline topological insulators [236]. In these systems, the metallic states occur at the surface if the latter preserves the C_4 symmetry of the bulk. Thus, the topological classification is based on point group symmetry arguments rather than on time reversal symmetry. In the present work, however, we focus on the standard types of topological insulators.

The chapter is organized as follows. We first present a simplified atomistic one-dimensional tight-binding model that elucidates the physical origin of the edge channel in topological insulators in Sec. 10.3. In Sec. 10.4, this model is extended to two dimensions in order to be able to explain the influence of spin-orbit interaction.

10.3. One-dimensional atomistic tight-binding model

In this section, we show that a very simple 1D atomistic tight-binding model already exhibits the $\mathbb{Z}_2$ topological invariant of topological insulators on a microscopic level even without spin-orbit interaction. Our model system (see inset of Fig. 10.1) consists of an infinite atomic chain with two atoms per unit cell of length a, one with a single s-state and the other one with a single p- state that is stretched along the chain axis. We assume half-occupancy, i.e. in the absence of any coupling, each atomic state is occupied by one electron per atom. The s-states and p-states, respectively, are coupled among themselves by a second-nearest neighbor Hamiltonian matrix element $t_{ss\sigma} = -t_{pp\sigma} = -1$ and we measure all energies in units of $t_{pp\sigma}$. This second-nearest neighbor coupling produces an energy band width of $W = 4$ for each band. This band width is a measure of the metallicity of a material, i.e. of the overlap of the atomic states forming the solid. The on-site s- and p- matrix elements are taken as $\varepsilon_s = \Delta/2\,, \varepsilon_p = -\Delta/2$, respectively, where Δ may be positive or negative. In physical terms, Δ represents an ionicity, i.e. the difference in the atomic character of anions and cations. In addition, there is a nearest neighbor coupling $t_{sp\sigma} = T$ between adjacent s and p-states. The Hamiltonian matrix in k-space reads,

$$H(k_x) = \begin{bmatrix} \Delta/2 - 2\cos 2\pi k & 2iT\sin\pi k \\ -2iT\sin\pi k & -\Delta/2 + 2\cos 2\pi k \end{bmatrix}. \tag{10.1}$$

where the electron momentum $k \in (-1/2, 1/2]$ is given in units of $2\pi/a$. The eigenvalues E_k of $H(k)$ are given by

$$E_k^{\pm} = \pm\frac{1}{2}\left[(\Delta - 4\cos 2\pi k)^2 + 16T^2\sin^2\pi k\right]^{1/2}. \tag{10.2}$$

We first discuss the case for zero nearest-neighbor coupling, $T = 0$. In this case, the s- and p-bands are independent of each other and have a width equal to $W = 4$ each. Depending on the ratio Δ/W, i.e. the ratio of ionicity and metallicity, this model

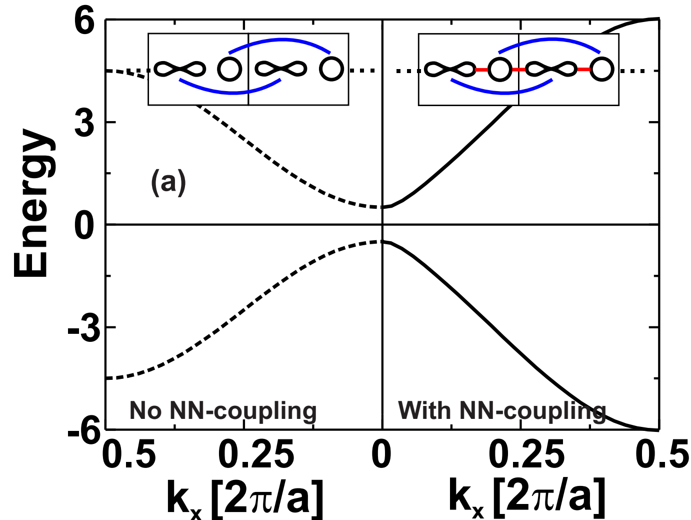

Figure 10.1.: Dispersion of the 1D atomistic tight-binding model for the case of normal band alignment for $\Delta = 5$ The dashed lines (left side) show the case of zero nearest-neighbor interaction T, while T is nonzero ($T = 2$) for the solid lines (right side). This difference is illustrated schematically by the inset showing the sites with uncoupled and coupled s and p orbitals, respectively.

yields three different types of band structures. The first type resembles the common type of bandstructure in semiconductor heterostructures and superlattices with an s- derived conduction band and a p- derived valence band. We term this situation *normal band alignment* and define it by the condition $\Delta > W$. In this case, a finite energy gap separates the filled valence band from the empty conduction band with the Fermi energy lying in the middle of the gap. The system is insulating at zero temperature and the band structure is shown in the left part of Fig. 10.1 The second type, that we call *inverted band alignment*, is defined by the condition $-W < \Delta < W$. In this case, the two bands intersect each other within the Brillouin zone. Thus, no energy gap is formed, the atomic character of the conduction and valence band gets switched somewhere within the Brillouin zone due to this band crossing, and the system is metallic. This situation is depicted in the left portion of Fig. 10.2. The third case, that we term *non-crossing inverted band alignment*, occurs for $\Delta < -W$. Here, the band inversion exceeds the band width. This alignment yields an insulating ground state. In contrast to the first case, however, the minimal gap lies at the edge of the Brillouin zone as shown in Fig. 10.3.

Now we turn on the nearest neighbor interaction T. This coupling affects these three band alignment cases in a radically different way. In the case of a normal band alignment, T has only a small effect as shown on the right half of Fig. 10.1. Importantly, it does not affect the minimal energy gap. In the inverted case, on the other hand, the band structure is drastically changed as shown in the right portion of Fig. 10.2. The nearest neighbor coupling T opens an energy gap so that

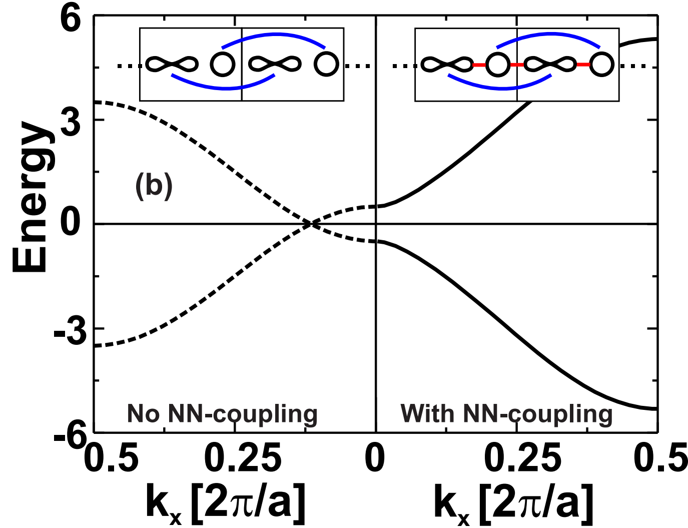

Figure 10.2.: Dispersion of the 1D atomistic tight-binding model for the case of an inverted band alignment for $\Delta = 3$. The dashed lines (left side) show the case of zero nearest-neighbor interaction T, while T is nonzero ($T = 2$) for the solid lines (right side). This difference is illustrated schematically by the inset showing the sites with uncoupled and coupled s and p orbitals, respectively.

the material becomes insulating. For small values of T, the minimal gap lies near the crossing point ($k \approx .15$ in the left part of Fig. 10.2) and switches to the center at $k = 0$ for $T \geq W/2$. This situation is closely related to the band structure of wider HgTe quantum wells which is commonly referred to as inverted band structure in the literature [37, 71]. As we will show below, this particular insulating state actually corresponds to a topological insulator. In the case of the non-crossing inverted band structure, the effect of T is less drastic but the nearest-neighbor coupling increases the minimal energy gap significantly as well. Valence and conduction band exhibit a weakly avoided crossing behavior so that the minimal gap lies in the interior of the Brillouin zone.

We now consider an extended but finite system with boundaries. To this end, we terminate the atomic chain on one end at a site s_{boundary} and on the opposite side at a site p_{boundary}. This produces a dangling s-bond and p-bond at the corresponding chain ends, respectively. We assume the boundaries to lie sufficiently far apart from each other that they do not influence each other. As we will now show, terminated bonds will induce bound states within the energy gap if and only if the band alignments are inverted, irrespective of any detailed parameters, and irrespective of how we terminate the chain. Mathematically, the simplest way to calculate the eigenstates of a solid with boundaries is to start from the infinite system that can be described by the Green's function matrix $G_{ij}(E)$ with i, j labeling the atomic sites, and to describe the boundaries by a localized defect matrix V_{ij}. Cutting all bonds

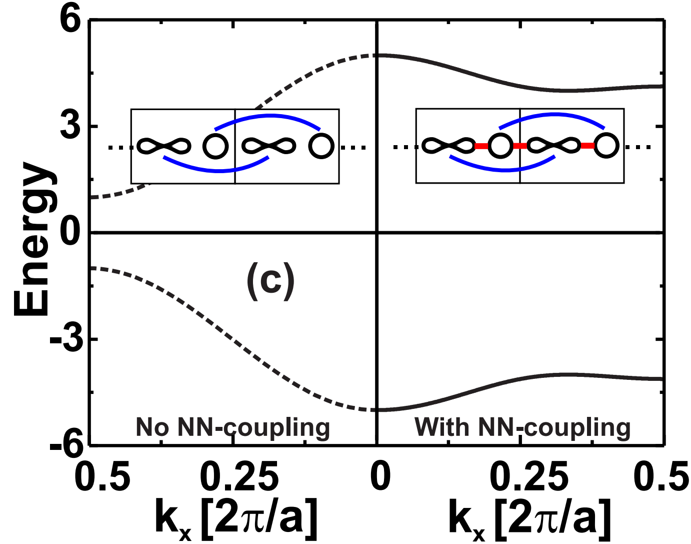

Figure 10.3.: Dispersion of the 1D tight-binding model for the case of non-crossing inverted band alignment with $\Delta = -6$. The dashed lines (left side) show the case of zero NN interaction $T = 0$, while for the solid lines (right side) $T = 2$. Each inset shows a schematic picture of the corresponding tight binding model.

between two adjacent sites is equivalent of letting the last chain-sided on-site energy ε_b tend to plus or minus infinity which implies $1/V_{bb} \to 0$ [237, 238]. Therefore, the eigenstates of the chain with a single s-type dangling bond on one end follow from

$$G_{ss}(E) = \sum_{k,n} \frac{|\langle s_{\text{boundary}}|\psi_n(k)\rangle|^2}{E - E_n(k)} = 0, \tag{10.3}$$

where $E_{k,n}$ and $\psi_{k,n}$ are the Bloch eigenstates of the infinite chain. With two surfaces, one s-type and the other one p-type dangling bond, the eigenstate energies follow from the equation

$$G_{ss}(E)G_{pp}(E) = \sum_{k,n} \frac{|\langle s_{\text{boundary}}|\psi_n(k)\rangle|^2}{E - E_n(k)} \sum_{k,n} \frac{|\langle p_{\text{boundary}}|\psi_n(k)\rangle|^2}{E - E_n(k)} = 0. \tag{10.4}$$

For the tight-binding model at hand, one can show analytically (see Appendix A) that this equation yields exactly two eigenstates E that lie within the energy gap if and only if the band alignment is inverted (crossing or non-crossing). In Fig. 10.4, we show the two bound states for the inverted band alignment with $\Delta = 0$ as a function of the nearest neighbor coupling T, together with the square of one bound state wave function in the inset. Note that the energy gap increases with T itself but we have normalized the vertical axis to the minimal energy gap. These results can be explained in a physically transparent way. The characteristic property of the inverted band alignments lies in the effect of the nearest neighbor coupling T. Only

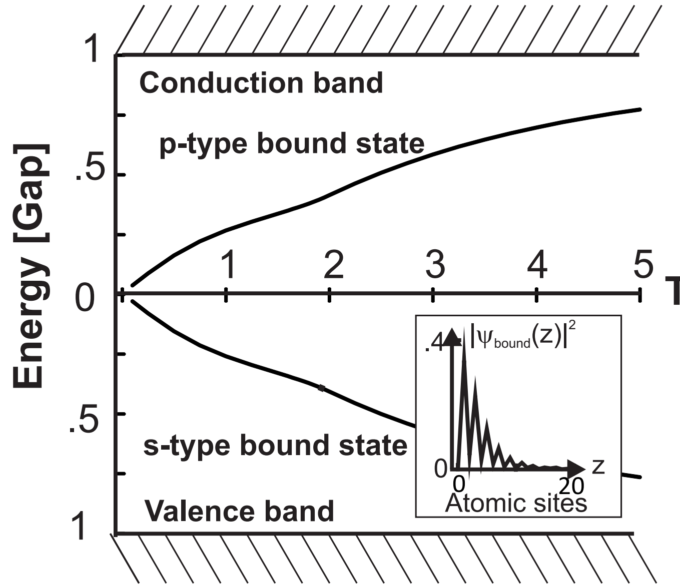

Figure 10.4.: Calculated energies of the bound states within the energy gap in the case of an inverted band structure ($\Delta = 0$) as a function of the nearest-neighbor interaction T. The inset shows the absolute square of the p-type edge state's wave function for $T = 5$. The energy scale is normalized to the energy gap for given T.

for the two inverted band cases, T increases the minimal energy gap. This essential physics can be captured by a simplified k-independent version of the Hamiltonian Eq. (10.1),

$$H_{mol} = \frac{1}{2} \begin{bmatrix} \Delta - W & 2iT \\ -2iT & -\Delta + W \end{bmatrix}. \tag{10.5}$$

This is the Hamiltonian of a molecule with basis states $\pm D$, where $D = \Delta - W$. Note that $D < 0$ for inverted band alignment and $D > 0$ otherwise. As indicated by the schematic drawing in Fig. 10.5, the nearest neighbor coupling T increases the energy gap for the inverted band alignments. Therefore, cutting the bonds leads to dangling bond states at the surface that lie within the energy gap. By contrast, T does not increase the energy gap for normal band alignment. Correspondingly, the dangling bond states at the surface do not lie within the energy gap (cf. Fig. 10.6) for normal band situations.

10.3.1. Topological quantum number

We now proceed by proofing that the present atomistic 1D model is indeed a topological insulator based on the symmetry arguments that discriminate topological from normal ("trivial") insulators [216, 225, 226]. In particular, we focus on the $\mathbb{Z}_2$ topological index I introduced by Kane and Mele [216]. The topological invariant I can be constructed form the time reversal properties of the Bloch wave functions of

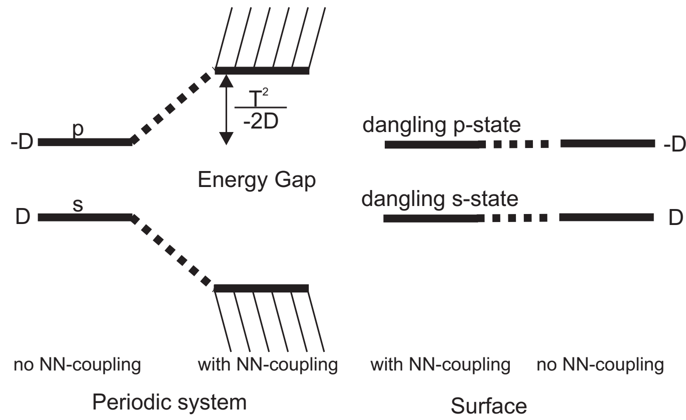

Figure 10.5.: Schematic band diagram for the inverted band alignment. The nearest-neighbor interaction leads to a bonding-antibonding splitting that increases the energy gap. The energies of the dangling bonds at the surface fall within the energy gap.

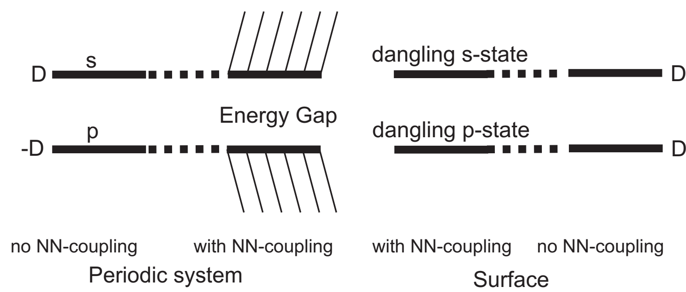

Figure 10.6.: Schematic band diagram for the normal band alignment. In this case, the nearest-neighbor interaction does not affect the energy gap. Therefore, no gap states occur.

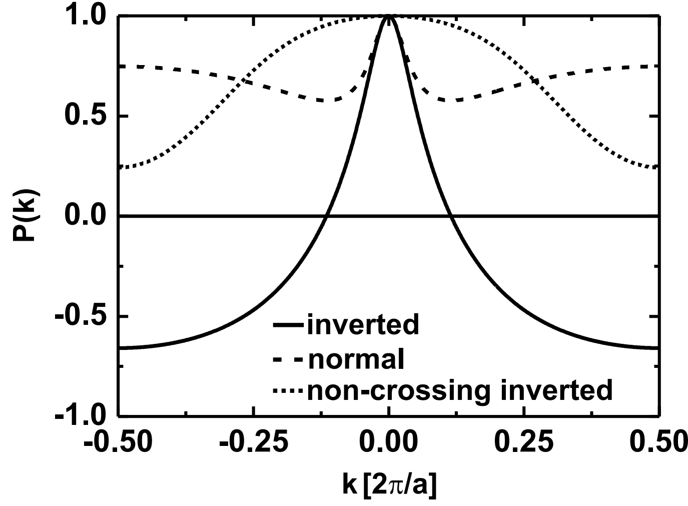

Figure 10.7.: Pfaffian $P(k)$ for normal (dashed line, for $\Delta = 5$), inverted (solid line, for $\Delta = 3$), and non-crossing inverted (dotted line, for $\Delta = -6$) band alignment, respectively. In all cases, the nearest-neighbor coupling is set to $T = 2$.

the bulk Hamiltonian. Applied to the present 1D model, this invariant is given by the closed loop integral,

$$I = \frac{1}{2\pi i} \oint \mathrm{d}z \left\{ \frac{\mathrm{d}}{\mathrm{d}z} \log\left[P(z)\right] \right\} \tag{10.6}$$

where z is the complex extension of the wave number k. The closed path encircles the real axis between $k = 0$ and $k = \pi/a$ (i.e. for half of the Brillouin zone) infinitesimally above and below the real axis. The generally complex function $P(k)$ is given by the Pfaffian of the time reversal operator Θ represented in the basis of the occupied (valence) periodic part u_v of the Bloch wave functions $\psi_v(k; z) = \exp(ikz)u_v(k; z)$ [216]. In the present case without spin-orbit interaction and with a single valence band, the valence Bloch function is a product of spatial and spin functions, $|u_v(\mathbf{k})\rangle|\chi_\sigma\rangle$, so that we obtain

$$P(k) = \mathrm{Pf}[\langle\chi_\sigma|\langle u_v(k)|\Theta\,|u_v(k)\rangle|\chi_{\sigma'}\rangle] = \mathrm{Pf}[\langle u_v(k)|\langle\chi_\sigma|\,i\sigma^y\,|u_v^*(k)\rangle|\chi_{\sigma'}\rangle] = [u_v^*(k)]^2 \tag{10.7}$$

where σ^y denotes the standard Pauli matrix. The number of zeros of $P(k)$ is a $\mathbb{Z}_2$ topological invariant. Due to time reversal symmetry, these zeros occur in pairs at $\pm k_0$. In fact, the path integral in Eq. (10.6) counts the number of zeros in one half of the Brillouin zone. For ordinary insulators $I = 0$ holds, whereas topological insulators have $I = 1$. In the present case, $P(k)$ turns out to be real and is depicted in Fig. 10.7 for the three types of band alignments.

We find no zeros for the normal and non-crossing inverted band alignment which results in $I = 0$. By contrast, the inverted alignment yields $I = 1$ corresponding to

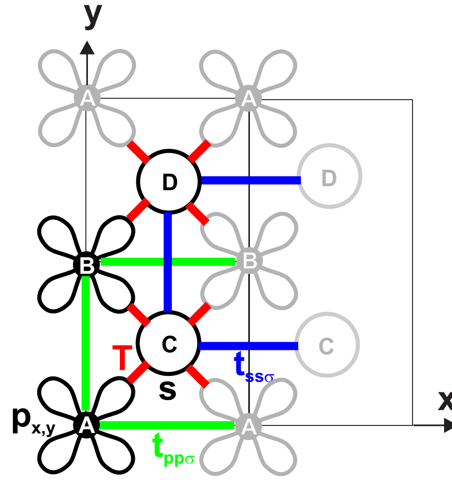

Figure 10.8.: Primitive unit cell with atomic character of the 4 atoms and symmetry of tight-binding matrix elements for the 2D tight-binding model. Atoms that do not belong to the unit cell are grayed out.

a topological insulator. These zeros in $P(k)$ occur exactly at the k-points where the bands cross when we set $T = 0$, as shown in the left part of Fig. 10.2. Thus, we have constructed a simple 1D tight-binding model without spin-orbit coupling, that has the required symmetry properties for topological insulators and shows states in the energy gap, provided the system is terminated by one or two surfaces.

10.4. Two-dimensional tight-binding model

In this section, we extend the model from the previous section to a situation where we can add a spin-orbit interaction to make contact with the conventional understanding of topological insulators. This requires an extension of the model to two dimensions. The atomistic 2D tight binding model that we have constructed is schematically shown in Fig. 10.8. We consider a rectangular unit cell containing 4 atoms with a total of 8 electrons. The atoms of type A and B each carry two fully occupied p_x and p_y states, whereas atoms C and D each contain an empty s-state. We take into account nearest and second-nearest neighbor interaction and employ the usual two-center approximation. The included matrix elements are indicated in Fig. 10.8. Concretely, we set $t_{pp\pi} = 0, t_{ss\sigma} = -1, T = t_{sp\sigma} = 2$, in units of the matrix element $t_{pp\sigma}$. Additionally, we define the on-site matrix elements in such a way that one obtains an inverted band alignment with band crossing when the nearest neighbor coupling T is set equal to zero. This can be achieved by the values $\varepsilon_{sC} = \varepsilon_{p_xA} = 3.5$, $\varepsilon_{p_yA} = -2.5$, $\varepsilon_{sD} = \varepsilon_{p_xB} = 0.5$, $\varepsilon_{p_yA} = -5.5$. The s-states form the conduction bands, the p_x- states the top valence bands, and the p_y-states low lying valence bands. In the empirical tight binding framework, the spin-orbit interaction can be incorporated by adding an intra-atomic Hamiltonian matrix element

between p-states [22]. This adds the following k-independent Hamiltonian matrix elements,

$$\langle p_{x,A}\uparrow| H |p_{y,A}\uparrow\rangle = \langle p_{x,B}\uparrow| H |p_{y,B}\uparrow\rangle = i\Delta_{\mathrm{SO}}, \tag{10.8}$$

$$\langle p_{x,A}\downarrow| H |p_{y,A}\downarrow\rangle = \langle p_{x,B}\downarrow| H |p_{y,B}\downarrow\rangle = -\, i\Delta_{\mathrm{SO}}. \tag{10.9}$$

These equations complete the definition of the Hamiltonian matrix.

10.4.1. Model without spin-orbit interaction

As a first step, we investigate the eigenstates for zero spin-orbit coupling. Without the NN interaction (i.e. for $T = 0$), we obtain two overlapping bands, one derived from the p_x-derived upper valence bands and the other one from the s-type conduction bands. Due to the band crossing, the system is metallic with a half filled band, just as in the 1D case. Once we turn on the nearest-neighbor interaction $T \neq 0$, the band degeneracy of the crossing bands is lifted throughout the Brillouin zone and the system becomes insulating in the 2D bulk. In order to investigate the symmetry of this system, we calculate the $\mathbb{Z}_2$ topological index I. In the present 2D case, I follows from the two-dimensional closed path integral

$$I = \frac{1}{2\pi i} \oint \mathrm{d}\mathbf{k} \cdot \boldsymbol{\nabla}_{\mathbf{k}} \log P(\mathbf{k}), \tag{10.10}$$

where the path encircles the boundary of one half of the rectangular Brillouin zone. The determination of the Pfaffian $P(\mathbf{k})$ is analogous to Eq. (10.7) but requires the calculation of the square root of an 8×8 determinant, since the 2D Hamiltonian yields 4 doubly degenerate valence bands instead of only 1 valence band as in the 1D model. The Pfaffian remains nonzero on the entire path in $\mathbf{k}$-space so that the integration variable remains real, but the determinant and its square root is complex in the present case. The absolute value of $P(\mathbf{k})$ is shown as a function of $\mathbf{k} = (k_x, k_y)$ for the entire Brillouin zone in Fig. 10.9 on a logarithmic scale. The function possesses only a single pair of zeros, one lying in a narrow region close to $\mathbf{k} \approx (.1, -.4)$ and the other one near $\mathbf{k} \approx (-.1, .4)$. We have evaluated the winding of the phase of $P(\mathbf{k})$ along the closed path and find a winding of 2π and thus a topological index $I = 1$ in Eq. (10.10). Thus, the system forms a topological insulator [216].

In order to illustrate the consequences of this symmetry, we cut out a wire from the bulk 2D structure that has finite width along the x-direction and extends infinitely along the y-direction. Thus, all bonds along the two rims of the wire are cut and we obtain a 1D chain of dangling bonds on each side of the wire. This system retains its Bloch symmetry in reciprocal space only along the k_y-direction, whereas the states along the former k_x-direction become folded up. We set a sufficiently wide wire width so that the left and right boundaries do not affect each other. Concretely, a width of 50 unit cells obeys this condition. Note that all states are spin degenerate due to the absence of spin-orbit coupling in this sub-section. In Fig. 10.10, we show

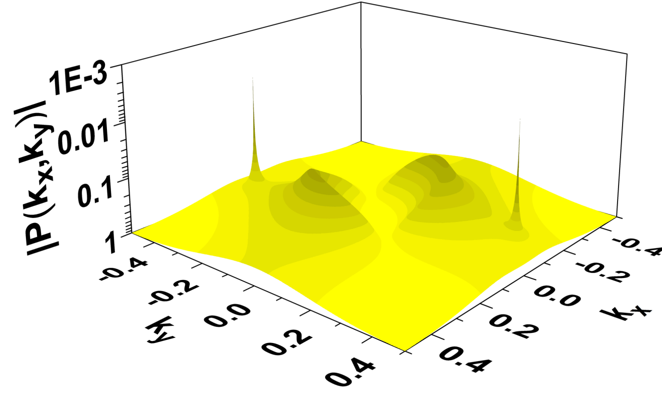

Figure 10.9.: Absolute value of Pfaffian $P(k_x, k_y)$ as a function of wave vector (in units of $2\pi/a$) for the 2D model without spin-orbit interaction. The two sharp peaks indicate zeros of the function.

the band structure of this wire as a function of the wave number k_y along the wire direction. The folded conduction band (red) and valence band states (blue) have wave functions that extend over the entire width of the wire. While the conduction and valence bands are overall dominantly s-states and p_x-states, respectively, the situation is reversed near $k_y = 0$ due to the inverted band alignment. Therefore, the conduction band edge states near the center $k_y\tilde{}0$ are dominantly p_x-states, whereas the top valence states are s-like. In analogy to the bound states that appeared within the energy gap in the 1D case due to the confinement, in 2D we obtain two energy bands that span the energy gap. Indeed, these gap bands in Fig. 10.10 are highly localized channel states along the edges of the wire. The localized gap band (shown in red) that merges the conduction bands for large wave numbers is derived from dangling s-states in accordance with the terminating atoms consisting of dangling s-states. On the opposite side of the wire, the wire ends with dangling p_x-orbitals. They yield the localized band (shown in blue) that merges into the valence bands and consists mainly of p_x-states within the energy gap. For both edge channels, the calculated dispersion resembles closely that of a 1D chain of atomic states, coupled by second-nearest neighbor interaction. Since we have a half-filled band situation, the system will thus be conducting over the whole energy range in contrast to an ordinary insulator.

10.4.2. Model with spin-orbit coupling

We now consider the same 2D system with inverted band alignment but turn on the spin-orbit coupling according to Eq. (10.8). Even for a strong spin-orbit coupling, the Pfaffian $P(\mathbf{k})$ does not change qualitatively for the 2D bulk system relative to the case of no spin-orbit coupling. Figure (10.11) depicts the modulus of the Pfaffian as a function of the wave vector $\mathbf{k}$ for a spin-orbit coupling of $\Delta_{\text{SO}} = 3$. Importantly,

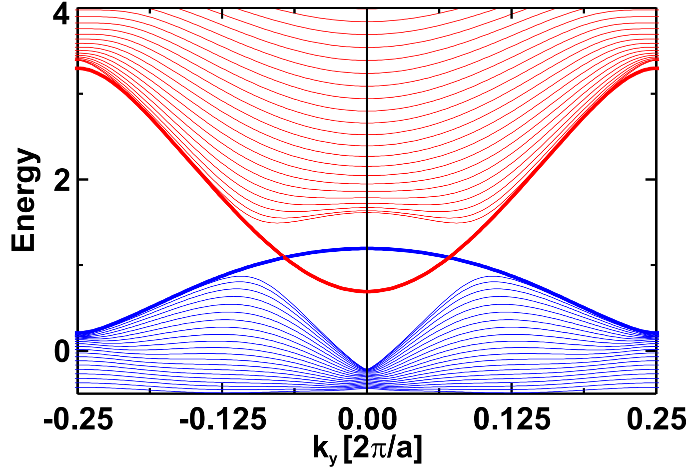

Figure 10.10.: Calculated 2D band structure as a function of wave vector for a 50 unit cell wide wire. The spin-orbit interaction is set to zero. The thin lines show the bulk conduction bands (red) and the valence bands (blue). The thick lines indicate the edge states. The lower one (blue) is a p-type state localized at the left boundary of the wire, whereas the upper one (red) is an s-type state localized at the opposite boundary.

the topological $\mathbb{Z}_2$ index remains $I = 1$ the same. We now study the bound states within the band gap that appear for the quantum wire system, but now with spin-orbit interaction turned on. For weak spin-orbit interaction, $\Delta_{\mathrm{SO}} = .5$, we find a k-linear splitting of the gap states that correspond to the edge channels that form along the surfaces, shown in Fig. 10.12. These bound states are already helical, but the separation of the two spin states within one channel in k-space is small so that, in practice, any k -mixing scattering would couple these spin channels. The spin-splitting can be attributed to the small admixture of $|p_y\rangle$- orbitals to the upper valence and conduction states. The red thick lines in Fig. 10.12 are derived from the dangling s-state channel, while the blue thick lines are formed by dangling by p-states. The spin orientations are marked by small arrows.

When the strength of the spin-orbit coupling gets increased by a factor of 6, $\Delta_{\mathrm{SO}} = 3$, the resulting edge channels are now completely helical but the character of the edge channel states in the gap changes qualitatively compared to small values of Δ_{SO}. As shown in Fig. 10.13, the dispersion of the edge channels now connects the spin states with $k_y > 0$ in the conduction band with the spin states with $k_y < 0$ in the valence band and vice versa. The physical origin of this effect stems from the interaction of the bound states with close lying continuum band states that induces a strong repulsion between same-spin bound states. To better understand this effect, let us follow the two bound states of one spin state, say spin-up, from positive values of k_y towards the center of the Brillouin zone in Fig. 10.13. They start from the conduction and valence-band, respectively, cross each other, and approach the opposite band edge in the region $k_y \gtrsim 0$. In this region, these spin-up bound states

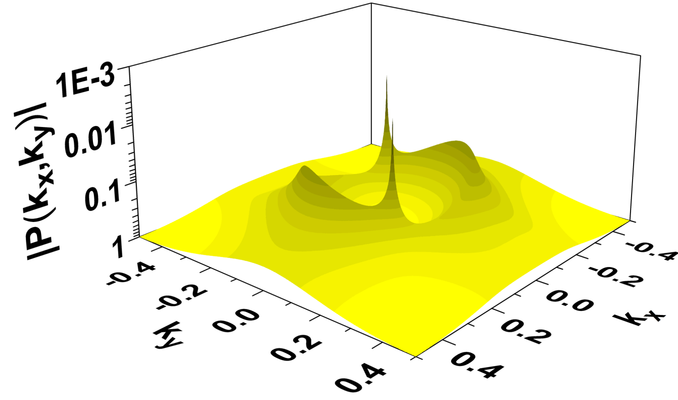

Figure 10.11.: Absolute value of Pfaffian $P(k_x, k_y)$ as a function of wave vector (in units of $2\pi/a$) for the 2D model with large spin-orbit interaction ($\Delta_{\mathrm{SO}} = 3$). The two peaks indicate zeros of the function.

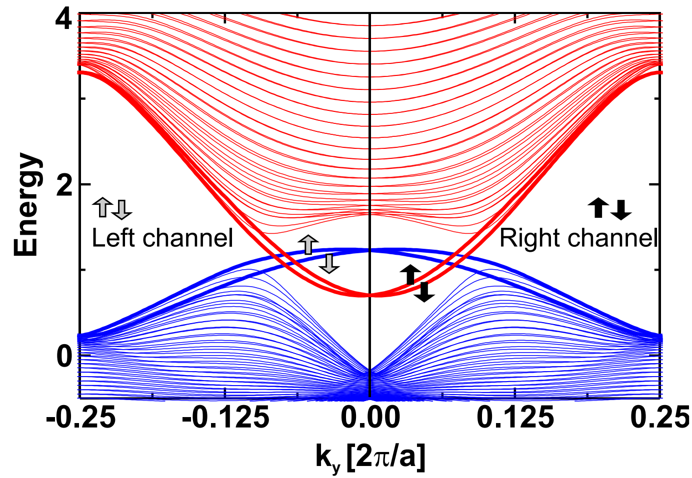

Figure 10.12.: Calculated 2D subband structure as a function of wave vector for a 50 unit cell wide wire with small spin-orbit interaction $\Delta_{\mathrm{SO}} = .5$. The thin lines show the conduction (red) and the valence bands (blue), respectively. The thick lines indicate the bound edge states in the energy gap. The lower (blue) ones are p-type states localized at the left boundary of the wire, the upper (red) one are s-type states localized at the opposite boundary. The small arrows denote the spin state and spatial location of the edge states.

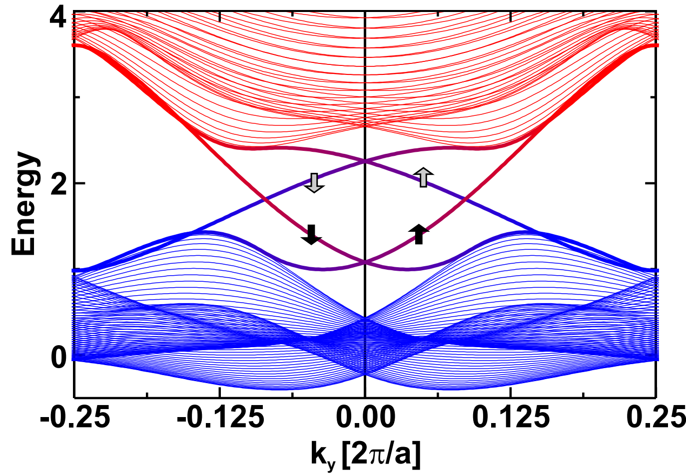

Figure 10.13.: Calculated 2D subband structure as a function of wave vector for a 50 unit cell wide wire with large spin-orbit interaction $\Delta_{SO} = 3$. The thin lines show the conduction (red) and the valence bands (blue), respectively. The thick lines indicate the bound edge states in the energy gap. The lower (blue) ones are p-type states localized at the left boundary of the wire, the upper (red) one are s-type states localized at the opposite boundary. The small arrows denote the spin state and spatial location of the edge states.

are no longer strongly localized but form hybrid states between localized surface and bulk-like spatially extended states. When we continue along the spin-up bound states towards negative values of k_y, the orthogonality of the continuum band states causes the two same-spin bound states to effectively repel each other and merge into that band they dominantly consist of. In accordance with this effect, the atomic s- and p- character of the channel states changes across the gap, and this is indicated by the color coding of the bound states in Figure 10.13.

10.5. Band inversion in real semiconductors

The crucial parameters in the two simple tight binding models of the previous sections that lead to band inversion are nearest-neighbor versus second-nearest neighbor interaction matrix elements. In a real semiconductor, the energy gap in a semiconductor arises from a competition between the bonding-antibonding splitting between anion and cation in each unit cell and the longer-range electron-ion interaction that broadens the molecular bonding and antibonding states into bands. An energy gap can occur in two situations. In an ionic material, the highest occupied atomic cation and anion valence electron energies are very different so that the gap reflects this difference in energies, reduced by the broadening of the atomic orbital energies. This situation never leads to band inversion and so we can ignore this limit. In covalent

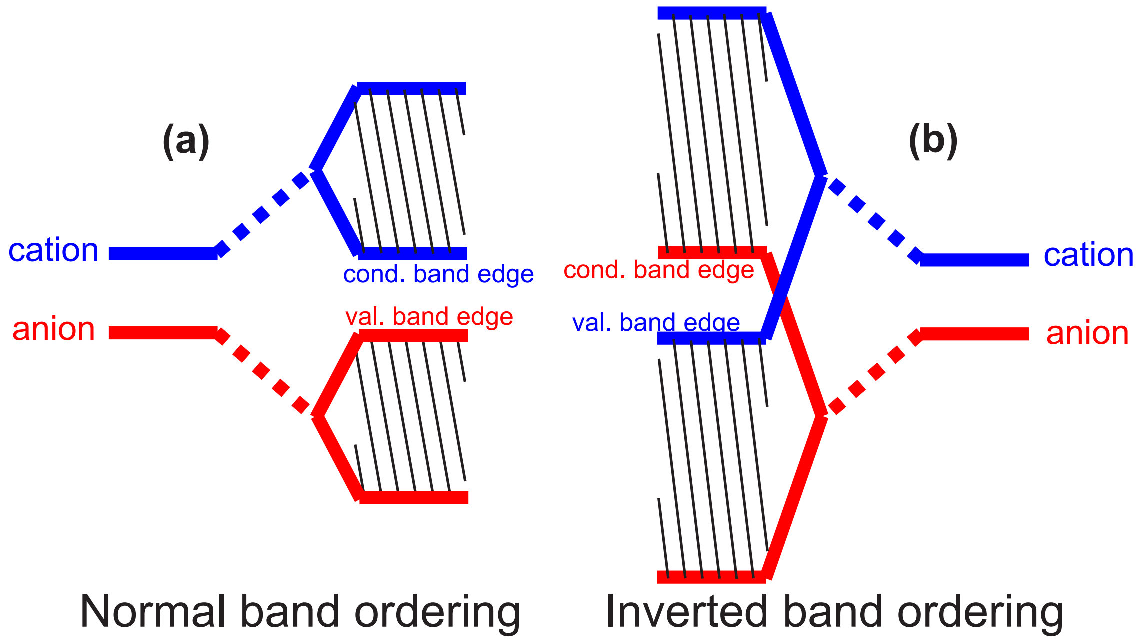

Figure 10.14.: Schematic picture of the interaction of the bonding-antibonding splitting versus the band broadening in semiconductors. (a) Normal band alignment. (b) Inverted band alignment.

semiconductors, two situations with finite energy gaps can arise that are depicted schematically in Fig. 10.14. In normal semiconductors (Fig. 10.14 (a)), the bonding-antibonding splitting between the highest occupied atomic anion states and lowest unoccupied cation states exceeds the broadening of these states by the longer-range interaction in the solid. In this case, the conduction and valence band edge is dominantly formed by the cation and anion basis states, respectively. In semiconductors with large atoms such as Sn or HgCdTe, by contrast, the large cation-anion distances lead to a smaller bonding-antibonding splitting and simultaneously to larger band widths. Such materials can either be metallic or show an inverted band structure in some portion of the Brillouin zone as indicated schematically in Fig. 10.14 (b). In this case, the atomic nature of the band edge states is inverted. This situation leads to a topological insulator. The third case that we discussed in Sec. 10.3, namely the case of a non-crossing inverted band structure, is unlikely to occur in nature. It corresponds to case Fig. 10.14 (a), but with flipped cation and anion energies.

We show now that realistic electronic structure calculations of HgTe:$Cd_{.7}Hg_{.3}Te$ heterostructures fully support the qualitative conclusions and physical insights that we have provided so far. To this end we rely on results of the electronic structure calculations presented in Chapter 4. We have seen there that for wider HgTe quantum wells with a width larger than 7 nm an inverted band structure is realized. Analogously to our 2D model, we now consider a quantum wire structure as shown schematically in Fig. 10.15 (left). The wire width has been chosen as 240 nm and the HgTe well thickness is 7.8 nm so that its band alignment is inverted. This structure

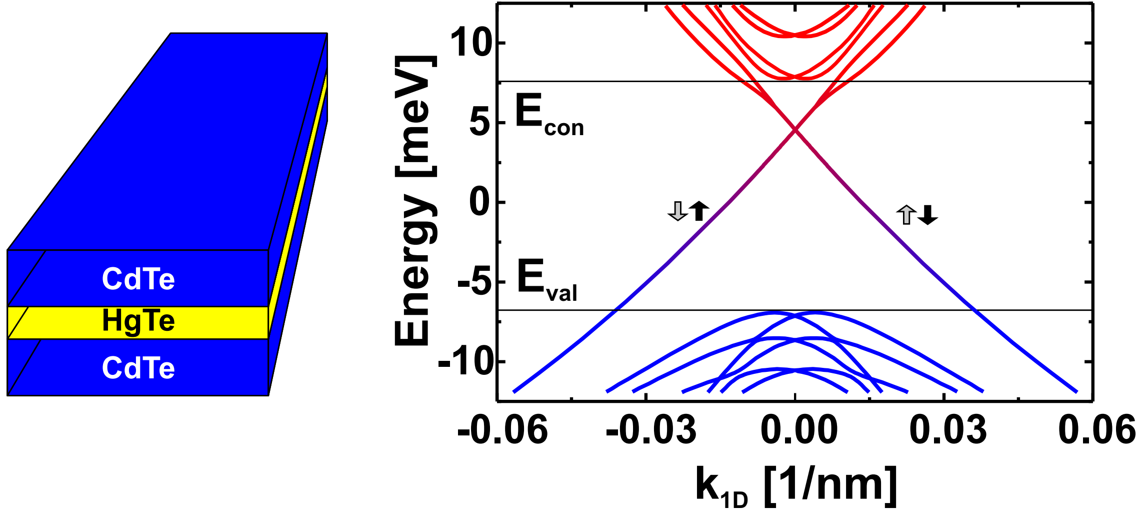

Figure 10.15.: (left) Schematic picture of a HgTe quantum wire formed by edging. (right) Subband dispersion in a 240 nm wide quantum wire defined in a 7.8 nm wide $HgTe/Hg_{.3}Cd_{.7}Te$ quantum well calculated with the relativistic 4-band model. The helical edge states within the energy gap are almost spin degenerate as indicated by the small arrows, however, on different sides of the wire. Black arrows denote right channels and gray ones left channels. The conduction and valence band states are spin split due to the Dresselhaus like spin-orbit interaction.

yields a topological insulator with edge states within the energy gap, as shown in Fig. 10.15 (right). The spin-up and spin-down states are energetically almost degenerate across the energy gap, but they lie at different edges of the wire and are therefore independent spatially as indicated in the figure. The k-linear spin splitting (so-called Dresselhaus effect) becomes significant only very close to the band edges which can be seen by the splitting of states close to the band edges. If we apply a small bias along the wire, the current that is driven through the wire is almost perfectly spin-polarized, provided the Fermi energy lies with in the gap of the infinite system and the transport is thus given through the helical edge channels only. We show the calculated relative out of plane spin polarization in the case of $E_F = 0$ in Fig. 10.16. We find indeed that the spin polarization at the edges is almost 100%. The small deviation from full spin polarization is due to Dresselhaus alike spin-orbit interaction that mixes spin-up and spin-down states. For a source drain bias $V_{\mathrm{SD}} > 0$ and consequently a Fermi wave vector $k_F > 0$, we find that in the left edge channel only spin-up electrons can propagate while in the right channel only spin-down electrons are allowed. If the bias is reversed and therefore $k_F < 0$, the polarization change sign in both channels due to the time reversal symmetry.

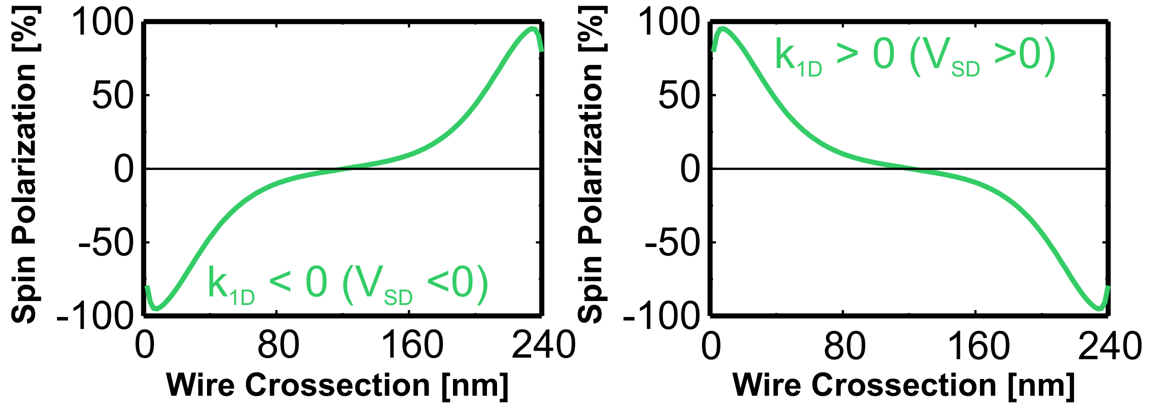

Figure 10.16.: Relative out-of-plane spin polarization S_z at the Fermi energy in a quantum wire with a cross section of 240 nm defined in a 7.8 nm wide HgTe/Hg$_{.3}$Cg$_{.7}$Te quantum well within the quantum spin Hall state as a function of the cross sectional coordinate of the wire, for negative source drain voltage (left) and for positive source drain voltage (right).

10.6. Prediction of spin transistor in HgTe quantum wells

In this section, we propose a highly sensitive spin transistor based on the quantum spin Hall effect in topological insulators as a possible spintronic application and realization of a Datta–Das-like transistor [1]. Concretely, we study quantum spin transport in HgTe/Hg$_{.3}$Cd$_{.7}$Te quantum wells (QWs) that have been found [9, 23] to be topological insulators and support the quantum spin Hall (QSH) effect [215, 216]. HgTe quantum wells of a thickness d larger than a critical thickness d_{crit} have a so called inverted band structure as has been shown in Sec. 4.2. As we have seen in the previous section, an inverted band structure is important for the realization of a topological insulator. We find that for quantum wells wider than approximately 7 nm the first heavy hole subband lies above the first electron subband. Due to the symmetry of the involved states, we expect fully helical edge states to form if the system is confined appropriately. Lateral confinement for HgTe quantum well is realized in experiment by deep edging, such that a semiconductor–vacuum interface is realized for the quantum well. In that way a confinement potential for both electrons and holes is realized. Note that a confinement for both kinds of carriers could not be achieved by a simple top gate structure, which would only confine one kind of carriers depending on the applied gate voltage. We model the geometry by impenetrable barriers for both kind of carriers. In this section, we employ the effective 4-band model developed in Sec. 4.3.

The transistor structure that we predict is schematically shown in Fig. 10.17 (left). It consists of “injector” and “collector” regions that are in the QSH-state so that transport occurs within fully spin-polarized edge channels. This state can be reached

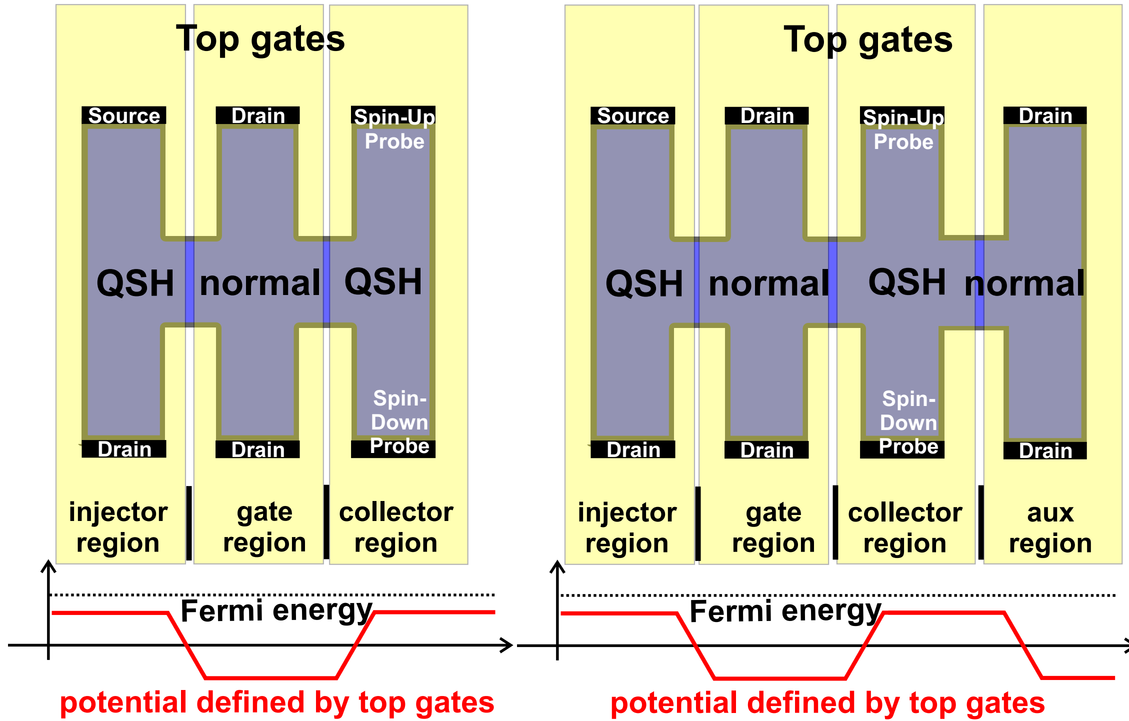

Figure 10.17.: Scheme of the proposed spin transistor. (left) Top view of the HgTe quantum well with the nanostructure defined by edging and the three split top gates, that define the transistor. Below the structure an illustration of the local gate potential: injector and collector region are brought to the quantum spin Hall regime while the gate region is normal n-conducting. (right) Improved transistor design with an additional n-conducting auxiliary region to enhance the induced voltage.

by appropriately biased top gates. The “gate” region, on the other hand, is in a normal conducting (NC) state. In the NC area, the Rashba and Dresselhaus type spin-orbit interaction lead to a spin precession and therefore mixes spin-up and spin-down components of the carriers. The amount of mixing can be tailored and controlled by the geometry of the 2DEG or 2DHG device structure. This concept requires neither external magnetic fields nor ferromagnetic contacts. The regions of the transistor are defined by three split gates that cover the edging defined nanostructure geometry. These gates are shown in semitransparent yellow in the schematic drawing. The top gate potential induced by the three split gates is shown schematically in Fig. 10.17 below the structure on the left. Split gate defined devices in HgTe quantum wells have recently been successfully realized experimentally [73]. The working principle of the proposed transistor is as follows. The left injector and right collector region are brought into the QSH state by top gates, whereas the central gate region in between is kept in the NC state. We apply a small bias between the spin-unpolarized source and drain contacts. This drives a fully spin-polarized charge current in the

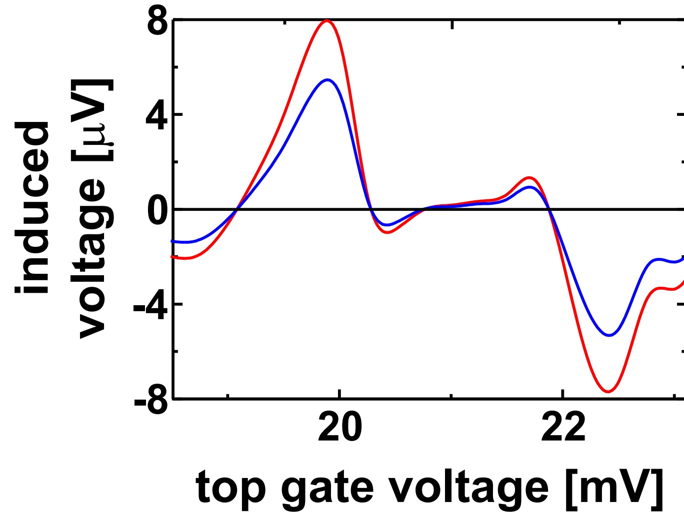

Figure 10.18.: Induced voltage between the two spin probe contacts at the injector side of the spin transistor defined in a 7.8 nm wide HgTe/$Hg_{.3}Cg_{.7}$Te quantum well as a function of the top gate voltage applied to the gate region. The blue line shows results for the three split gate design while the red line is for four split gates.

injector region's edge states which in turn injects a fully spin-polarized current into the normal conducting gate region, the spin of the carriers starts to precess with a spatial period that can be tuned by the applied top gate voltage. The collector region again possesses helical edge channels. Carriers reaching this region with spin-up are transported to one of the probe contacts, while carriers with spin-down are transported to the opposite one. This induces a voltage V between the probes that quantitatively reflects the spin polarization that reaches the collector region. In this way, one can tune the initial complete spin polarization to any specified degree via a gate voltage. In passing, we note that the inverse intrinsic spin-Hall effect can induce a small voltage in the collector region as well, provided only the lowest conducting sublevel is occupied. This effect, however, requires extremely low densities, see Sec. 9.3 or gate widths below 50 nm, see Sec. 8.4. In the present case of the QSH state, the charge densities and structure sizes can be significantly larger which guarantees a large and robust effect. In Fig. 10.17 (right), we show an improved design of the transistor. At the right side of the collector region we add an auxiliary region, which is brought to the NC state by a fourth split gate. The potential profile, which is induced by the four top gates is again shown schematically in the figure below the structure. This auxiliary region enhances the induced voltage between the spin probes. Without the additional region the conductance between the two spin probes is approximately $e^2/(2\pi\hbar)$ due to the edge channel that connects them directly whereas the conductance between the source and spin probes through the NC region is only about 10% of that value. This missmatch reduces the induced voltage. By adding the NC auxialary region the conductance between the spin probes

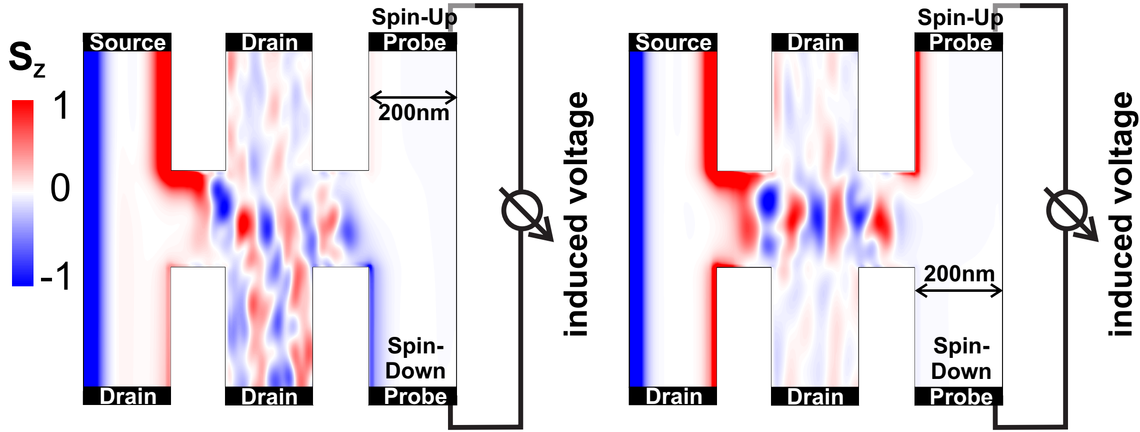

Figure 10.19.: Peak normalized out-of-plane spin polarization S_z at the Fermi energy in the proposed spin transistor geometry defined in a 7.8 nm wide HgTe/Hg$_{.3}$Cg$_{.7}$Te quantum well for a top gate voltage at the gate region of 20 mV (left) and 22.5 mV (right).

is effectively reduced, which in turn enhances the spin voltage signal. In Fig. 10.18, we plot the calculated induced voltage between the probe contacts as a function of applied top gate voltage V_G. The cross section of the wires amounts to .2 μm. The applied source drain voltage is taken to be $V_{SD} = .1$mV. The charge density in the NC region amounts to about 2×10^{11} cm^{-2} at a temperature of $T = .1$ K. We model scattering by band-independent Büttiker probes, that are phase breaking and energy relaxing. The mean free path is assumed to exceed the structure's dimensions and is set to 2.5 μm, which is a realistic value for HgTe quantum wells [24]. The applied bias drives a charge current between the top source and the bottom drain, that amounts to approximately $I_{SD} = 3.8$ nA due to the quantized conductance. In Fig. 10.18, we show the calculated spin-voltage signal as a function of the top gate voltage for the three split gate design by the blue line while the red line shows the results for the four split gate design. In both cases, we find a pronounced maximum of the signal at a gate voltage of about $V_G = 20$ mV and a minimum of the same magnitude at about $V_G = 22.5$ mV. For the four split gate design, the signal is enhanced by about 50% compared to the three split gate design. The quantum spin Hall resistance, i.e. the induced voltage devided by the source drain current, amounts to 1.4 kΩ for the three split-gate design and 2.1 kΩ for the four split-gate design respectively. To demonstrate that the induced voltage signal is indeed related to spin-orbit controlled spin precession within the gate region, we have calculated the locally resolved out-of-plane spin polarization for the two extremal values of the induced spin-voltage signal in the three split-gate structure. The results are shown in Fig. 10.19. The left side of the figure shows the situation for $V_G = 20$ mV while for the right side, we have set $V_G = 22.5$ mV. The calulations show, that indeed a fully spin-up polarized current is injected into the gate region of the transistor due to the helical edge channel in both cases. Within the gate region, we find clear

spin precession, as can be infered from sucessive pattern positive and negative spin polarization. For $V_G = 20\,\mathrm{mV}$ the carriers arrive with spin-down at the collector region. As the calculation shows, carriers can only enter the helical edge channel leading to the spin-down probe. The current, that arrives at the spin-down probe cantact is thus fully spin polarized, while almost no current arrives at spin-up probe. Indeed, we find that the conductance from the source to the spin-up probe is surpressed by a factor of 20 compared to the conductance to the spin-down probe. For $V_G = 22.5\,\mathrm{mV}$, on the other hand, the spin precession within the NC region leads to a spin-up polarization in the collector region. Thus, the carriers can only enter the edge channel to the spin-up probe where the current is fully spin-up polarized. The spin precession in the NC region is due to Dresselhaus and Rashba type spin-orbit coupling. Additionally, there is a spin-orbit coupling term due to the in plane electric fields which has been called Darwin term in the literature [28]. We find for our structure, that it is actually this Darwin term which dominatly causes the spin precesion. The applied gate voltage thus influences the spin-precession length mostly via the induced inplane elctric fields.

Please note that the gate regions of both transistor designs as shown in Fig. 10.17 are assumed to be open quantum wires as indicated by the two drain contacts that we assume to be grounded. It is necessary to have an open gate region in order to get a plane wave like transport form the injector to the collector region. If we assume a simple confined wire acting as gate region, we get strong oscillations in the calculated induced voltage which can not be attributed to spin precession but are dominantly due to ballistic charge reflections in combination with a geometry induced interaction between the sublevels of the wire.

10.7. Summary

In this chapter, we have investigated the origin of topological insulators and particularly the origin of the appearance of edge channels in terms of the atomistic electronic structure of the materials. We have found that the topologically induced formation of gap states in inverted 2D band systems is completely independent of and does not require spin-orbit interaction. These states show a dispersion along the translational invariant direction that is governed by the symmetry of the originally overlapping bands. By contrast, the spin-orbit coupling is required for the edge states to become helical and we therefore propose to discriminate the term topological insulator from the (experimentally observed) quantum spin Hall effect in HgTe nanostructures where spin-orbit effects play a crucial role.

We have also presented our proposal of a spin transistor in two-dimensional topological insulators, namely HgTe quantum wells with an inverted band structure, that employs a combination of the quantum spin Hall effect and the strong spin-orbit interaction in the metallic state. We have calculated the current and spin polarization in the proposed device geometry and find, that a top gate voltage gives complete electrical control over the spin polarization in the structure and allows for almost

perfectly spin-polarized currents. We have further demonstrated that the spin polarization can be measured quantitatively by a simple dc-voltage measurement. We have further shown, how the basic design can be improved, to increase the spin-induced voltage signal by 50%. The prediced resistance signals are $1.4\,\mathrm{k}\Omega$ for the basic design and $2.1\,\mathrm{k}\Omega$ for the improved one.

11. Summary

The main goal of this work was quantitatively predict devices for spintronic applications, which polarize, manipulate, and detect the spin degree of freedom of the charge carriers in semiconductor nanstructures. To predict quantum spin transport properties of nanstructures, we have employed the non-equilibrium Green's function (NEGF) method in this work. For realistic predictions it is vital to include inelastic and phase-breaking scattering in the calculations. However, a full NEGF-implementation for realistic arbitrarily shaped nanostructures is numerically extremely costly and time consuming. That lead us to develop the novel multi scattering Büttiker probe (MSB) model, which takes into account individual scattering mechanisms, is orders of magnitude faster and more stable than the full NEGF scheme, and reproduces experimental results. We have applied this method to predict several nanostructures based on two-dimensional electron and hole gases with and without external magnetic fields.

Our predictions are based on multi-band envelop function approximations that include several electric band-structure and spin-orbit coupling parameters. We have employed the atomistic semi-empirical tight-binding theory to calculate these parameters. We have found, that n-InSb quantum wells have a strong spin-orbit interaction that can be excellently tuned by an applied top gate voltage. InSb quantum wells are thus very interesting for spintronic applications. We have also predicted exceptionally large spin-orbit interaction effects for the top valence band in tensile strained GaAa quantum wells, which is tunable by the applied strain.

We have studied transverse electron focusing for Insb quantum wells in external magnetic field. We predict a large spin-dependent splitting of the electron beam, which polarization direction depends on the applied gate voltage. We have studied and predicted several all semiconductor based device geometries that generate, manipulate, and detect spin polarization or spin-polarized charge current in zero external magnetic field on the basis of spin-orbit coupling effects in complex device geometry. In particular, we have predicted giant inverse intrinsic spin-Hall effect in a H-shaped geometry in tensile strained p-GaAs, which allows to measure pure spin currents all electrically. We have predicted a T-shaped geometry as very efficient spin polarizer and have proposed an all electrical detection scheme for the current induced spin polarization, that is based on the anomalous Hall effect in zero external magnetic field. We have shown how the spin polarization of the charge current in the T-shaped structure can be tuned to any desired value by the applied bias voltage. We have predicted large tunable spin polarization in such structures in n-InSb quantum wells as well as in tensile strained p-GaAs quantum wells.

We have also studied topological insulators, as they came into focus recently due

to the large application potential of the quantum spin Hall effect in these materials. In the quantum spin Hall effect, quantized dissipationless transport is realized in helical edge channels. We have studied the origin of the quantum spin Hall effect and could demonstrate the microscopic origin of the edge channels. We have shown that in contrast to the wide spread assumption spin-orbit coupling is not fundamental for topological insulators but nonrelativistic band structure effects account for the formation of the edge channels. As an application of the quantum spin Hall effect, we have predicted a highly sensitive realization of spin transistor in nanostructured HgTe quantum wells. To this end, we have developed a multi-band envelop function approximation, that captures the relevant features of the bandstructure in these structures and includes all relevant spin-orbit coupling mechanisms. We have based the model on our newly developed atomistic semi-empirical tight-binding parametrization for HgTe and CdTe.

A. Analytic calculation of the Green's function for the 1D-model of a topological insulator

The eigenstates of the semiinfinite system which ends with a dangling s-state are obtained from the zeros of the bulk Green's function in Eq. (10.3),

$$G_{ss}(E) = \sum_{k,n} \frac{\left|\langle s_{\text{boundary}}|\psi_{k,n}\rangle\right|^2}{E - E_{k,n}} = 0, \tag{A.1}$$

For the 1-D tight-binding model in Sec. (10.3), there are two bands, namely one valence band and one conduction band, $n \in \{c, v\}$. Furthermore, band energies and Bloch functions obey the symmetry relations $E_{k,c} = -E_{k,v} := E_k > 0$ and $\left|\langle s_{\text{boundary}}|\psi_{k,c}\rangle\right|^2 = 1 - \left|\langle s_{\text{boundary}}|\psi_{k,v}\rangle\right|^2 := s_k^2$. With these relations, Eq. (A.1) can be written in the form

$$\sum_k \frac{E - E_k\,(1 - 2s_k^2)}{E^2 - E_k^2} = 0. \tag{A.2}$$

Inserting the analytic band energies of Eq. (10.2), one obtains

$$\sum_k \frac{E - \Delta/2 + 2\cos(2\pi k)}{E^2 - 2(1+T^2) - (\Delta/2)^2 + 2(T^2+\Delta)\cos(2\pi k) - 2\cos(4\pi k)} = 0. \tag{A.3}$$

One can easily convince oneself that in the Brillouin zone with $k \in [-1/2, 1/2)$ this Green's function remains nonzero for energies within the energy gap, provided the relation $\Delta/2 > 2$ holds. This relation corresponds precisely to the normal band alignment. For the inverted band alignment with $\Delta/2 < 2$, Eq. () yields exactly one bound state within the energy gap. It is possible to evaluate this energy E_0 analytically and one finds

$$E_0 = \frac{1}{4}\left(4 + \Delta + T^2 - \sqrt{16 + 8\Delta + \Delta^2 + (24 - 2\Delta)T^2 + T^4}\right). \tag{A.4}$$

This corresponds to a p-type bound state. If we terminate the chain at a p-site, we get one zero exactly at $-E_0$ that corresponds to the s-type bound state. The result for $\Delta = 0$ is depicted in Fig. 10.4. When the nearest neighbor coupling T increases, the bound state approaches the corresponding band edge.

B. Discrete Hamilton operators

Within the finite differences scheme the Hamilton operator is discretized on a finite rectangular lattice. The general form of the discrete operator reads:

$$H = \sum_{\mathbf{m}\nu\mu} \varepsilon_{\mathbf{m}}^{\nu,\mu} C_{\mathbf{m},\nu}^{\dagger} C_{\mathbf{m},\mu} + \sum_{\mathbf{m},i,\mu\nu} \left(t_{\mathbf{m},\mathbf{m}+\boldsymbol{\epsilon}_\mathbf{i}}^{\mu\nu} C_{\mathbf{m},\nu}^{\dagger} C_{\mathbf{m}+\boldsymbol{\epsilon}_\mathbf{i},\mu} + t_{\mathbf{m}+\boldsymbol{\epsilon}_\mathbf{i},\mathbf{m}}^{\mu\nu} C_{\mathbf{m}+\boldsymbol{\epsilon}_\mathbf{i},\nu}^{\dagger} C_{\mathbf{m},\mu} \right), \quad \text{(B.1)}$$

where $C_{\mathbf{m},\nu}^{\dagger}$ creates a particle at site $\mathbf{m}$ in band ν and $C_{\mathbf{m},\nu}$ annihilates the same particle. $\varepsilon_{\mathbf{m}}^{\nu,\mu}$ are the on-site elements, while $t_{\mathbf{m},\mathbf{m}+\boldsymbol{\epsilon}_\mathbf{i}}^{\mu\nu}$ are the hopping elements between site $\mathbf{m}$ and site $\mathbf{m}+\boldsymbol{\epsilon}_\mathbf{i}$. $\boldsymbol{\epsilon}_\mathbf{i}$ connects points on the on the lattice, e.g. nearest neighbors or 2$^{\text{nd}}$ nearest neighbors, as specified by the model at hand. Note that both on-site elements and hopping elements include coupling between different bands, with $t_{\mathbf{m},\mathbf{m}+\boldsymbol{\epsilon}_\mathbf{i}} = (t_{\mathbf{m}+\boldsymbol{\epsilon}_\mathbf{i},\mathbf{m}})^{\dagger}$. We always use Dirichlet boundary conditions in the Hamilton operator by putting the hopping elements to zero at the boundary of the rectangular lattice.

k-linear Dresselhaus and Rashba model

For the k-linear model of spin-orbit coupling Eq. (3.1), we have only nearest neighbor coupling in x- and y-direction. That means we have $\boldsymbol{\epsilon}_x = \epsilon_x \mathbf{e}_x$ and $\boldsymbol{\epsilon}_y = \epsilon_y \mathbf{e}_y$, where ϵ_i is the lattice spacing in the direction i and $\mathbf{e}_i$ the corresponding unit vector. The band indices μ and ν become the spin indices σ and σ', that run over the two values $\{\uparrow,\downarrow\}$. Note that we use the standard representation of the Pauli-matrices, where $\hat{\sigma}_z$ is diagonal. For the on-site elements in the mixed Dresselhaus and Rashba model, we get:

$$\varepsilon_{\mathbf{m}}^{\sigma} = V(\mathbf{m}) + 2t_x + 2t_y, \quad \text{(B.2)}$$

where $V_{\mathbf{m}}$ denotes an on-site potential and $t_i = \hbar^2/(2m^*\epsilon_i^2)$. Note that the on-site elements are independent of the spin index. For the hopping element in x-direction, we get:

$$t_{\mathbf{m},\mathbf{m}+\boldsymbol{\epsilon}_x} = \begin{pmatrix} -t_x & i\alpha_{\text{BIA}} + \alpha_{\text{SIA}} \\ i\alpha_{\text{BIA}} - \alpha_{\text{SIA}} & -t_x \end{pmatrix}, \quad \text{(B.3)}$$

while the hopping element in y-direction reads:

$$t_{\mathbf{m},\mathbf{m}+\boldsymbol{\epsilon}_y} = \begin{pmatrix} -t_y & -\alpha_{\text{BIA}} - i\alpha_{\text{SIA}} \\ \alpha_{\text{BIA}} - i\alpha_{\text{SIA}} & -t_y \end{pmatrix}. \quad \text{(B.4)}$$

k-cubic Dresselhaus model

For the cubic Dresselhaus model Eq. (3.12), we have the same k-quadratic and k-linear terms as in the linear Dresselhaus and Rashba Hamiltonian. In particular, we have the same on-site elements. Therefor, we will give here only the additional couplings, that add to the ones given above. We use the following notation:

$$\gamma_x = \frac{c_1}{2\epsilon_x\epsilon_y^2}, \quad \gamma_y = \frac{c_1}{2\epsilon_x^2\epsilon_y},$$
$$\xi_x = \frac{c_2}{2\epsilon_x^3}, \quad \xi_y = \frac{c_2}{2\epsilon_y^3}$$

The additional hopping element in x-direction reads:

$$t_{\mathbf{m},\mathbf{m}+\boldsymbol{\epsilon}_x} = \begin{pmatrix} 0_x & -2i(\gamma_x + \xi_x) \\ -2i(\gamma_x + \xi_x) & 0 \end{pmatrix}. \tag{B.5}$$

The additional hopping element in y-direction reads:

$$t_{\mathbf{m},\mathbf{m}+\boldsymbol{\epsilon}_y} = \begin{pmatrix} 0 & 2(\gamma_y + \xi_y) \\ -2(\gamma_y + \xi_y) & 0 \end{pmatrix}. \tag{B.6}$$

In addition to the nearest neighbor coupling we get also 2nd and 3rd nearest neighbor coupling in the cubic Dresselhaus model. The second nearest neighbors are connected by the vector $\boldsymbol{\epsilon}_{xy} = \epsilon_x\mathbf{e}_x + \epsilon_y\mathbf{e}_y$ and $\boldsymbol{\epsilon}_{x\bar{y}} = \epsilon_x\mathbf{e}_x - \epsilon_y\mathbf{e}_y$. For the corresponding hopping elements, we get:

$$t_{\mathbf{m},\mathbf{m}+\boldsymbol{\epsilon}_{xy}} = \begin{pmatrix} 0 & i\gamma_x - \gamma_y \\ i\gamma_x + \gamma_y & 0 \end{pmatrix}, \tag{B.7}$$

and

$$t_{\mathbf{m},\mathbf{m}+\boldsymbol{\epsilon}_{x\bar{y}}} = \begin{pmatrix} 0 & -i\gamma_x - \gamma_y \\ -i\gamma_x + \gamma_y & 0 \end{pmatrix}. \tag{B.8}$$

The 3rd nearest neighbors are connected by $\boldsymbol{\epsilon}_{xx} = 2\epsilon_x\mathbf{e}_x$ and $\boldsymbol{\epsilon}_{yy} = 2\epsilon_y\mathbf{e}_y$ and yield the hopping matrices:

$$t_{\mathbf{m},\mathbf{m}+\boldsymbol{\epsilon}_{xx}} = \begin{pmatrix} 0 & i\xi_x \\ i\xi_x & 0 \end{pmatrix}, \tag{B.9}$$

and

$$t_{\mathbf{m},\mathbf{m}+\boldsymbol{\epsilon}_{yy}} = \begin{pmatrix} 0 & -\xi_y \\ \xi_y & 0 \end{pmatrix}, \tag{B.10}$$

Four and six-band model for HgTe quantum wells

For the four-band model, we have again only nearest neighbor coupling. For the matrix elements we use the following notation:

$$\begin{gathered}
S_x = \frac{S}{\epsilon_x^2}, \quad S_y = \frac{S}{\epsilon_y^2}, \\
t_x^h = \frac{D}{\epsilon_x^2}, \quad t_y^h = \frac{D}{\epsilon_y^2}, \quad t_x^e = \frac{B}{\epsilon_x^2}, \quad t_y^e = \frac{B}{\epsilon_y^2}, \\
A_x = \frac{A}{2\epsilon_x}, \quad A_y = \frac{A}{2\epsilon_y}, \\
\gamma_x = \frac{\gamma}{2\epsilon_x}, \quad \gamma_y = \frac{\gamma}{2\epsilon_y}, \quad T_x = \frac{T}{2\epsilon_x}, \quad T_y = \frac{T}{2\epsilon_y}
\end{gathered} \tag{B.11}$$

For the on-site elements, we get:

$$\begin{aligned}
\varepsilon_{\mathbf{m}} = &\begin{pmatrix} 2t_x^e + 2t_y^e & 0 & 0 & -2S_x - 2S_y \\ 0 & 2t_x^h + 2t_y^h & 2S_x + 2S_y & 0 \\ 0 & 2S_x + 2S_y & 2t_x^e + 2t_y^e & 0 \\ -2S_x - 2S_y & 0 & 0 & 2t_x^h + 2t_y^h \end{pmatrix} + \\
&\mathrm{Diag}\left\{V(\mathbf{m}), -M - V(\mathbf{m}), V(\mathbf{m}), -M - V(\mathbf{m})\right\},
\end{aligned} \tag{B.12}$$

where Diag$\{\dots\}$ denotes a diagonal matrix and we have assumed the potential to be staggered, such that it has the same (confining) effect on electrons and holes. The hopping matrices are:

$$t_{\mathbf{m},\mathbf{m}+\boldsymbol{\epsilon}_x} = \begin{pmatrix} -t_x^e & -iA_x & -i\gamma_x & S_x \\ -iA_x & -t_x^h & -S_x & -iT_x \\ -i\gamma_x & -S_x & -t_x^e & iA_x \\ S_x & -iT_x & iA_x & -t_x^h \end{pmatrix}, \tag{B.13}$$

and

$$t_{\mathbf{m},\mathbf{m}+\boldsymbol{\epsilon}_y} = \begin{pmatrix} -t_y^e & A_y & \gamma_y & S_y \\ -A_y & -t_y^h & -S_y & -T_y \\ -\gamma_y & -S_y & -t_y^e & A_y \\ S_y & T_y & -A_y & -t_y^h \end{pmatrix}, \tag{B.14}$$

For the six band model, we have additionally coupling to the 2$^{\text{nd}}$ nearest neighbors. For the six band models we use the following notation for the additional matrix

elements:

$$A_x^2 = \frac{A_2}{2\epsilon_x}, \quad A_y^2 = \frac{A_2}{2\epsilon_y},$$
$$t_x^{h2} = \frac{D_2}{\epsilon_x^2}, \quad t_y^{h2} = \frac{D_2}{\epsilon_y^2},$$
$$S_x^2 = \frac{S_2}{\epsilon_x^2}, \quad S_y^2 = \frac{S_2}{\epsilon_y^2}, \quad S_x^3 = \frac{S_2}{\epsilon_x^2}, \quad S_y^3 = \frac{S_2}{\epsilon_y^2}$$
$$T_x^2 = \frac{T_2}{2\epsilon_x}, \quad T_y^2 = \frac{T_2}{2\epsilon_y}, \quad T_x^3 = \frac{T_2}{2\epsilon_x}, \quad T_y^3 = \frac{S_2}{2\epsilon_y}$$
$$S_{xy}^2 = \frac{S_2}{2\epsilon_x\epsilon_y}, \quad S_{xy}^3 = \frac{S_3}{2\epsilon_x\epsilon_y}$$

The on-site matrix for this model is given by:

$$\varepsilon_{\mathbf{m}} =$$
$$\begin{bmatrix} 2(t_x^e + t_y^e) & 0 & 0 & 0 & -2(S_x + S_y) & 2(S_y^2 - S_x^2) \\ 0 & 2(t_x^h + t_y^h) & 2(S_x^3 - S_y^3) & 2(S_x + S_y) & 0 & 0 \\ 0 & 2(S_x^3 - S_y^3) & 2(t_x^{h2} + t_y^{h2}) & 2(S_x^2 - S_y^2) & 0 & 0 \\ 0 & 2(S_x + S_y) & 2(S_x^2 - S_y^2) & 2(t_x^e + t_y^e) & 0 & 0 \\ -2(S_x + S_y) & 0 & 0 & 0 & 2(t_x^h + t_y^h) & 2(S_x^3 - S_y^3) \\ 2(S_y^2 - S_x^2) & 0 & 0 & 0 & 2(S_x^3 - S_y^3) & 2(t_x^{h2} + t_y^{h2}) \end{bmatrix}$$
$$+\mathrm{Diag}\left\{V(\mathbf{m}), -M - V(\mathbf{m}), -M2 - V(\mathbf{m}), V(\mathbf{m}), -M - V(\mathbf{m}), -M2 - V(\mathbf{m})\right\}. \tag{B.15}$$

For the hopping element in x-direction, we have:

$$t_{\mathbf{m},\mathbf{m}+\boldsymbol{\epsilon}_x} = \begin{pmatrix} -t_x^e & -iA_x & -iA_x^2 & -i\gamma_x & S_x & S_x^2 \\ -iA_x & -t_x^h & -S_x^3 & -S_x & -iT_x & -iT_x^3 \\ -iA_x^2 & -S_x^3 & -t_x^{h2} & -S_x^2 & -iT_x^3 & -iT_x^2 \\ -i\gamma_x & -S_x & -S_x^2 & -t_x^e & iA_x & iA_x^2 \\ S_x & -iT_x & -iT_x^3 & iA_x & -t_x^h & -S_x^3 \\ S_x^2 & -iT_x^3 & -iT_x^2 & iA_x^2 & -S_x^3 & -t_x^{h2} \end{pmatrix}, \tag{B.16}$$

while the hopping element in y-direction reads:

$$t_{\mathbf{m},\mathbf{m}+\boldsymbol{\epsilon}_x} = \begin{pmatrix} -t_y^e & A_y & A_y^2 & \gamma_y & S_y & -S_y^2 \\ -A_y & -t_y^h & S_y^3 & -S_y & -T_y & -T_y^3 \\ -A_y^2 & S_y^3 & -t_y^{h2} & S_y^2 & -T_y^3 & -T_y^2 \\ -\gamma_y & -S_y & S_y^2 & -t_y^e & A_y & A_y^2 \\ S_y & T_y & T_y^3 & -A_y & -t_y^h & S_y^3 \\ -S_y^2 & T_y^3 & T_y^2 & -A_y^2 & S_y^3 & -t_y^{h2} \end{pmatrix}. \tag{B.17}$$

Finally for the coupling to the next nearest neighbors, we have $t_{\mathbf{m},\mathbf{m}+\boldsymbol{\epsilon}_{xy}} = -t_{\mathbf{m},\mathbf{m}+\boldsymbol{\epsilon}_{x\bar{y}}}$ with:

$$t_{\mathbf{m},\mathbf{m}+\boldsymbol{\epsilon}_{xy}} = \begin{pmatrix} 0 & 0 & 0 & 0 & 0 & iS_{xy}^2 \\ 0 & 0 & iS_{xy}^3 & 0 & 0 & 0 \\ 0 & -iS_{xy}^3 & 0 & -iS_{xy}^2 & 0 & 0 \\ 0 & 0 & iS_{xy}^2 & 0 & 0 & 0 \\ 0 & 0 & 0 & 0 & 0 & -iS_{xy}^3 \\ -iS_{xy}^2 & 0 & 0 & 0 & iS_{xy}^3 & 0 \end{pmatrix}. \tag{B.18}$$

C. The local current operator for the cubic Dresselhaus model

In the cubic Dresselhaus model, due to the additional couplings in the Hamilton operator, we have also additional terms for the calculation of the local current. We write here only the additional terms, that have to be added to the expression for the k-linear model Eq. (5.97) and Eq. (5.98). For the x-component, we get:

$$
\begin{aligned}
j_x(\mathbf{m}) = -i\left(\frac{c_1}{\epsilon_y^2}+\frac{c_2}{\epsilon_x^2}\right)\big(&G^<_{\mathbf{m},\mathbf{m}+\boldsymbol{\epsilon}_x}(\uparrow\downarrow)+G^<_{\mathbf{m},\mathbf{m}+\boldsymbol{\epsilon}_x}(\downarrow\uparrow)+\\
&G^<_{\mathbf{m}+\boldsymbol{\epsilon}_x,\mathbf{m}}(\uparrow\downarrow)+G^<_{\mathbf{m}+\boldsymbol{\epsilon}_x,\mathbf{m}}(\downarrow\uparrow)\big)\\
+\left(i\frac{c_1}{2\epsilon_y^2}-\frac{c_1}{2\epsilon_x\epsilon_y}\right)\Big(&G^<_{\mathbf{m}+\boldsymbol{\epsilon}_y,\mathbf{m}+\boldsymbol{\epsilon}_x}(\uparrow\downarrow)+G^<_{\mathbf{m}+\boldsymbol{\epsilon}_{xy},\mathbf{m}}(\downarrow\uparrow)+\\
&G^<_{\mathbf{m}+\boldsymbol{\epsilon}_{x\bar{y}},\mathbf{m}}(\uparrow\downarrow)+G^<_{\mathbf{m}-\boldsymbol{\epsilon}_y,\mathbf{m}+\boldsymbol{\epsilon}_x}(\downarrow\uparrow)\Big)+\\
\left(i\frac{c_1}{2\epsilon_y^2}+\frac{c_1}{2\epsilon_x\epsilon_y}\right)\Big(&G^<_{\mathbf{m}-\boldsymbol{\epsilon}_y,\mathbf{m}+\boldsymbol{\epsilon}_x}(\uparrow\downarrow)+G^<_{\mathbf{m}+\boldsymbol{\epsilon}_{x\bar{y}},\mathbf{m}}(\downarrow\uparrow)+\\
&G^<_{\mathbf{m}+\boldsymbol{\epsilon}_{xy},\mathbf{m}}(\uparrow\downarrow)+G^<_{\mathbf{m}+\boldsymbol{\epsilon}_y,\mathbf{m}+\boldsymbol{\epsilon}_x}(\downarrow\uparrow)\Big)+\\
+i\frac{c_2}{2\epsilon_x^2}\big(&G^<_{\mathbf{m},\mathbf{m}+\boldsymbol{\epsilon}_{xx}}(\uparrow\downarrow)+G^<_{\mathbf{m},\mathbf{m}+\boldsymbol{\epsilon}_{xx}}(\downarrow\uparrow)+G^<_{\mathbf{m}+\boldsymbol{\epsilon}_{xx},\mathbf{m}}(\uparrow\downarrow)+G^<_{\mathbf{m}+\boldsymbol{\epsilon}_{xx},\mathbf{m}}(\downarrow\uparrow)+\\
&G^<_{\mathbf{m}-\boldsymbol{\epsilon}_x,\mathbf{m}+\boldsymbol{\epsilon}_x}(\uparrow\downarrow)+G^<_{\mathbf{m}-\boldsymbol{\epsilon}_x,\mathbf{m}+\boldsymbol{\epsilon}_x}(\downarrow\uparrow)+G^<_{\mathbf{m}+\boldsymbol{\epsilon}_x,\mathbf{m}-\boldsymbol{\epsilon}_x}(\uparrow\downarrow)+G^<_{\mathbf{m}+\boldsymbol{\epsilon}_x,\mathbf{m}-\boldsymbol{\epsilon}_x}(\downarrow\uparrow)\big)\,. \qquad \text{(C.1)}
\end{aligned}
$$

The last two lines denote the contributions of the 3$^{\text{rd}}$ nearest neighbor contribution. Since Eq. (5.97) is a master equation, that effectively describes the imbalance between carriers jumping from $\mathbf{m}\rightarrow\mathbf{m}+\epsilon_x$ and back $\mathbf{m}\leftarrow\mathbf{m}+\epsilon_x$, it actually describes the current through a surface in the middle between $\mathbf{m}$, $\mathbf{m}+\epsilon_x$. Therefor, we have to average the contributions from $\mathbf{m}\rightarrow\mathbf{m}+\epsilon_{xx}$ and $\mathbf{m}-\epsilon_x\rightarrow\mathbf{m}+\epsilon_x$ in the case of 3$^{\text{rd}}$ nearest neighbor interaction, to be consistent with the other contributions. The

same arguments hold for the y-direction, which reads:

$$
\begin{aligned}
j_y(\mathbf{m}) = \left(\frac{c_1}{\epsilon_y^2} + \frac{c_2}{\epsilon_x^2}\right) \Big(& G^<_{\mathbf{m},\mathbf{m}+\boldsymbol{\epsilon}_y}(\downarrow\uparrow) - G^<_{\mathbf{m},\mathbf{m}+\boldsymbol{\epsilon}_y}(\uparrow\downarrow) - \\
& G^<_{\mathbf{m}+\boldsymbol{\epsilon}_x,\mathbf{m}}(\uparrow\downarrow) + G^<_{\mathbf{m}+\boldsymbol{\epsilon}_x,\mathbf{m}}(\downarrow\uparrow)\Big) \\
& + \left(i\frac{c_1}{2\epsilon_x\epsilon_y} + \frac{c_1}{2\epsilon_x^2}\right)\Big(G^<_{\mathbf{m}+\boldsymbol{\epsilon}_{xy},\mathbf{m}}(\uparrow\downarrow) + G^<_{\mathbf{m}+\boldsymbol{\epsilon}_{\bar{x}y},\mathbf{m}}(\downarrow\uparrow) - \\
& G^<_{\mathbf{m}-\boldsymbol{\epsilon}_x,\mathbf{m}+\boldsymbol{\epsilon}_y}(\uparrow\downarrow) - G^<_{\mathbf{m}+\boldsymbol{\epsilon}_x,\mathbf{m}+\boldsymbol{\epsilon}_y}(\downarrow\uparrow)\Big) + \\
& \left(i\frac{c_1}{2\epsilon_x\epsilon_y} - \frac{c_1}{2\epsilon_x^2}\right)\Big(G^<_{\mathbf{m}+\boldsymbol{\epsilon}_{\bar{x}y},\mathbf{m}}(\uparrow\downarrow) + G^<_{\mathbf{m}+\boldsymbol{\epsilon}_{xy},\mathbf{m}}(\downarrow\uparrow) - \\
& G^<_{\mathbf{m}+\boldsymbol{\epsilon}_x,\mathbf{m}+\boldsymbol{\epsilon}_y}(\uparrow\downarrow) - G^<_{\mathbf{m}-\boldsymbol{\epsilon}_x,\mathbf{m}+\boldsymbol{\epsilon}_y}(\downarrow\uparrow)\Big) + \\
& + \frac{c_2}{\epsilon_y^2}\Big(G^<_{\mathbf{m},\mathbf{m}+\boldsymbol{\epsilon}_{yy}}(\uparrow\downarrow) - G^<_{\mathbf{m},\mathbf{m}+\boldsymbol{\epsilon}_{yy}}(\downarrow\uparrow) + G^<_{\mathbf{m}+\boldsymbol{\epsilon}_{yy},\mathbf{m}}(\uparrow\downarrow) - G^<_{\mathbf{m}+\boldsymbol{\epsilon}_{yy},\mathbf{m}}(\downarrow\uparrow) + \\
G^<_{\mathbf{m}-\boldsymbol{\epsilon}_y,\mathbf{m}+\boldsymbol{\epsilon}_y}(\uparrow\downarrow) - G^<_{\mathbf{m}-\boldsymbol{\epsilon}_y,\mathbf{m}+\boldsymbol{\epsilon}_y}(\downarrow\uparrow) & + G^<_{\mathbf{m}+\boldsymbol{\epsilon}_y,\mathbf{m}-\boldsymbol{\epsilon}_y}(\uparrow\downarrow) - G^<_{\mathbf{m}+\boldsymbol{\epsilon}_y,\mathbf{m}-\boldsymbol{\epsilon}_y}(\downarrow\uparrow)\Big)\,. \qquad \text{(C.2)}
\end{aligned}
$$

D. The mean free path in the Büttiker probe model

We now want to describe how the Büttiker probes can be connected to the mean free path of the carriers. We consider a one dimensional system discrete lattice, with lattice constant ϵ and parabolic dispersion. To each lattice site, a Büttiker probe is attached. We assume the scattering potential of the probes to be:

$$B(\mathbf{m})^R = \eta_p t e^{ik\epsilon}, \tag{D.1}$$

with the phenomenological coupling $\eta_p > 0$, independent of the lattice point $\mathbf{m}$. The wave vector k follows from the usual dispersion relation on a discrete lattice:

$$E(k) = 2t(1 - \cos(k\epsilon)), \tag{D.2}$$

with the hopping element $t = \hbar^2/2m^*\epsilon^2$. We consider a lattice with N grid points which is attached to leads at the left and at the right end, see Fig. D.1. The coupling self-energy to the semi-infinite one dimensional leads reads:

$$\Sigma_C^R = t e^{ik\epsilon}. \tag{D.3}$$

First consider, a system with only one device point. Hence, an electron originating from the left contact can either jump directly into the right contact or enter the probe. In the first case, we call the transport coherent, while in the latter one, we call the transport incoherent due to the scattering with the probe. The probabilities for coherent $P(c)$ and incoherent $P(p)$ transport clearly depend on the coupling constant η_p and are given by:

$$P(c) = \frac{1}{1+\eta_p}, \quad P(p) = \frac{c}{1+\eta_p}. \tag{D.4}$$

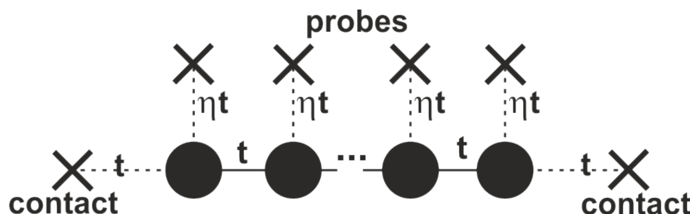

Figure D.1.: Schematic drawing of the one dimensional lattice, attached to semi-infinite leads at the left and at the right end of the lattice. To each grid point, a Büttiker probe with coupling parameter η_p is attached.

Note that, $\eta_p \to 0$ is the ballistic limit, such that the probability for coherent transmission is $P(c) = 1$. In the case $\eta_p = 1$, the probabilities are equal $P(p) = P(c) = .5$, while $\eta_p \to \infty$ constitutes the diffusive limit, with $P(c) \to 0$. Now consider a chain with N sites, each with an attached Büttiker probe. The probability for an electron to propagate from the left to the right contact coherently, i.e. without entering any probe, $P(c)_N$ is then given by:

$$P(c)_N = (1 - P(p))^N = \left(\frac{1}{1 + \eta_p} \right)^N . \tag{D.5}$$

We define the mean free path $l_{MF} = \epsilon N_{MF}$, in such a way, that $P(c)_{N_{MF}} = e^{-1}$. Thus, we get for the mean free path as a function of the scattering strength η_p:

$$l_M F = \frac{\epsilon}{\ln(1 + \eta_p)} \approx \frac{\epsilon}{\eta_p}, \tag{D.6}$$

which is independent of the energy of the electron. The last approximation holds for near ballistic transport, with $\eta_p \ll 1$. Numerically, we find exact agreement with Eq. (D.6) for a one dimensional lattice. For the quasi one dimensional quantum wire, the agreement is not exact, but reasonable, with a weak dependence on the energy and the wire sublevel. Since all our transport calculations in this work are performed at low densities, mostly within the lowest sublevel, Eq. (D.6) is a good approximation, to calculate the mean free path from the numerical parameter η_p.

Bibliography

[1] S. Datta and B. Das, Appl. Phys. Lett. **56**, 665 (1990).

[2] D. D. Awschalom, D. Loss, and N. Samarth, eds., *Semiconductor Spintronics and Quantum Computation*, NanoScience and Technology (Springer Berlin / Heidelberg, 2002).

[3] J. Fabian, A. Matos-Abiague, C. Ertler, P. Stano, and I. Žutić, acta phys. slovaca **57**, 565 (2007).

[4] H.-A. Engel, E. I. Rashba, and B. I. Halperin, *Handbook of Magnetism and Advanced Magnetic Materials* (John Wiley & Sons, Ltd, 2007), chap. Theory of Spin Hall Effects in Semiconductors, pp. 2858–2877.

[5] J. Schliemann, Int. J. Mod. Phys. B **20**, 1015 (2006).

[6] J. E. Moore, Nature **464**, 194 (2010).

[7] M. Z. Hasan and C. L. Kane, Rev. Mod. Phys. **82**, 3045 (2010).

[8] M. König, H. Buhmann, L. W. Molenkamp, T. Hughes, C.-X. Liu, X.-L. Qi, and S.-C. Zhang, Journal of the Physical Society of Japan **77**, 031007 (2008).

[9] M. König, S. Wiedmann, C. Brüne, A. Roth, H. Buhmann, L. W. Molenkamp, X.-L. Qi, and S.-C. Zhang, Science **318**, 766 (2007).

[10] L. Fu, C. L. Kane, and E. J. Mele, Phys. Rev. Lett. **98**, 106803 (2007).

[11] J. C. Slater and G. F. Koster, Phys. Rev. **94**, 1498 (1954).

[12] W. Harrison, *Electronic Structure and the Theory of Solids: The Physics of the Chemical Bond* (Dover Publications, New York, 1989).

[13] P. Y. Yu and M. Cardona, *Fundamentals of Semiconductors* (Springer Berlin / Heidelberg, 2010), 4th ed.

[14] A. D. Carlo, Semicond. Sci. Technol. **18**, R1 (2003).

[15] P.-O. Löwdin, J. Chem. Phys. **18**, 365 (1950).

[16] D. J. Chadi and M. L. Cohen, phys. status solidi (b) **68**, 405 (1975).

[17] P. Vogl, H. P. Hjalmarson, and J. D. Dow, J. Phys. Chem. Solids **44**, 365 (1983).

[18] J.-M. Jancu, R. Scholz, F. Beltram, and F. Bassani, Phys. Rev. B **57**, 6493 (1998).

[19] A. V. Podolskiy and P. Vogl, Phys. Rev. B **69**, 233101 (2004).

[20] S.-H. Wei and A. Zunger, Appl. Phys. Lett. **72**, 2011 (1998).

[21] S.-H. Wei and A. Zunger, Phys. Rev. B **60**, 5404 (1999).

[22] D. J. Chadi, Phys. Rev. B **16**, 790 (1977).

[23] B. A. Bernevig, T. L. Hughes, and S.-C. Zhang, Science **314**, 1757 (2006).

[24] C. Brüne, A. Roth, E. G. Novik, M. König, H. Buhmann, E. M. Hankiewicz, W. Hanke, J. Sinova, and L. W. Molenkamp, Nature Phys **6**, 448 (2010).

[25] E. G. Novik, A. Pfeuffer-Jeschke, T. Jungwirth, V. Latussek, C. R. Becker, G. Landwehr, H. Buhmann, and L. W. Molenkamp, Phys. Rev. B **72**, 035321 (2005).

[26] M. Penna, A. Marnetto, F. Bertazzi, E. Bellotti, and M. Goano, Journal of Electronic Materials **38**, 1717 (2009).

[27] K. Boujdaria and O. Zitouni, Solid State Commun. **129**, 205 (2004).

[28] D. G. Rothe, R. W. Reinthaler, C.-X. Liu, L. W. Molenkamp, S.-C. Zhang, and E. M. Hankiewicz, New J. Phys. **12**, 065012 (2010).

[29] B. A. Bernevig and S.-C. Zhang, Phys. Rev. Lett. **96**, 106802 (2006).

[30] A. Kobayashi, O. F. Sankey, and J. D. Dow, Phys. Rev. B **25**, 6367 (1982).

[31] K. C. Hass, H. Ehrenreich, and B. Velický, Phys. Rev. B **27**, 1088 (1983).

[32] J. N. Schulman and Y.-C. Chang, Phys. Rev. B **33**, 2594 (1986).

[33] N. J. Shevchik, J. Tejeda, M. Cardona, and D. W. Langer, physica status solidi (b) **59**, 87 (1973).

[34] B. Ray, *II–VI Compounds* (Pergamon Press, New York, 1969).

[35] F. H. Pollak, *Proc. Intern. Conf. II–VI Semiconducting Compounds* (Benjamin, 1968), chap. Experimental studies of interband transitions above the fundamental edge in II-VI semiconducting compounds, p. 552.

[36] Y. Guldner, C. Rigaux, M. Grynberg, and A. Mycielski, Phys. Rev. B **8**, 3875 (1973).

[37] J. M. Berroir, Y. Guldner, J. P. Vieren, M. Voos, X. Chu, and J. P. Faurie, Phys. Rev. Lett. **62**, 2024 (1989).

[38] J. Tersoff, Phys. Rev. B **40**, 10615 (1989).

[39] C. A. Hoffman, J. R. Meyer, F. J. Bartoli, Y. Lansari, J. W. Cook, and J. F. Schetzina, Phys. Rev. B **40**, 3867 (1989).

[40] C. R. Becker, V. Latussek, A. Pfeuffer-Jeschke, G. Landwehr, and L. W. Molenkamp, Phys. Rev. B **62**, 10353 (2000).

[41] K. Ortner, X. C. Zhang, A. Pfeuffer-Jeschke, C. R. Becker, G. Landwehr, and L. W. Molenkamp, Phys. Rev. B **66**, 075322 (2002).

[42] A. Fleszar and W. Hanke, Phys. Rev. B **71**, 045207 (2005).

[43] J. R. Chelikowsky and M. L. Cohen, Phys. Rev. B **14**, 556 (1976).

[44] D. J. Chadi, J. P. Walter, M. L. Cohen, Y. Petroff, and M. Balkanski, Phys. Rev. B **5**, 3058 (1972).

[45] S. ichi Katsuki and M. Kunimune, Journal of the Physical Society of Japan **31**, 415 (1971).

[46] S. Sapra, N. Shanthi, and D. D. Sarma, Phys. Rev. B **66**, 205202 (2002).

[47] R. Viswanatha, S. Sapra, T. Saha-Dasgupta, and D. D. Sarma, Phys. Rev. B **72**, 045333 (2005).

[48] R. Viswanatha and D. Sarma, Chem. Asian J. **4**, 904 (2009).

[49] S.-H. Wei and A. Zunger, J. Cryst. Growth **86**, 1 (1990).

[50] N. N. Berchenko and M. V. Pashkovskiĭ, Soviet Physics Uspekhi **19**, 462 (1976).

[51] N. Cade and P. Lee, Solid State Commun. **56**, 637 (1985).

[52] S. Chadov, X. Qi, J. Kübler, G. H. Fecher, C. Felser, and S. C. Zhang, Nature Mater **9**, 541 (2010).

[53] A. Delin and T. Klüner, Phys. Rev. B **66**, 035117 (2002).

[54] M. Cardona, R. K. Kremer, R. Lauck, G. Siegle, A. Muñoz, and A. H. Romero, Phys. Rev. B **80**, 195204 (2009).

[55] G. Dresselhaus, Phys. Rev. **100**, 580 (1955).

[56] Y. A. Bychkov and E. I. Rashba, Journal of Physics C: Solid State Physics **17**, 6039 (1984).

[57] J. Nitta, T. Akazaki, H. Takayanagi, and T. Enoki, Phys. Rev. Lett. **78**, 1335 (1997).

[58] R. Winkler, *Spin-Orbit Coupling Effects in Two-Dimensional Electron and Hole Systems*, vol. 191 of *Springer Tracts in Modern Physics* (Springer Berlin / Heidelberg, 2003).

[59] W. Zawadzki and P. Pfeffer, Semicond. Sci. Technol. **19**, R1 (2004).

[60] P. Pfeffer and W. Zawadzki, Phys. Rev. B **59**, R5312 (1999).

[61] D. Grundler, Phys. Rev. Lett. **84**, 6074 (2000).

[62] K. L. Litvinenko, B. N. Murdin, J. Allam, C. R. Pidgeon, M. Bird, K. Morris, W. Branford, S. K. Clowes, L. F. Cohen, T. Ashley, et al., New J. Phys. **8**, 49 (2006).

[63] J. M. S. Orr, A. M. Gilbertson, M. Fearn, O. W. Croad, C. J. Storey, L. Buckle, M. T. Emeny, P. D. Buckle, and T. Ashley, Phys. Rev. B **77**, 165334 (2008).

[64] K. J. Goldammer, W. K. Liu, G. A. Khodaparast, S. C. Lindstrom, M. B. Johnson, R. E. Doezema, and M. B. Santos, J. Vac. Sci. Technol. B **16**, 1367 (1998).

[65] E. S. Koteles, D. A. Owens, D. C. Bertolet, J.-K. Hsu, and K. M. Lau, Surface Science **228**, 314 (1990).

[66] L. Viña, L. Muñoz, N. Mestres, E. S. Koteles, D. C. Bertolet, and K. M. Lau, Philosophical Magazine Part B **70**, 397 (1994).

[67] T. G. Andersson, Z. G. Chen, V. D. Kulakovskii, A. Uddin, and J. T. Vallin, Appl. Phys. Lett. **51**, 752 (1987).

[68] M. Nakayama, T. Doguchi, and H. Nishimura, J. Appl. Phys. **72**, 2372 (1992).

[69] J.-M. Jancu, R. Scholz, E. A. de Andrada e Silva, and G. C. La Rocca, Phys. Rev. B **72**, 193201 (2005).

[70] P. von Allmen, Phys. Rev. B **46**, 15382 (1992).

[71] N. F. Johnson, P. M. Hui, and H. Ehrenreich, Phys. Rev. Lett. **61**, 1993 (1988).

[72] A. Roth, C. Brüne, H. Buhmann, L. W. Molenkamp, J. Maciejko, X.-L. Qi, and S.-C. Zhang, Science **325**, 294 (2009).

[73] C. Brüne, A. Roth, H. Buhmann, E. M. Hankiewicz, L. W. Molenkamp, J. Maciejko, X.-L. Qi, and S.-C. Zhang (2011), arXiv: 1107.0585 [cond-mat.mes-hall].

[74] Y.-H. Li, A. Walsh, S. Chen, W.-J. Yin, J.-H. Yang, J. Li, J. L. F. D. Silva, X. G. Gong, and S.-H. Wei, Appl. Phys. Lett. **94**, 212109 (2009).

[75] X. Dai, T. L. Hughes, X.-L. Qi, Z. Fang, and S.-C. Zhang, Phys. Rev. B **77**, 125319 (2008).

[76] M. Schultz, F. Heinrichs, U. Merkt, T. Colin, T. Skauli, and S. Løvold, Semiconductor Science and Technology **11**, 1168 (1996).

[77] S. Birner, Ph.D. thesis, Technische Universität München (2011).

[78] Y. S. Gui, C. R. Becker, N. Dai, J. Liu, Z. J. Qiu, E. G. Novik, M. Schäfer, X. Z. Shu, J. H. Chu, H. Buhmann, et al., Phys. Rev. B **70**, 115328 (2004).

[79] J. A. Majewski and P. Vogl, *Physics of Semiconductors* (Institute of Physics Publ., Bristol, 2003), chap. Resonant spin-orbit interactions and phonon spin relaxation rates in superlattices, p. 305.

[80] M. Fornari, H. H. Chen, L. Fu, R. D. Graft, D. J. Lohrmann, S. Moroni, G. P. Parravicini, L. Resca, and M. A. Stroscio, Phys. Rev. B **55**, 16339 (1997).

[81] M. Graf and P. Vogl, Phys. Rev. B **51**, 4940 (1995).

[82] T. Kubis, C. Yeh, P. Vogl, A. Benz, G. Fasching, and C. Deutsch, Phys. Rev. B **79**, 195323 (2009).

[83] L. V. Keldysh, Sov. Phys. JETP **20**, 1018 (1965).

[84] L. P. Kadanoff and G. A. Baym, *Quantum Statistical Mechanics* (W.A. Benjamin, Inc., New York, 1962).

[85] J. Schwinger, J. Math. Phys. **2**, 407 (1961).

[86] O. K. Ferry and C. Jacoboni, *Quantum Transport in Semiconductors* (Plenum Press, New York, 1992).

[87] S. Datta, *Electronic Transport in Mesoscopic Systems* (Cambridge University Press, 1995).

[88] R. Lake, G. Klimeck, R. C. Bowen, and D. Jovanovic, J. Appl. Phys. **81**, 7845 (1997).

[89] M. P. Anantram and T. R. Govindan, Phys. Rev. B **58**, 4882 (1998).

[90] X. Zheng, W. Chen, M. Stroscio, and L. F. Register, Phys. Rev. B **73**, 245304 (2006).

[91] S. Cauley, M. Luisier, V. Balakrishnan, G. Klimeck, and C.-K. Koh, J. Appl. Phys. **110**, 043713 (2011).

[92] T. Kubis and P. Vogl, Phys. Rev. B **83**, 195304 (2011).

[93] D. Mamaluy, M. Sabathil, and P. Vogl, J. Appl. Phys. **93**, 4628 (2003).

[94] D. Mamaluy, D. Vasileska, M. Sabathil, T. Zibold, and P. Vogl, Phys. Rev. B **71**, 245321 (2005).

[95] H. Haug and A.-P. Jauho, *Quantum Kinetics in Transport and Optics of Semiconductors*, vol. 123 of *Springer Series in Solid-State Sciences* (Springer Berlin / Heidelberg, 2008), 2nd ed.

[96] M. Büttiker, IBM J. Res. Develop. **32**, 317 (1988).

[97] M. Luisier, A. Schenk, W. Fichtner, and G. Klimeck, Phys. Rev. B **74**, 205323 (2006).

[98] M. Luisier, A. Schenk, W. Fichtner, and G. Klimeck, Journal of Computational Electronics **6**, 199 (2007).

[99] M. Luisier, Journal of Computational Electronics **7**, 309 (2008).

[100] M. P. L. Sancho, J. M. L. Sancho, and J. Rubio, J. Phys. F: Met. Phys. **14**, 1205 (1984).

[101] M. P. L. Sancho, J. M. L. Sancho, and J. Rubio, J. Phys. F: Met. Phys. **15**, 851 (1985).

[102] C. Rivas and R. Lake, phys. stat. sol. (b) **239**, 94 (2003).

[103] H. Jiang, S. Shao, W. Cai, and P. Zhang, J. Comp. Phys. **227**, 6553 (2008).

[104] T. Kubis, Ph.D. thesis, Technische Universität München (2009).

[105] B. K. Nikolić, L. P. Zârbo, and S. Souma, Phys. Rev. B **73**, 075303 (2006).

[106] B. K. Nikolić, L. P. Zârbo, and S. Souma, Phys. Rev. B **72**, 075361 (2005).

[107] B. K. Nikolić, S. Souma, L. P. Zârbo, and J. Sinova, Phys. Rev. Lett. **95**, 046601 (2005).

[108] L. Sheng, D. N. Sheng, and C. S. Ting, Phys. Rev. Lett. **94**, 016602 (2005).

[109] D. C. Langreth and E. Abrahams, Phys. Rev. B **24**, 2978 (1981).

[110] S. Datta, Superlattice. Microst. **28**, 253 (2000).

[111] K. Maschke and M. Schreiber, Phys. Rev. B **44**, 3835 (1991).

[112] R. Venugopal, M. Paulsson, S. Goasguen, S. Datta, and M. S. Lundstrom, J. Appl. Phys. **93**, 5613 (2003).

[113] S. Wang and N. Mingo, Phys. Rev. B **79**, 115316 (2009).

[114] M. Büttiker, A. Prêtre, and H. Thomas, Phys. Rev. Lett. **70**, 4114 (1993).

[115] Y. Meir and N. S. Wingreen, Phys. Rev. Lett. **68**, 2512 (1992).

[116] S. Li, S. Ahmed, G. Klimeck, and E. Darve, J. Comput. Phys. **227**, 9408 (2008).

[117] S. Li and E. Darve, J. Comput. Phys. **231**, 1121 (2011).

[118] R. Kubo, Reports on Progress in Physics **29**, 255 (1966).

[119] P. Greck, Ph.D. thesis, Technische Universität München (2012).

[120] L. P. Rokhinson, V. Larkina, Y. B. Lyanda-Geller, L. N. Pfeiffer, and K. W. West, Phys. Rev. Lett. **93**, 146601 (2004).

[121] M. S. Garelli and J. Schliemann, Phys. Rev. B **80**, 155321 (2009).

[122] T. Andlauer, R. Morschl, and P. Vogl, Phys. Rev. B **78**, 075317 (2008).

[123] P. Brusheim and H. Q. Xu, Phys. Rev. B **75**, 195333 (2007).

[124] M. J. McLennan, Y. Lee, and S. Datta, Phys. Rev. B **43**, 13846 (1991).

[125] Y. Lee, M. J. McLennan, and S. Datta, Phys. Rev. B **43**, 14333 (1991).

[126] H. U. Baranger, D. P. DiVincenzo, R. A. Jalabert, and A. D. Stone, Phys. Rev. B **44**, 10637 (1991).

[127] H. U. Baranger and A. D. Stone, Phys. Rev. B **40**, 8169 (1989).

[128] H. Tamura and T. Ando, Phys. Rev. B **44**, 1792 (1991).

[129] Y. Wang, J. Wang, and H. Guo, Phys. Rev. B **49**, 1928 (1994).

[130] M. Leng and C. S. Lent, Phys. Rev. Lett. **71**, 137 (1993).

[131] D. Guan and U. Ravaioli, in *Nanotechnology, 2002. IEEE-NANO 2002. Proceedings of the 2002 2nd IEEE Conference on* (2002), pp. 413 – 416.

[132] K. E. Aidala, R. E. Parrott, T. Kramer, E. J. Heller, R. M. Westervelt, M. P. Hanson, and A. C. Gossard, Nature Phys **3**, 464 (2007).

[133] Y. Li and R. Tao, Phys. Rev. B **75**, 075319 (2007).

[134] G. D. Mahan, *Many Particle Physics*, Physics of Solids and Liquids (Springer Berlin / Heidelberg, 2000), 3rd ed.

[135] A. Cresti, R. Farchioni, G. Grosso, and G. P. Parravicini, Phys. Rev. B **68**, 075306 (2003).

[136] Q.-f. Sun and X. C. Xie, Phys. Rev. B **72**, 245305 (2005).

[137] J. Shi, P. Zhang, D. Xiao, and Q. Niu, Phys. Rev. Lett. **96**, 076604 (2006).

[138] P. Zhang, Z. Wang, J. Shi, D. Xiao, and Q. Niu, Phys. Rev. B **77**, 075304 (2008).

[139] Q.-f. Sun, X. C. Xie, and J. Wang, Phys. Rev. B **77**, 035327 (2008).

[140] Q.-f. Sun, H. Guo, and J. Wang, Phys. Rev. B **69**, 054409 (2004).

[141] H. van Houten, C. W. J. Beenakker, J. G. Williamson, M. E. I. Broekaart, P. H. M. van Loosdrecht, B. J. van Wees, J. E. Mooij, C. T. Foxon, and J. J. Harris, Phys. Rev. B **39**, 8556 (1989).

[142] J. Heremans, M. Santos, and M. Shayegan, Surface Science **305**, 348 (1994).

[143] A. A. Reynoso, G. Usaj, and C. A. Balseiro, Phys. Rev. B **78**, 115312 (2008).

[144] A. Reynoso, G. Usaj, and C. A. Balseiro, Phys. Rev. B **75**, 085321 (2007).

[145] R. M. Potok, J. A. Folk, C. M. Marcus, and V. Umansky, Phys. Rev. Lett. **89**, 266602 (2002).

[146] L. P. Rokhinson, L. N. Pfeiffer, and K. W. West, Phys. Rev. Lett. **96**, 156602 (2006).

[147] S. Bellucci and P. Onorato, Phys. Rev. B **68**, 245322 (2003).

[148] U. Zülicke, J. Bolte, and R. Winkler, New J. Phys. **9**, 355 (2007).

[149] J. Schliemann, Phys. Rev. B **77**, 125303 (2008).

[150] A. Reynoso, G. Usaj, M. J. Sánchez, and C. A. Balseiro, Phys. Rev. B **70**, 235344 (2004).

[151] G. Usaj and C. A. Balseiro, Phys. Rev. B **70**, 041301 (2004).

[152] X. F. Wang and P. Vasilopoulos, Phys. Rev. B **67**, 085313 (2003).

[153] C. W. J. Beenakker and H. v. Houten, Phys. Rev. B **39**, 10445 (1989).

[154] L. W. Molenkamp, A. A. M. Staring, C. W. J. Beenakker, R. Eppenga, C. E. Timmering, J. G. Williamson, C. J. P. M. Harmans, and C. T. Foxon, Phys. Rev. B **41**, 1274 (1990).

[155] T. Usuki, M. Saito, M. Takatsu, R. A. Kiehl, and N. Yokoyama, Phys. Rev. B **52**, 8244 (1995).

[156] V. Teodorescu and R. Winkler, Phys. Rev. B **80**, 041311 (2009).

[157] M. Dyakonov and V. Perel, Physics Letters A **35**, 459 (1971).

[158] J. E. Hirsch, Phys. Rev. Lett. **83**, 1834 (1999).

[159] E. M. Hankiewicz and G. Vignale, Phys. Rev. Lett. **100**, 026602 (2008).

[160] E. M. Hankiewicz, G. Vignale, and M. E. Flatté, Phys. Rev. Lett. **97**, 266601 (2006).

[161] S. Murakami, N. Nagaosa, and S.-C. Zhang, Science **301**, 1348 (2003).

[162] J.-i. Inoue, G. E. W. Bauer, and L. W. Molenkamp, Phys. Rev. B **67**, 033104 (2003).

[163] E. Hankiewicz, N. Sinitsyn, and J. Sinova, Journal of Superconductivity **18**, 151 (2005).

[164] R. Raimondi and P. Schwab, Phys. Rev. B **71**, 033311 (2005).

[165] A. Khaetskii, Phys. Rev. Lett. **96**, 056602 (2006).

[166] Y. Jiang and L. Hu, Phys. Rev. B **75**, 195343 (2007).

[167] J. J. Krich and B. I. Halperin, Phys. Rev. B **78**, 035338 (2008).

[168] Y. Xing, Q.-f. Sun, and J. Wang, Phys. Rev. B **77**, 115346 (2008).

[169] R. S. Chang, C. S. Chu, and A. G. Mal'shukov, Phys. Rev. B **79**, 195314 (2009).

[170] P. Brusheim and H. Q. Xu, Phys. Rev. B **74**, 205307 (2006).

[171] M. Governale and U. Zülicke, Phys. Rev. B **66**, 073311 (2002).

[172] B. K. Nikolić, L. P. Zârbo, and S. Welack, Phys. Rev. B **72**, 075335 (2005).

[173] B. K. Nikolić and L. P. Zârbo, EPL **77**, 47004 (2007).

[174] C. A. Perroni, D. Bercioux, V. M. Ramaglia, and V. Cataudella, J. Phys.: Condens. Matter **19**, 186227 (2007).

[175] F. Mireles and G. Kirczenow, Phys. Rev. B **64**, 024426 (2001).

[176] V. A. Zyuzin, P. G. Silvestrov, and E. G. Mishchenko, Phys. Rev. Lett. **99**, 106601 (2007).

[177] V. Edelstein, Solid State Commun. **73**, 233 (1990).

[178] M. Trushin and J. Schliemann, Phys. Rev. B **75**, 155323 (2007).

[179] J. Sinova, D. Culcer, Q. Niu, N. A. Sinitsyn, T. Jungwirth, and A. H. MacDonald, Phys. Rev. Lett. **92**, 126603 (2004).

[180] J. Wunderlich, B. Kaestner, J. Sinova, and T. Jungwirth, Phys. Rev. Lett. **94**, 047204 (2005).

[181] K. Nomura, J. Wunderlich, J. Sinova, B. Kaestner, A. H. MacDonald, and T. Jungwirth, Phys. Rev. B **72**, 245330 (2005).

[182] Y. K. Kato, R. C. Myers, A. C. Gossard, and D. D. Awschalom, Science **306**, 1910 (2004).

[183] V. Sih, W. H. Lau, R. C. Myers, V. R. Horowitz, A. C. Gossard, and D. D. Awschalom, Phys. Rev. Lett. **97**, 096605 (2006).

[184] N. P. Stern, S. Ghosh, G. Xiang, M. Zhu, N. Samarth, and D. D. Awschalom, Phys. Rev. Lett. **97**, 126603 (2006).

[185] B. A. Bernevig and S.-C. Zhang, Phys. Rev. Lett. **95**, 016801 (2005).

[186] A. Reynoso, G. Usaj, and C. A. Balseiro, Phys. Rev. B **73**, 115342 (2006).

[187] G. Y. Guo, Y. Yao, and Q. Niu, Phys. Rev. Lett. **94**, 226601 (2005).

[188] H.-A. Engel, B. I. Halperin, and E. I. Rashba, Phys. Rev. Lett. **95**, 166605 (2005).

[189] P. Lucignano, R. Raimondi, and A. Tagliacozzo, Phys. Rev. B **78**, 035336 (2008).

[190] K. Hattori and H. Okamoto, Phys. Rev. B **74**, 155321 (2006).

[191] L. Sheng and C. Ting, Physica E **33**, 216 (2006).

[192] C. Juan, Y. Yong-Hong, and W. Jun, Commun. Theor. Phys. **52**, 949 (2009).

[193] E. M. Hankiewicz, L. W. Molenkamp, T. Jungwirth, and J. Sinova, Phys. Rev. B **70**, 241301 (2004).

[194] J. Li, L. Hu, and S.-Q. Shen, Phys. Rev. B **71**, 241305 (2005).

[195] J. Li and S.-Q. Shen, Phys. Rev. B **76**, 153302 (2007).

[196] J. ichiro Ohe, A. Takeuchi, G. Tatara, and B. Kramer, Physica E **40**, 1554 (2008).

[197] J. J. Zhang, F. Liang, and J. Wang, Euro. Phys. J. B **72**, 105 (2009).

[198] E. Saitoh, M. Ueda, H. Miyajima, and G. Tatara, Appl. Phys. Lett. **88**, 182509 (2006).

[199] T. Kimura, Y. Otani, T. Sato, S. Takahashi, and S. Maekawa, Phys. Rev. Lett. **98**, 156601 (2007).

[200] S. O. Valenzuela and M. Tinkham, J. Appl. Phys. **101**, 09B103 (2007).

[201] S. O. Valenzuela and M. Tinkham, Nature **442**, 176 (2006).

[202] E. M. Hankiewicz, J. Li, T. Jungwirth, Q. Niu, S.-Q. Shen, and J. Sinova, Phys. Rev. B **72**, 155305 (2005).

[203] B. K. Nikolić and S. Souma, Phys. Rev. B **71**, 195328 (2005).

[204] J. Jacob, G. Meier, S. Peters, T. Matsuyama, U. Merkt, A. W. Cummings, R. Akis, and D. K. Ferry, J. Appl. Phys. **105**, 093714 (2009).

[205] A. A. Kiselev and K. W. Kim, Appl. Phys. Lett. **78**, 775 (2001).

[206] M. Yamamoto, T. Ohtsuki, and B. Kramer, Phys. Rev. B **72**, 115321 (2005).

[207] S. Bellucci, F. Carillo, and P. Onorato, J. Phys.: Condens. Matter **19**, 395018 (2007).

[208] S. Bellucci and P. Onorato, Phys. Rev. B **77**, 075303 (2008).

[209] T. Kubis and P. Vogl, phys. stat. sol. (c) **5**, 290 (2008).

[210] A. W. Cummings, R. Akis, D. K. Ferry, J. Jacob, T. Matsuyama, U. Merkt, and G. Meier, J. Appl. Phys. **104**, 066106 (2008).

[211] G. Schmidt, D. Ferrand, L. W. Molenkamp, A. T. Filip, and B. J. van Wees, Phys. Rev. B **62**, R4790 (2000).

[212] G. Khodaparast, R. Meyer, X. Zhang, T. Kasturiarachchi, R. Doezema, S. Chung, N. Goel, M. Santos, and Y. Wang, Physica E **20**, 386 (2004).

[213] A. M. Gilbertson, M. Fearn, J. H. Jefferson, B. N. Murdin, P. D. Buckle, and L. F. Cohen, Phys. Rev. B **77**, 165335 (2008).

[214] A. M. Gilbertson, W. R. Branford, M. Fearn, L. Buckle, P. D. Buckle, T. Ashley, and L. F. Cohen, Phys. Rev. B **79**, 235333 (2009).

[215] C. L. Kane and E. J. Mele, Phys. Rev. Lett. **95**, 226801 (2005).

[216] C. L. Kane and E. J. Mele, Phys. Rev. Lett. **95**, 146802 (2005).

[217] B. Büttner, C. X. Liu, G. Tkachov, E. G. Novik, C. Brüne, H. Buhmann, E. M. Hankiewicz, P. Recher, B. Trauzettel, S. C. Zhang, et al., Nature Phys **7**, 418 (2011).

[218] L. Fu and C. L. Kane, Phys. Rev. Lett. **100**, 096407 (2008).

[219] C. Nayak, S. H. Simon, A. Stern, M. Freedman, and S. Das Sarma, Rev. Mod. Phys. **80**, 1083 (2008).

[220] M. Büttiker, Science **325**, 278 (2009).

[221] R. Roy, Phys. Rev. B **79**, 195322 (2009).

[222] W. Feng, D. Xiao, J. Ding, and Y. Yao, Phys. Rev. Lett. **106**, 016402 (2011).

[223] S. Chen, X. G. Gong, C.-G. Duan, Z.-Q. Zhu, J.-H. Chu, A. Walsh, Y.-G. Yao, J. Ma, and S.-H. Wei, Phys. Rev. B **83**, 245202 (2011).

[224] H.-J. Zhang, S. Chadov, L. Müchler, B. Yan, X.-L. Qi, J. Kübler, S.-C. Zhang, and C. Felser, Phys. Rev. Lett. **106**, 156402 (2011).

[225] L. Fu and C. L. Kane, Phys. Rev. B **74**, 195312 (2006).

[226] X.-L. Qi, Y.-S. Wu, and S.-C. Zhang, Phys. Rev. B **74**, 045125 (2006).

[227] J. E. Moore and L. Balents, Phys. Rev. B **75**, 121306 (2007).

[228] R. Yu, X. L. Qi, A. Bernevig, Z. Fang, and X. Dai, Phys. Rev. B **84**, 075119 (2011).

[229] L. Fu and C. L. Kane, Phys. Rev. B **76**, 045302 (2007).

[230] D. Hsieh, D. Qian, L. Wray, Y. Xia, Y. S. Hor, R. J. Cava, and M. Z. Hasan, Nature **452**, 970 (2008), ISSN 0028-0836.

[231] Y. Xia, D. Qian, D. Hsieh, L. Wray, A. Pal, H. Lin, A. Bansil, D. Grauer, Y. S. Hor, R. J. Cava, et al., Nature Phys **5**, 398 (2009), ISSN 1745-2473.

[232] D. Pesin and L. Balents, Nature Phys **6**, 376 (2010), ISSN 1745-2473.

[233] C.-C. Liu, W. Feng, and Y. Yao, Phys. Rev. Lett. **107**, 076802 (2011).

[234] H. Zhang, C.-X. Liu, X.-L. Qi, X. Dai, Z. Fang, and S.-C. Zhang, Nature Phys **5**, 438 (2009).

[235] J. Vidal, X. Zhang, L. Yu, J.-W. Luo, and A. Zunger, Phys. Rev. B **84**, 041109 (2011).

[236] L. Fu, Phys. Rev. Lett. **106**, 106802 (2011).

[237] J. Pollmann and S. T. Pantelides, Phys. Rev. B **18**, 5524 (1978).

[238] P. Vogl (Academic Press, 1984), vol. 62 of *Advances in Electronics and Electron Physics*, pp. 101 – 159.

List of publications

- *Prediction of all electrical spin polarizer in InSb quantum wells*
  C. Schindler, and P. Vogl
  in preparation for Appl. Phys. Lett.

- *Relativistic sp^3d^5 tight-binding parametrization and effective envelope function approximation for HgTe/CdTe quantum wells*
  C. Schindler, and P. Vogl
  in preparation for Phys. Rev. B

- *Microscopic origin of topological insulators and the quantum spin Hall effect*
  C. Schindler, and P. Vogl
  submitted to Phys. Rev. B

- *Efficient method for the calculation of dissipative quantum transport*
  P. Greck, C. Schindler, and P. Vogl
  in preparation for Phys. Rev. B (rapid)

- *The nonequilibrium Green's function method and descendants: ways to avoid and to go*
  P. Greck, C. Schindler, T. Kubis, and P. Vogl
  doi: 10.1109/IWCE.2010.5677996 (2010)

- *Prediction of giant intrinsic spin-Hall effect in strained p-GaAs quantum wells*
  C. Schindler and P. Vogl
  Journal of Physics: Conference Series **193**, 012103 (2009)

- *Ballistic quantum transport using the contact block reduction (CBR) method*
  R. Birner, C. Schindler, P. Greck, M. Sabathil, and P. Vogl
  Journal of Computational Electronics **8**, 267 (2009)

- *Coherent potential approximation for spatially correlated disorder*
  R. Zimmermann and C. Schindler
  Phys. Rev. B **80**, 144202 (2009)

- *Analysis of exciton-exciton interaction in semiconductor quantum wells*
  C. Schindler and R. Zimmermann
  Phys. Rev. B **78**, 045313 (2008)

- *Exciton-Exciton interaction in coupled quantum wells*
  R. Zimmermann and C. Schindler
  Solid State Comm. **144**, 395 (2007)

Acknowledgments

Ich möchte die Gelegenheit nutzen, um all denen zu danken, die mich während der Zeit der Doktorarbeit unterstützt haben. Allen voran danke ich meinem Betreuer Prof. Dr. Peter Vogl für die Ermöglichung der Arbeit, die fortwährende Betreuung und konstruktive Zusammenarbeit sowie die großzügige Förderung duch Bereitstellung einer idealen Arbeitsumgebung. Mein besonderer Dank gilt Prof. Vogls Verständnis und Entgegenkommen sowohl bei wissenschaftlichen Fragen und Problemen als auch bei privaten Angelegenheiten.

Allen derzeitigen und ehemaligen Kollegen am Lehrstuhl T33 danke ich für die gute Zusammenarbeit und Arbeitsatmosphäre. Dabei möchte ich besonders Dr. Stefan Birner, Thomas Eisfeller und Peter Greck hervorheben. Durch die vielen fachlichen Diskussionen und den ständigen wissenschaftlichen Austausch wurde meine Arbeit sehr bereichert.

Ich möchte mich ebenso bei unseren Sekretärinnen Veronika Enter und Joana Figueiredo für die große Hilfsbereitschaft bei allen Verwaltungsaufgaben und organisatorischen Problemen bedanken.

Mein Dank gilt weiterhin meiner Mutter, die mir duch ihre ständige Unterstützung die Ausbildung bis hin zur Promotion überhaupt erst ermöglicht hat und meiner Freundin Sabine Teichmann für die liebevolle und geduldige Unterstützung gerade in der heißen Phase meiner Arbeit.